

# **Ultra-Short Nacelles for Low Fan Pressure Ratio Propulsors**

by

Andreas Peters

Submitted to the Department of Aeronautics and Astronautics  
in partial fulfillment of the requirements for the degree of

Doctor of Philosophy

at the

MASSACHUSETTS INSTITUTE OF TECHNOLOGY

February 2014

© Massachusetts Institute of Technology 2014. All rights reserved.

Author .....  
Department of Aeronautics and Astronautics  
November 27, 2013

Certified by .....  
Zoltán S. Spakovszky  
Professor of Aeronautics and Astronautics  
Thesis Supervisor

Certified by .....  
Edward M. Greitzer  
Professor of Aeronautics and Astronautics  
Thesis Committee

Certified by .....  
Mark Drela  
Professor of Aeronautics and Astronautics  
Thesis Committee

Accepted by .....  
Paulo C. Lozano  
Associate Professor of Aeronautics and Astronautics  
Chair, Graduate Program Committee



# Ultra-Short Nacelles for Low Fan Pressure Ratio Propulsors

by

Andreas Peters

Submitted to the Department of Aeronautics and Astronautics  
on November 27, 2013, in partial fulfillment of the  
requirements for the degree of  
Doctor of Philosophy

## Abstract

This thesis addresses the uncharted inlet and nacelle design space for low pressure ratio fans for advanced aeroengines. A key feature in low fan pressure ratio (FPR) propulsors with short inlets and nacelles is the increased coupling between fan and inlet. The thesis presents an integrated fan-nacelle design framework, combining a spline-based tool for the definition of inlet and nacelle surfaces with a fast and reliable body-force-based approach for the fan rotor and stator blade rows. The new capability captures the inlet-fan and fan-exhaust interactions and the flow distortion at the fan face and enables the parametric exploration of the short-inlet design territory. The interaction of the rotor with a region of high streamwise Mach number at the fan face is identified as the key aerodynamic mechanism limiting the design of short inlets. The local increase in streamwise Mach number is due to flow acceleration along the inlet internal surface coupled with a reduction in effective flow area. For a candidate short-inlet design with inlet length to fan diameter ratio  $L/D = 0.19$ , the streamwise Mach number at the fan face near the shroud increases by up to 0.16 at cruise and by up to 0.36 at off-design conditions relative to a long-inlet baseline propulsor with  $L/D = 0.5$ . As a consequence, the rotor locally operates close to choke, resulting in fan efficiency penalties of up to 1.6 % at cruise and 3.9 % at off-design. For inlets with  $L/D < 0.25$ , the benefit from reduced nacelle drag is offset by the reduction in fan efficiency, resulting in propulsive efficiency penalties. Based on a parametric inlet study, the recommended inlet  $L/D$  for engine propulsive efficiency benefits is suggested to be between 0.25 and 0.4. A candidate design with  $L/D = 0.25$  maintains the cruise propulsive efficiency of the baseline case without jeopardizing fan and LPC stability at off-design conditions. On the aircraft system level, fuel burn benefits are conjectured to be feasible due to the reductions in nacelle weight and drag compared to an aircraft powered by the long-inlet baseline propulsor.

Thesis Supervisor: Zoltán S. Spakovszky  
Title: Professor of Aeronautics and Astronautics



## Acknowledgments

There are many to whom I owe a debt of gratitude, and without each of these people I would not have been able to succeed at MIT. First and most importantly, I would like to thank my advisor Professor Zoltán Spakovszky for giving me the opportunity to join the Gas Turbine Laboratory and introducing me to the turbomachinery community. His enthusiasm, knowledge, and guidance were invaluable in my growth as an engineer. He has been a tremendous mentor and an indispensable source of advice both within and outside of academic research and I am extremely grateful for his support and encouragement throughout my MIT career. I will never forget our great discussions during the many trips to East Hartford.

I would like to thank all members of my thesis committee for both their time and helpful feedback. I am greatly indebted to Professor Ed Greitzer, who was a source of clear advice and provided perspective and insight on the research at all times. I wish to thank Professor Mark Drela for sharing his great expertise and ideas throughout this project. I am most grateful to Professor Nick Cumpsty for his feedback and advice.

This thesis was supported by Pratt & Whitney, which is gratefully acknowledged. At Pratt & Whitney, I wish to first thank Wes Lord, Gavin Hendricks, Becky Rose, and Yuan Dong for their support, insight, and many inspiring and fruitful discussions. I am indebted to Robert Malecki, Yuan Qiu, and Steven Zysman for their essential help in the design of the baseline configuration and their input on the inlet and nacelle design process and criteria. I would like to thank Kingsley Chuang, Ding Li, Aamir Shabbir, and Beth Lurie for the insightful discussions about this research, in particular regarding the development and implementation of the body force method. I greatly appreciate the invaluable perspective provided by Jayant Sabnis, Stephen Morford, Alan Epstein, Ray-Sing Lin, Ed Gallagher, Greg Tillman, and Robert Miller throughout this project.

At Numeca USA, I would like to thank Róque Lopez and Alain Demeulenaere for their patient assistance with FINE/Turbo and David Gutzwiller for his support

in providing a custom version of the solver which enabled the implementation of the body force method.

I owe thanks to many members of the Gas Turbine Laboratory for making the lab a great place to work. Their camaraderie and feedback were great motivators for tackling the challenges of this research. I am most thankful to Choon Tan for always being available to answer fluid dynamic and turbomachinery questions and for the many enlightening discussions about the state of the aerospace industry and the global economy. I am particularly indebted to my labmates Jon Everitt, Jeff Defoe, Sho Sato, and David Hall for their friendship, help, and encouragement at all times. A special thanks to Jeff for his extraordinary efforts in solving computer issues and for teaching me how to run a network. I am also grateful to Max Brand and Anjaney Kottapalli for many helpful discussions on the intricacies of body force modeling.

At MIT, I would like to thank my friends François, Björn, Leo, Sunny, Glenn, Jaime, Sam, Beenie, Britt, Josh, Irene, Fabio, Blair, Arde, Liz, and Jeff for making Cambridge such a great place to live and work and for distracting me just enough that I did not start seeing body forces everywhere. A special shout-out to my best friends Philip, Timo, Holger, and especially David and Johannes back in Germany for always being there for me and keeping the cross-Atlantic phone lines busy.

To my family, I would like to express the deepest gratitude for shaping me into the person I am today. Finally, I want to thank my wife Anneli for her unwavering encouragement and support. Without her love, friendship, and understanding, I could not have made it to this point.

# Contents

<b>1</b>	<b>Introduction</b>	<b>31</b>
1.1	Motivation . . . . .	34
1.2	Research Questions and Goals . . . . .	34
1.3	Challenges . . . . .	35
1.4	Major Findings and Contributions . . . . .	36
1.4.1	A New Capability to Design Short Inlets and Nacelles . . . . .	38
1.4.2	Characterization of Limiting Aerodynamic Mechanisms . . . . .	39
1.4.3	Candidate Short-Inlet Design ( $L/D = 0.25$ ) with System Level Performance Benefits . . . . .	42
1.4.4	Pushing the Limits in Short-Inlet Designs . . . . .	45
1.5	Organization of Thesis . . . . .	46
<b>2</b>	<b>Literature Review</b>	<b>47</b>
2.1	Previous Work on Low-FPR Propulsor Performance . . . . .	47
2.2	Foundational Work on Body Force Approaches in Turbomachinery . .	51
<b>3</b>	<b>Body Force Source Term Modeling for Turbomachinery Flows</b>	<b>55</b>
3.1	Body Force Representation of Axial Rotor and Stator Blade Rows . .	55
3.2	Governing Equations for the Body Force Approach . . . . .	59
3.3	Modified Body Force Method . . . . .	61
3.3.1	Modified Normal Force Description . . . . .	63
3.3.2	Modified Viscous Force Description . . . . .	65
3.4	Force Extraction from Steady RANS Simulations . . . . .	66
3.5	Applicability and Limitations of the Body Force Method . . . . .	69

<b>4 Capabilities and Validation of Body Force Method</b>	<b>73</b>
4.1 Off-Design Performance . . . . .	73
4.1.1 Inlet Flow-Fan Coupling . . . . .	79
4.1.2 Distortion Transfer . . . . .	81
4.1.3 System-Level Propulsor Performance . . . . .	84
<b>5 Inlet and Nacelle Design Framework</b>	<b>87</b>
5.1 Inlet and Nacelle Design Parameters . . . . .	87
5.2 Inlet Length Study . . . . .	89
5.3 New Capability to Define Inlet and Nacelle Geometries . . . . .	91
5.4 Computational Approach . . . . .	95
5.4.1 CFD Tool Description . . . . .	96
5.4.2 Full-Domain Computational Setup . . . . .	97
5.4.3 Full-Domain Unsteady RANS Simulations . . . . .	99
5.4.4 Validation and Grid Convergence . . . . .	100
<b>6 Long-Inlet Baseline Configuration</b>	<b>105</b>
6.1 Baseline Propulsor Design Characteristics . . . . .	105
6.2 Dissection of Distortion Transfer Mechanisms . . . . .	108
<b>7 Metrics and Sensitivities</b>	<b>113</b>
7.1 Operating Conditions . . . . .	113
7.2 Performance Metrics . . . . .	117
7.3 Calculation of Engine Propulsive Efficiency from CFD Simulations . .	119
7.3.1 Net Thrust Minus Nacelle External Drag . . . . .	119
7.3.2 Thrust/Drag Split and Nacelle Drag Breakdown . . . . .	121
7.3.3 Shaft Power Input . . . . .	126
7.4 Sensitivity Analysis - What Matters Most? . . . . .	127
<b>8 Short Inlet and Nacelle Design Strategy</b>	<b>129</b>
8.1 Design Requirements and Challenges . . . . .	129
8.2 Limiting the Short-Inlet Design Space . . . . .	136

8.3	Design Approach and Guidelines . . . . .	140
8.3.1	Top Inlet and Nacelle Section . . . . .	141
8.3.2	Bottom Inlet and Nacelle Section . . . . .	142
8.4	Spinner Design . . . . .	144
8.5	Re-Cambered Rotor Blade Design . . . . .	148
8.6	Mitigating the Pylon Upstream Influence . . . . .	154
<b>9</b>	<b>Candidate Short-Inlet Design - L/D = 0.25</b>	<b>157</b>
9.1	Overview of Design Characteristics and Performance . . . . .	157
9.2	Performance at Cruise . . . . .	161
9.3	Performance at Off-Design Conditions . . . . .	165
9.4	Evaluation of Design Criteria at Wing C <sub>Lmax</sub> . . . . .	171
9.4.1	Core Inflow Stagnation Pressure Distortion . . . . .	172
9.4.2	Time-Dependent Blade Loading . . . . .	173
<b>10</b>	<b>Candidate Short-Inlet Design - L/D = 0.19</b>	<b>175</b>
10.1	Overview of Design Characteristics and Performance . . . . .	175
10.2	Performance at Cruise . . . . .	178
10.3	Performance at Off-Design Conditions . . . . .	181
10.4	Advanced Concepts . . . . .	185
10.4.1	Pitched Fan Case . . . . .	185
10.4.2	Blow-In Doors at Cross-Wind . . . . .	187
<b>11</b>	<b>Conclusions and Future Work</b>	<b>193</b>
11.1	Summary . . . . .	193
11.2	Synthesis of Short-Inlet Design Strategy . . . . .	196
11.3	Key Outcomes and Conclusions . . . . .	198
11.4	Recommendations for Future Work . . . . .	201
<b>A</b>	<b>Original Blade Passage Model by Gong</b>	<b>217</b>
A.1	Interpretation of Normal Force Formulation . . . . .	217

A.1.1	Derivation of Normal Force Component Due to Blade Loading $\vec{f}_{n_{\nabla p}}$	217
A.1.2	Derivation of Normal Force Component Due to Response to Change in Local Deviation $\vec{f}_{n_\delta}$	220
A.2	Discussion of Gong's Body Force Model	223
<b>B</b>	<b>Force Extraction from Steady RANS Simulations</b>	<b>227</b>
<b>C</b>	<b>Implementation of Body Force Method in Existing Flow Solvers</b>	<b>235</b>
<b>D</b>	<b>Improved Body Force Method</b>	<b>237</b>
D.1	Improved Normal Body Force Model	237
D.2	Improved Parallel Body Force Model	242
D.3	Validation of Improved Body Force Model	243
<b>E</b>	<b>Pylon and Bifurcation Geometry Definition and Grid Generation</b>	<b>245</b>

# List of Figures

1-1	Trends in fuel burn (from [1]) . . . . .	32
1-2	Trends in bypass ratio (from [2]). . . . .	32
1-3	Increase in bypass propulsive efficiency with reduction in fan pressure ratio (from [3]). . . . .	33
1-4	Influence of fan diameter on noise and fuel burn (from [4]). . . . .	34
1-5	Axial Mach number and streamline distribution based on body force simulations for $L/D = 0.5$ baseline (left) and $L/D = 0.25$ candidate short-inlet (right) propulsors at the cruise aerodynamic design point (ADP) with flight Mach number $M_0 = 0.8$ and angle-of-attack $AoA = 5^\circ$ (the dashed lines represent the approximate fan rotor and FEGV leading and trailing edges). . . . .	41
1-6	Axial Mach number and streamline distribution based on body force simulations for $L/D = 0.5$ baseline (left) and candidate $L/D = 0.25$ (right) short-inlet configurations at the wing $C_{L\max}$ operating condition with flight Mach number $M_0 = 0.25$ and angle-of-attack $AoA = 29^\circ$ . . . . .	42
1-7	Top and bottom inlet and nacelle sections for the $L/D = 0.5$ baseline design and the $L/D = 0.19$ and $L/D = 0.25$ candidate short-inlet designs. . . . .	43
1-8	Contributions to change in cruise engine propulsive efficiency relative to long-inlet baseline from reduction in inlet length and re-design of baseline rotor and FEGV. . . . .	44

3-1	Baseline fan stage modeled with body force fields (geometry distorted). . . . .	56
3-2	Relative flow through discrete blade passage (left) and relative flow through body force field (right). . . . .	57
3-3	Dependence of axisymmetric body force field on local flow conditions (from Kerner [5]). . . . .	58
3-4	Blade passage flow with forces normal and parallel $f_{n'}$ and $f_{p'}$ (from Gong [6], left) and definition of blade lean (right). . . . .	64
3-5	Fan pressure ratio at the take-off operating condition ( $M_0 = 0.25$ ). The results from RANS and body force simulations are plotted as solid and dashed lines, respectively. A constant viscous body force coefficient $K_p = const.$ is used in the body force simulations. As a result, the off-design loss generation is not captured. . . . .	65
3-6	Overview of body force methodology. A single set of body force distributions captures the fan stage performance over the entire speedline. . . . .	67
3-7	Polynomial body force description determined from blade force and flow field results extracted from steady, single-passage RANS results. . . . .	68
4-1	Stagnation pressure rise coefficient at the take-off operating condition ( $M_0 = 0.25$ ) for uniform inlet flow and 5° counter- and co-swirl. For a single set of body force coefficients, the rotor performance is captured over the entire speedline. . . . .	74
4-2	Fan efficiency at the take-off operating condition ( $M_0 = 0.25$ ) for uniform inlet flow and 5° counter- and co-swirl. . . . .	75
4-3	Rotor stagnation pressure loss at the take-off operating condition ( $M_0 = 0.25$ ) for uniform inlet flow and 5° counter- and co-swirl. . . . .	75
4-4	Quantitative (left) and qualitative (right) comparison of absolute flow angle from steady, single-passage RANS and body force simulations. . . . .	76



4-11	Variation of local rotor operating conditions along the circumference at mid-span for the baseline configuration with $L/D = 0.5$ (left) and the candidate short-inlet configuration with $L/D = 0.19$ (right) at wing $C_{L\max}$ operating condition ( $M_0 = 0.25$ and $AoA = 29^\circ$ ). . . . .	83
4-12	Stagnation pressure distribution for baseline $L/D = 0.5$ configuration at cruise ( $M_0 = 0.8$ and $AoA = 5^\circ$ ). Distortion transfer and interaction of bypass stream with pylon and nacelle downstream of the propulsor are captured in the body force simulations. . . . .	85
5-1	Inlet and nacelle design parameters for the baseline propulsor. . . . .	88
5-2	Cruise nacelle drag breakdown from preliminary parametric inlet length study using body force simulations. . . . .	90
5-3	Piecewise inlet and nacelle geometry definition using Bezier curves.	92
5-4	Bezier curve description of top inlet and nacelle shapes with control points marked by x-symbols. . . . .	93
5-5	Inlet and nacelle solid surfaces for grid generation. . . . .	95
5-6	Overview of inlet and nacelle design framework. . . . .	96
5-7	Modular grid setup for full-domain body force or URANS simulations. . . . .	98
5-8	Fan pressure ratio (left) and rotor efficiency (right) from internal steady, single-passage RANS simulations at cruise for coarse, medium, and fine grid levels. . . . .	101
5-9	Cruise engine propulsive efficiency from preliminary parametric inlet length study using body force simulations on coarse and medium level grids. . . . .	104
5-10	Nacelle viscous drag (left) and total equivalent shaft power input from preliminary parametric inlet length study using body force simulations for coarse and medium grid levels. . . . .	104
6-1	Baseline propulsor with $L/D = 0.5$ . The variable-area nozzle is set to the cruise condition. . . . .	106

6-2	Core inflow and exhaust domains for the baseline propulsor with absolute Mach number distribution at cruise. . . . .	107
6-3	Overview of computational approach for the dissection of the distortion transfer mechanisms in the long-inlet baseline propulsor at cruise ( $M_0 = 0.8$ ). . . . .	109
6-4	Fan face incidence and stagnation pressure distortion downstream of the rotor at cruise. . . . .	110
6-5	Superposition of the contributions from non-uniform inflow and pylion/bifurcation upstream influence to the circumferential stagnation pressure distortion in the long-inlet baseline propulsor at cruise. . .	111
7-1	Mach number distribution and upstream dividing streamlines at cruise (top left), wing $C_{L\max}$ (top right), and cross-wind (bottom) operating conditions for baseline propulsor. . . . .	115
7-2	Mach number distribution and upstream dividing streamlines at take-off rotation (left) and take-off level operating conditions for baseline propulsor. . . . .	116
7-3	Control volume definition for the calculation of propulsive efficiency. .	118
7-4	Control volume 1 for the calculation of net thrust minus nacelle external drag from three-dimensional CFD simulations. . . . .	121
7-5	Control volumes 2 and 3 for the breakdown of thrust and nacelle viscous and pressure drag from three-dimensional CFD simulations. .	122
7-6	Pressurization of core cowl and plug due to external flow effect in an unchoked nozzle. . . . .	123
7-7	Engine capture streamtube (upstream dividing stream-surface) and bypass exhaust streamtube (downstream dividing stream-surface) extracted from body force results for the baseline propulsor at cruise. .	124
7-8	Comparison of propulsive efficiency computed based on two different formulations for net thrust minus nacelle external drag. . . . .	126

7-9	Core exhaust streamtube and axial velocity distribution at $p = p_0$ (left) and core exhaust streamtube cross-section (right) extracted from body force simulation for baseline propulsor at cruise. . . . .	127
7-10	Sensitivity of engine propulsive efficiency with respect to changes in rotor efficiency and nacelle drag contributions at cruise. . . . .	128
8-1	Dividing streamlines between internal and external flows for a candidate inlet design with $L/D = 0.19$ at critical operating conditions. . .	130
8-2	Distributions of inlet area (top) and averaged Mach number (center) through the inlet and isentropic Mach number along the bottom inlet surface (bottom) for $L/D = 0.5$ , $L/D = 0.25$ , and $L/D = 0.19$ propulsors at cruise. . . . .	133
8-3	Rotor incidence distortion mechanisms (incidence distribution shown at wing $C_{L\max}$ operating condition for candidate short-inlet design with inlet $L/D = 0.19$ ). . . . .	135
8-4	Mach number distribution at cruise (left) and axial Mach number distribution at wing $C_{L\max}$ operating condition (right) for candidate short-inlet propulsors with $L/D = 0.10$ and $L/D = 0.02$ . . . . .	137
8-5	Time-averaged URANS results of the circumferential variation of rotor incidence at mid-span (left) and orbits of local rotor operating conditions along the circumference at mid-span for the baseline configuration with $L/D = 0.5$ and the short-inlet configurations with $L/D = 0.1$ and $L/D = 0.02$ at wing $C_{L\max}$ operating condition. . .	137
8-6	Example for top inlet and nacelle shape description based on the supercritical airfoil NASA SC(2)-0170 [7]. . . . .	142
8-7	Parametric description of bottom inlet leading edge. . . . .	143
8-8	Axial Mach number and streamline distributions based on body force simulations for $L/D = 0.2$ inlet with baseline spinner (top), extended spinner (center), and bulged spinner (bottom) designs at cruise (left) and wing $C_{L\max}$ (right). . . . .	145

8-9	Isentropic Mach number along nacelle external and inlet surfaces at top (left) and bottom (right) for $L/D = 0.2$ nacelle design with baseline and extended spinner shapes at cruise. . . . .	146
8-10	Spanwise profiles of axial Mach number (left) and rotor incidence relative to mid-span incidence (right) for $L/D = 0.2$ nacelle with baseline and extended spinner shapes at wing $C_{L\max}$ . . . . .	147
8-11	Increase in the rotor incidence distortion for the candidate short-inlet designs with $L/D = 0.25$ (center) and $L/D = 0.19$ (right) at cruise compared to the long-inlet baseline propulsor (left). The results are for the baseline rotor design and were computed using URANS simulations. . . . .	149
8-12	Rotor stagnation pressure loss at cruise (left) and wing $C_{L\max}$ (right) operating conditions. . . . .	150
8-13	Absolute flow angle distributions at the fan face for the candidate short-inlet designs with $L/D = 0.25$ (center) and $L/D = 0.19$ (right) compared to the long-inlet baseline propulsor (left) at the wing $C_{L\max}$ operating condition. . . . .	151
8-14	Camber line distribution for baseline and re-cambered blade (left) and change in local blade metal angle $\kappa$ along the chord (right) for $\Delta\kappa_{LE,tip} = -2^\circ$ . . . . .	152
8-15	Fan efficiency results from steady, single-passage RANS simulations with uniform inflow at cruise with shift of peak efficiency operating point to higher corrected flows for re-cambered rotor designs relative to baseline rotor. . . . .	153
8-16	Change in fan efficiency for re-cambered rotor design relative to baseline rotor in the $L/D = 0.25$ candidate short-inlet design from steady, full-domain RANS simulations at the cruise and wing $C_{L\max}$ operating conditions. . . . .	154

8-17	Instantaneous static pressure coefficient distribution at 95 % span for the $L/D = 0.19$ candidate short-inlet design at cruise extracted from a URANS simulation. . . . .	155
9-1	Top and bottom inlet and nacelle sections for the baseline configuration with $L/D = 0.5$ and the $L/D = 0.25$ candidate short-inlet design. . . . .	158
9-2	Mach number distribution (top) and axial Mach number distribution (bottom) for the baseline propulsor (left) and the candidate short-inlet design with $L/D = 0.25$ (right) at cruise. . . . .	162
9-3	Isentropic Mach number along nacelle external surface at three circumferential locations for the baseline propulsor ( $L/D = 0.5$ ) and the candidate short-inlet configuration ( $L/D = 0.25$ ) at cruise. . . . .	163
9-4	Time-averaged spanwise profiles of axial Mach number (left) and rotor incidence relative to mid-span incidence (right) at the fan face for the baseline propulsor ( $L/D = 0.5$ ) and the candidate short-inlet configuration ( $L/D = 0.25$ ) at cruise. . . . .	165
9-5	Mach number distribution (top) and axial Mach number distribution (bottom) for the baseline propulsor (left) and the candidate short-inlet design with $L/D = 0.25$ (right) at the wing $C_{L_{max}}$ condition. . . . .	166
9-6	Static pressure coefficient along lower inlet lip for the baseline propulsor ( $L/D = 0.5$ ) and the candidate short-inlet configuration ( $L/D = 0.25$ ) at the wing $C_{L_{max}}$ operating condition. . . . .	167
9-7	Time-averaged spanwise profiles of axial Mach number (left) and rotor incidence relative to mid-span incidence (right) at the fan face for the baseline propulsor ( $L/D = 0.5$ ) and the candidate short-inlet configuration ( $L/D = 0.25$ ) at the wing $C_{L_{max}}$ operating condition. . . . .	168
9-8	Difference in rotor incidence (left) and fan efficiency (right) for the candidate short-inlet design with $L/D = 0.25$ relative to the long-inlet baseline propulsor (left) at the wing $C_{L_{max}}$ condition. . . . .	168

9-9	Mach number distributions for the baseline propulsor (left) and the candidate short-inlet design with $L/D = 0.25$ (right) at the T/O rotation and T/O level operating conditions. . . . .	169
9-10	Circumferential stagnation pressure variation at mid-span of core inlet duct for the baseline propulsor ( $L/D = 0.5$ ) and the candidate short-inlet configurations ( $L/D = 0.25$ and $L/D = 0.19$ ) at the wing $C_{L\max}$ operating condition. . . . .	172
9-11	Time-dependent variation of blade lift coefficient at mid-span (top) and 90 % span for the baseline ( $L/D = 0.5$ ) and the candidate short-inlet configurations ( $L/D = 0.25$ and $L/D = 0.19$ ) at the wing $C_{L\max}$ operating condition. . . . .	174
10-1	Top and bottom inlet and nacelle sections for the baseline $L/D = 0.5$ and the $L/D = 0.25$ and $L/D = 0.19$ candidate short-inlet designs. . .	176
10-2	Mach number distribution (top) and axial Mach number distribution (bottom) for the baseline propulsor (left) and the candidate short-inlet design with $L/D = 0.19$ (right) at cruise. . . . .	178
10-3	Isentropic Mach number along nacelle external surface at three circumferential locations for the baseline propulsor ( $L/D = 0.5$ ) and the candidate short-inlet configurations ( $L/D = 0.25$ and $L/D = 0.19$ ) at cruise. . . . .	179
10-4	Time-averaged spanwise profiles of axial Mach number (left) and rotor incidence relative to mid-span incidence (right) at the fan face for the baseline propulsor ( $L/D = 0.5$ ) and the candidate short-inlet configurations ( $L/D = 0.25$ and $L/D = 0.19$ ) at cruise. . . . .	180
10-5	Mach number distribution (top) and axial Mach number distribution (bottom) for the baseline propulsor (left) and the candidate short-inlet design with $L/D = 0.19$ (right) at the wing $C_{L\max}$ condition. .	181

10-6	Static pressure coefficient along lower inlet lip for the baseline propulsor ( $L/D = 0.5$ ) and the candidate short-inlet configurations ( $L/D = 0.25$ and $L/D = 0.19$ ) at the wing $C_{L\max}$ operating condition. . . . .	182
10-7	Time-averaged spanwise profiles of axial Mach number (left) and rotor incidence relative to mid-span incidence (right) at the fan face for the baseline propulsor ( $L/D = 0.5$ ) and the candidate short-inlet configurations ( $L/D = 0.25$ and $L/D = 0.19$ ) at the wing $C_{L\max}$ operating condition. . . . .	183
10-8	Difference in rotor incidence (left) and fan efficiency (right) for the candidate short-inlet design with $L/D = 0.19$ relative to the long-inlet baseline propulsor (left) at the wing $C_{L\max}$ condition. . . . .	183
10-9	Mach number distribution for the baseline propulsor (left) and the candidate short-inlet design with $L/D = 0.19$ (right) at the T/O rotation and T/O level operating conditions. . . . .	184
10-10	Pitched fan case concept. . . . .	186
10-11	Rotor incidence distortion for the baseline long-inlet configuration (left) and the short-inlet designs without (center) and with a pitched fan case (right) at the cruise condition. . . . .	186
10-12	Variation of rotor incidence at 10 % span (left), 50 % span (center), and 90 % span (right) for the baseline inlet and the $L/D = 0.19$ design with and without pitched fan case configuration at cruise. . .	187
10-13	Time-averaged distributions of Mach number (left) and entropy (right) for the baseline inlet (left) and the candidate short-inlet design with $L/D = 0.19$ (right) at the cross-wind operating condition. . . . .	188
10-14	Computational model of blow-in doors in inlet of $L/D = 0.19$ candidate design. . . . .	190
10-15	Time snapshot of distributions of Mach number (top) and stagnation pressure at the fan face (bottom) for the candidate short-inlet design with solid inlet (right) and blow-in doors in the inlet (right) at the cross-wind operating conditions. . . . .	191

10-16 Increase in corrected flow and fan efficiency due to blow-in doors in the candidate short inlet with $L/D = 0.19$ at the cross-wind operating condition. . . . .	191
11-1 Hypothesized optimum in propulsive efficiency with inlet $L/D$ (bottom) as a result of the competing effects between fan efficiency, nacelle external drag and inlet pressure recovery (top). . . . .	200
A-1 Normal force component due to blade loading. . . . .	218
A-2 Gong's blade passage with forces normal and parallel to local flow direction, $f_{n_\delta}$ and $f_p$ . . . . .	221
A-3 Example blade passage with blade metal angle $\kappa = 0$ to illustrate inconsistency in Equation A.24. . . . .	224
A-4 Normal force at positive incidence (near stall), zero incidence (design), and negative incidence (near choke). . . . .	225
A-5 Normal force due to change in local deviation $\frac{f_{n_\delta}}{A(p_{t0}-p_0)B}$ for T/O corrected speed. Positive leading edge incidence near stall results in a positive $f_{n_\delta}$ , while negative incidence near choke leads to negative force values (geometry distorted). . . . .	226
B-1 Overview of the calculation of the net blade force normal to the pitchwise-averaged relative flow from single-passage RANS simulations. . . . .	228
B-2 Interpolation of camber surface geometry and blade metal angle onto body force grid (geometry distorted). . . . .	230
B-3 Blade leading edge geometry near rotor hub with unit vectors normal to relative flow along camber line (geometry distorted). . . . .	231
B-4 Cross-passage length normal to the local pitchwise-averaged relative flow direction used in the calculation of the net blade force. . . . .	233
B-5 Net force normal to relative flow along camber line on body force grid near rotor hub (geometry distorted). . . . .	234

C-1	Meridional grid used for body force simulations (distorted). . . . .	236
D-1	Relative streamlines through passage with discrete blades (left) and pitchwise-averaged relative streamlines (right). . . . .	238
D-2	Chordwise distributions of the smeared out blade force determined from the surface pressures and the normal force computed from the pitchwise-averaged streamline curvature and normal pressure gradient components for the fan rotor at mid-span. . . . .	241
D-3	Spanwise profile of relative difference in stagnation pressure rise coefficient between improved body force method and steady, single-passage RANS results at the cruise design point (left) and mass-averaged stagnation pressure rise coefficient across the fan operating range (right). The dashed lines correspond to $\pm 7\%$ relative error. The plots are adopted from Brand [8]. . . . .	243
E-1	Pylon fairing cross-sections at the hub and shroud (top, distorted) and leading and trailing edge locations in the meridional plane (bottom). . . . .	246
E-2	Pylon mesh at mid-span (coarse grid level). . . . .	247
E-3	Extent of pylon grid domain in meridional plane. . . . .	247

# List of Tables

5.1	Range of typical values for inlet and nacelle design parameters . . . . .	89
5.2	Comparison of computational cost for unsteady RANS and body force simulations . . . . .	99
5.3	Computed baseline configuration performance at cruise normalized by design point cycle data provided by the industry partner. . . . .	102
7.1	Operating conditions. . . . .	114
8.1	Performance overview of short-inlet propulsors with $L/D = 0.19$ , $L/D = 0.10$ and $L/D = 0.02$ relative to $L/D = 0.5$ baseline configuration. . . . .	138
8.2	Evaluation of inlet leading edge orientation angle $\gamma$ as part of a parameter study for the bottom inlet shape. . . . .	143
9.1	Inlet and nacelle design parameters for the baseline and be $L/D = 0.25$ candidate short-inlet designs. . . . .	159
9.2	Performance overview of the $L/D = 0.25$ candidate short-inlet propulsor relative to the $L/D = 0.5$ baseline. . . . .	160
9.3	Relative change in nacelle drag for the $L/D = 0.25$ design compared to the $L/D = 0.5$ baseline. . . . .	163
9.4	Drag breakdown for the $L/D = 0.25$ design compared to the $L/D = 0.5$ baseline. . . . .	163

9.5	Loss breakdown relative to an isolated ducted propulsor with ideal propulsive efficiency into internal and external losses for the $L/D = 0.25$ design with pylon and bifurcation compared to the $L/D = 0.5$ baseline. . . . .	164
10.1	Inlet and nacelle design parameters for the baseline and the $L/D = 0.25$ and $L/D = 0.19$ candidate short-inlet designs. . . . .	177
10.2	Performance overview of the $L/D = 0.19$ and $L/D = 0.25$ candidate short-inlet propulsors relative to the $L/D = 0.5$ baseline. . . . .	177
10.3	Relative change in nacelle drag for the $L/D = 0.25$ and $L/D = 0.19$ designs compared to the $L/D = 0.5$ baseline. . . . .	179
10.4	Drag breakdown for the $L/D = 0.25$ and $L/D = 0.19$ designs compared to the $L/D = 0.5$ baseline. . . . .	180
10.5	Loss breakdown relative to an isolated ducted propulsor with ideal propulsive efficiency into internal and external losses for the $L/D = 0.25$ and $L/D = 0.19$ designs compared to the $L/D = 0.5$ baseline. . . . .	180

# Nomenclature

## Roman Symbols

$a$	Speed of sound, semi-diameter of super-ellipse describing inlet LE
$A$	Area, surface
$AoA$	Engine angle-of-attack (relative to engine axis of rotation)
$b$	Semi-diameter of super-ellipse describing inlet LE
$B$	Number of blades in blade row
$B_{i,n}$	Bernstein polynomial
$BPR$	Bypass ratio
$c$	Blade chord
$c_l$	Blade lift coefficient
$C$	Constant introduced to eliminate singularities in $K_n$
$C(t)$	Bezier curve
$C_d$	Drag coefficient
$C_{d,visc}$	Viscous drag coefficient
$C_{d,wave}$	Pressure drag coefficient
$D$	Rotor diameter
$D_{max}$	Maximum nacelle diameter
$D_{nac}$	Nacelle external drag
$D_{nac,visc}$	Nacelle viscous drag
$D_{nac,p}$	Nacelle pressure drag
$D_{ram}$	Ram drag
$e_t$	Absolute stagnation internal energy per unit mass

$f$	Body force per unit mass
$f_{n_\delta}$	Normal body force per unit mass due to local change in deviation
$f_{n_{\nabla p}}$	Normal body force per unit mass due to pressure gradient in staggered channel
$f_{n,A}$	Normal body force per unit area
$\bar{f}_n^{bl}$	Circumferentially-averaged normal blade force from surface pressure distributions
$\bar{f}_n^{pa}$	Normal blade force from pitchwise-averaged streamline curvature and normal pressure gradient force components
$F$	Body force per unit volume
$F_{pylon}$	Force exerted by propulsor on pylon
$F_{p,boattail}$	Boattail suction force
$FPR$	Fan pressure ratio
$h$	Staggered spacing in blade row, flight altitude
$h_t$	Stagnation enthalpy
$H_{sp}$	Spinner bulge height
$i$	LE incidence
$k$	Coordinate in direction of local blade surface, curvature
$K$	Body force coefficient, free-area ratio
$K_1, K_2$	Constants in inlet and nacelle surface parameterization
$L$	Inlet length
$L_{max}$	Distance between highlight and maximum nacelle diameter locations
$L_{sp}$	Spinner axial length
$\hat{l}, \hat{n}$	Natural coordinates along relative streamline
$m$	Meridional coordinate, exponent in super-ellipse describing inlet LE
$M$	Absolute Mach number
$M_{is}$	Isentropic Mach number
$M_{rel}$	Relative Mach number
$MFR$	Inlet mass flow ratio
$n$	Exponent in super-ellipse describing inlet LE
$\hat{n}$	Unit vector
$p$	Static pressure

$p_t$	Absolute stagnation pressure
$p_{t,rel}$	Relative stagnation pressure
$P_i$	i-th control point in Bezier curve definition
$P_{shaft}$	Shaft power input
$P_{fan}$	Power input to fan bypass
$P_{core}$	Equivalent power in core exhaust
$\dot{q}$	Heat release per unit mass
$Q$	Flow quantity
$\dot{Q}$	Heat release per unit volume
$r$	Radial coordinate
$r_c$	Radius of curvature
$\Delta r_{C.L.}$	Inlet highlight radial center line offset
$R$	Rotor tip radius
$Re$	Reynolds number
$s$	Entropy
$t$	Time, blade or airfoil thickness
$T$	Static temperature, thrust, period of rotor revolution
$T_t$	Absolute stagnation temperature
$T_{gross}$	Gross thrust
$T_{net}$	Net thrust
$U$	Rotor velocity
$V$	Velocity
$V_{Xwind}$	Velocity at cross-wind operating condition
$w$	Mass flow
$W$	Relative velocity
$\dot{W}_{source}$	Source term for energy equation in work per unit volume
$x, y, z$	Cartesian coordinates
$\alpha$	Absolute flow angle
$\alpha_{boat tail}$	Nacelle trailing edge angle

## Greek Symbols

$\beta$	Reduced frequency, relative flow angle
$\gamma$	Ratio of specific heats, bottom inlet LE orientation relative to axial direction
$\delta$	Deviation
$\epsilon_{1,2}$	Angle used in setting the FEGV-pylon axial spacing and the pylon TE sweep
$\eta_{fan}$	Fan rotor adiabatic efficiency
$\eta_{stage}$	Fan stage adiabatic efficiency
$\eta_{prop}$	Engine propulsive efficiency
$\eta, \eta'$	Coordinate in blade passage direction
$\theta$	Circumferential coordinate
$\kappa$	Local blade metal angle
$\Delta\kappa$	Change in the local blade metal angle relative to baseline rotor design
$\lambda$	Wavelength
$\xi, \xi'$	Coordinate normal to blade passage
$\pi_{inlet}$	Inlet stagnation pressure recovery
$\rho$	Density
$\sigma$	Solidity
$\tau$	Shear stress
$\phi$	Flow coefficient
$\Psi_{h_t}$	Rotor work coefficient
$\Psi_{p_t}$	Rotor stagnation pressure rise coefficient
$\omega$	Angular frequency, Loss coefficient
$\Omega$	Rotor rotational speed

## Subscripts

$bl$	Blade loading
$base$	Baseline propulsor

$c$	Corrected quantity
$des$	Design point quantity
$fan\ face$	Fan face quantity
$HL$	Inlet highlight
$inlet$	Inlet quantity
$LE$	Leading edge
$n, n'$	Normal to relative flow direction
$max$	Maximum quantity
$p, p'$	Parallel to relative flow direction
$ps$	Blade pressure surface quantity
$r$	Radial quantity
$ref$	Reference quantity
$rotor$	Rotor blade row
$ss$	Blade suction surface quantity
$stator$	Stator blade row
$t$	Stagnation quantity
$throat$	Inlet throat
$tip$	Rotor tip quantity
$TE$	Trailing edge
$x$	Axial quantity
$\eta, \eta'$	In-blade passage direction
$\theta$	Circumferential quantity
$\xi, \xi'$	Normal to blade passage
0	Free-stream condition
2	Fan rotor inlet condition for core stream
12	Fan rotor inlet condition for bypass stream
12.5	Fan rotor exit condition for bypass stream
4	Turbine inlet condition
5	Turbine exit condition

## Superscripts

$M$	Mass-averaged quantity
$T$	Transpose of vector/matrix

## Abbreviations

ADP	Aerodynamic design point
BF	Body force
CAD	Computer-aided design
CFD	Computational fluid dynamics
FEGV	Fan exit guide vanes
F/T	Numeca FINE/Turbo flow solver
IGV	Inlet guide vanes
LE	Leading edge
LPC	Low pressure compressor
LPT	Low pressure turbine
NASA	National Aeronautics and Space Administration
OPR	Overall pressure ratio
RANS	Reynolds-averaged Navier-Stokes
SA	Spalart-Allmaras turbulence model
TE	Trailing edge
T/O	Take-off operating condition
URANS	Unsteady Reynolds-averaged Navier-Stokes
VAN	Variable-area nozzle

# Chapter 1

## Introduction

The next-generation turbofan engine designs for commercial transport aircraft seek higher bypass ratios (BPR) and lower fan pressure ratios (FPR) for improved fuel burn and reduced emissions and noise [9–13]. The trend in fuel burn reduction and BPR is illustrated in Figs. 1-1 and 1-2. Low fan pressure ratios lead to increased bypass stream propulsive efficiencies as shown in Fig. 1-3 and enable higher overall pressure ratios (OPR) and turbine inlet temperatures at cruise as the increase in OPR and turbine inlet temperature at take-off is reduced compared to engines with higher FPR [13]. In addition, significant noise benefits can be achieved in low-speed, low-FPR fan designs by potentially avoiding buzz-saw noise, reducing fan broadband and rotor-stator interaction noise, reducing cabin noise, and enabling steeper take-off profiles for far-field noise reductions due to excess thrust capability at take-off [14–16].

Reductions in fan pressure ratio can be realized for example through low-speed geared fans. First-generation geared turbofans with  $BPR = 12$  and  $FPR \approx 1.4$  for short-to-medium range, twin engine aircraft are expected to deliver fuel burn reductions of up to 16 % compared to current engines in the same thrust segment [17]. From engine cycle analysis, second-generation geared fans with pressure ratios of 1.3 and lower are expected to offer fuel burn benefits of up to 25 % [9, 10, 18, 19]. The gear system allows the fan rotor and the low spool with the low pressure compressor (LPC) and low pressure turbine (LPT) to operate at different rotational speeds. The fan speed can be reduced to limit tip speed and noise while compressor and turbine

speeds can be increased to limit stage counts and core weight [4]. The geared turbofan engine cycle is one of the advanced technologies enabling a design point shift to higher fuel burn benefits as shown in Fig. 1-4.

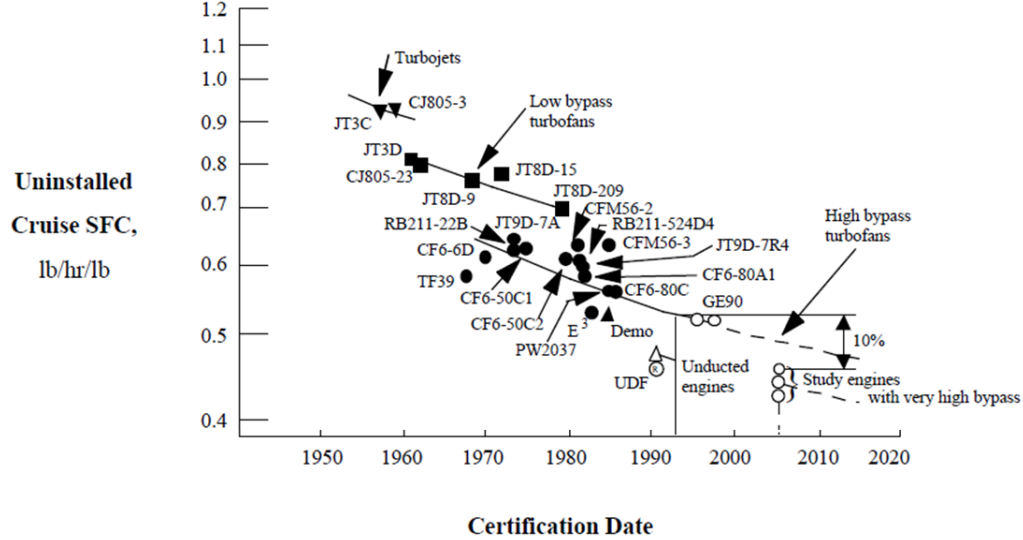


Figure 1-1: Trends in fuel burn (from [1]).

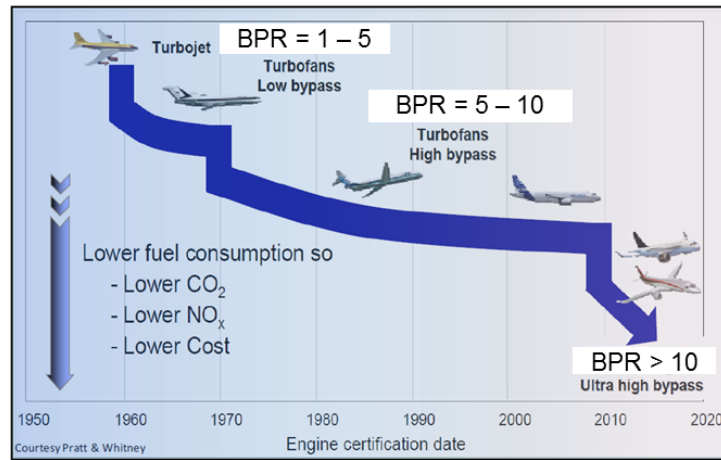


Figure 1-2: Trends in bypass ratio (from [2]).

High bypass and low fan pressure ratios require large engine diameters, increasing the engine contribution to overall drag and compounding adverse installation effects on the wing aerodynamics. Translating the potential for fuel burn benefits in low-FPR propulsors into an efficient installation requires the development of advanced

nacelle designs limiting weight and drag penalties [4, 13, 18, 20, 21]. Shorter inlet and exhaust ducts will be required to minimize the impact of larger diameter fans on nacelle weight and drag. However, short inlets have reduced internal diffusion capability and inlet flow distortion effects can be exacerbated, leading to reduced rotor performance, potential stability challenges for the fan and the LPC, and increased levels of circumferential blade loading variation causing aero-mechanical challenges. In addition, shorter inlets provide reduced fan noise attenuation and shielding opportunities.

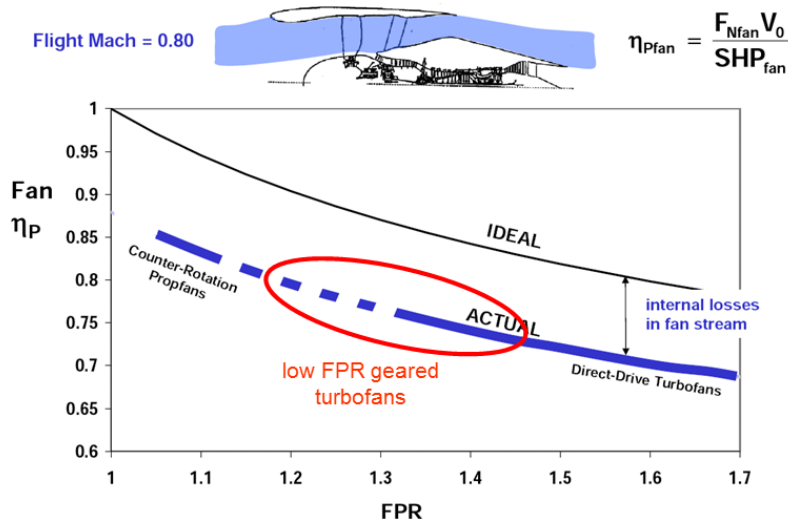


Figure 1-3: Increase in bypass propulsive efficiency with reduction in fan pressure ratio (from [3]).

Current engines for short-to-medium range civil transport twin engine aircraft feature inlets with an L/D of between 0.65 and 0.85. The inlet  $L/D$  of current engines for long-range aircraft is typically in the range of 0.5 and 0.65 [22]. In this work, a baseline configuration at the low end of current design practice for current fans is defined. The baseline propulsor is based on an advanced geared fan stage with  $BPR = 20$  and a non-axisymmetric inlet with  $L/D = 0.5$ . Changes in propulsor performance for inlets with  $L/D$  as low as 0.02 are quantified and a candidate short-inlet configuration with equal propulsor performance relative to the baseline case is demonstrated for an inlet design with  $L/D = 0.25$ .

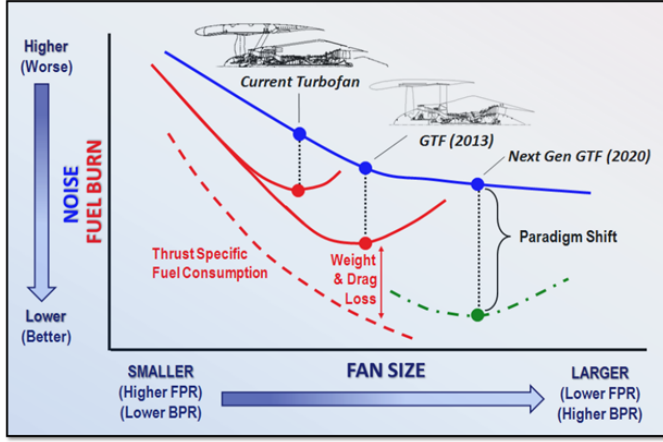


Figure 1-4: Influence of fan diameter on noise and fuel burn (from [4]).

## 1.1 Motivation

In the light of increasing fuel costs and noise restrictions, identifying and quantifying the design requirements and limits of short nacelles is critical for advancing the technology readiness of low-FPR powerplants. The present research is aimed at determining the potential of short-inlet configurations to reduce nacelle drag without jeopardizing fan and compressor stability. The emphasis is on the aerodynamic propulsor performance including inlet-fan and fan-exhaust nozzle interactions.

## 1.2 Research Questions and Goals

This thesis seeks to answer three distinct research questions. First, what are the key fluid dynamic processes limiting the design of short inlets? The focus is on identifying the flow features which govern aerodynamic mechanisms causing performance penalties for low-FPR propulsors with short nacelles relative to a baseline configuration with a conventional inlet.

Second, how short an inlet design can be achieved while meeting internal and external aerodynamic performance criteria? Engine propulsive efficiency<sup>1</sup> is used to

---

<sup>1</sup>In this thesis, engine propulsive efficiency  $\eta_{prop}$  is defined as the ratio of flight velocity times the engine net thrust  $T_{net}$  minus nacelle external drag  $D_{nac}$  over the sum of the power input to the fan bypass  $P_{fan}$  and the equivalent power in the core exhaust  $P_{core}$ :  $\eta_{prop} = \frac{V_0(T_{net}-D_{nac})}{P_{fan}+P_{core}}$ .

quantify the overall performance of the candidate short-inlet configuration at cruise. The key metrics governing propulsive efficiency are fan efficiency and nacelle total drag with contributions from viscous and pressure drag. At off-design operating conditions, design criteria for conventional inlets such as for example separation-free inlet flow cannot always be satisfied in short-inlet designs. This thesis recommends criteria more adequate for the design of short inlets.

Lastly, what benefits in performance can a coupled low-FPR/short-nacelle propulsion system achieve and do inlet length reductions enable an improvement in propulsive efficiency relative to a long-inlet baseline case? Shortening inlet and nacelle results in reduced wetted area and nacelle viscous drag. However, the flow non-uniformity at the fan face is potentially increased, leading to rotor efficiency penalties.

The specific goal is to define a candidate low-FPR/short-inlet configuration with equal or improved propulsive efficiency at cruise compared to the baseline case while limiting rotor performance penalties at off-design conditions. Aircraft system level effects are not accounted for in this work but candidate short-inlet configurations with equal or better engine propulsive efficiency will offer benefits on the aircraft system level due to the reductions in nacelle drag and weight.

### 1.3 Challenges

The onset of flow separation at off-design operating condition with large angles-of-attack is one of the critical considerations in the design of subsonic inlets [22]. Conventional methods that determine whether the inlet flow is separated are based on through-flow nacelle models which do not account for the effects induced by the rotor including blockage, swirl, and suction [23]. A coupled fan-nacelle design approach is required as the inlet length is reduced and the interaction between inlet flow and fan stage increases. Including the influence of rotor and stator in the design of inlet and nozzle is important to capture mechanisms such as the increase in separation-free angle-of-attack due to the presence of the fan [24–26]. In addition, determining the distortion transfer and stability margin requires modeling the complete fan stage.

In the past, several numerical studies using potential flow [27] and Euler [28–30] analyses, or two-dimensional actuator disk models with a Navier-Stokes code [31] were conducted to simulate the flow through the fan rotor. However, potential flow simulations are limited to subsonic, non-separated flows. Euler calculations can be used in sub- and supersonic conditions but are also limited to attached flows. The two-dimensional actuator disk model does not capture swirl effects and usually requires the input of prescribed stagnation pressure and temperature changes across the rotor.

Direct CFD simulations are another approach but full-annulus domains are needed to capture the once-per-revolution inlet distortion patterns and unsteady computations without mixing planes are required to assess the distortion transfer through the fan stage. A full-annulus simulation of a fan stage/pylon configuration requires up to 50 million grid points and needs to be run on 100 or more processors for reasonable computation times [32]. The large computational resources associated with full-annulus unsteady RANS (URANS) calculations render the direct CFD approach unsuitable in the design phase or the parametric exploration of coupled inlet-fan systems. In this work, a body force method is developed which provides an affordable and accurate approach to assess the aerodynamic performance of novel nacelle configurations. In the body-force-based approach, the fan rotor blade row is replaced with a force field which produces the same pressure rise and flow turning. This technique was first described by Marble [33] and is commonly referred to as using a *body force representation* of the blade row.

## 1.4 Major Findings and Contributions

The major findings and the four main contributions of the thesis are summarized next and followed by a more detailed discussion.

1. This work provides a new design capability for short inlets and nacelles based on the combination of a spline-based tool to define inlet and nacelle surface geometries and three-dimensional body force simulations.

2. The thesis provides the first characterization of the fluid dynamic processes limiting the design of short inlets. The critical mechanism is the increase in the Mach number at the fan face as the inlet length is reduced. At cruise, this increase is due to flow acceleration along the inlet internal surface coupled with a reduction in effective flow area throughout the inlet. In contrast to a conventional inlet, there is no well-defined throat area and insufficient length to straighten the flow. At low-speed, high angle-of-attack conditions, the local increase in Mach number is due to acceleration around the bottom inlet lip. As the inlet is shortened, the rotor locally operates close to choke leading to large rotor efficiency penalties and potential aero-mechanical challenges due to increased levels of unsteady loading.
  
3. A short-inlet design with an inlet  $L/D = 0.25$  maintains the propulsive efficiency of the baseline configuration with  $L/D = 0.5$  ( $\Delta\eta_{prop} = -0.01\%$ ). An additional propulsive efficiency benefit of 0.26% is possible by tailoring the FEGV to offset the pylon upstream influence. With the reductions in nacelle drag and weight obtained by shortening the nacelle, this candidate propulsor is expected to enable a lower aircraft thrust requirement and consequently lead to reduced fuel burn compared to the baseline case. At low-speed, high angle-of-attack off-design operating conditions, the candidate short-inlet configuration has sufficient LPC stability margin and rotor efficiency penalties are limited to a maximum of 1.5% compared to the baseline propulsor. The parametric inlet study and the evaluation of the candidate short-inlet design suggest that a maximum in propulsive efficiency exists for an  $L/D$  between 0.25 and 0.4.
  
4. In order to take advantage of additional nacelle drag and weight savings from shortening the inlet below an  $L/D$  of 0.25, advanced concepts are required such as intake blow-in doors to limit flow separation at the cross-wind operating condition or pitching the fan case to align the inlet with the angle-of-attack flow due to the wing upwash and avoid large rotor efficiency penalties at cruise. To push the limits in the short-inlet design space, an  $L/D = 0.19$  configuration with

the potential for increased aircraft system level performance is demonstrated. Inlets with length below  $L/D = 0.19$  are not viable due to exacerbated rotor efficiency penalties at cruise and off-design and the potential for LPC stall due to increased stagnation pressure distortion levels in the core inlet duct.

#### 1.4.1 A New Capability to Design Short Inlets and Nacelles

Current design methods for conventional nacelles are typically based on through-flow nacelle approaches with the presence of the rotor simulated through the use of outlet boundary conditions at the fan face. As the inlet is shortened, the coupling between rotor and inlet flow is increased and needs to be accounted for in order to determine the incidence distribution at the fan face, which governs the rotor performance and engine propulsive efficiency.

Representing the rotor and stator blade rows with body force distributions enables the high-fidelity determination of the three-dimensional flow field in the inlet and the blade domains. The body force method developed in this work is capable of capturing the interaction of rotor and non-uniform inlet flow and the distortion transfer through the fan stage. The key advantages of the body-force-based approach include reductions in computational cost due to simplified mesh topologies and the possibility for steady simulations without rotor-stator interfaces. In addition, the method provides a versatile platform to explore the direct effect of force field distributions on the flow field without having to consider the details of the blade geometry.

In order to explore the short-inlet design space and to determine the limiting aerodynamic processes, a parametric definition of the inlet and nacelle shapes is required. A description based on the same characteristic parameters used in the design of conventional nacelles does not provide the flexibility needed to produce viable short-inlet configurations. For example, a key parameter in the design of conventional long inlets is typically the inlet contraction ratio, defined as the ratio of inlet highlight area  $A_{HL}$  to inlet throat area  $A_{throat}$ . In short inlet designs, there is insufficient axial length to accommodate a distinct inlet throat upstream of the fan face and it can be impractical to design for a specific throat area. In the light of the

increased flexibility required to design short inlets and nacelles, this thesis couples the body force method with a spline-based three-dimensional geometry definition tool.

By simplifying the mesh topology and enabling non-uniform inflow effects to be captured using steady calculations, computation times are reduced by two orders of magnitude compared to full-annulus URANS simulations. This reduction allows to model the entire propulsor including the bypass duct with the pylon and bifurcation as well as the core inflow and core exhaust flow. The framework developed in this work enables one to quantify the impact of changes in inlet and nacelle shape on engine propulsive efficiency in the design process, providing a new capability to design short inlets and nacelles for low pressure ratio propulsors.

The distortion transfer through the rotor is captured by the body force method and the circumferential stagnation pressure non-uniformity in the core inlet flow can be extracted directly from the body force simulations. Based on the level of core inlet stagnation pressure distortion, the LPC stability margin can be quantified by the engine manufacturer [34]. The developed methodology therefore allows to assess the change in LPC stability margin with changes in inlet and spinner length and shape in the early stages of the design process, which represents an additional advantage over current inlet and nacelle design methods.

#### 1.4.2 Characterization of Limiting Aerodynamic Mechanisms

The uncharted design space of short inlets and nacelles for low-FPR propulsors is addressed in this thesis. Based on the results of a parametric inlet study, the recommended inlet length for maximized engine propulsive efficiency without jeopardizing fan and LPC stability is suggested to be an  $L/D$  between 0.25 and 0.4.

At the low end of this range, a candidate  $L/D = 0.25$  configuration was demonstrated to come to within 0.01 % of reaching the propulsive efficiency provided by the  $L/D = 0.5$  baseline case. However, at off-design operating conditions such as take-off rotation ( $\Delta\eta_{fan} = -1.3 \%$ ) or wing  $C_{Lmax}$  ( $\Delta\eta_{fan} = -1.5 \%$ ), the rotor performance is significantly degraded due to the increased incidence distortion at the fan face. In addition, the maximum variation of blade loading around the circumference is in-

creased by a factor of four at the wing  $C_{L\max}$  operating condition compared to the baseline configuration which has to be accounted for in the structural design of the rotor blades.

At the upper end of the recommended inlet  $L/D$  range, incidence distortion and resulting rotor efficiency penalties are mitigated while nacelle drag increases due to the larger surface area. A low-FPR propulsor with an inlet  $L/D$  between 0.25 and 0.4 is expected to offer performance benefits on the aircraft system level relative to an  $L/D = 0.5$  baseline while reducing rotor performance penalties, alleviating fan blade structural requirements, and reducing core inlet stagnation pressure distortion compared to the  $L/D = 0.25$  candidate design presented in this thesis.

The main aerodynamic mechanism limiting the design of inlets with length lower than  $L/D = 0.25$  is the enhanced interaction of the rotor with a region of high streamwise Mach number. At the cruise aerodynamic design point (ADP) with flight Mach number  $M_0 = 0.8$  and angle-of-attack  $AoA = 5^\circ$ , the Mach number is increased locally due to the acceleration along the bottom inlet internal surface and the reduction in effective flow area. For a conventional long inlet, the Mach number is highest at the throat as shown on the left in Fig. 1-5. In the case of a short inlet, the effective flow area decreases throughout the inlet, contributing to a region of high Mach number near the shroud just upstream of the fan face as shown on the right in Fig. 1-5. As a consequence, the local rotor operating point is shifted to higher mass flows leading to increased fan rotor losses.

At low-speed, high angle-of-attack operating conditions such as for example wing  $C_{L\max}$  with flight Mach number  $M_0 = 0.25$  and angle-of-attack  $AoA = 29^\circ$ , the region of increased streamwise Mach number is due to the flow acceleration around the inlet lip as depicted in Figure 1-6. Over the outer span, the maximum streamwise Mach number at the fan face increases from  $M_{x,max} = 0.71$  for the baseline case to  $M_{x,max} = 0.88$  for the  $L/D = 0.25$  configuration, resulting in a rotor efficiency penalty of  $\Delta\eta_{fan} = -1.5\%$  and a 10.8% increase in the circumferential blade loading variation at the tip.

In addition to the interaction of the rotor with the region of high streamwise Mach

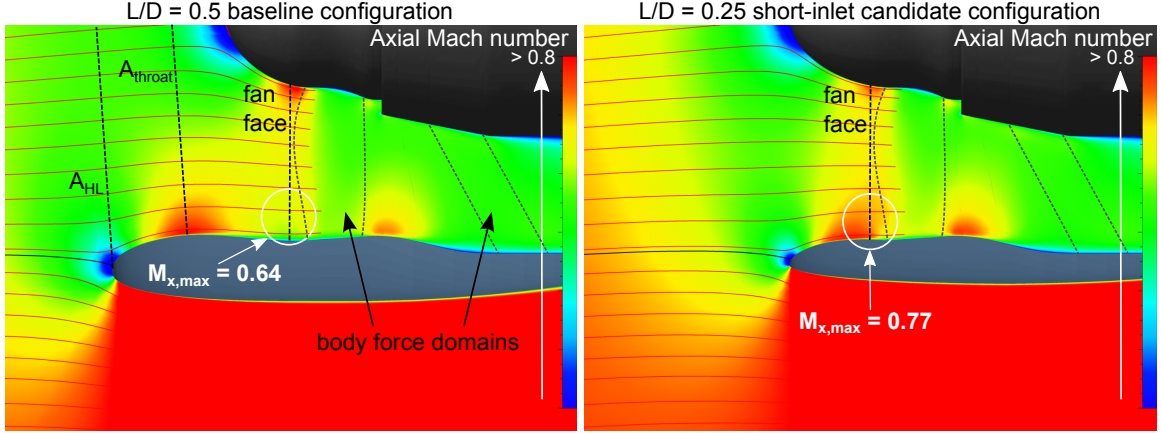


Figure 1-5: Axial Mach number and streamline distribution based on body force simulations for  $L/D = 0.5$  baseline (left) and  $L/D = 0.25$  candidate short-inlet (right) propulsors at the cruise aerodynamic design point (ADP) with flight Mach number  $M_0 = 0.8$  and angle-of-attack  $AoA = 5^\circ$  (the dashed lines represent the approximate fan rotor and FEGV leading and trailing edges).

number at the fan face, the following mechanisms limit the design of short inlets and nacelles: (1) angle-of-attack flow at the fan face due to reduced flow straightening in the inlet causing increased incidence distortion and rotor efficiency penalties at cruise and off-design, (2) locally increased streamwise Mach number at the hub due to the flow upwash around the spinner and angle-of-attack flow at the fan face resulting in increased stagnation pressure distortion downstream of the rotor in the core inflow and reduced LPC stability margin [34, 35], and (3) an increase of up to 20 % in the circumferential blade loading variation for an inlet with  $L/D = 0.25$ , yielding aero-mechanical challenges.

The trade-offs between the performance at cruise and off-design need to be carefully balanced in the design of short inlets. Thin inlet shapes are preferred at cruise to limit nacelle wave drag and mitigate the local increase in streamwise Mach number at the fan face. However, thick inlet contours are needed at off-design to avoid regions of separated inlet flow. Conventional inlet design criteria demand fully attached flow at off-design conditions such as wing  $C_{L\max}$  or cross-wind ( $V_{cross} = 30 \text{ kt}$ ). Based on the lessons learned in this work, a new set of design criteria is suggested for the wing  $C_{L\max}$  condition. Some inlet flow separation is acceptable, as long as a critical values for the following metrics are not surpassed: (1) rotor efficiency penalty, (2) stagna-

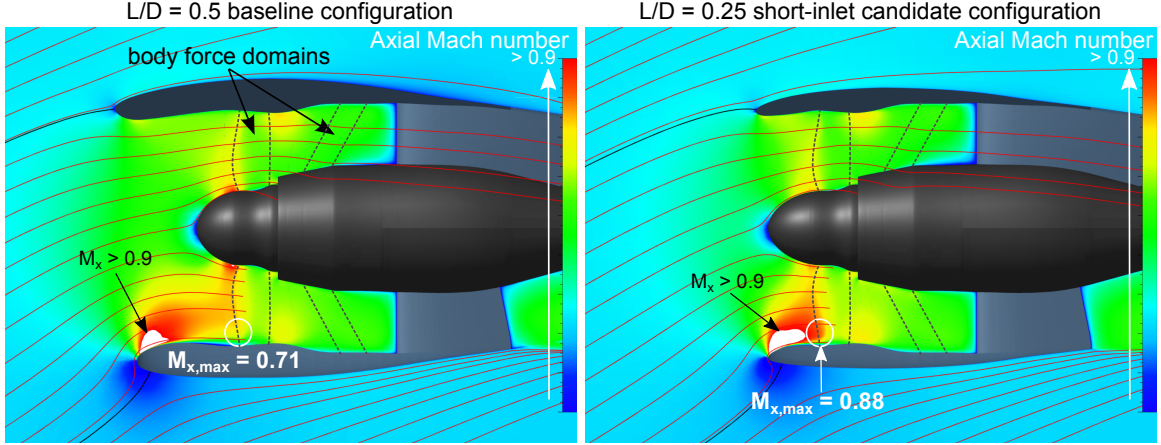


Figure 1-6: Axial Mach number and streamline distribution based on body force simulations for  $L/D = 0.5$  baseline (left) and candidate  $L/D = 0.25$  (right) short-inlet configurations at the wing  $C_{L\max}$  operating condition with flight Mach number  $M_0 = 0.25$  and angle-of-attack  $AoA = 29^\circ$ .

tion pressure circumferential variation (important for LPC stability), and (3) blade loading circumferential variation (important for the fan blade structural design).

#### 1.4.3 Candidate Short-Inlet Design ( $L/D = 0.25$ ) with System Level Performance Benefits

Inlet and nacelle were parametrically shortened using body force simulations to quantify the trades between reduced nacelle drag and increased rotor efficiency penalties due to enhanced incidence distortion. Based on the results for rotor performance and nacelle drag, the shortest possible inlet length for improved propulsive efficiency compared to the baseline configuration without jeopardizing fan or LPC stability was determined as  $L/D = 0.25$ . The two-dimensional top and bottom inlet and nacelle shapes of the  $L/D = 0.5$  baseline and the  $L/D = 0.25$  short-inlet configuration are presented in Figure 1-7. As the inlet is shortened, the spinner is extended to enhance flow straightening and limit circumferential incidence variation near the hub.

An inlet length of  $L/D = 0.25$  represents a step change with respect to current engine technology. Engines with thrust output similar to the baseline case feature inlets with  $L/D$  between 0.65 and 0.85. The  $L/D = 0.25$  configuration presented in this thesis meets the conventional inlet and nacelle design requirements used by the

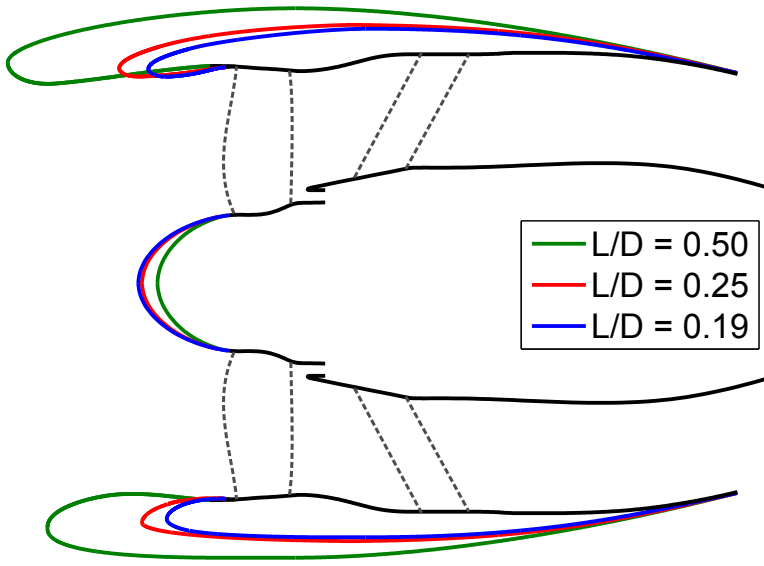


Figure 1-7: Top and bottom inlet and nacelle sections for the  $L/D = 0.5$  baseline design and the  $L/D = 0.19$  and  $L/D = 0.25$  candidate short-inlet designs.

industry partner at cruise, take-off rotation, and wing  $C_{L\max}$ . The engine propulsive efficiency of the baseline configuration is maintained while rotor efficiency penalties at take-off rotation ( $\Delta\eta_{fan} = -1.3\%$ ) or wing  $C_{L\max}$  ( $\Delta\eta_{fan} = -1.5\%$ ) are limited. Circumferential blade loading variations and core inflow stagnation pressure distortion are within acceptable ranges according to the industry partner such that structural changes to the fan blade or modifications to the LPC would not be required. This design demonstrates the feasibility of a low-FPR/short-inlet configuration with equal or higher propulsive efficiency at cruise compared to the baseline case, meeting the project success goal.

For the cruise flight condition, the changes in propulsive efficiency relative to the  $L/D = 0.5$  long-inlet baseline propulsor are shown in Fig. 1-8. The reduction in the rotor efficiency decreases the propulsive efficiency by  $0.85\%$ . An additional propulsive efficiency penalty of  $-0.10\%$  is due to a small increase in the maximum external Mach number, leading to an increase in nacelle pressure drag. The reductions in the viscous nacelle drag approximately offset the fan efficiency penalty and increase the

propulsive efficiency by 0.81 %. Finally, a rotor re-design accounting for inlet-rotor coupling effects enables an additional 0.13 % benefit in propulsive efficiency, such that the net change in propulsive efficiency relative to the long-inlet baseline case is approximately zero. By re-designing the fan exit guide vanes (FEGV) to offset the rotor back pressure distortion due to the pylon upstream influence, additional performance benefits are feasible.

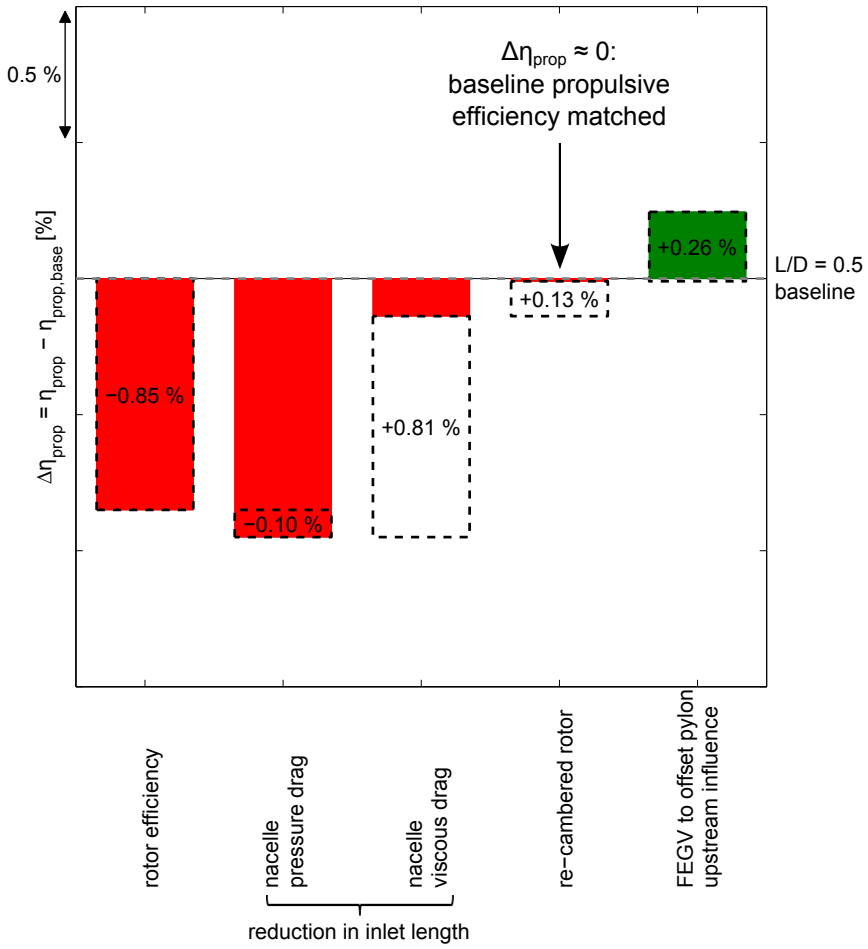


Figure 1-8: Contributions to change in cruise engine propulsive efficiency relative to long-inlet baseline from reduction in inlet length and re-design of baseline rotor and FEGV.

Aircraft system level benefits can be achieved relative to the baseline propulsor for this short-inlet design as the thrust requirement at cruise is reduced due to reductions in propulsor drag and weight. By reducing the thrust requirement, the propulsor can be scaled to a smaller size, enabling further drag and weight benefits, which ultimately

result in a fuel burn advantage over the baseline case. In the light of the weight and drag reductions due to shortening the nacelle, the aircraft performance is expected to improve for the  $L/D = 0.25$  candidate propulsor even if the FEGV is not altered.

#### 1.4.4 Pushing the Limits in Short-Inlet Designs

To benefit from additional reductions in nacelle drag by shortening the inlet beyond  $L/D = 0.25$ , the performance of a configuration with an inlet of length  $L/D = 0.19$  was quantified. The top and bottom inlet nacelle shapes for this design are shown in Figure 1-7.

At cruise, the engine propulsive efficiency for this case is reduced by 0.8 % relative to the baseline as the benefits in nacelle drag ( $\Delta D_{nac} = -17.8\%$ ) are outweighed by the fan efficiency penalty due to the enhanced incidence distortion ( $\Delta \eta_{fan} = -1.6\%$ ).

At the wing  $C_{L_{max}}$  off-design condition, there is a small region of separated flow as well as an additional increase in the interaction of the high streamwise Mach number inlet flow with the rotor compared to the  $L/D = 0.25$  design (the maximum streamwise Mach number increases from  $M_{x,max} = 0.88$  to  $M_{x,max} = 1.07$ ) resulting in a fan efficiency penalty of  $\Delta \eta_{fan} = -3.9\%$  relative to the baseline case. The increased incidence distortion leads to a core inflow stagnation pressure distortion large enough that modifications to the LPC such as variable-pitch inlet guide vanes (IGVs) may be required to ensure an appropriate LPC stability margin. At the cross-wind condition, the corrected flow is reduced by 32 % due to flow blockage caused by separated flow. Consequently, the rotor efficiency is reduced by 8.5 % relative to the long-inlet baseline configuration.

To make an  $L/D = 0.19$  design work, advanced concepts are needed. The potential of two such concepts for improved rotor performance were determined in this thesis. First, a blow-in door system in the inlet was demonstrated to eliminate flow separation at the cross-wind condition and raise the rotor efficiency to within 1.5 % of the performance achieved by the baseline case. Second, the fan case was pitched by 5° to align the rotor axis of rotation with the incoming flow at cruise and thereby mitigate the rotor incidence distortion. The fan efficiency is increased by 0.8 % at

cruise and rotor performance benefits are also demonstrated at off-design due to lower incidence distortion levels.

## 1.5 Organization of Thesis

The remainder of the thesis is organized as follows: The relevant literature is reviewed in Chapter 2. Chapter 3 presents the body-force-based approach to model the rotor and stator blade rows and Chapter 4 highlights the method’s capabilities to capture the off-design performance and rotor-inlet coupling under non-uniform inflow conditions. The body force method enables the development of a design framework for short inlets and nacelles, which is presented in Chapter 5. A description of the spline-based geometry definition capability is provided, followed by details of the computational setup used in the full-annulus body force and URANS simulations. The baseline long inlet configuration with an advanced geared turbofan stage with fan pressure ratio  $FPR < 1.4$  and bypass ratio  $BPR$  near 20 is defined in Chapter 6 and the computational setup is validated using cycle data provided by the industry partner. The mechanisms governing the distortion transfer through the fan stage are identified, serving as an initial investigation into the impact of incidence distortion in low-FPR propulsors. Engine propulsive efficiency is presented as the key performance metric in Chapter 7, followed by a sensitivity analysis to identify the critical component performance metrics: rotor adiabatic efficiency and nacelle drag. Based on the outcomes of a parametric inlet study, the design strategy for the candidate short-inlet configurations is discussed in Chapter 8. The first candidate short-inlet design with  $L/D = 0.25$  is assessed in Chapter 9. Chapter 10 discusses the change in propulsor performance as the inlet length is further reduced to  $L/D = 0.19$  and highlights the advanced technologies needed to achieve system level performance benefits at this inlet length relative to the long-inlet baseline powerplant. Finally, Chapter 11 presents a summary of the thesis, conclusions, and recommendations for future work.

# Chapter 2

## Literature Review

### 2.1 Previous Work on Low-FPR Propulsor Performance

One of the early studies to quantify the potential fuel burn benefits of advanced high-BPR propulsors was by Zimbrick and Colehour [21]. Using a three-dimensional transonic potential flow method in combination with a three-dimensional boundary layer method, inlets were designed for fans with bypass ratios of up to 17.5. A main conclusion was the need to consider several new fan design features such as variable pitch, geared fans, and variable-area nozzles. The authors emphasized the importance of coupled inlet-fan approaches and the demand for innovative nacelle designs as bypass ratios and fan diameters are increased.

Similar to the conclusions of numerical investigations of high-bypass nacelle aerodynamics by Iek et al. [36,37], Larkin and Schweiger [26] experimentally demonstrated that the presence of the fan increased separation-free angle-of-attack operation by  $4^\circ$  to  $5^\circ$  compared to the nacelle-only case. The increase in separation angle-of-attack is due to the favorable pressure gradient in the inlet, induced by the rotor suction. Hsiao et al. [23] later validated Gong's [38] body-force-based approach in complete powered-nacelle simulations, also demonstrating the increase in separation-free angle-of-attack due to the fan rotor interaction with the inlet flow. Larkin and Schweiger [26] ad-

ditionally discussed a configuration featuring an external plug with a center body extending forward of the inlet highlight plane and a short inlet with  $L/D = 0.2$ . The experimental results indicated that this configuration allowed operating at up to  $12^\circ$  larger angles-of-attack than the conventional inlet prior to separation but other test data indicated high-speed performance penalties. The results underline the requirement of a coupled fan-spinner-nacelle analysis to determine propulsor performance in short-inlet designs with increased inlet-fan interaction.

In a more recent study by Daggett [39], the integration of advanced technology engines developed under the NASA Ultra Efficient Engine Technology (UEET) program on advanced technology airframes was evaluated and compared to datum baseline configurations for several aircraft size categories. For large aircraft (Boeing 747 size), a 30 % increase in nacelle drag was estimated when replacing a baseline turbofan with  $BPR = 7$  and 125" fan diameter with a candidate geared turbofan with  $BPR = 14.3$  and 152" diameter. In a follow-up analysis by Daggett et al. [40], the integration of several high-bypass ratio powerplant candidates on a Boeing 777 aircraft was assessed. The candidate propulsion architectures included a counter-rotating fan, a direct-drive advanced turbofan, and a geared fan with and without variable-area nozzle (VAN) with bypass ratios ranging from 7.5 to 21.5. Fuel burn reductions of up to 16 % were estimated for an  $FPR = 1.45$  propulsor with geared fan. It was concluded that a lower pressure ratio fan ( $FPR = 1.32$ ) with VAN capability was not required as the additional fuel efficiency benefits were offset by increased drag of the larger-diameter nacelle. Nacelles in both studies featured conventional inlets and were not optimized. These results highlight the need for the design of new nacelle concepts to limit nacelle and drag penalties due to larger diameter nacelles and to take advantage of the potential for additional fuel burn reductions in propulsors with fan pressure ratios lower than 1.45.

Primary drivers of engine installation drag are profile and wave drag on the nacelle and strut, interference drag from installation effects of the engine on the wing, and excrescence drag due to manufacturing imperfections. In independent experimental studies, McCall et al. [41] and Ingraldi et al. [42] reported that interference drag

penalties in high-bypass ratio nacelle installations were approximately the same as for conventional-type nacelles ( $BPR = 18$  vs.  $BPR = 6$  in the latter study). Instead, wave drag due to shock waves forming on the nacelle surface was identified a challenge in short nacelles [40]. For low ratios of nacelle length to maximum diameter, high curvatures lead to rapid acceleration and deceleration, resulting in increased wave drag while reducing curvatures by lengthening the nacelle increases skin friction drag. Using a new spline-based design method, this thesis demonstrates that short-inlet configurations can have wave drag as low as a long-inlet propulsor and that wave drag is not limiting the design of short inlets. Wave drag can be controlled by shaping the outer nacelle contour and limiting the maximum nacelle diameter as will be discussed in Chapters 9 and 10.

Another approach to reduce drag in high-bypass ratio fans is flow control as presented for example in studies by Wie et al. [43] or Lord et al. [18]. Drag reductions are realized either through a conventional-length nacelle design with regions of laminar flow or by reducing cruise drag through a thin nacelle design and applying separation control such as inlet blow-in doors at high angle-of-attack conditions during take-off and climb.

In a recent study, Albert and Bestle [44] demonstrated reductions in external drag at cruise and inlet flow non-uniformity at a low-speed condition relative to a reference design obtained in an iterative manual design process by using a genetic optimization method in combination with two-dimensional RANS simulations. Three different parameterization techniques (super-ellipse polynomial, class-shape-transformation, B-splines) were assessed to describe changes in the inlet and nacelle shapes during the optimization. All three approaches resulted in performance benefits: the maximum external Mach number at cruise was reduced by up to 14 % and the maximum internal Mach number used to describe flow acceleration around the inlet lip at the low-speed condition was reduced by up 29 %. While the optimization led to performance improvements at the level inflow operating conditions addressed in this study, a two-dimensional design approach is unlikely to provide inlet and nacelle shapes feasible for operation at angle-of-attack conditions.

The studies of high-BPR, low-FPR propulsors and investigations of nacelles for large-diameter fans mentioned above have provided important insight into certain performance aspects but the fluid dynamic processes limiting the design of short inlets for low pressure ratio fans have not been defined. As a result, the nacelle and inlet lengths required to maximize the performance of a next-generation turbofan powerplant with pressure ratios below 1.4 and bypass ratios above 15 have not been quantified.

The main purpose of the inlet is to provide the fan with (1) a uniformly distributed airflow (2) with minimum stagnation pressure losses (3) over a wide range of incidence angles and engine operating conditions. In contrast to the cruise design point at which the streamtube capture area is generally smaller than the inlet highlight area and the main challenge is to minimize flow acceleration around the external nacelle part, low-speed, high angle-of-attack conditions such as cross-wind, take-off rotation, or wing  $C_{L\max}$  can result in regions of separated inlet flow [17, 22], particularly as the inlet length is shortened, as will be shown in Chapters 9 and 10.

To explore the design space of low-FPR propulsors and their nacelles, identify the aerodynamic mechanisms limiting the design of short nacelles, and quantify the required inlet length for optimum performance of a low pressure ratio fan, a design methodology is needed which is capable of accounting for angle-of-attack flight conditions and capturing inlet flow separation, fan-inlet coupling, and distortion transfer through the fan stage. A three-dimensional parametric description of inlet and nacelle shapes is required to quantify the influence of changes in the geometry and design and off-design propulsor performance in a tractable manner. Finally, a computationally efficient method is needed to enable parametric studies of candidate short-inlet designs at multiple operating conditions.

The body-force-based approach presented in Chapter 3 provides a new platform enabling the parametric exploration of the short-inlet design territory at low computational cost. Coupled with a Bezier-spline based parameterization for three-dimensional inlet and nacelle shapes, the body fore method is used to define a short-inlet configuration with improved performance relative to the long-inlet baseline case.

## 2.2 Foundational Work on Body Force Approaches in Turbomachinery

In the body-force-based approach, the blade row is replaced with a force field which generates the same stagnation pressure rise and flow turning. The approach has been used to address a large variety of turbomachinery problems, including compressor stall inception and compressor stability estimation, the assessment of rotor noise propagation, and the analysis of the impact of stagnation pressure distortion on rotor performance. The body-force-based approach typically requires a reduced-order model to define the body force representation of the blade row and formulate the functional dependence between force and inflow. Often, some empiricism (correlations, experiments, or CFD calculations) is needed to bridge the gap between the actual blade row geometry and the body force representation. In this section, an overview of past work on the body force method and different implementations is provided and the reasons behind the selection of Gong's method as the basis for the framework developed in this thesis are given.

The body force approach to represent the overall characteristics of a blade row was first introduced by Marble [33]. Marble derived formulations for body forces required to produce a given change in swirl and entropy along a streamline. This approach was incorporated in the development of the streamline curvature approach, which can be viewed as an axisymmetric body force method. Expositions of this approach are presented by Hawthorne and Novak [45] or Smith [46]. Marble's ideas were later used for example by Hynes and Greitzer [47], Escuret and Garnier [48] and Longley [49] to simulate the onset of rotating stall from long-wavelength disturbances. Takato and Nagano [50] presented a non-linear method to describe rotating stall by modeling incompressible flow through a two-dimensional isolated blade row with infinitesimal pitch but finite chord. For a given functional dependence of static pressure loss and exit flow angle on incidence and assuming the change in loss to lag in time behind changes in incidence, the method was demonstrated to capture stall inception, stall cell growth, and stall cell propagation velocity. Extending these ideas,

Longley's method uses an unsteady two-dimensional model of compressor stability, first applying it to a hypothetical four-stage compressor [49] and later to four different real compressors [51].

Escuret and Garnier [48] developed two unsteady methods for the assessment of compressor stability. The first was a two-dimensional approach based on an unsteady compressible throughflow code solving the circumferentially-averaged Euler equations in the blade rows. This approach was used to predict the onset of primarily axisymmetric flow instabilities such as surge. The second method was a three-dimensional stall model based on an unsteady Euler solution outside of the blade rows coupled with multiple throughflow solutions within the blade rows. The approach's main benefit is to provide a three-dimensional small length-scale discretization of the compressor flow field and it was demonstrated to predict the growth of three-dimensional compressible long length-scale instabilities.

Hale and O'Brien [52] presented a method to determine the change in steady performance of an isolated rotor due to circumferential distortion effects by coupling a two-dimensional throughflow code with a three-dimensional unsteady Euler code. Stagnation pressure and efficiency results from inlet distortion simulations compared to within 3% and 7% with experimental data, respectively, and captured the magnitude and shape of radial profiles of exit stagnation pressure and temperature. The method was later used to assess the performance of a three-stage fan coupled to a forebody and inlet of an advanced military fighter aircraft [53].

More recently, the body force idea was extended by Xu et al. [54] to capture long-scale unsteady disturbances up to engine order (once per revolution) and at the same time resolve relatively short wavelengths down to the order of blade passage, bridging the gap between computationally expensive unsteady RANS solvers and the one- or two-dimensional body force/actuator disk models.

A passage-averaged multistage flow model representing the blade effects with both inviscid and viscous forces was presented by Adamczyk [55]. Based on a circumferentially passage-averaged body force model, a three-dimensional method for long-scale problems was developed by Gong [6, 38]. One of the main advantages inherent to

Gong's approach when compared to actuator disk concepts is that the source terms are distributed both radially and axially in the circumferentially passage-averaged body force model, enabling the method to capture some of the dynamic blade row response to the unsteady flow field, e.g. due to inertial and/or convection effects [56]. In addition, numerical issues associated with waves reflecting from the actuator disk boundaries are eliminated in distributed source term approaches including the method proposed by Gong.

Gong's method to simulate axial compressor stall inception and distortion transfer was used by Hsiao et al. [23] to determine the rotor effect on inlet flow separation in a powered nacelle simulation at significantly reduced computational cost compared to full-annulus direct CFD simulations including rotor and stator blade geometries. In this approach, the body force terms are distributed radially and axially in the blade row and the blade performance is a function of local flow conditions instead of conditions at the blade row inlet only as in previous two-dimensional actuator disk simulations such as the one proposed by Bush [31]. Defoe et al. [57, 58] used a modified version of Gong's time-mean body force model to compute the generation and propagation of fan noise through non-uniform flow conditions in a boundary-layer-ingesting serpentine inlet. The key idea here was the addition of a rotating disturbance force field to model rotor shock noise. The rotor shock noise depends on the shock Mach numbers, which vary around the annulus as the time-mean rotor body force field reacts to the non-uniform inflow.

Chima [59] developed a three-dimensional unsteady CFD method for inlet distortion and compressor stability assessment. In this approach, Marble's formulations for turning and loss forces [33] was used for steady calculations and Stewart's iterative formulation for body forces required to turn the flow to a specified angle [60] was employed for unsteady simulations. Body force input data was calculated using steady RANS simulations [61] for one operating point near stall and scaled to other operating points using normalized characteristic maps without requiring any additional information about stalled compressor characteristics. Chima's method can be used in different modes: fast two-dimensional throughflow simulations provide oper-

ating maps and estimations for stall points, a three-dimensional steady mode can be used to assess circumferential inlet distortion, and three-dimensional unsteady calculations are required to assess rotating stall in a compressor stage. The code was validated against NASA stage 35 [62] experimental data, with the computed stall point at approximately 3.2 % lower corrected flow than the experimental data. This discrepancy was attributed to the linear extrapolation approach used for scaling the body force data into stall based on normalized characteristic maps. Improvements were suggested to be possible if the body force data is determined from steady RANS solutions over a range of operating conditions but this approach was not investigated.

Due to its capability to capture fan-inlet coupling and distortion transfer, the approach by Gong [6, 38] is the basis for the body force method developed in this work. In the approach, the force expressions depend on blade geometry, local flow variables, and two coefficients associated with the forces for flow turning and stagnation pressure loss due to viscous effects. The force descriptions are determined based on the axisymmetric flow field through the blade row, computed using steady RANS simulations over multiple operating conditions along a given speedline. The dependence of the force field on the local flow is based on a blade passage model which is the focus of the next chapter.

# Chapter 3

## Body Force Source Term Modeling for Turbomachinery Flows

This chapter describes the body force method to model the fan rotor and stator blade rows in the inlet and nacelle design framework employed in this research. The objective is to develop a body-force-based approach to provide the stagnation pressure rise and flow turning through the fan rotor and stator blade rows. The approach must be capable of capturing the effects of rotor-inlet coupling and distortion transfer.

### 3.1 Body Force Representation of Axial Rotor and Stator Blade Rows

The physical effects of compressor or fan blades on the flow are due to pressure and viscous forces at the solid surfaces. The fundamental idea behind the body force modeling approach is to redistribute the blade forces in the circumferential direction. The blades are replaced by a body force field in the swept volume of the actual blade row, as illustrated in Fig. 3-1. Inside the body force field region, source terms are added to the momentum and energy equations to produce the same pitchwise-averaged flow turning, enthalpy change, and entropy generation as the blades. Individual blades exerting surface forces on the fluid are not captured by the body force representation

of the blade row. Replacing the discrete blades with body force distributions leads to simplified grid topologies and reductions in grid point counts since fine mesh resolutions near the blade surfaces are no longer needed. In body force simulations, the computational domain is an axisymmetric, three-dimensional channel bound by hub and shroud endwalls.

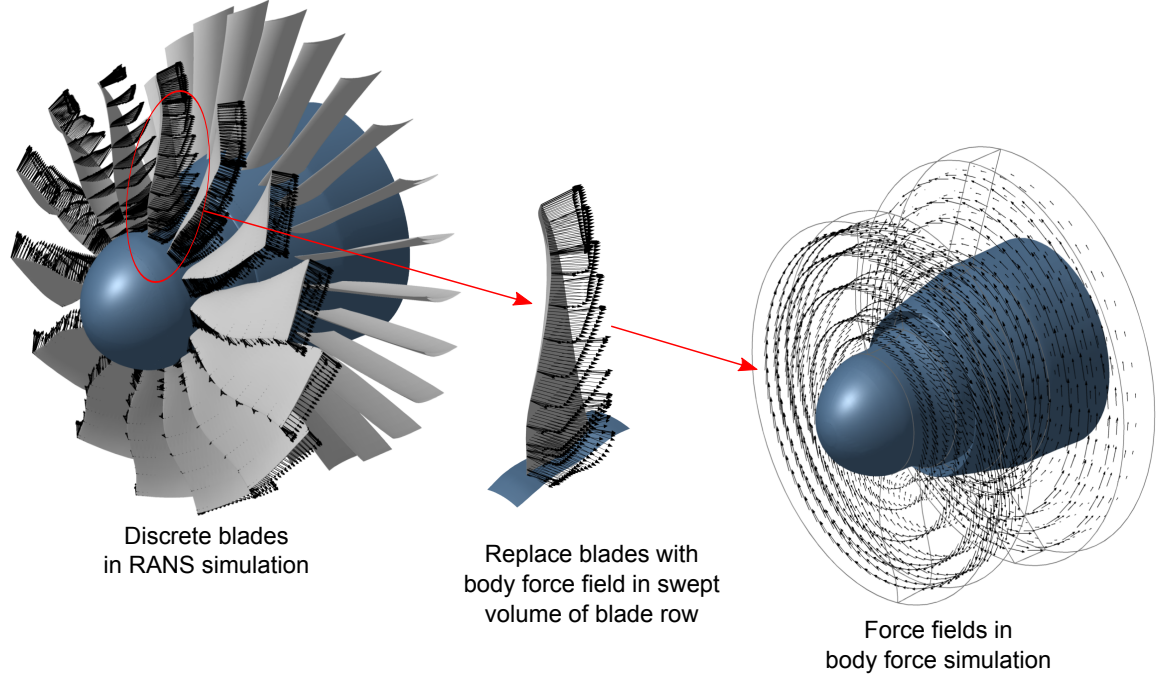


Figure 3-1: Baseline fan stage modeled with body force fields (geometry distorted).

Following Marble's foundational work on through-flow methods [33], the blade force per unit mass,  $\vec{f}$ , is divided into a force component normal to the flow and a force component parallel to the flow in the blade row frame of reference, denoted by  $\vec{f}_n$  and  $\vec{f}_p$ , respectively. The normal force represents the blade loading and provides the flow turning. The parallel force is responsible for generating the viscous losses in the blade row. The body force field re-constructs the pitchwise-averaged flow field generated by the discrete blades. This concept is depicted in Fig. 3-2.

The first step in a body-force-based approach is to extract the blade forces which re-create the axisymmetric mean flow field. The second step is to define the relationship which governs how the body force locally responds to changes in the flow. The dependency of the body force on the local flow is derived from a circumferentially

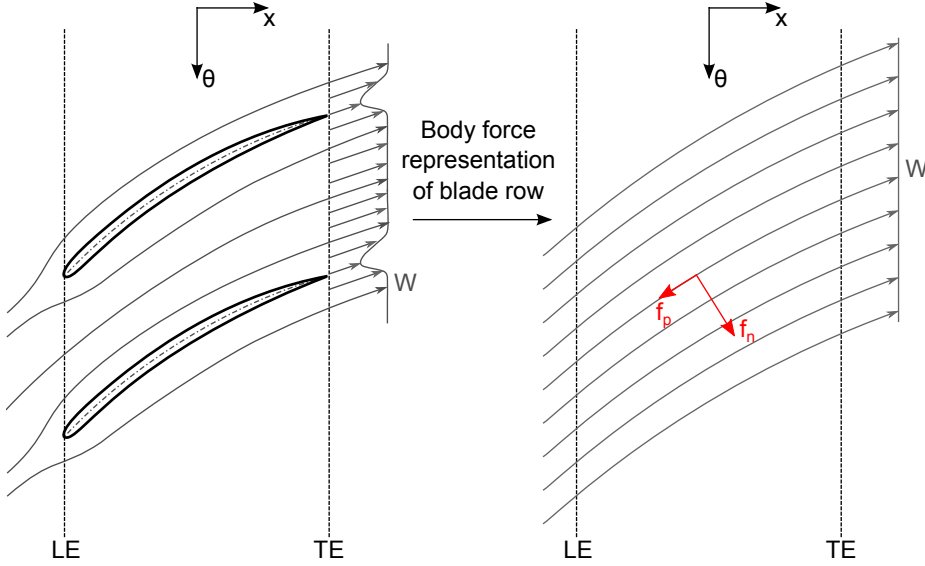


Figure 3-2: Relative flow through discrete blade passage (left) and relative flow through body force field (right).

passage-averaged flow field over a range of operating conditions and therefore not directly a function of angular position. However, the body force field responds to local flow properties so a non-axisymmetric flow field results in a non-axisymmetric force field as illustrated schematically in Fig. 3-3.

Two different approaches have been used in the past to define the relationship between the body force field and the local flow conditions. In the first approach, the body force field is extracted from a control volume analysis for each blade row at different operating conditions. The body force description is governed by a look-up table, where the body forces are functions of local flow quantities. This method was implemented for example by Benneke [63].

In the second approach, the body force field is extracted from the blade surface pressures and averaged (or “smeared out”) over a blade passage. The dependency of the body force on the local flow is derived from analytical formulations. In the current work, analytical expressions for the normal and parallel body force are based on a blade passage model. The blade passage model was originally developed by Gong [38] and is modified and extended in this thesis to account for the coupling between the inlet flow and a three-dimensional fan stage.

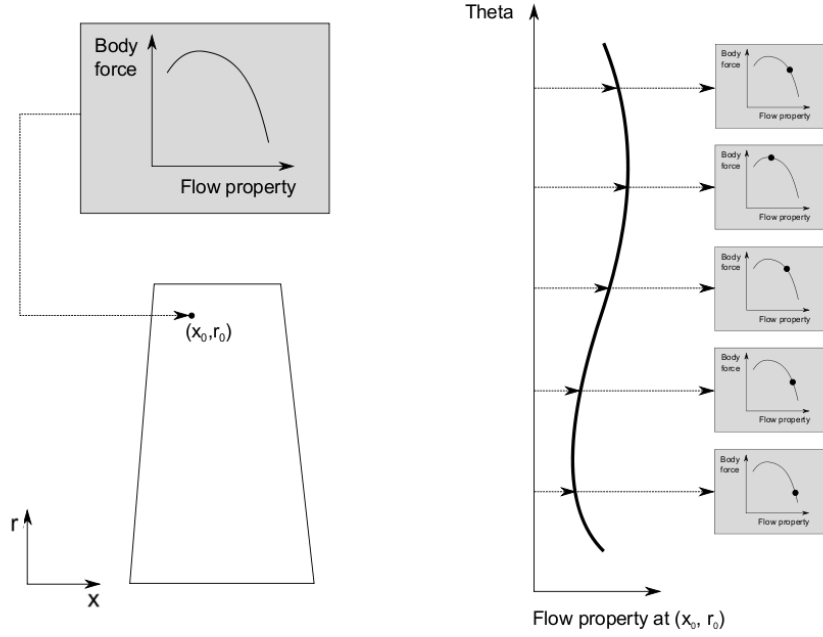


Figure 3-3: Dependence of axisymmetric body force field on local flow conditions (from Kerner [5]).

In the blade passage approach, the blade rows are assumed to consist of an infinite number of thin blades restricting the redistribution of circumferential flow variations. Flow disturbances are locked to these infinitesimally thin channels and circumferential gradients do not change the flow dynamics in the bladed regions. The flow in neighboring streamtubes is affected by local disturbances only due changes in the flow field upstream of the body force domain. Outside of the body force domain, the flow field is affected by circumferential gradients. The changes in the flow field are propagated downstream into the body force domain, resulting in changes in the local body force response [63]. Gong's body force approach implies that a three-dimensional flow field can be modeled by an infinite number of axisymmetric flow fields.

There are several approaches to define the body force source terms. Gong et al. [6] determined the source terms from known compressor characteristics and correlated their chordwise distributions using empirical assumptions. Since the fidelity of the body force method depends directly on the accuracy of the definition of the source terms, an improvement to this approach is to define the body forces based on the blade forces and the pitchwise-averaged flow field from three-dimensional steady, single-

passage RANS simulations<sup>1</sup>, thereby reducing the dependency on empiricism [56]. This approach is employed in the present work.

### 3.2 Governing Equations for the Body Force Approach

For flow in the blade rows, the full three-dimensional unsteady Euler equations with body forces in cylindrical coordinates  $x$ ,  $r$ , and  $\theta$  are given by

$$\begin{aligned} \frac{\partial}{\partial t} \begin{bmatrix} r\rho \\ r\rho V_x \\ r\rho V_r \\ r\rho V_\theta \\ r\rho e_t \end{bmatrix} + \frac{\partial}{\partial x} \begin{bmatrix} r\rho V_x \\ r\rho V_x^2 + rp \\ r\rho V_x V_r \\ r\rho V_x V_\theta \\ rV_x (\rho e_t + p) \end{bmatrix} + \frac{\partial}{\partial r} \begin{bmatrix} r\rho V_r \\ r\rho V_r V_x \\ r\rho V_r^2 + rp \\ r\rho V_r V_\theta \\ rV_r (\rho e_t + p) \end{bmatrix} + \frac{\partial}{\partial \theta} \begin{bmatrix} \rho V_\theta \\ \rho V_\theta V_x \\ \rho V_\theta V_r \\ \rho V_\theta^2 + p \\ V_\theta (\rho e_t + p) \end{bmatrix} \\ = \begin{bmatrix} 0 \\ rF_x \\ \rho V_\theta^2 + p + rF_r \\ -\rho V_r V_\theta + rF_\theta \\ r(\vec{F} \cdot \vec{V} + \dot{Q}) \end{bmatrix}. \end{aligned} \quad (3.1)$$

In Equation 3.1, the density is denoted by  $\rho$ ,  $\vec{V} = (V_x, V_\theta, V_r)^T$  is the velocity vector,  $p$  is the static pressure, and  $e_t$  is the absolute stagnation internal energy per unit mass, such that the stagnation enthalpy is given by  $h_t = e_t + \frac{p}{\rho}$ . The body force source terms (in units of force per unit volume) and the heat source term (in units of heat release per unit volume) are denoted by  $\vec{F} = (F_x, F_\theta, F_r)^T = \rho(f_x, f_\theta, f_r)^T$  and  $\dot{Q}$ , respectively. If there is no heat source in the fluid, the energy source term in Equation 3.1,  $\vec{F} \cdot \vec{V} + \dot{Q}$ , reduces to the work done by the body force on the flow,

---

<sup>1</sup>The term RANS simulation is used in this thesis for a CFD calculation which includes the blade surfaces. In contrast, a body force simulation denotes a CFD calculation with the blade rows replaced by a body force field.

$$\dot{W}_{source} = \vec{F} \cdot \vec{V} + \dot{Q} = F_\theta \Omega r. \quad (3.2)$$

The body force  $\vec{F} = (F_x, F_r, F_\theta)$  represents the influence of the blade row on the flow and varies both with spatial location in the blade row and operating condition.

Following Marble's analysis [33], relations can be derived to demonstrate how the body forces change the enthalpy and entropy of the flow. Substituting for the pressure gradient in the Gibbs equation,  $Tds = dh - \frac{1}{\rho}dp$ , using the steady inviscid momentum equations in cylindrical coordinates yields

$$W_m \frac{\partial h_t}{\partial m} - F_\theta \Omega r = TW_m \frac{\partial s}{\partial m} + \vec{W} \cdot \vec{F}, \quad (3.3)$$

where  $m$  is in the direction of a meridional streamline,  $\vec{W}$  is the relative velocity vector,  $s$  is the entropy, and  $T$  denotes the static temperature. The parallel body force component is parallel to the relative flow,  $\vec{W} \cdot \vec{F} = WF_p$ . The circumferential momentum equation and the Euler turbine equation can be combined to give

$$\frac{\partial h_t}{\partial m} = \frac{F_\theta \Omega r}{W_m}. \quad (3.4)$$

Equation 3.4 implies that the rate of change of stagnation enthalpy along a meridional streamline is proportional to the rate at which the torque applied by the circumferential body force does work on the fluid. Combining Equations 3.4 and 3.3 yields

$$\frac{\partial s}{\partial m} = -\frac{W}{W_m T} F_p. \quad (3.5)$$

Equation 3.5 states that the changes in entropy along a meridional streamline are due to the parallel force which accounts for the losses by the viscous shear stresses.

The following section introduces the functional dependence of the force field on the local flow conditions in the blade row frame of reference,

$$\vec{F} = \rho \left[ \vec{f}_n (\rho, p, \vec{W}) + \vec{f}_p (\rho, p, \vec{W}) \right]. \quad (3.6)$$

### 3.3 Modified Body Force Method

The blade passage model used in the present work is a modified version of the approach presented in [38]. The normal force is decomposed into a part due blade loading, denoted here by  $\vec{f}_{n_{\nabla p}}$ , and a part to account for the response of the blade loading to local changes in deviation, denoted by  $\vec{f}_{n_\delta}$ ,

$$\vec{f}_n = \vec{f}_{n_{\nabla p}} + \vec{f}_{n_\delta}. \quad (3.7)$$

Gong used two different approaches to formulate the dependence of the two normal force components in Equation 3.7 on the local flow conditions. A force balance for a two-dimensional blade channel with discrete blades was employed to derive the body force due to blade loading,  $\vec{f}_{n_{\nabla p}}$ . The response of the normal force  $\vec{f}_{n_\delta}$  due to differences between the relative streamline and the local camber line, i.e. changes in deviation, was derived based on the cross-passage momentum balance in a staggered channel. The derivations of the two force components are presented in Appendix A and the resulting formulation for the normal force magnitude is given by

$$f_n = f_{n_{\nabla p}} + f_{n_\delta} = \frac{1}{\rho} \frac{\partial p}{\partial x} \frac{\sin \kappa}{\cos^2 \kappa} + \frac{K_n(x, r)}{h} W^2 \frac{1}{2} \sin(2\delta). \quad (3.8)$$

In Equation 3.8,  $\kappa = \kappa(x, r)$  denotes the local blade metal angle,  $h$  is the staggered spacing between two blades, and  $\frac{\partial p}{\partial x}$  is the axial component of the pressure gradient. The deviation angle is defined as the angle between the local relative flow direction and the local camber line,  $\delta = \beta - \kappa$ . The normal force component due to changes in the deviation includes a scaling function  $K_n = K_n(x, r)$ , which is labeled the normal body force coefficient. The body force coefficient can be viewed as the empirical link between force and flow field and must be determined before a body force simulation can be carried out, either from experiments or computations.

Similar to the drag relationship for an airfoil, the body force representing the viscous losses acts opposite to the relative flow direction and the magnitude can be written as

$$f_p = \frac{K_p(x, r)}{h} W^2. \quad (3.9)$$

If the parallel force magnitude and the velocity in the blade domain are known from experimental data, empirical correlations, or CFD results, the parallel body force coefficient  $K_p$  can be calculated from Equation 3.9.

The original body force method as proposed by Gong was applied to the advanced fan stage ( $FPR < 1.4$ ,  $BPR$  near 20), resulting in the identification of the following shortcomings. First, blade metal and aerodynamic blockage are not accounted for. The implementation of blockage terms is challenging as it requires the modification of the left-hand sides of the governing equations [63], which is not usually possible in commercial flow solvers. For the advanced fan geometry used in the current work, blade metal blockage is small due to the low number of thin rotor blades.

In addition to neglecting blockage effects, there are three important limitations in Gong's body force approach when used in powered-nacelle simulations with advanced fan stage designs:

1. The approach was originally developed for compressor stability investigations and radial force and velocity components due to blade lean were assumed negligible. These can be up to 25 % of total blade force and velocity magnitudes in the three-dimensional blade design.
2. The parallel force description does not accurately capture the off-design loss generation for operating conditions near stall and choke, which the rotor can be locally subjected to at low-speed, high-AoA operating conditions.
3. The body force distributions in the blade rows were based on experimental data at radial sections, for example at mid-span and near the blade tip [23]. Experimental data is usually not available in the fan design phase. As observed in [23], inaccuracies can arise in the body force simulations compared to the measured rotor performance if the force distributions are not based on data on the entire blade domain.

In the present work, the first limitation is addressed by extending the two-dimensional blade passage model to account for blade lean. The second limitation is addressed by re-formulating the viscous force component based on a quadratic dependence of stagnation pressure loss on relative Mach number so as to represent a rotor loss bucket. Finally, rather than depending on experimental data, force and flow fields are extracted from steady RANS simulations at every grid point on the blade, and distributions of the body force coefficients  $K_n$  and  $K_p$  are computed for the entire blade domain as discussed in Section 3.4.

The modified body force model is defined by four control parameters:

- Local stagger angle  $\kappa$  as function of axial and radial coordinate,
- Local blade lean angle  $\lambda$  as function of axial and radial coordinate,
- Solidity  $\sigma$  as a function of radial coordinate, and
- Rotational speed  $\Omega$ .

It is important to note the differences and advantages of the body-force-based approach compared to a conventional two-dimensional actuator disk model. In the actuator disk model, a plane of discontinuity is used to represent a blade row and the flow property changes across the blade row are assumed to be concentrated at the disk. In the body-force-based approach used in the current work, the flow property changes are spread over the swept volume of the actual blade row. While an actuator disk model could theoretically be used to capture the fan-inlet coupling and the distortion transfer through the rotor, a three-dimensional body force method additionally enables the assessment of the impact of changes in the blade geometry (e.g. stagger or camber variations) on the inlet flow and the rotor performance at low computational cost.

### 3.3.1 Modified Normal Force Description

To include the radial component of the normal force due to blade lean, the blade passage presented in Fig. A-2 is rotated by the local lean angle  $\lambda$  around the  $\eta$ -axis.

The blade lean is defined as the angle between the blade camber surface and the radial axis and the coordinate  $k$  points in the direction of the local camber surface. In the rotated blade passage, the coordinates  $\eta'$  and  $\xi'$  are parallel and normal to the camber surface at any given point on the blade. The equation for the normal force changes to

$$\vec{f}_{n'} = \begin{bmatrix} f_{n',k} \\ f_{n',\eta'} \\ f_{n',\xi'} \end{bmatrix} = \frac{K_n(x, r, \delta, M_{rel})}{h} \frac{W_{\eta'} W_{\xi'}}{|\vec{W}|} \begin{bmatrix} 0 \\ W_{\xi'} \\ -W_{\eta'} \end{bmatrix} + \vec{f}'_{n'_{\nabla p}}, \quad (3.10)$$

where  $k$  is normal to the rotated blade passage and the velocities  $W_{\eta'}$  and  $W_{\xi'}$  now depend on both blade metal angle  $\kappa$  and lean angle  $\lambda$ , as well as all three velocity components  $W_x$ ,  $W_r$ , and  $W_\theta$ . The transformation of the blade forces to cylindrical coordinates gives a non-zero radial component for the normal body force due to blade loading.

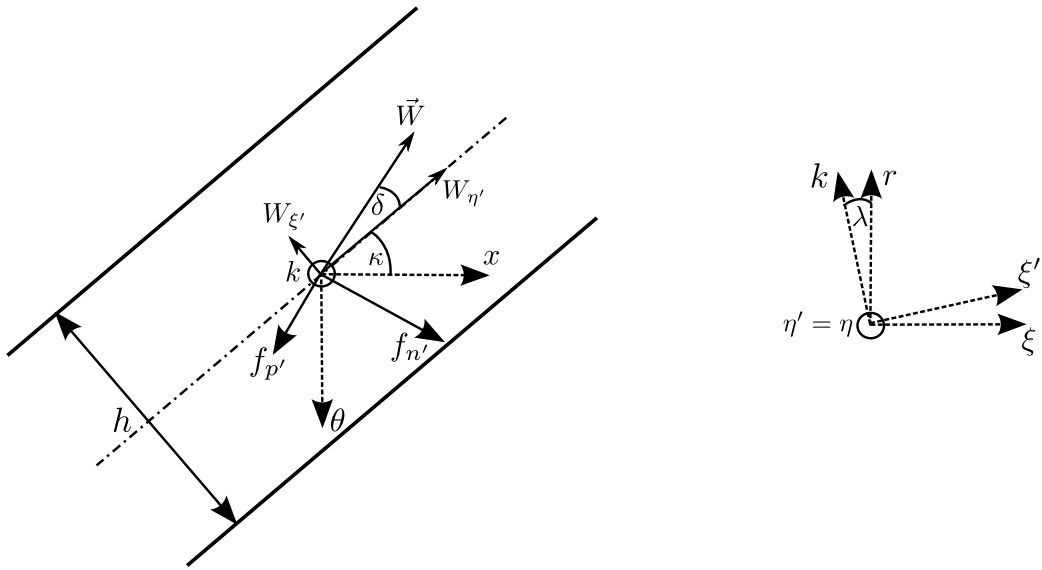


Figure 3-4: Blade passage flow with forces normal and parallel  $f_{n'}$  and  $f_{p'}$  (from Gong [6], left) and definition of blade lean (right).

### 3.3.2 Modified Viscous Force Description

The original formulation for the parallel force is given in Equation 3.9. In [38] and [23], the formulation was applied assuming a constant body force coefficient  $K_p$  over the entire blade domain. For  $K_p = \text{const.}$ , the body force results for the fan stage used in the present work are shown along the take-off speedline in Fig. 3-5, where the fan rotor stagnation pressure ratio,  $FPR$ , is plotted against the fan face corrected flow,  $w_c$ , normalized by the corrected flow at the cruise aerodynamic design point (ADP),  $w_{cADP}$ . The body force results agree with the steady RANS data only near design. The off-design loss generation is not captured with the parallel force formulation given in Equation 3.9.

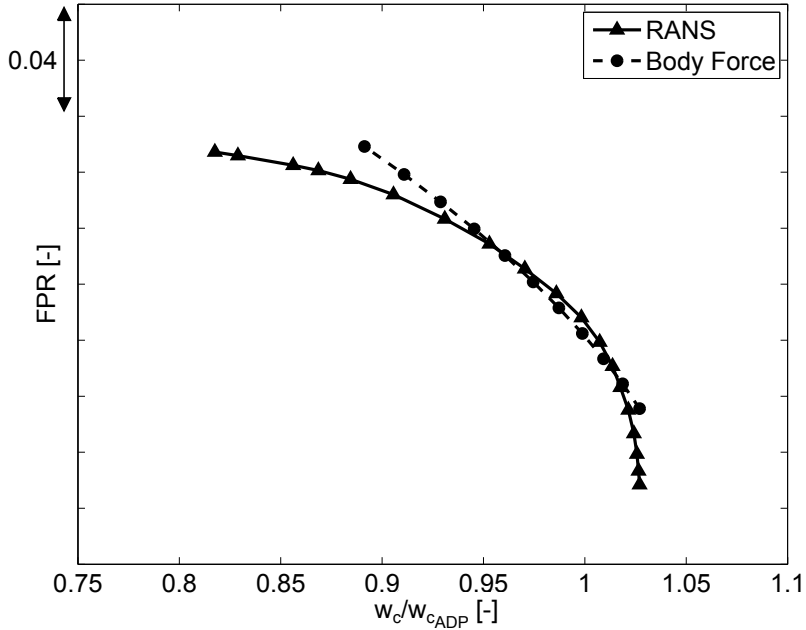


Figure 3-5: Fan pressure ratio at the take-off operating condition ( $M_0 = 0.25$ ). The results from RANS and body force simulations are plotted as solid and dashed lines, respectively. A constant viscous body force coefficient  $K_p = \text{const.}$  is used in the body force simulations. As a result, the off-design loss generation is not captured.

To capture the increase in the blade losses at off-design operating conditions, a quadratic relative Mach number dependence was introduced. From Equation 3.9, the magnitude of the viscous force is given by  $f_p = \frac{K_p}{h} W^2$ . Introducing a quadratic dependence yields

$$f_p = \frac{K_{p1}}{h} [M_{rel}^2 + K_{p2} (M_{rel} - M_{ref})^2] W^2. \quad (3.11)$$

Here,  $M_{ref}$  is the averaged relative Mach number at the blade row inlet at peak efficiency for a given speedline, which can be determined a-priori from RANS simulations. At the design point, with  $M_{rel} = M_{ref}$ , the formulation is consistent with the original model. The components of the parallel body force in cylindrical coordinates are given by

$$\vec{f}_p = \begin{bmatrix} f_{p,x} \\ f_{p,r} \\ f_{p,\theta} \end{bmatrix} = -f_p W \begin{bmatrix} W_x \\ W_r \\ W_\theta \end{bmatrix}. \quad (3.12)$$

The body force coefficients  $K_{p1}$  and  $K_{p2}$  are determined iteratively by comparing the results of body force simulations to the results of steady, single-passage RANS calculations. As discussed in Chapter 4, the results of body force simulations with the viscous force formulation in Equation 3.11 demonstrated good agreement with RANS data over an entire speedline.

### 3.4 Force Extraction from Steady RANS Simulations

As discussed in Section 3.1, the body force representation of a blade row re-constructs the pitchwise-averaged flow field. Bridging the gap between the reduced-order blade passage modeling approach and the actual case with discrete blades requires determination of the body force coefficient  $K_n$  derived from Equation 3.8,

$$K_n(x, r) = \frac{\bar{f}_{n_\delta} h}{\bar{W}^2 \frac{1}{2} \sin(2\bar{\delta})} = \frac{(\bar{f}_n - \bar{f}_{n_{\nabla p}}) h}{\bar{W}^2 \frac{1}{2} \sin(2\bar{\delta})}. \quad (3.13)$$

In Equation 3.13, the pitchwise-averaged relative velocity and deviation are denoted by  $\bar{W}$  and  $\bar{\delta}$ , respectively, and the normal force, averaged over one blade passage, is given by  $\bar{f}_n = \bar{f}_{n_{\nabla p}} + \bar{f}_{n_\delta}$ .

An overview of the body force methodology developed in this thesis is depicted in Fig. 3-6. Steady, single-passage RANS simulations are carried out at multiple operating conditions on a given speedline ranging from the maximum pressure ratio condition to choke. The deviation,  $\bar{\delta} = \bar{\beta} - \bar{\kappa}$ , the relative velocity magnitude  $\bar{W}$ , and the axial component of the pressure gradient are extracted from the pitchwise-averaged flow solution and blade surface pressures are extracted from the three-dimensional flow field to compute the net normal force  $\bar{f}_n$ . Next, the body force coefficient  $K_n$  is determined at each grid point in the rotor and stator domains using a least-square polynomial approach. A *single set* of body force distributions captures the performance over the entire speedline as demonstrated in Chapter 4.

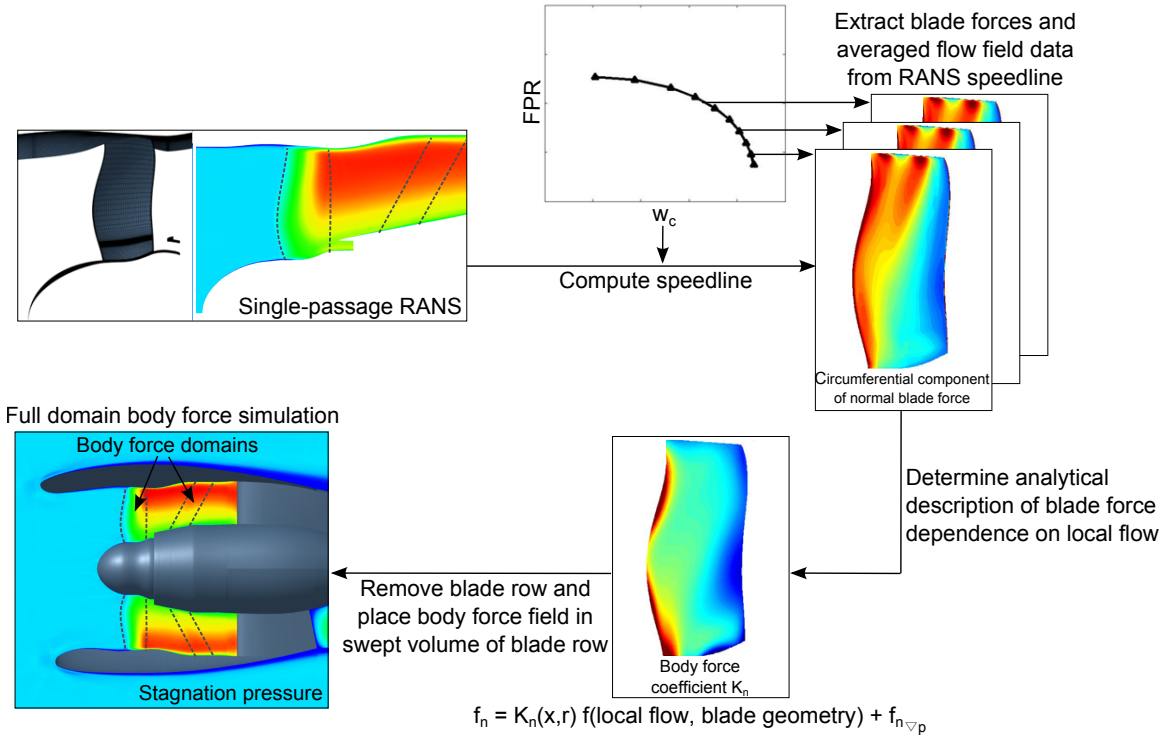


Figure 3-6: Overview of body force methodology. A single set of body force distributions captures the fan stage performance over the entire speedline.

At every grid point,  $K_n$  is constant over the speedline. However, the body force  $f_n$  changes along the speedline in response to the changes in the flow field. The rotor and stator blade rows are removed and the body force field is placed in the swept volume of the blade rows. The details of the force extraction from steady RANS

simulations are presented in Appendix B. The force extraction procedure and the blade passage model described in the previous chapter were combined in the current work to provide an integrated methodology.

An example for the extraction of the blade forces and the description of the body force field using a polynomial in the axial and radial coordinate is illustrated in Fig. 3-7 for the circumferential component of the normal force due to changes in deviation,  $f_{n\delta,\theta}$ , non-dimensionalized by the blade area  $A$ , inlet dynamic pressure  $p_{t0} - p_0$ , and blade count  $B$ . The approximation is in agreement with the blade force extracted from the RANS calculation over most of the blade domain. The force gradients are largest near the leading and trailing edges and the polynomial fit technique produces the largest errors in these regions. However, the affected blade area is small (2 – 4 % blade chord) and the validation cases discussed in Chapter 4 demonstrate good agreement with the RANS results for stagnation pressure rise, fan efficiency, and loss coefficient (with errors below 1 %).

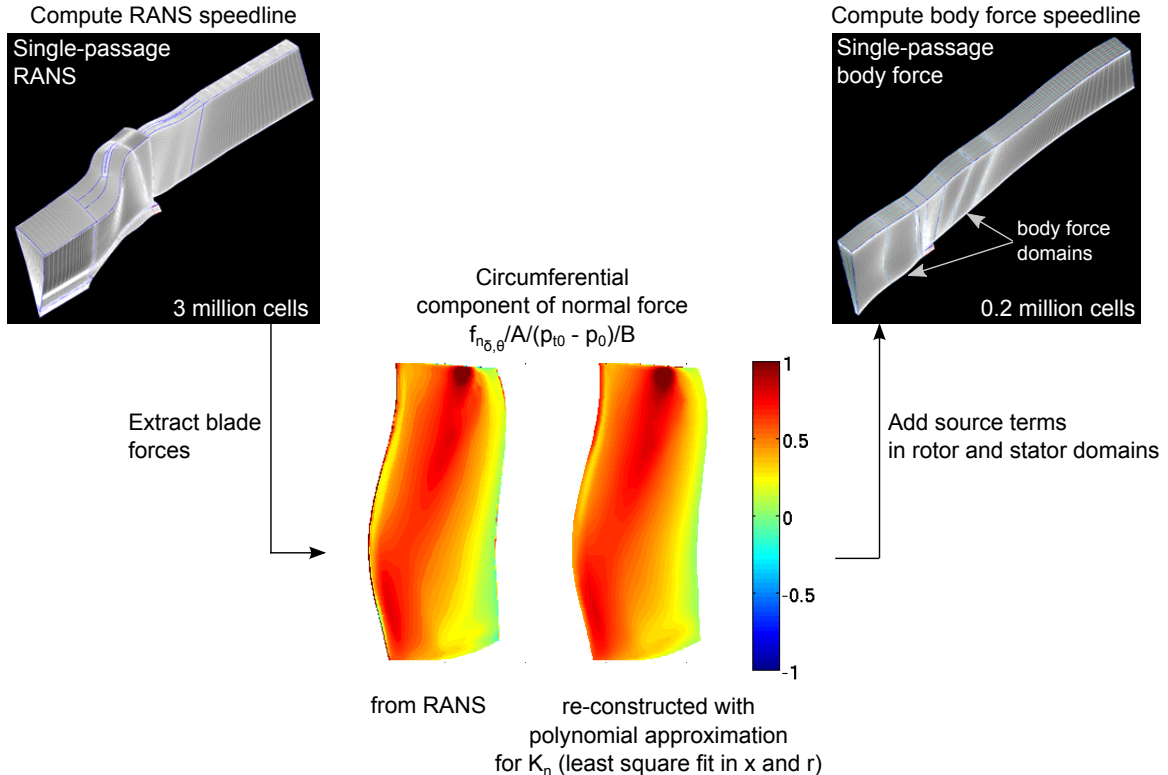


Figure 3-7: Polynomial body force description determined from blade force and flow field results extracted from steady, single-passage RANS results.

With the normal body force coefficient  $K_n$  and the parallel body force coefficients  $K_{p1}$  and  $K_{p2}$ , the normal and parallel body forces are computed in a body force simulation from Equations 3.10 and 3.12 and source terms are added to the right-hand side of the momentum and energy equations inside the rotor and stator domains. The implementation of the modified body force method in a commercial flow solver is further discussed in Appendix C.

## 3.5 Applicability and Limitations of the Body Force Method

The following list includes the main limitations of the developed body-force-based approach:

1. Unsteady terms are neglected in the derivation of the blade passage model. In the present work, steady body force simulations are shown to capture the interaction of the rotor with the non-uniform inlet flow with circumferential disturbances characterized by reduced frequencies of 0.4 and lower. The implications of neglecting the unsteady terms for the applicability of the developed method are discussed below.
2. For rotor or stator geometries with zero blade metal angle,  $\kappa = 0$ , and zero deviation,  $\delta = 0$ , at some axial or radial location, the body force model dictates a zero normal force which is inconsistent with the non-zero force manifested in relative streamline curvature. The rotor and stator geometries used in the current work did not have locations with  $\kappa = \delta = 0$ .
3. The body force coefficient  $K_n$  is assumed to be a function of geometry only and to be constant over an entire speedline in the current method. In reality, the distribution of  $K_n$  varies with changes in operating condition.
4. The viscous body force formulation in Equation 3.11 requires the calibration of the body force coefficients  $K_{p1}$  and  $K_{p2}$ .

5. Blade metal and aerodynamic blockage are not modeled in the current implementation of the body force method. The fan stage used in the present work consists of a low number of thin blades and accounting for blockage was not critical in the inlet and nacelle design studies.
6. Viscous wakes cannot be modeled in the body-force-based approach since there are no discrete blades. The losses due to viscous wake mixing downstream of the blade rows can be book-kept in the viscous body force applied inside of the blade row or captured by applying parallel body forces in the domains between blade rows. In the current work, the wake mixing losses are accounted for by adjusting the stator viscous body force in order to match the fan stage performance computed in the steady, single-passage RANS simulations.
7. Tip leakage flow is not modeled in the developed body force methodology since the emphasis in the parametric inlet and nacelle design assessment is not on the flow details but on the bulk effects.

In the present work, the objective for the developed body force method was to capture fan-inlet coupling for non-uniform inlet flow due to angle-of-attack inflow. The reduced frequency is a measure of the relative importance of unsteady effects and is defined as the ratio of the time for fluid particle transport through the rotor,  $\frac{c}{V_x}$ , and the time scale associated with the unsteadiness,  $\frac{\lambda}{2\pi R\Omega}$ , where  $\lambda$  denotes the circumferential wavelength of the disturbance [64],

$$\beta = \frac{2\pi R\Omega c}{\lambda V_x}. \quad (3.14)$$

Shaft-order disturbances associated with angle-of-attack inflow are characterized by wavelengths of  $\lambda = 2\pi R$ . For the low-FPR propulsors investigated in this thesis, the reduced frequency is given by  $\beta = \frac{\Omega c}{V_x}$ , with values between 0.3 and 0.4 depending on operating condition, indicating that unsteady effects are small. Steady body force simulations are demonstrated in Chapter 4 to capture the circumferential variation in the local operating condition due to non-uniform inflow, thereby justifying the

assumption of steady flow in the derivation of the blade passage model for the normal and parallel force formulations.

Unsteady body force simulations would be required to assess flow phenomena associated with reduced frequencies larger than one, such as short-wavelength stall inception with disturbance wavelengths as low as two blade pitches,  $\lambda = \frac{2\pi R}{B/2}$ . The capability to capture short-wavelength disturbances with circumferential flow redistribution within an individual blade passage was demonstrated in [6] for unsteady body force simulations which include the unsteady terms in the governing equations but (unlike other models for compressor stability assessment [47,65]) neglect the unsteady terms in the dependence of the force on the local flow conditions.

The body forces are functions of local flow conditions and respond instantaneously to changes in the inflow. In reality, the blade force response is gradual and time-lag models are commonly implemented to simulate the delayed response of the body force to changes in the flow [49, 59, 66]. The implementation of a time-lag model may be required to use the developed method to study short-wavelength disturbances but further work is required to assess the fidelity of body force method in flow conditions with reduced frequencies much larger than unity.

The modified body force method provides a flexible platform to explore the short-inlet design space but due to the limitations of the body force method, higher-fidelity URANS simulations were always carried out to verify the performance of propulsors with candidate short-inlet designs. The shortcomings listed in 2-5 above were addressed by Brand [8] in the development of an improved body force method. The improved method is based on a re-derived blade passage model, based on natural coordinates along a relative streamline, to capture the effects of relative streamwise curvature. The empirical link between the force and the flow field includes a dependency on local flow conditions instead of depending on geometry only. The loss force is be formulated in terms of the entropy flux in the blade row, which can be extracted from single-passage RANS simulations, thereby avoiding the need to calibrate body force coefficients. Finally, metal and aerodynamic blockage are accounted for. A summary of the re-derived blade passage model is presented in Appendix D.



# Chapter 4

## Capabilities and Validation of Body Force Method

Results from internal single-passage body force and steady RANS simulations were compared first to validate the capability of the developed body-force-based approach to capture the rotor and stator performance along a speedline and the change in performance for inlet swirl distortion. In a second step, full-domain calculations including the external nacelle flow were carried out to demonstrate that fan-inlet coupling and distortion transfer at high angle-of-attack conditions are captured.

### 4.1 Off-Design Performance

In short-inlet configurations, operation at angle-of-attack conditions leads to non-uniform flow at the fan face, resulting in circumferential incidence variations and changes in the local operating conditions. The capability to assess changes in the rotor performance due to changes in the inflow conditions is a key feature of the developed body force method.

Results for the stagnation pressure rise coefficient, defined as  $\Psi_{pt} = \frac{p_{t,ds} - p_{t,us}}{p_{t,us} - p_{us}}$ , where  $us$  and  $ds$  denote the axial locations up- and downstream of the rotor, the fan efficiency  $\eta_{fan}$ , and the relative stagnation pressure loss  $\omega = \frac{p_{t,rel,us} - p_{t,rel,ds}}{p_{t,rel,us} - p_{us}}$  are shown in Figs. 4-1, 4-2, and 4-3, respectively. To demonstrate the robustness of the method

to changes in incidence, the rotor performance is presented for no inlet swirl (marked in black), 5° counter-swirl (marked in red) and 5° co-swirl (marked in blue). The body force description was not changed from the baseline case without inlet swirl.

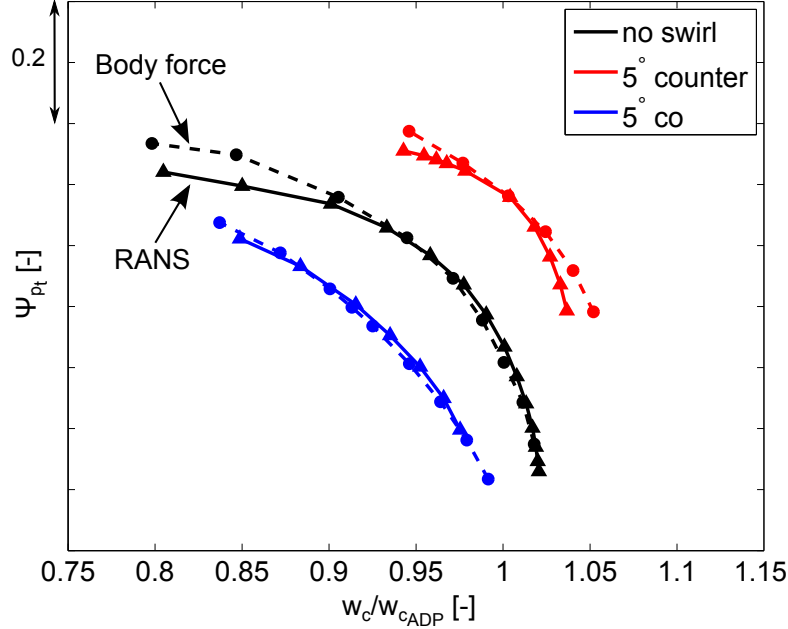


Figure 4-1: Stagnation pressure rise coefficient at the take-off operating condition ( $M_0 = 0.25$ ) for uniform inlet flow and 5° counter- and co-swirl. For a single set of body force coefficients, the rotor performance is captured over the entire speedline.

The off-design increase in the blade losses is captured in the body force simulations. In the baseline case without inlet swirl, the stagnation pressure loss is under-predicted at low flows, leading to a 4 % over-prediction in the stagnation pressure rise coefficient and a 0.5 % higher efficiency. This discrepancy is attributed to the selection of  $K_{p1}$  and  $K_{p2}$  in the viscous force description (Equation 3.11). The discrepancy near stall could be reduced by re-formulating the viscous body force in terms of entropy or dissipation. The body force method captures the changes in performance in the counter- and co-swirl cases. As the corrected flow is increased, the differences increase because blockage effects are not accounted for in the body force simulations.

To assess the rotor and stator flows produced by the body force fields, pitchwise-averaged contours of absolute flow angle and stagnation pressure distributions are presented in the left-hand plots in Figs. 4-4 and 4-5, respectively, for steady, single-

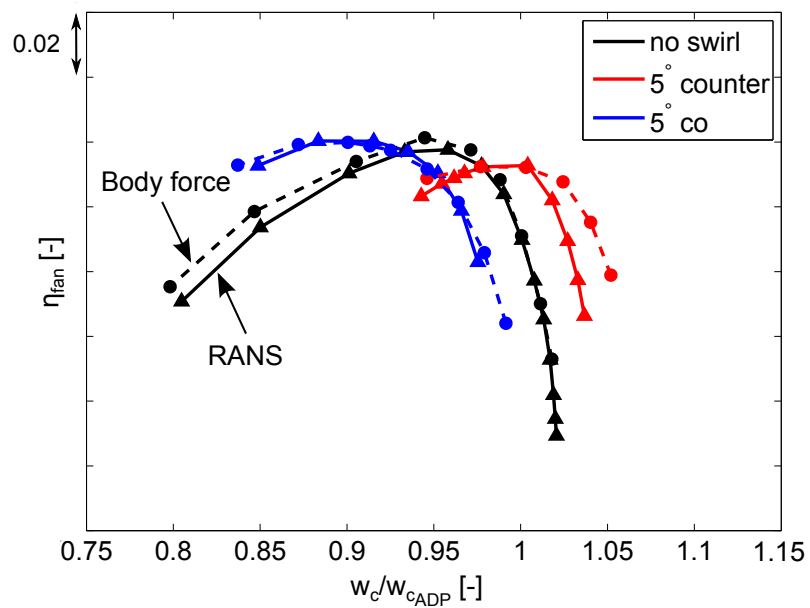


Figure 4-2: Fan efficiency at the take-off operating condition ( $M_0 = 0.25$ ) for uniform inlet flow and  $5^\circ$  counter- and co-swirl.

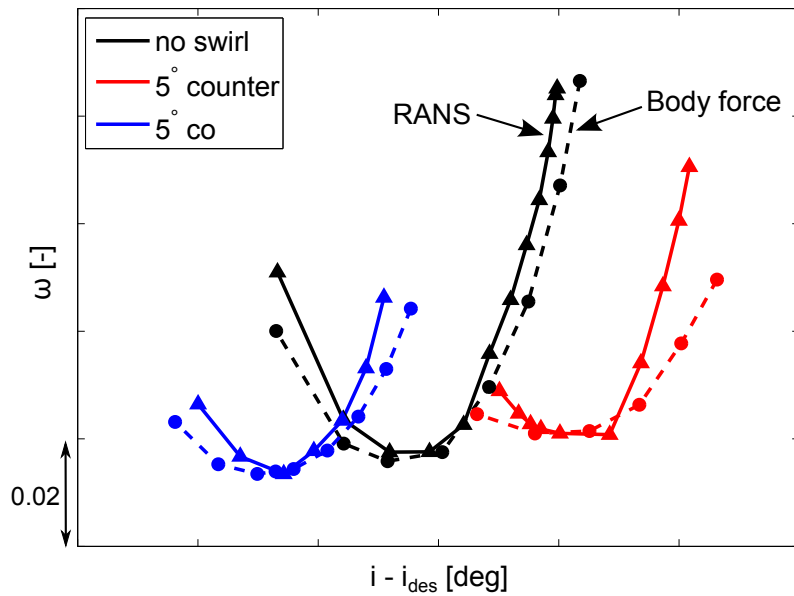


Figure 4-3: Rotor stagnation pressure loss at the take-off operating condition ( $M_0 = 0.25$ ) for uniform inlet flow and  $5^\circ$  counter- and co-swirl.

passage RANS and body force simulations. The spanwise distribution of the difference in absolute flow angle,  $\alpha_{BF} - \alpha_{RANS}$ , is shown in the right-hand plot of Fig. 4-4. The absolute flow angle results agree to within  $1.5^\circ$  between 20 % and 80 % span. Near the endwalls, three-dimensional flow mechanisms such as tip leakage or the interaction of the blade with the hub boundary layer are not captured in the body force simulations, leading to differences of up to  $5^\circ$ .

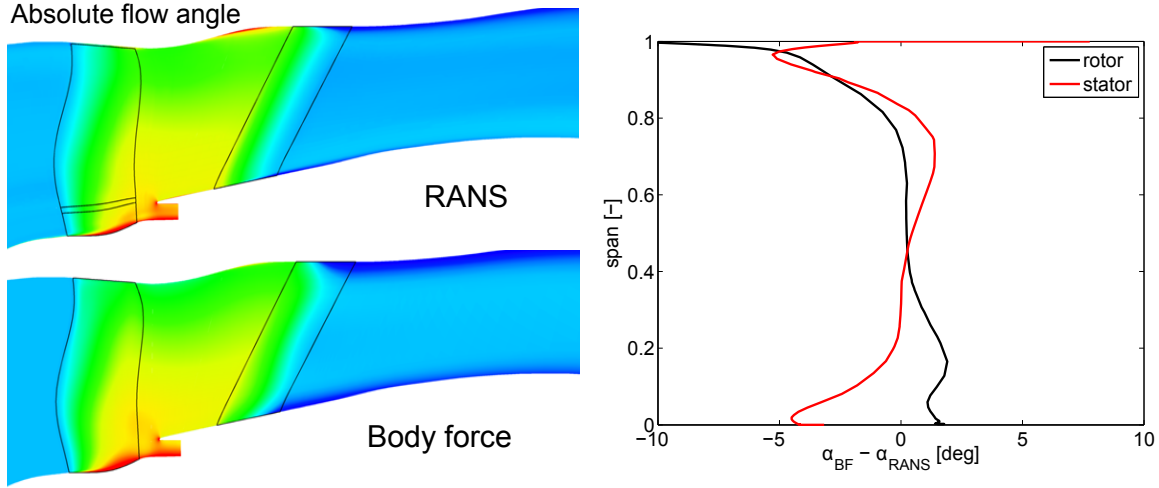


Figure 4-4: Quantitative (left) and qualitative (right) comparison of absolute flow angle from steady, single-passage RANS and body force simulations.

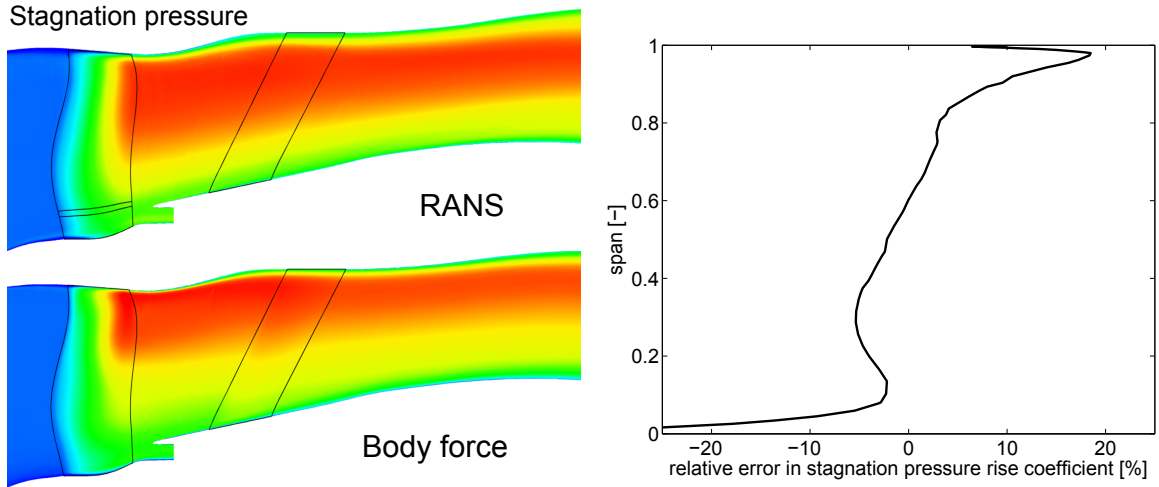


Figure 4-5: Quantitative comparison of stagnation pressure from steady, single-passage RANS and body force simulations (left) and relative error in stagnation pressure work coefficient  $\frac{\Psi_{pt,BF} - \Psi_{pt,RANS}}{\Psi_{pt,RANS}}$  (right).

The agreement in the stagnation pressure is evaluated based on the relative difference in the stagnation pressure rise coefficient. Between 10 % and 80 % span, the stagnation pressure rise agrees to within 5 %. Because tip leakage flow effects are not accounted for, stagnation pressure is over-predicted in the tip region. The discrepancies between the body force and RANS results could be improved by adjusting the viscous body force coefficients  $K_{p1}$  and  $K_{p2}$  and refining the polynomial approximations for the normal body force coefficient  $K_n$ .

The relative streamlines through the rotor domain at mid-span are shown in Fig. 4-6 for three operating points on the take-off speedline. The relative flow angle at the leading edge is highest near stall and lowest near choke. At the blade row exit, the flow angle variation between the three operating points is reduced as expected since the direction of the flow must be close to the blade metal angle due to the Kutta condition.

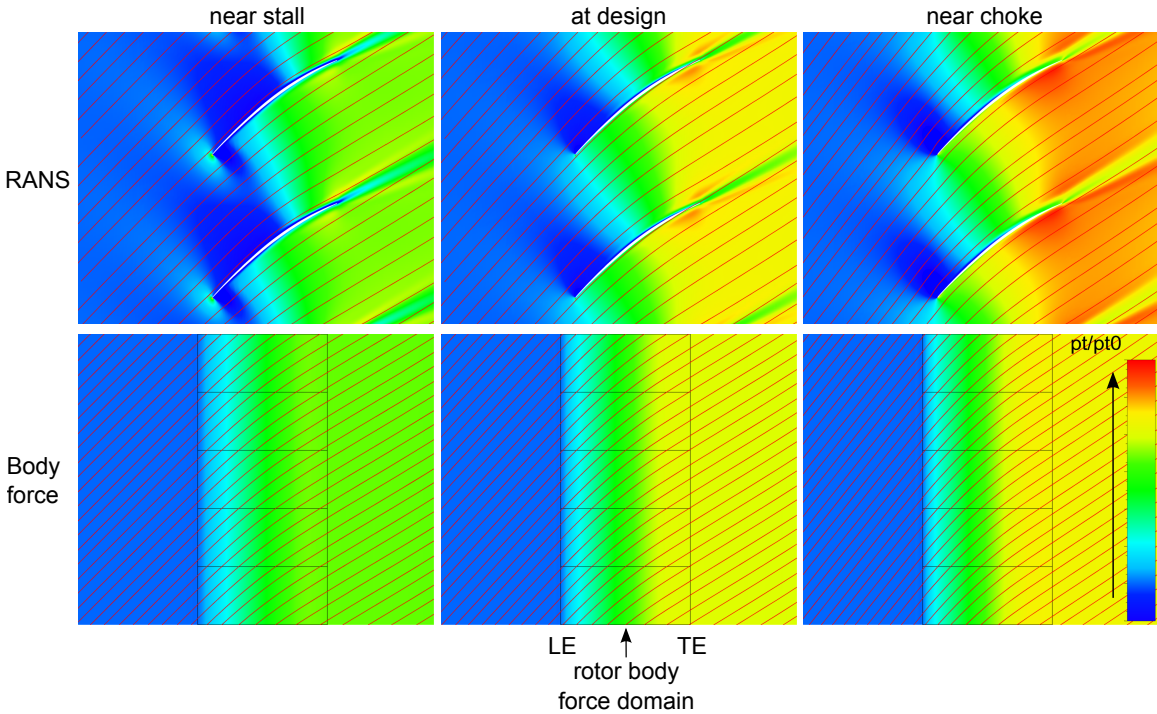


Figure 4-6: Stagnation pressure distribution and relative streamlines through the rotor blade row at mid-span extracted from single-passage RANS and body force simulations for T/O corrected speed near stall, at design, and near choke operating points. Body force simulations capture the increase in flow turning through the rotor as the mass flow is reduced from choke to stall.

The streamwise evolution of the relative flow angle along a streamline at mid-span is presented in Fig. 4-7 for the three operating points. The relative flow angle of the inflow varies by  $\Delta\beta = 7^\circ$  along the speedline. At the blade row exit, there is a non-zero variation of  $\Delta\beta = 3^\circ$  since the deviation at the trailing edge depends on the operating condition. In general, the body force results agree to within  $1.5^\circ$  with the RANS results. Upstream influence effects due to the discrete blades lead to a change in the flow angle upstream of the leading edge in the RANS simulations. Since blockage is not accounted for, this upstream adjustment is not captured in the body force computations.

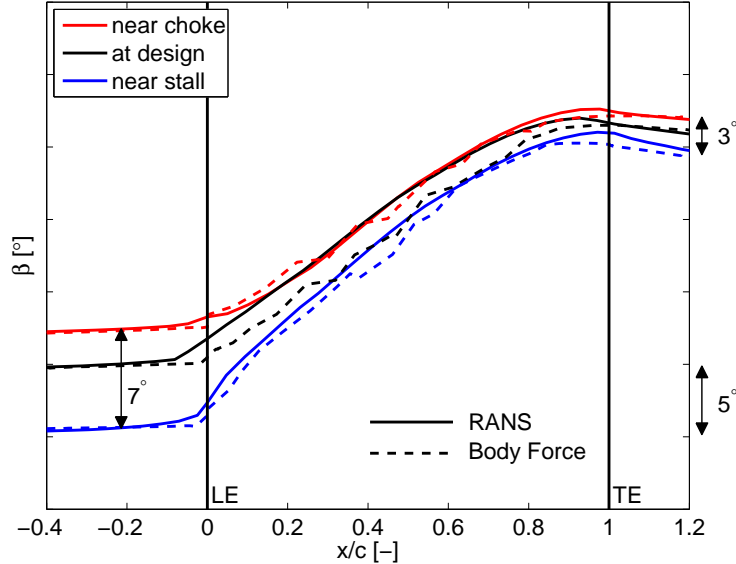


Figure 4-7: Relative flow angle along pitchwise-averaged streamline through rotor blade row at mid-span for T/O corrected speed. Body force results (dashed lines) agree to within 1.5% with data extracted from single-passage steady RANS simulations near stall (blue line), at design (black line), and near choke (red line).

The body force distributions are determined only once for a given speedline and are not changed when different inlet and nacelle concepts are evaluated. Since candidate short-nacelle configurations are assessed relative to the baseline configurations and the dependence of rotor performance on inflow is captured, the current force descriptions were deemed adequate for use in the parametric exploration of short-inlet designs.

In short-inlet propulsors at off-design conditions, the rotor can be subjected to

local inflow conditions ranging from near-choke to near-stall, making it important to capture the rotor performance over an entire speedline. The capability of the body force method to address fan or compressor stability could be assessed in future work. In this case, it is not as important to capture the rotor performance near choke. Instead of including operating conditions over the entire speedline in the determination of  $K_n$ , it would be sufficient to use operating conditions for a limited range, for example from design to stall. The fidelity of the body force method improves if a smaller range of operating conditions needs to be captured, since the error introduced by using a constant  $K_n$ -distribution decreases.

#### 4.1.1 Inlet Flow-Fan Coupling

The increased interaction between the inlet flow and the rotor is a key feature in short-inlet configurations and needs to be captured in the body force simulations for the method to be useful in the exploration of short-nacelle concepts. For a candidate short-inlet design, the absolute Mach number distributions in the inlet computed from URANS and body force simulations are shown in the left- and right-hand plots in Fig. 4-8, respectively, at the wing  $C_{L\max}$  condition with flight Mach number  $M_0 = 0.25$  and  $29^\circ$  angle-of-attack. The body force results for streamlines, shape of the region of accelerated flow along the inner surface of the inlet, and maximum Mach number inside of this region are in agreement with the time-averaged URANS calculation.

The spanwise profile of rotor incidence is extracted along the fan face location depicted on the left in Fig. 4-8 and a comparison of the profiles from time-averaged URANS and body force results is presented in Fig. 4-9. The body force results agree with the URANS data to within  $1^\circ$ , with the highest discrepancies near the endwalls. At the hub, metal blockage is largest and the upstream influence of the blade results in flow deceleration at the fan face. Since blockage is not captured in the body force simulations, incidence is under-predicted. Near the shroud, the streamwise Mach number is increased due to the flow acceleration around the bottom inlet lip and the rotor operating point locally shifts towards choke. The differences near the shroud are attributed to the assumption of  $K_n = \text{const.}$  along the entire speedline.

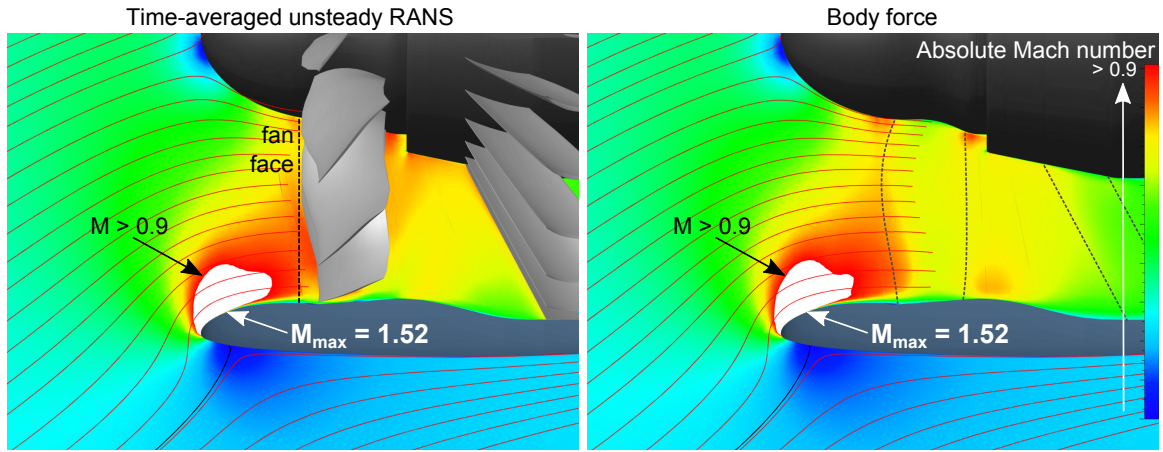


Figure 4-8: Candidate short-inlet configuration with  $L/D = 0.25$  at the wing  $C_{L\max}$  operating condition ( $M_0 = 0.25$  and  $AoA = 29^\circ$ ). Using body force distributions obtained from steady, single-passage RANS simulations, the body force method is capable of capturing the interaction between the rotor and the inlet flow.

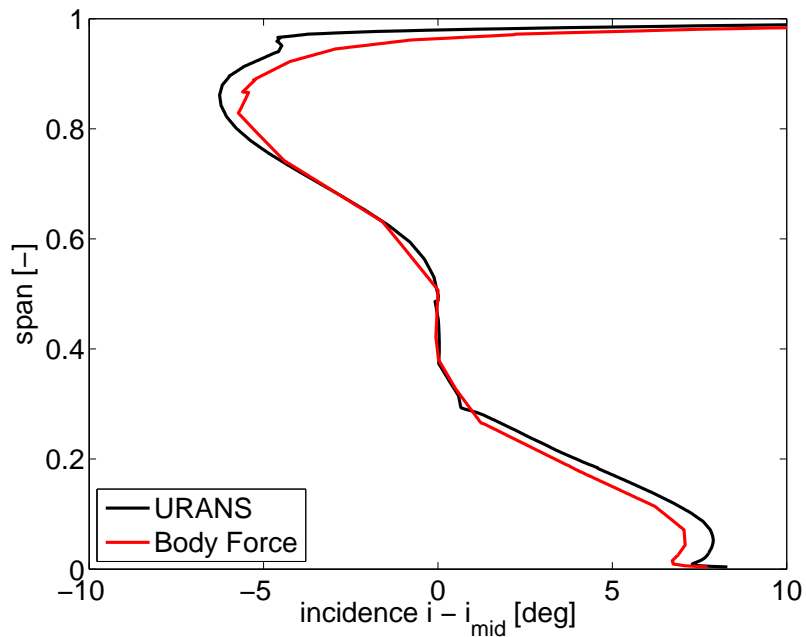


Figure 4-9: Spanwise profile of fan face incidence relative to mid-span incidence for a short-inlet configuration with  $L/D = 0.25$  at the wing  $C_{L\max}$  operating condition ( $M_0 = 0.25$  and  $AoA = 29^\circ$ ).

### 4.1.2 Distortion Transfer

Circumferential variations in incidence caused by angle-of-attack inflow lead to circumferential stagnation pressure variations downstream of the rotor. To validate the capability of the body force method to capture the distortion transfer through the rotor, body force results are compared to time-averaged URANS data in Fig. 4-10 for the baseline configuration at wing  $C_{L\max}$  ( $M_0 = 0.25$  and  $AoA = 29^\circ$ ). Fan face incidence is presented in the top plots and the difference of local stagnation pressure and mass-averaged stagnation pressure,  $p_t - p_t^M$ , is shown in the bottom plots. The inlet flow is non-uniform at the fan face and circumferential incidence variations of up to  $6.5^\circ$  are observed near the hub. The incidence distribution computed from the body force simulations agrees to within  $1^\circ$  with the URANS result. The overall patterns of incidence and resulting rotor stagnation pressure distortion are captured in the body force calculations. The circumferential locations of the minimum and maximum stagnation pressure levels agree to within  $5^\circ$  with the URANS results. The discrepancies in incidence and stagnation pressure are again due to differences in the normal body force distributions, leading to increased stagnation pressure between mid-span and shroud and reduced stagnation pressure between hub and mid-span compared to the RANS simulations (see Fig. 4-5).

The rotor performance at the wing  $C_{L\max}$  condition is further examined by tracking fluid particles through the rotor at a given spanwise location and determining the work coefficient  $\Psi_{h_t} = \frac{\Delta h_t}{U_{tip}^2}$  from the stagnation enthalpy change  $\Delta h_t$  across the rotor and the rotor tip velocity  $U_{tip}^2$ . The work coefficient for particles along the circumferential coordinate  $\theta$  (with the direction indicated in Fig. 4-10) at mid-span is plotted against rotor incidence in Fig. 4-11. The loci of operating points (or orbits) were extracted from URANS and body force simulations for the long-inlet baseline propulsor and a candidate short-inlet configuration with  $L/D = 0.19$ . In addition to the full-domain URANS and body force results, the pitchwise-averaged speedline data from steady, single-passage RANS simulations with uniform inflow is presented to highlight the range of operating points used in the definition of the body force distribution. The

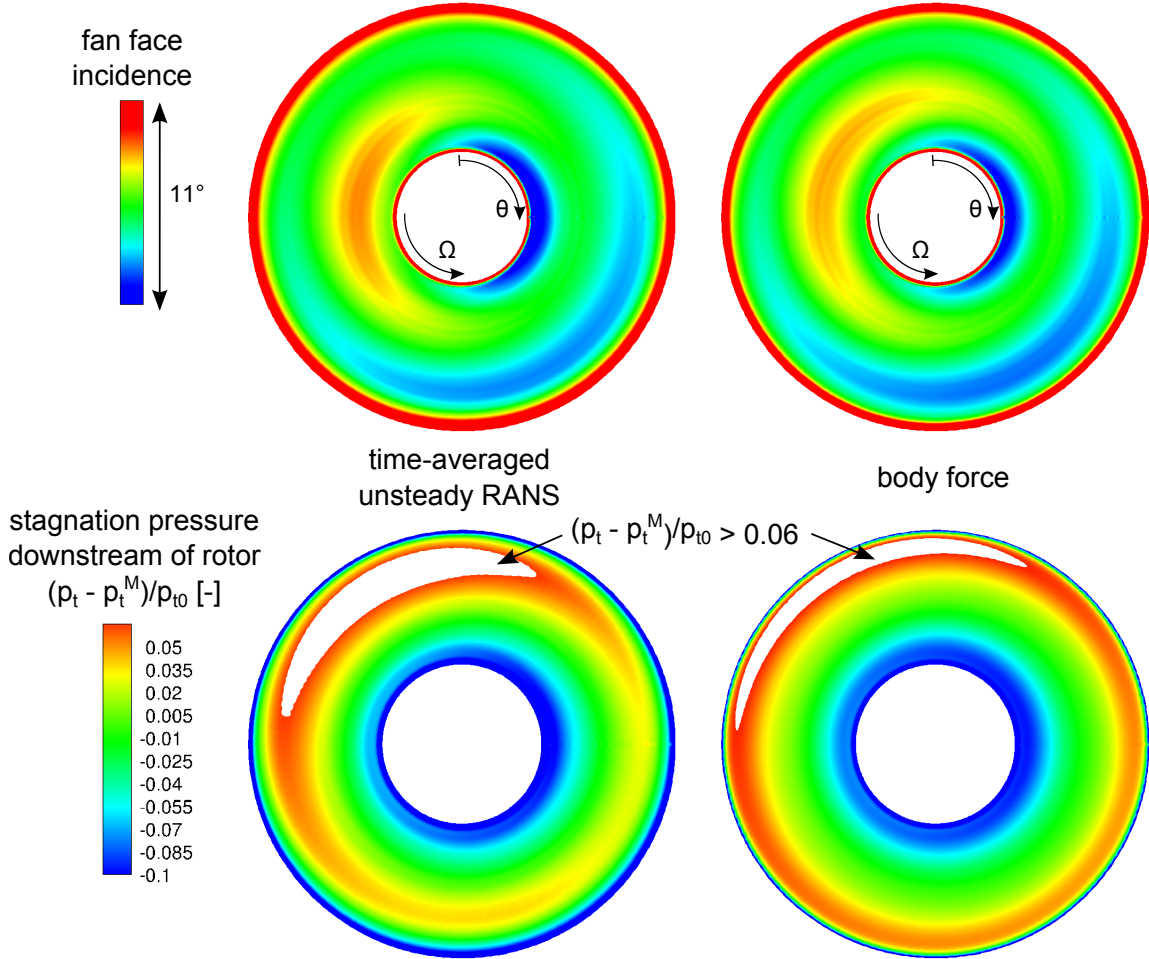


Figure 4-10: Fan face incidence and stagnation pressure distribution downstream of rotor for the baseline propulsor with  $L/D = 0.5$  at the wing  $C_{L\max}$  operating condition ( $M_0 = 0.25$  and  $AoA = 29^\circ$ ). Incidence distortion and distortion transfer are captured in the body force simulations.

peak-efficiency operating point on the speedline is marked by the gray x-symbol, whereas the circumferentially-averaged results for the URANS and the body force simulations are marked by the blue and red x-symbols, respectively.

At the wing  $C_{L\max}$  operating condition, there are regions of positive and negative circumferential Mach number at the fan face due to the high-AoA inflow. As a consequence, the rotor incidence varies by  $3.5^\circ$  along the circumference for the baseline propulsor. The rotor work is increased at positive incidence and decreased at negative incidence. The circumferential incidence variation is captured by the steady body force simulations. For the baseline configuration, the body force results for the work

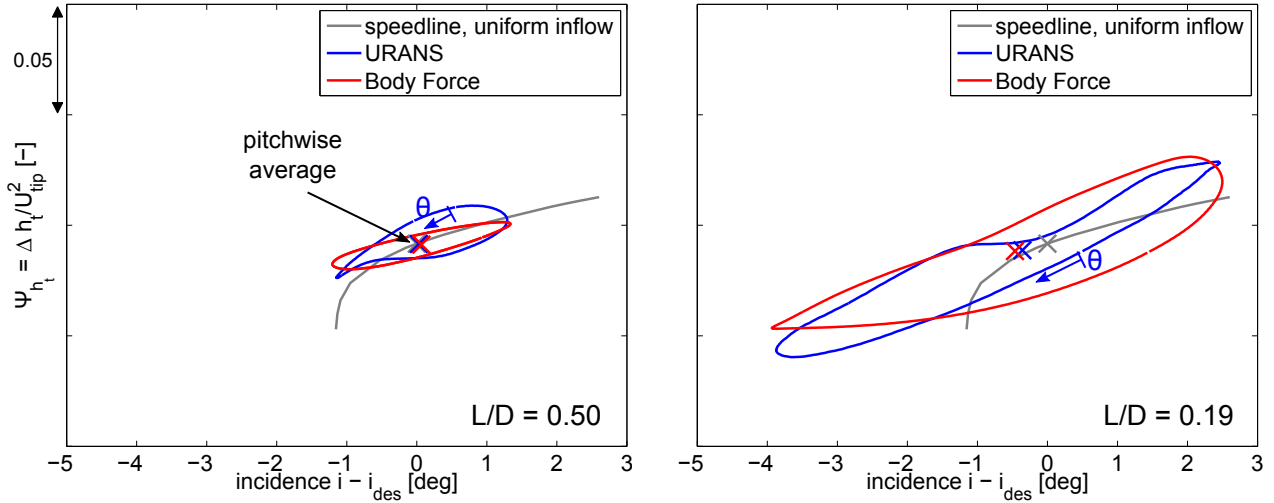


Figure 4-11: Variation of local rotor operating conditions along the circumference at mid-span for the baseline configuration with  $L/D = 0.5$  (left) and the candidate short-inlet configuration with  $L/D = 0.19$  (right) at wing  $C_{L\max}$  operating condition ( $M_0 = 0.25$  and  $AoA = 29^\circ$ ).

coefficient are within 3 % of the URANS results. For an ultra-short inlet design with  $L/D = 0.19$ , shown on the right in Fig. 4-11, the flow straightening in the inlet is reduced and the circumferential variation in rotor incidence increases to  $7^\circ$ . Even at these high levels of incidence distortion, the body force simulations were found to be robust, with convergence similar to long-inlet cases. The incidence variation is in agreement with the URANS results. However, discrepancies of up to 7 % in the work coefficient are observed near the minimum incidence operating point. The agreement with URANS results is expected to improve in unsteady body force simulations since the unsteadiness associated with the inflow distortion contributes to the change in stagnation enthalpy. As described in Section 3.5, the implementation of a time lag model to account for the finite response rate of the body force to changes in the flow would further reduce the discrepancies.

In summary, the body force method captures the interaction of the rotor with the inlet flow and the distortion transfer through the fan stage. The method's robustness is demonstrated for increased levels of incidence distortion, which the rotor is subjected to in short-inlet configurations. When compared to URANS results, local differences in the rotor performance grow with increasing distance between the local

operating point and the speedline data used to define the body force distribution. The fidelity of the method could be improved by introducing a dependence on local flow conditions in the determination of the body force coefficient instead of assuming a constant  $K_n$  along the speedline. In the parametric inlet study, the body force method is used to quantify the trade-offs in performance relative to the baseline configuration and the level of agreement with the URANS data was considered acceptable for this purpose. Absolute performance levels of selected candidate short-inlet designs were always computed using higher-fidelity URANS simulations in this work.

#### 4.1.3 System-Level Propulsor Performance

The propulsive efficiency metrics defined in Chapter 7 require the computation of net thrust minus nacelle external drag and power input. Using a control volume as indicated in the top plot in Fig. 4-12, net thrust minus nacelle external drag and shaft power input are computed from conservation of momentum and energy. The propulsive efficiency depends on the flow field quantities downstream of the engine and it is important that the interaction of the bypass stream with pylon, bifurcation, and external flows is captured in the body force simulations. The stagnation pressure distributions from medium and coarse grid level body force simulations on a vertical plane and a cut 2.5 diameters downstream are compared to URANS results on the top left and right, respectively, in Fig. 4-12 for the baseline propulsor at cruise. The stagnation pressure distributions on a horizontal plane are shown on the bottom in Fig. 4-12. The stagnation pressure downstream of rotor and stator is circumferentially non-uniform due to the non-uniform inlet flow and the back pressure distortion generated by the pylon and bifurcation.

The interaction of vorticity generated in the nacelle and pylon boundary layers with the angle-of-attack free-stream results in axial vorticity at the nacelle and pylon trailing edges. As a consequence of the axial vorticity, the high stagnation pressure bypass flow is shifted radially inward downstream of the engine. The interaction of the bypass stream with the pylon and free stream flows is captured in the medium and coarse grid body force simulations.

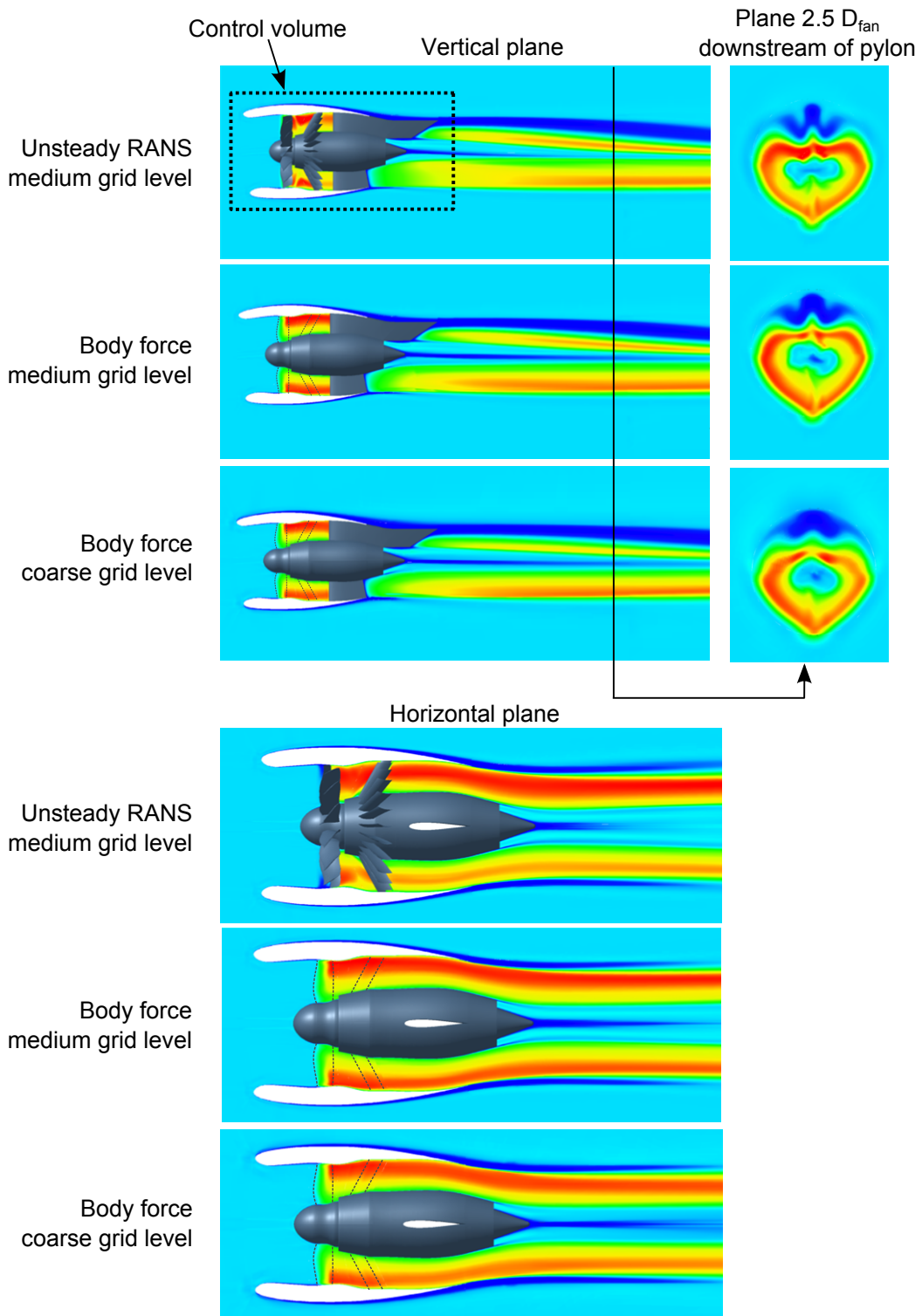


Figure 4-12: Stagnation pressure distribution for baseline  $L/D = 0.5$  configuration at cruise ( $M_0 = 0.8$  and  $AoA = 5^\circ$ ). Distortion transfer and interaction of bypass stream with pylon and nacelle downstream of the propulsor are captured in the body force simulations.

Compared to the URANS result, the engine propulsive efficiency is under-predicted by 1% and 5% for the medium and coarse grid level body force simulations, respectively, due to differences in the blade force field and the increased numerical dissipation on the coarse grid. However, coarse grid level body force simulations can be used to evaluate the relative changes in performance between different configurations in the proposed parametric inlet study. The influence of the grid density on the performance metrics is further discussed in the next chapter.

# Chapter 5

## Inlet and Nacelle Design Framework

In this chapter, an integrated inlet and nacelle design framework is presented. The key features of the new methodology are the body force representations of the rotor and stator blade rows and a spline-based approach to define inlet and nacelle surfaces.

### 5.1 Inlet and Nacelle Design Parameters

The characteristic parameters used in conventional inlet and nacelle designs are depicted in Fig. 5-1 for the baseline configuration with  $L/D = 0.5$ . The ratio of highlight to nacelle maximum diameter,  $D_{HL}/D_{max}$ , governs the flow acceleration on the outer nacelle and the maximum nacelle diameter must be chosen large enough to meet structural requirements and accommodate any engine systems and accessories.

The contraction ratio,  $A_{HL}/A_{throat}$ , affects both the cruise and off-design performance. Small contraction ratios with thin inlet lips offer low pressure drag at cruise while thicker inlet lips with increased contraction ratios are needed for separation-free inlet performance at off-design conditions, such as take-off or cross-wind. The nacelle design is axisymmetric downstream of the axial location of  $D_{max}$ , whereas the inlet geometry up to the fan face and the front outer nacelle shape are three-dimensional, with the characteristic parameters depending on the circumferential location  $\theta$ .

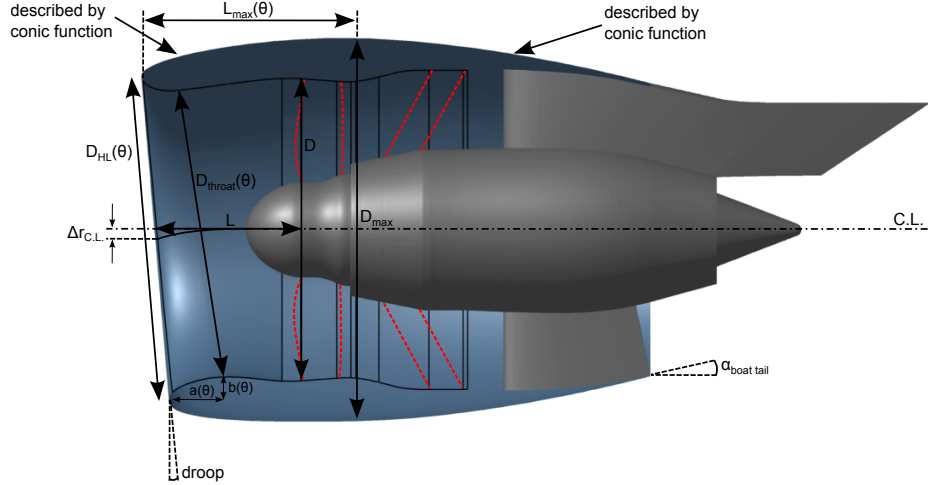


Figure 5-1: Inlet and nacelle design parameters for the baseline propulsor.

The front part of the inlet is described by a super-ellipse with circumferentially-varying semi-diameters  $a(\theta)$  and  $b(\theta)$  and exponents  $n(\theta)$  and  $m(\theta)$ ,

$$\left(\frac{x}{a(\theta)}\right)^{n(\theta)} + \left(\frac{y}{b(\theta)}\right)^{m(\theta)}. \quad (5.1)$$

Engine droop and highlight center line offset  $\Delta r_{C.L.}$  are selected to align the engine highlight with upwash created by the wing potential field at cruise. Typical values for the inlet and nacelle design parameters are presented in Table 5.1. The ratio of streamtube capture area,  $A_0$ , and inlet highlight area,  $A_{HL}$ , is denoted the inlet mass flow ratio, used as a reference aerodynamic parameter for the inlet,

$$MFR = \frac{w_{inlet}}{\rho_0 V_0 A_{ref}} = \frac{A_0}{A_{HL}}, \quad (5.2)$$

where  $w_{inlet}$  is the inlet mass flow, the inlet highlight area is chosen as reference area,  $A_{ref} = A_{HL}$ , and the free-stream density and flight velocity are denoted by  $\rho_0$  and  $V_0$ , respectively. The inlet mass flow ratio varies with operating condition. At low-speed conditions, the streamtube capture area is larger than the inlet highlight area and the stagnation point is located on the outer nacelle surface. At cruise, the streamtube capture area is smaller than the inlet highlight area and the stagnation point shifts to inside of the inlet surface.

Table 5.1: Range of typical values for inlet and nacelle design parameters.

	Typical values
Inlet $L/D$	0.55 – 0.9
Inlet aspect ratio $a/b$	2.25
Inlet droop	5°
Highlight to max. diameter ratio $D_{HL}/D_{max}$	0.75 – 0.88
Contraction ratio $A_{HL}/A_{throat}$	1.2 – 1.3
Inlet mass flow ratio $MFR = A_0/A_{HL}$	0.7 – 0.8 at cruise ~ 1.5 at T/O rotation

## 5.2 Inlet Length Study

A parametric study was carried out to determine the impact of shortening the inlet and nacelle on the propulsor performance at design and off-design operating conditions. The baseline long-inlet and -nacelle geometry with  $L/D = 0.5$ , shown in Fig. 5-1, was designed by the industry partner using an in-house design method. Inlet and nacelle surface geometries are defined based on circumferential distributions of the design parameters introduced in the previous section. The details of the baseline propulsor characteristics are discussed in Chapter 6.

Inlet designs with  $L/D$  between 0.1 and 0.5 were considered in the parametric study. The upper bound was set by the baseline configuration. On the lower end, an axisymmetric inlet and nacelle design with  $L/D = 0.1$  from a previous in-house study was chosen. The inlet and nacelle design parameters were linearly interpolated between the  $L/D = 0.1$  and the  $L/D = 0.5$  designs and inlet and nacelle surfaces were generated for  $L/D = 0.2, 0.3$ , and  $0.4$ .

The propulsor performance was evaluated at cruise and wing  $C_{L\max}$  off-design conditions using body force simulations. At cruise, the engine propulsive efficiency as defined in Chapter 7 was found to decrease by 4 % as the inlet was shortened from  $L/D = 0.5$  to  $L/D = 0.4$ . This penalty is attributed to an increase in wave drag due to the increased shock strength on the outer nacelle surface. The total nacelle drag coefficient  $C_{d,nac}$  and the contributions from pressure and viscous drag are presented in Fig. 5-2. As the inlet and nacelle are shortened, the viscous drag decreases due

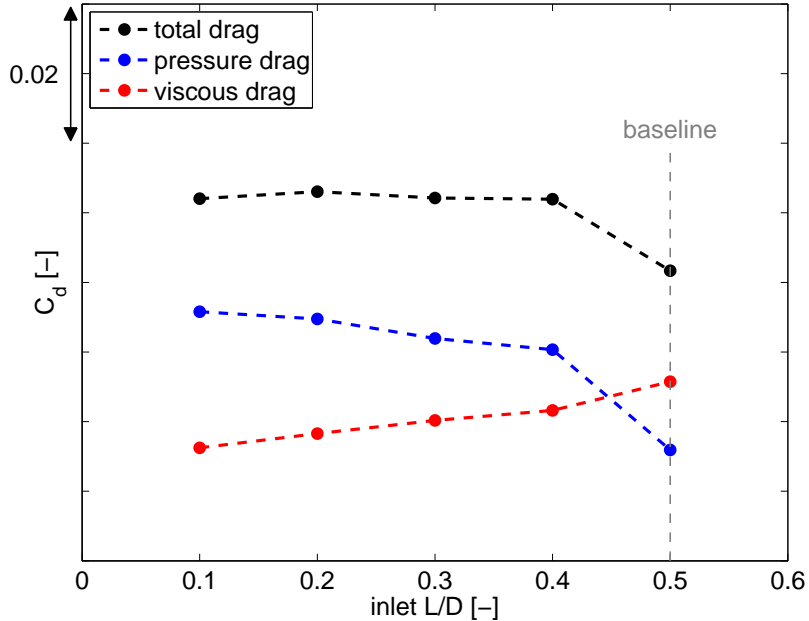


Figure 5-2: Cruise nacelle drag breakdown from preliminary parametric inlet length study using body force simulations.

to the reduction in wetted area. Between  $L/D = 0.5$  and  $L/D = 0.4$ , the wave drag penalty exceeds the benefits from viscous drag reductions and the total drag increases. As the inlet is shortened beyond  $L/D = 0.4$ , the additional increase in wave drag is offset by the reduction in viscous drag. As a result, the overall drag is approximately constant. In addition to the performance penalties at cruise, the inlet flow was found to separate for all short-inlet designs ( $L/D < 0.5$ ) at the wing  $C_{L\max}$  off-design condition with  $29^\circ$  angle-of-attack.

While some improvements in cruise and off-design performance would have been possible by iteratively modifying the inlet and nacelle shapes for each short-inlet design to reduce the shock strength and mitigate the inlet flow separation, it was concluded that the inlet and nacelle surface geometry definition tool used in the parametric study did not offer the design flexibility required to maximize the short-inlet propulsor performance. Additional flexibility was particularly needed in the definition of the outer nacelle shape, which was described by only two parameters, setting up conic functions.

## 5.3 New Capability to Define Inlet and Nacelle Geometries

A spline-based tool to define inlet and nacelle surface geometries was developed with the objective to offer increased flexibility in designing the inlet leading edge and outer nacelle shapes. Since increased wave drag was identified as one of the challenges in short-inlet designs, the ability to employ airfoil shapes in the description of inlet and nacelle geometry was one of the requirements in the development of the new tool.

The approach is to start the design process by defining the top and bottom two-dimensional sections independently of each other since their shapes are governed by different design objectives. The top part is typically slender to limit the shock strength on the outer nacelle at cruise. In contrast, a thicker inlet lip is required at the bottom to accommodate the flow acceleration around the leading edge at low-speed, high-AoA conditions and to avoid flow separation in the inlet.

Bezier splines were selected to describe the top and bottom two-dimensional sections. Each spline consists of a series of four Bezier curves, as shown in Fig. 5-3 for a candidate short-inlet design with  $L/D = 0.25$ . The Bezier curves are denoted (1) inlet, (2) nacelle front, (3) nacelle center, and (4) nacelle aft. Inlet and the front part of the nacelle are non-axisymmetric, with different Bezier curves at top and bottom. Downstream of the maximum nacelle diameter axial location, the nacelle surface is axisymmetric and the Bezier curves at top and bottom are the same.

Each Bezier curve is described by

$$C(t) = \sum_{i=0}^n P_i B_{i,n}(t), \quad (5.3)$$

where  $P_i$  is a control point and  $B_{i,n}(t)$  is a Bernstein polynomial of order  $n - 1$  and  $t \in [0, 1]$ , given as

$$B_{i,n}(t) = \binom{n}{i} t^i (1-t)^{n-i}, \quad (5.4)$$

where  $i = 0 \dots n$  [67]. The order of the polynomial is defined by the number of control points and, except for the two end points, the control points do not necessarily lie on the resulting Bezier curve. The control points for the inlet, front nacelle, and center nacelle pieces are illustrated in Fig. 5-4 for the  $L/D = 0.25$  candidate design. Matlab was used to implement the spline-based approach and a capability was set up to interactively change the shape of the Bezier curves by moving control points. The number of control points per Bezier curve can be varied depending on the required shape. At the start (or end), a given Bezier curve is always tangent to the line between the start point and the next control point (or the end point and the second-to-last control point). This characteristic feature is used to ensure tangency continuity at the joints between two Bezier curves.

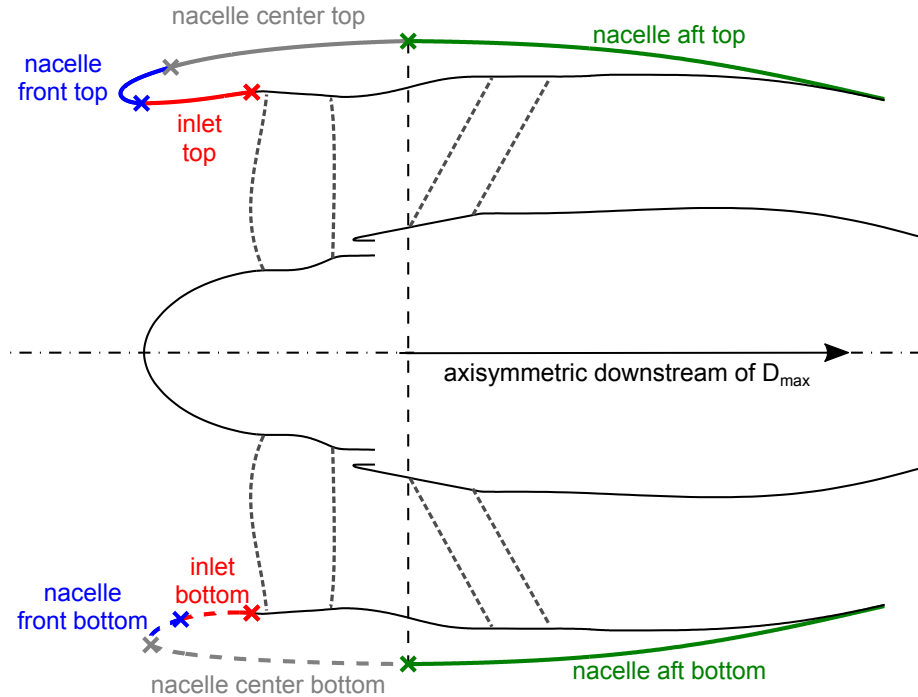


Figure 5-3: Piecewise inlet and nacelle geometry definition using Bezier curves.

The ability to modify the different pieces by moving control points without affecting neighboring curves is one of the main advantages of the developed approach. The inputs to the approach include nacelle trailing edge location and slope, the coordinates and slope at the fan case starting point (i.e. the location downstream of which

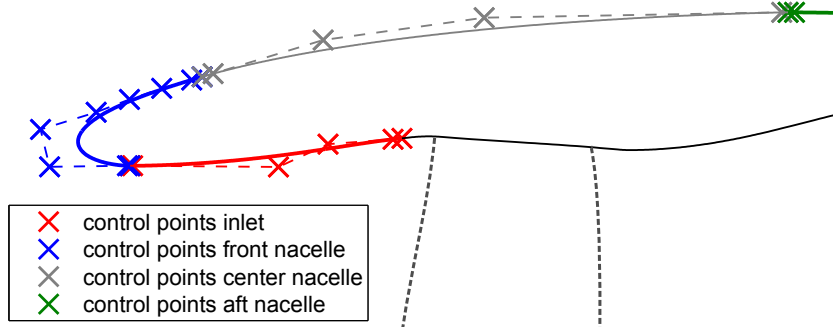


Figure 5-4: Bezier curve description of top inlet and nacelle shapes with control points marked by x-symbols.

the shroud is axisymmetric), as well as the maximum nacelle diameter,  $D_{max}$ , and the axial location of  $D_{max}$ . Inlet length and droop are set indirectly by controlling the inlet highlight location at top and bottom.

While tangency continuity is satisfied, curvature continuity cannot easily be maintained at the joints between two Bezier curves. Multiple control points are clustered close to each other at the start and end points to limit the curvature discontinuity across a joint. In addition, the curvature  $k$  is computed from the first and second derivatives of each Bezier curve,

$$k(t) = \frac{C'_x(t) C''_y(t) - C'_y(t) C''_x(t)}{(C'^2_x(t) + C'^2_y(t))^{3/2}}, \quad (5.5)$$

where the x- and y-components of the derivatives are calculated from

$$C'(t) = n \sum_{i=0}^{n-1} (P_{i+1} - P_i) B_{i,n-1}(t) \quad (5.6)$$

and

$$C''(t) = n(n-1) \sum_{i=0}^{n-2} (P_{i+2} - 2P_{i+1} + P_i) B_{i,n-2}(t), \quad (5.7)$$

respectively. In all of the designs generated with the Bezier-spline-based approach, difference between the curvature at the end points of neighboring Bezier curves was

ensured to be below 5 % of the curvature at the end point of the upstream Bezier curve. By limiting curvature continuities, unintended consequences for the inlet and nacelle flow such as separation can be avoided [68,69]. An alternative to Bezier-spline descriptions of inlet and nacelle shapes is the use of a single B-spline for the entire inlet and nacelle shape. Curvature continuity is maintained along the entire spline but moving a control point has a small influence over the two neighboring intervals and the independent manipulation of inlet and nacelle pieces is more challenging.

For each curve of the Bezier spline, the half-annulus surface description is computed by expressing radial and axial coordinates as functions of the two-dimensional sections at the top ( $\theta_{top} = 0$ ) and bottom ( $\theta_{bottom} = \pi$ ), the circumferential coordinate  $\theta$ , and the inlet droop angle. The radial distribution around the circumference is calculated from

$$r(\theta) - r_{top} = \frac{r_{bottom} - r_{top}}{\theta_{bottom} - \theta_{top}}\theta + K_1 \sin(K_2\theta), \quad (5.8)$$

where  $K_1$  and  $K_2$  are determined by applying tangency and curvature continuity in the circumferential direction at  $\theta = 0$  (top) and  $\theta = \pi$  (bottom). Next, the cylindrical coordinates  $r$  and  $\theta$  are transformed to Cartesian coordinates  $y$  and  $z$  and the axial coordinate distribution for each circumferential location  $\theta$  is obtained from

$$x(\theta) - x_{top} = (y(\theta) - y_{top}) \tan(\text{droop}). \quad (5.9)$$

The inlet and nacelle surfaces for the candidate  $L/D = 0.25$  design are presented in 5-5. The surface geometries are available in cylindrical and Cartesian coordinates and can be imported directly into the Numeca grid generation tool Numeca IGG [70].

The developed method can be extended in case additional control is required in the design of the inlet and nacelle surfaces. An example would be the modification of the two-dimensional profile at  $\theta = \frac{\pi}{2}$  to improve the inlet performance at the cross-wind operating condition. The control point coordinates define the entire inlet and nacelle surface geometry, eliminating the requirement to save surface coordinates with large file sizes during the design process.

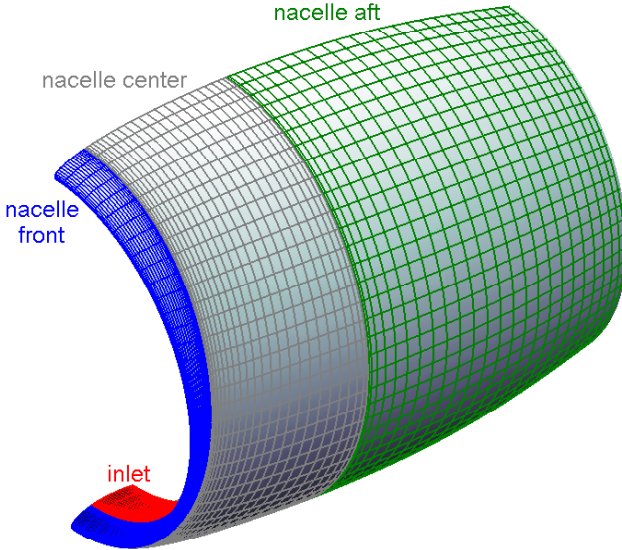


Figure 5-5: Inlet and nacelle solid surfaces for grid generation.

## 5.4 Computational Approach

The spline-based surface definition tool and the body force method are the main elements of the short-inlet design framework developed in this thesis. The framework is presented in Fig. 5-6. The design process begins with the definition of a candidate inlet and nacelle surface geometry as described in the previous section. An initial performance assessment providing preliminary design guidance can be obtained from axisymmetric simulations in MTFLOW [71]. Since angle-of-attack effects on the nacelle and rotor performance cannot be captured in MTFLOW, full-annulus body force simulations are set up in Numeca FINE/Turbo [72]. The framework can only be effectively used in the design process and in parametric studies of short-inlet geometries for low turn-around times of setting up and running full-domain three-dimensional simulations.<sup>1</sup> Each design is evaluated at multiple operating conditions, with each operating condition requiring a different grid due to changes in the variable-area nozzle setting. To limit computational cost, a modular grid topology was adopted and the grid generation and computational setup (definition of initial conditions and bound-

---

<sup>1</sup>In this thesis, the term “full-domain simulation” is used whenever the entire propulsor with internal and external flow is modeled. In contrast, single-passage calculation simulate the internal flow through the fan stage only.

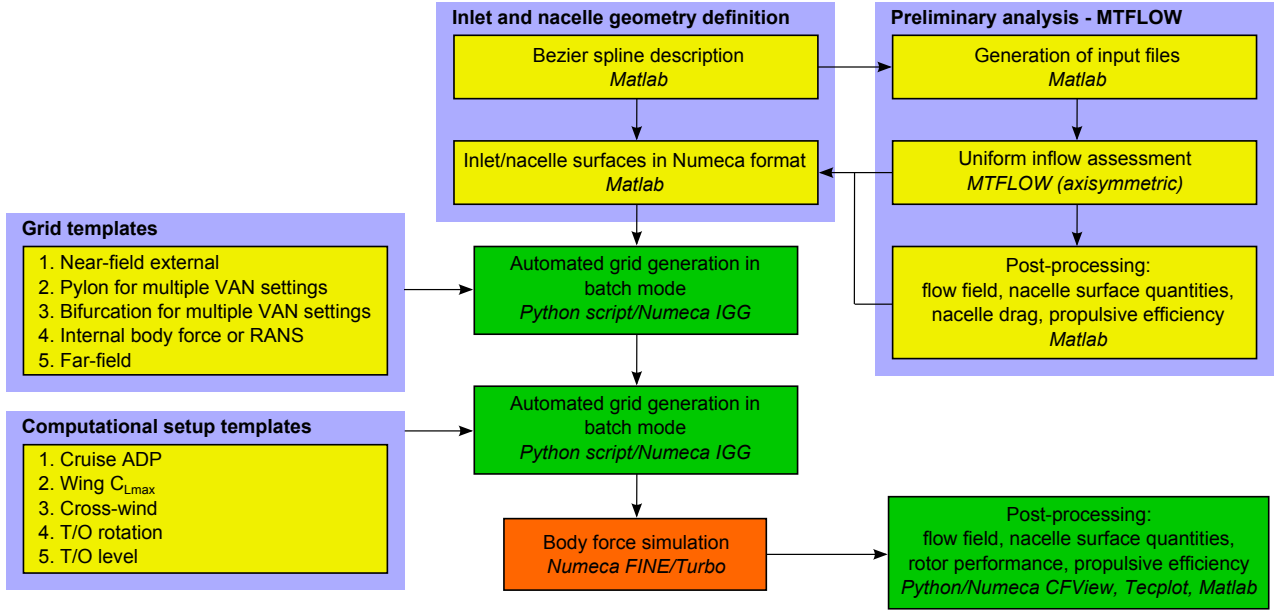


Figure 5-6: Overview of inlet and nacelle design framework.

ary conditions) was automated using Numeca's scripting capabilities. Generating the grids and FINE/Turbo computational setup files for a new inlet and nacelle design to be evaluated at five operating conditions takes approximately five minutes.

### 5.4.1 CFD Tool Description

All body force and steady and unsteady RANS simulations presented in this thesis were carried out using the commercial software package Numeca FINE/Turbo (F/T). Numeca F/T was originally tailored for internal flow turbomachinery applications but extended grid generation and flow solver capabilities for modeling external flow applications have been added in recent releases. The structured flow solver Euranus supports parallel computation on multiple processors and uses a multi-grid technique to accelerate convergence. The flow solutions are processed in Numeca's post-processing tool, CFView, using a graphical user interface and automated Python scripts, or in the external post-processing tool Tecplot 360 [73]. A more detailed description of Numeca F/T can be found in [72].

A custom version of Numeca F/T enabling the addition of source terms to the right-hand side of the governing equations was used for the body force simulations.

In all simulations, turbulence closure was achieved through the use of the Spalart-Allmaras (SA) one-equation turbulence model [74]. The assumption of fully turbulent flow on the nacelle possibly leads to conservative nacelle drag estimates, as modern nacelle designs can enable laminar flow over parts of the nacelle or the entire nacelle surface [18,75]. However, the propulsor performance results are consistently evaluated relative to the baseline configuration and absolute nacelle drag results are not used in the short-inlet design process.

### 5.4.2 Full-Domain Computational Setup

The grid generation tools Autogrid [76] and IGG [70] enabled the automated generation of full-domain meshes for parametric studies of inlet and nacelle shapes. The developed modular grid setup is depicted in Fig. 5-7. All modules consist of multi-block structured hexahedral grids. The first grid module includes the internal rotor and stator domains. Pylon and bifurcation domains make up the second component. The third grid module is denoted the external near-field mesh and consists of the inlet and external nacelle domains within two nacelle diameters around the engine. The final component includes the external far-field domains. For the cruise, wing  $C_{L\max}$ , and T/O conditions, the far-field module is cylindrical and extends 50 nacelle diameters radially and axially upstream and downstream of the engine to accurately capture the inlet streamtube at low-speed conditions. At the cross-wind condition with  $M_0 < 0.05$ , an additional domain extension up to 100 nacelle diameters in each direction is required to capture the inlet streamtube and the domain shape is changed to a rectangular cuboid. Since the emphasis was on determining inlet flow separation and its impact on fan performance in the short-inlet candidate designs, the ground plane is not included in the computational model at cross-wind and the inlet vortex formation is not captured. The performance of the baseline and short-inlet configurations at cross-wind is discussed in more detail in Chapters 6 and 9, respectively.

Pylon and bifurcation meshes can be generated in Numeca Autogrid with little user input. While the pylon and bifurcation geometries were not varied in this work, the automated grid generation is of particular importance in setting up computational

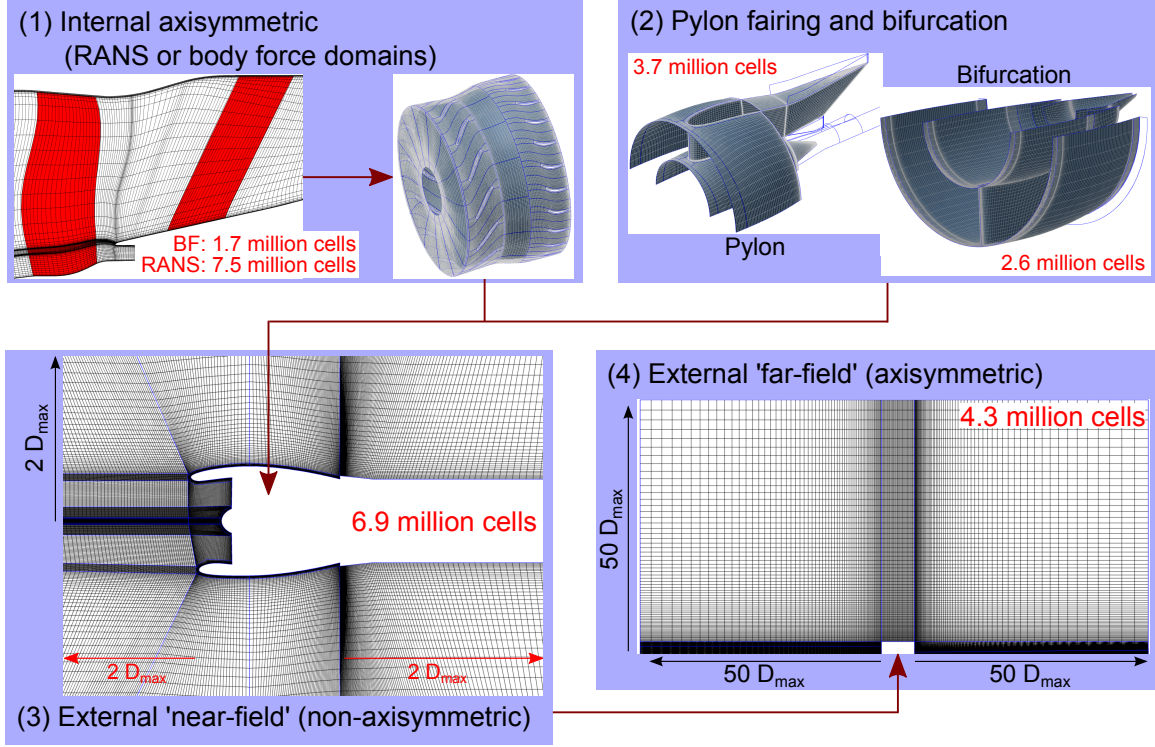


Figure 5-7: Modular grid setup for full-domain body force or URANS simulations.

models for low-FPR propulsors with variable-area nozzles. Since the bypass nozzle area varies with operating condition, the nacelle surface needs to be modified near the trailing edge and changing the operating condition requires a modified pylon and bifurcation grid. The adopted meshing strategy enables low turn-around times for obtaining pylon and bifurcation meshes with varying nozzle area requirements. A more detailed discussion of the pylon and bifurcation geometry definition and grid generation can be found in Appendix E.

Body force simulations are carried out in the parametric inlet study and the short-inlet design process but URANS simulations are used to check the performance of candidate short-inlet configurations. In the URANS simulations, the internal axisymmetric domains, consisting of an annular duct in the body force grid, are replaced by the blade meshes. To switch from one candidate short-inlet design to another, only the external near-field module needs to be modified. In the URANS assessment, the computational mesh features three grid levels with 3.125 (coarse), 25 (medium), and 200 (fine) million cells, respectively. The medium grid level is used here to limit

computational cost. The influence of grid resolution on performance metrics and the results of grid convergence studies are presented in Section 5.4.4.

Grid sizes and computation times are summarized in Table 5.2. A coarse grid body force calculation was analyzed in addition to the medium grid level. Compared to URANS simulations, computation times are reduced by two orders of magnitude.

Table 5.2: Comparison of computational cost for unsteady RANS and body force simulations.

	URANS medium grid level	Steady body force medium grid level	Steady body force coarse grid level
Total grid size (million cells)	25	19.2	2.4
1) Internal rotor and stator	7.5	1.7	0.2
2) Pylon and bifurcation	6.3	6.3	0.8
3) External near-field	6.9	6.9	0.9
4) External far-field	4.3	4.3	0.5
Computation time (40 – 50 processors)	7 days (7 revolutions)	8 hours	1 hour

External boundary conditions are defined at the far-field boundaries for all simulations. This type of boundary condition determines whether the flow is locally entering or leaving the flow domain and is based on the Riemann invariants [72]. The free-stream values of pressure, temperature, velocity vector, and turbulent viscosity are required inputs at external boundaries.

### 5.4.3 Full-Domain Unsteady RANS Simulations

In the full-domain unsteady RANS simulations used to validate the body force method and verify the performance of candidate short-inlet designs, the fan stage performance, nacelle drag, and propulsive efficiency are computed based on the time-averaged flow solution. In addition, the unsteady simulations were used to determine the time-dependent blade loading levels. This section details the computational procedure employed in the URANS calculations.

The first step towards determining a time-dependent flow solution and time-averaged propulsor performance involves setting up and carrying out steady computations in order to initialize the unsteady simulations. The second step is to com-

pute the blade surface pressures, fan efficiency, and engine propulsive efficiency using full-annulus unsteady simulations.

In the steady simulations used to initialize the unsteady calculations, two mixing planes were defined to transmit information at the interfaces between stationary and rotor reference frames upstream and downstream of the rotor. The details of the mixing plane approach are described in [72].

Continuous spanwise grid point distributions were defined across the interfaces between stationary and rotating domains to limit interpolation errors. After obtaining an initial flow field using steady calculations, unsteady simulations with sliding interfaces were carried out. Since the convection times through the fan stage are of the order of six rotor periods, the unsteady simulations were run for six rotor revolutions to obtain a settled unsteady flow solution. Static pressure probes at multiple axial locations (in the inlet and downstream of the rotor, stator, and pylon) and the mass flow through the sliding interfaces were monitored to verify convergence. The time-dependent static pressure and mass flow distributions extracted from a seventh rotor revolution were within 1 % of the results for the sixth revolution, indicating convergence and a settled unsteady solution. The flow fields at each time step during the seventh revolution were used to compute the time-averaged flow solution.

In general, about 100,000 iterations were required to reach a settled unsteady flow solution. 20 time steps were computed per pitch and the number of inner iterations was continuously reduced from 75 for the first revolution to 50 for the sixth revolution.

#### 5.4.4 Validation and Grid Convergence

A combination of single-passage steady and full-domain URANS simulations were used to determine the required mesh resolution. In addition to engine propulsive efficiency, the following metrics were checked to assess grid convergence due to their direct influence on propulsive efficiency: fan pressure ratio and efficiency, stator stagnation pressure loss, and nacelle drag. To further validate the computational setup, the steady and unsteady RANS results were compared against cycle data and results from a streamline curvature method provided by the industry partner.

Numeca's grid generation tools Autogrid and IGG provide the capability to set up meshes with multiple grid resolution levels. To obtain a higher density grid level from a baseline mesh, the cell count is doubled in every spatial direction. All the meshes used in this thesis include three levels, which are labeled as coarse, medium, and fine in the following analyses.

The rotor stagnation pressure ratio  $FPR$  and adiabatic efficiency  $\eta_{fan}$  at the cruise operating condition are presented on the left and on the right in Fig. 5-8, respectively. The medium grid level features 77 grid points along the rotor span, 35 grid points in circumferential direction for one blade passage, and 29 grid points on the blade pressure and suction surfaces. The single-passage coarse, medium, and fine grids consist of approximately 66,000, 450,000, and 3.6 million cells, respectively.

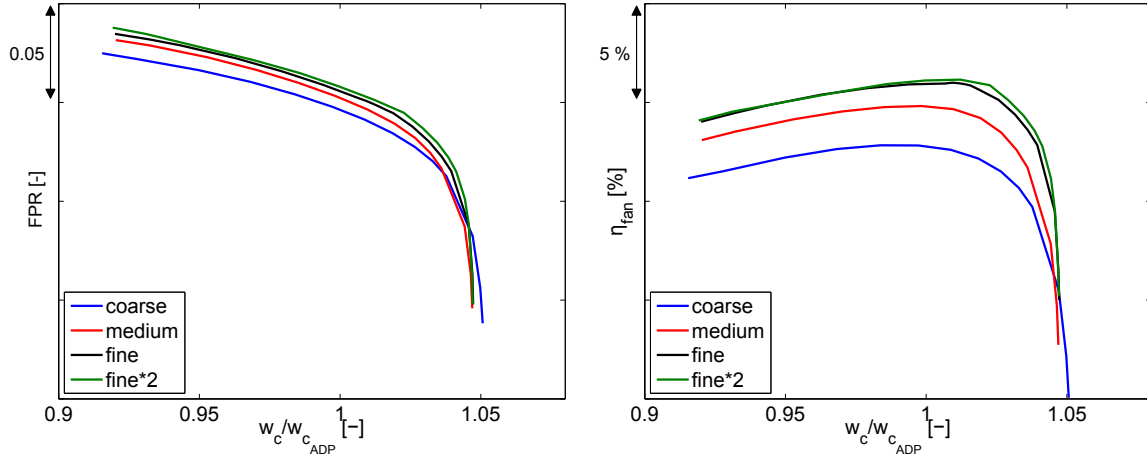


Figure 5-8: Fan pressure ratio (left) and rotor efficiency (right) from internal steady, single-passage RANS simulations at cruise for coarse, medium, and fine grid levels.

Differences of up to 2 % in fan efficiency between the coarse and medium grid level results are attributed to increased stagnation pressure losses on the coarse grid level due to increased numerical dissipation. As the grid resolution is further increased in the fine grid level, the differences in efficiency at a given corrected flow are reduced to approximately 1.3 %. To assess whether grid convergence was achieved, an additional single-passage mesh was generated with 29 million cells by doubling the cell count in each dimension. This grid is named *fine\*2* in Fig. 5-8. The maximum differences in efficiency are below 0.3 %, if the mesh density is increased beyond the fine grid level.

Grid convergence was additionally demonstrated for the fine level grid by evaluating spanwise profiles of rotor efficiency, stagnation pressure ratio, and flow angle.

The fine grid level was used in single-passage, steady RANS simulations to define the body force distributions in the rotor and stator blade rows. However, the full-domain URANS simulations were carried out on the medium level to limit computational cost as a full-domain mesh based on the fine grid level results in a cell count of approximately 200 million cells and computation times of 2 months per operating condition. Since the rotor efficiency difference between two grid level results is approximately constant over a wide range of operating points on a given speedline and the focus of this work is on determining the impact of shortening inlet and nacelle on propulsor performance relative to a baseline case, the use of the medium level grid was deemed adequate in the exploration of the short-inlet design space.

To check the calculated performance, the time- and mass-averaged performance characteristics computed from URANS simulations are compared to cruise design point cycle data provided by the industry partner in Table 5.3. Due to the use of the medium level grid, the stagnation pressure rise across the fan is under-estimated relative to the cycle data, and consequently fan and stage efficiencies are under-estimated by 1.2 % and 2.3 %, respectively.

Table 5.3: Computed baseline configuration performance at cruise normalized by design point cycle data provided by the industry partner.

Fan pressure ratio $FPR/FPR_{des}$	0.996
Bypass ratio $BPR/BPR_{des}$	0.990
Fan efficiency $\eta_{fan}/\eta_{fan,des}$	0.988
Stage efficiency $\eta_{stage}/\eta_{stage,des}$	0.977

Engine propulsive efficiency  $\eta_{prop}$  is determined in this thesis as the metric for system level propulsor performance. The details of computing  $\eta_{prop}$  from full-domain body force or time-averaged URANS results are discussed in Chapter 7. Computing the propulsive efficiency requires results for thrust, nacelle drag, and shaft power input. The impact of the grid resolution on these quantities is discussed next.

For a URANS simulation on the medium level grid, the computed propulsor net thrust minus nacelle external drag,  $T_{net} - D_{nac}$ , was found to be 3 % lower than the

data point provided by the industry partner. Numerical dissipation is suggested to be one contributor to the under-estimation of net thrust minus nacelle external drag. The difference is expected to decrease for URANS simulations on the fine grid level. The choice of the turbulence model and interpolation errors at non-matching grid interfaces also play a role in the accuracy of the numerical results.

Results from body force simulations carried out in the preliminary parametric inlet study presented in Section 5.2 were used to assess the influence of the grid size on performance metrics. The engine propulsive efficiency is presented for a coarse and medium level grid in Fig. 5-9, with the mesh sizes listed in Table 5.2. For the baseline propulsor, the body force result agrees to within 1 % with the URANS result and the discrepancy is suggested to be due to the under-estimation of stator wake losses (stator wake mixing is not captured in the body force simulations). The coarse level results are between 4 and 4.5 % lower than the medium level results due to increased numerical dissipation and differences in the resolution of the shock on the outer nacelle surface. However, body force simulations run on the coarse grid capture the trends in the propulsor performance as inlet and nacelle are shortened and the use of the coarse level grid was considered acceptable in parametric inlet design studies.

Results for nacelle viscous drag and total equivalent shaft power input (as defined in Chapter 7) are shown on the left and on the right in Fig. 5-10, respectively. The medium grid body force result for nacelle viscous drag is within 0.1 % of the URANS results. Good agreement is expected since the nacelle drag is not directly affected by representing the blade rows using body force distributions instead of modeling the discrete blades. The body force result for the shaft power input under-estimates the URANS result by 0.5 %. This difference is attributed to discrepancies in the enthalpy rise between RANS and body force representation of the rotor.

The coarse grid body force results for nacelle viscous drag differ by less than 3 % from the medium grid data and the shaft power input is under-estimated by up to 2 % due to increased numerical dissipation and differences in the mixing of core and bypass exhaust streams downstream of the propulsor. Again, the coarse level grid simulations are demonstrated to capture the trends as inlet and nacelle geometry

are modified and coarse grid level body force simulations are used extensively in the parametric short-inlet design process discussed in Chapter 8.

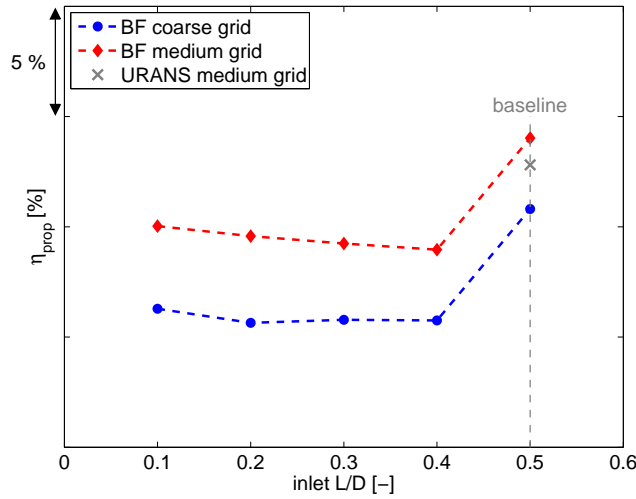


Figure 5-9: Cruise engine propulsive efficiency from preliminary parametric inlet length study using body force simulations on coarse and medium level grids.

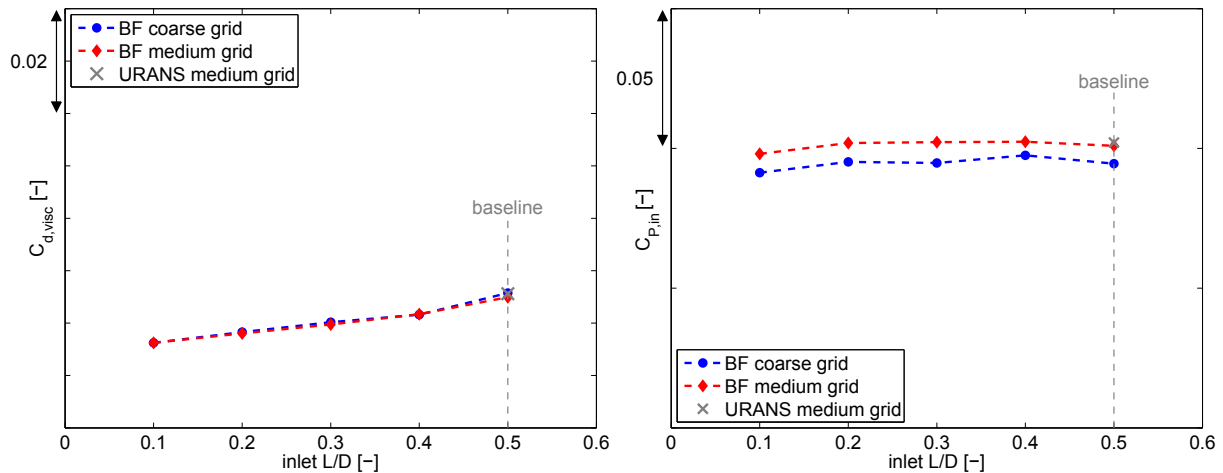


Figure 5-10: Nacelle viscous drag (left) and total equivalent shaft power input from preliminary parametric inlet length study using body force simulations for coarse and medium grid levels.

# Chapter 6

## Long-Inlet Baseline Configuration

A long-inlet propulsor was defined in collaboration with the industry partner to serve as the baseline configuration in the exploration of the short-inlet design territory. In defining the baseline propulsor, the objective was to model all relevant components which affect fan performance and govern the distortion transfer through the fan stage. The baseline configuration therefore includes the pylon and bifurcation in the bypass duct and the core in- and outflow are modeled.

### 6.1 Baseline Propulsor Design Characteristics

The baseline propulsor, depicted in Fig. 6-1, is designed to power a short-to-medium range, twin-engine aircraft and is based on a next-generation geared turbofan. The baseline design features a non-axisymmetric inlet with  $L/D = 0.5$  and  $5^\circ$  to align the inlet highlight with the wing upwash at cruise. The lower inlet lip is thicker than the upper inlet lip to mitigate nacelle drag at high flight Mach numbers and provide for separation-free operation at high angles-of-attack. The increase in the inlet lip thickness towards the bottom is achieved by a by 4% increase of the contraction ratio,  $A_{HL}/A_{throat}$ , and a variation of the inlet aspect ratio,  $a/b$ , and the super-ellipse exponents,  $n(\theta)$  and  $m(\theta)$ , around the circumference.

The core inlet flow is included in the computational model to capture the effect of the splitter potential field on the rotor performance and to quantify the stagnation

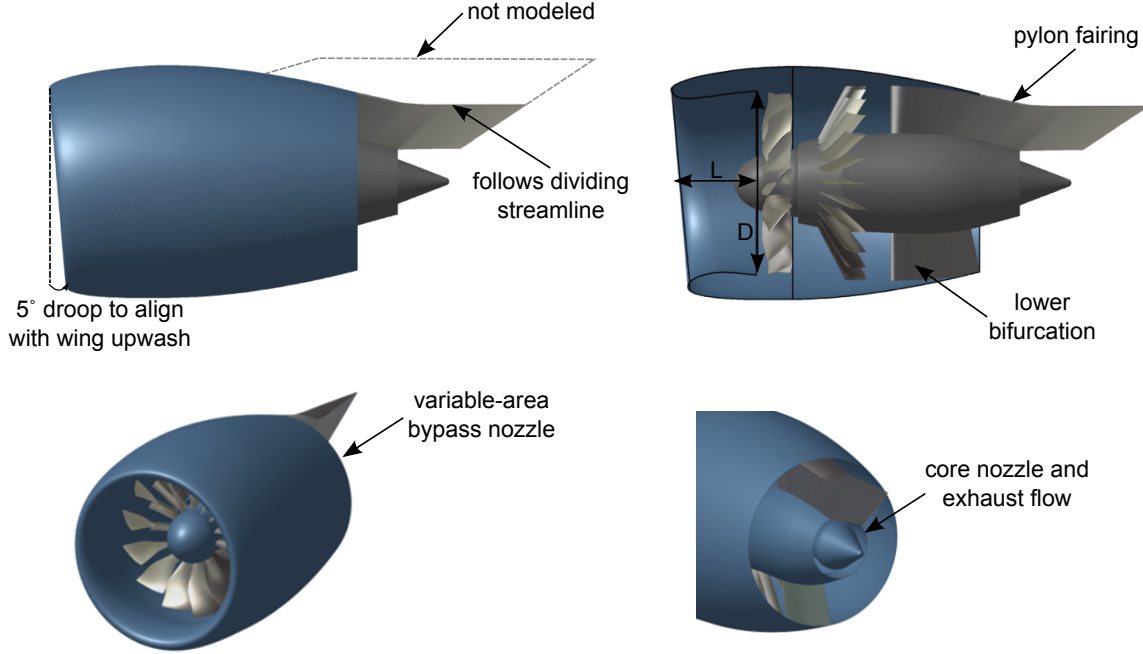


Figure 6-1: Baseline propulsor with  $L/D = 0.5$ . The variable-area nozzle is set to the cruise condition.

pressure distortion in the core inflow. The mass flow into the core is specified using a mass flow outlet boundary condition with pressure adaptation. At this boundary condition, the static pressure is iteratively updated until the specified mass flow is reached [72]. The core exhaust flow is modeled in the simulations to account for mixing effects between the bypass and core exhaust flows downstream of the propulsor in the determination of the engine propulsive efficiency, as discussed in more detail in Chapter 7. An inlet boundary condition upstream of the core exhaust nozzle is used and stagnation pressure and stagnation temperature are specified based on cycle data provided by the industry partner. The core in- and outflow regions included in the computational domain are illustrated in Fig. 6-2.

Fan rotor and FEGV interact with the potential pressure disturbances generated by the pylon and bifurcation, resulting in circumferential incidence variations and increased blade losses, increased levels of fan noise, and forced vibration of the rotor [32, 77, 78]. To quantify the influence of the back pressure distortion on the fan stage performance and the rotor loading, the pylon and bifurcation are included in the computations.

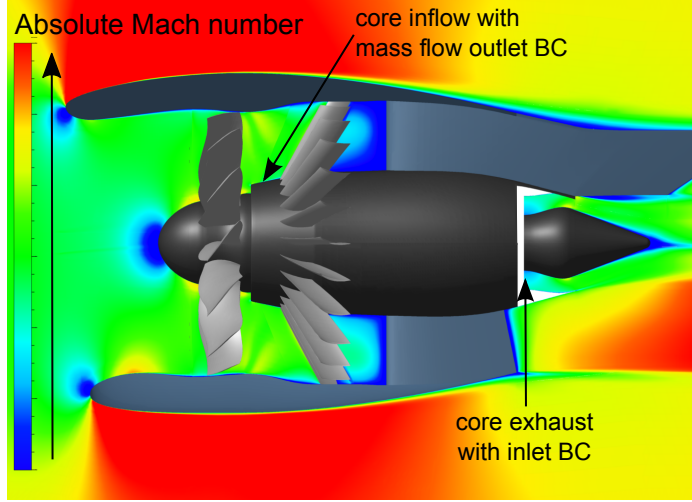


Figure 6-2: Core inflow and exhaust domains for the baseline propulsor with absolute Mach number distribution at cruise.

The pylon and bifurcation shapes were defined using NACA 0012 airfoils. The thickness-to-chord ratio  $t/c$  was held constant along the span and axial locations of the leading and trailing edges were set based on design guidelines provided by the industry partner. The pylon extends into the external flow and the upper surface was defined to follow the dividing streamline between bypass exhaust and external flows, as illustrated in Fig. 6-1. Details on the definition of the pylon and bifurcation geometries and the grid generation are presented in Appendix E.

In a complete engine-pylon-wing configuration, the shape of the pylon section in the external flow between nacelle surface and wing can play an important role in the overall aerodynamic performance of the nacelle installation and ultra-high BPR turbofan propulsors with short inlets and nacelles likely require advanced pylon designs [42, 79]. The impact of interference effects between wing, external pylon, and nacelle on nacelle aerodynamic performance and engine propulsive efficiency are not taken into account in the present analysis.

For fan pressure ratios below 1.45, the fan bypass nozzle is required to have variable-area capability in order to maintain design incidence on the rotor and stable fan operation throughout the operating envelope [13, 18]. A low-FPR propulsor with variable-area nozzle also offers fan and jet source noise benefits since high efficiency

at take-off corresponds to low fan source noise due to reduced self noise and reduced rotor wake interaction with the FEGV [80–82].

The advanced, low-FPR baseline propulsor defined in this work requires up to 25 % fan nozzle area control to allow the rotor to operate at peak efficiency at all critical operating conditions. The aft end of the nacelle internal and external surfaces is modified in the computational model to accommodate the increase in nozzle area at the low-speed off-design operating conditions.

The computational setup for the baseline propulsor was validated at design and off-design conditions using data provided by the industry partner. Some of the results of the validation effort are given in Section 5.4.4. The performance of the baseline propulsor at the cruise design point is further discussed next and off-design performance results are given in Chapter 7.

## 6.2 Dissection of Distortion Transfer Mechanisms

The rotor incidence distortion and the distortion transfer through the fan stage are governed by the following mechanisms: (1) the interaction of the fan stage with the pylon and bifurcation upstream influence and (2) the interaction of the rotor with the non-uniform inflow (with  $AoA > 0$ ) through the three-dimensional inlet. The relative importance of these mechanisms in the long-inlet baseline propulsor at cruise was quantified by carrying out URANS simulations for the following three cases, as illustrated in Fig. 6-3:

1. The first simulation includes the entire propulsor. Both the non-uniform inflow with 5° angle-of-attack through the non-axisymmetric inlet and the pylon and bifurcation are modeled.
2. The impact of the back pressure distortion generated by the pylon and bifurcation potential field on the fan stage performance is quantified by modeling the internal flow through the bypass duct at uniform inflow.
3. The contribution of the non-uniform inflow on the stagnation pressure distortion

downstream of the rotor is determined by removing the pylon and bifurcation geometries from the computational model. In this case, the nacelle trailing edge radius is reduced to match the bypass nozzle area of case 1 and enable a back-to-back comparison at constant corrected flow.

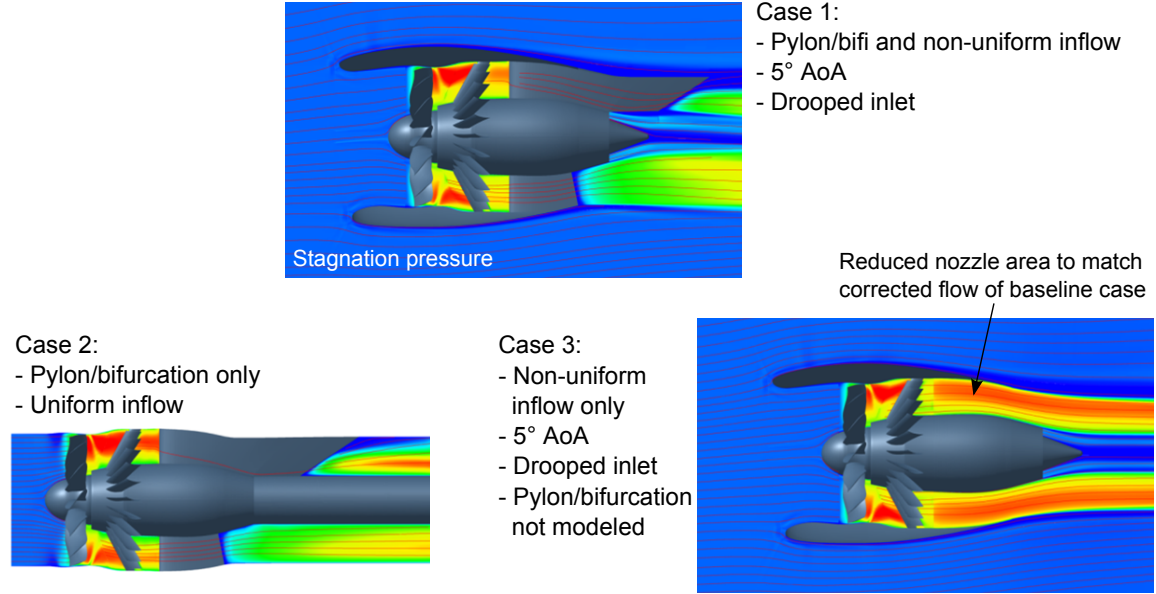


Figure 6-3: Overview of computational approach for the dissection of the distortion transfer mechanisms in the long-inlet baseline propulsor at cruise ( $M_0 = 0.8$ ).

The time-averaged distributions of rotor incidence are presented on the top in Fig. 6-4. Circumferential incidence variations of up to  $4^\circ$  are observed for case 1 due to the combined impact of the pylon and bifurcation upstream influence and non-uniform inflow. The pylon is located at  $\theta = 0^\circ$  and the pylon potential field increases the rotor incidence between  $\theta = 270^\circ$  and  $\theta = 0^\circ, 360^\circ$  relative to the circumferential average, as shown in the center in Fig. 6-4 for case 2. The thickness of the bifurcation is lower than the pylon thickness,  $\frac{t_{bifurcation}}{t_{pylon}} = \frac{1}{3}$  and the bifurcation upstream influence on the rotor incidence is smaller than the pylon upstream influence. As illustrated on the right in Fig. 6-4 for case 3, the non-uniform inflow leads to regions of reduced incidence between  $\theta = 0^\circ$  and  $\theta = 180^\circ$  and increased incidence between  $\theta = 180^\circ$  and  $\theta = 360^\circ$ . The region of reduced incidence is due to a vertical velocity component pointing upward, which results in a circumferential velocity in the direction of the

rotor rotation (co-swirl). In contrast, the region of increased incidence is due to a downward-pointing velocity component at the fan face, leading to a circumferential velocity opposite to the direction of the rotor (counter-swirl). The streamwise Mach number is locally increased between  $\theta = 90^\circ$  and  $\theta = 270$  due to the flow acceleration through the inlet throat (as shown in Fig. 1-5). Therefore, incidence is reduced in this circumferential region over the outer span between mid-span and the shroud.

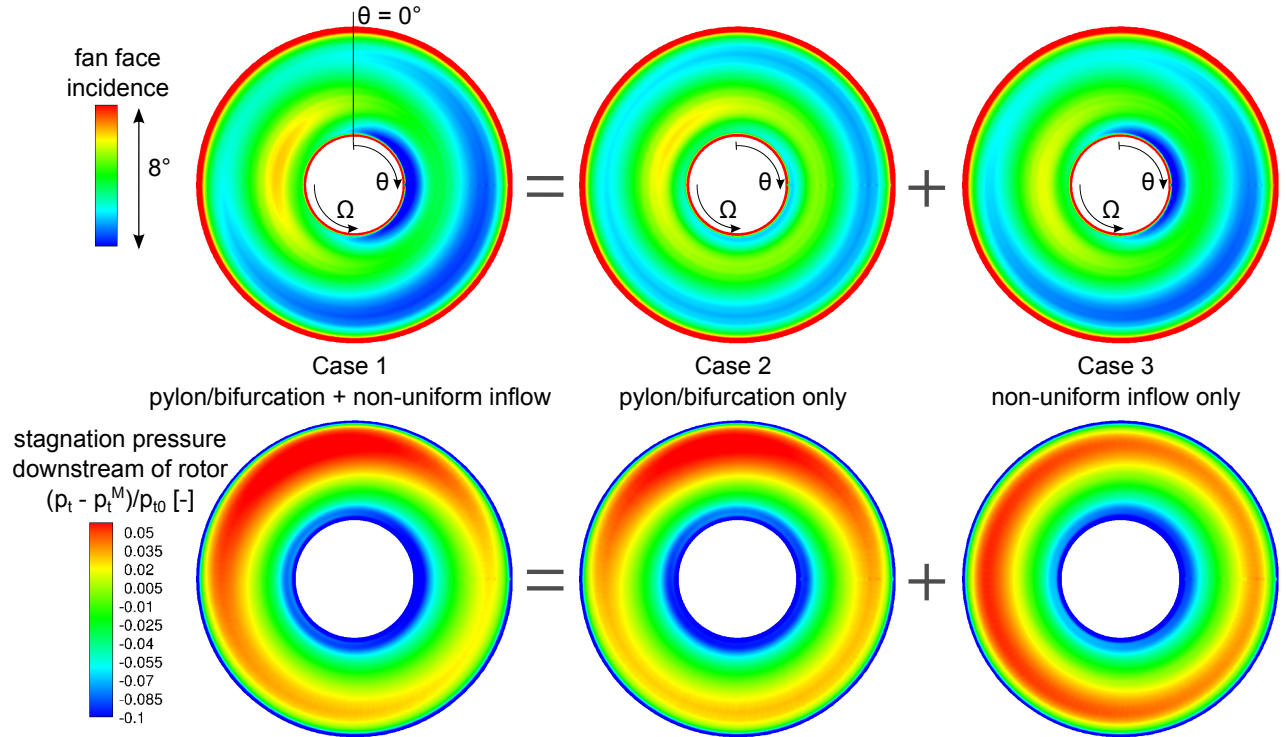


Figure 6-4: Fan face incidence and stagnation pressure distortion downstream of the rotor at cruise.

The distributions of the stagnation pressure relative to the mass-averaged value downstream of the rotor,  $\frac{p_t - p_t^M}{p_{t0}}$ , are shown on the bottom in Fig. 6-4 and plotted along the circumference at three spanwise positions in Fig. 6-5. In cases 1 and 2, the increased rotor back pressure due to the pylon leads to an increase in the rotor work input and a local increase in the stagnation pressure at  $\theta = 0^\circ, 360^\circ$ . The impact on the stagnation pressure increases towards the shroud due to the increased pylon thickness in the constant thickness-to-chord design. Compared to the local increase in the stagnation pressure due to the pylon potential field, the bifurcation upstream

influence causes a smaller local increase at  $\theta = 180^\circ$ . In case 3, the variation is approximately sinusoidal with reduced stagnation pressure over the first half of the rotor revolution due to reduced incidence and increased stagnation pressure over the second half due to increased incidence. Towards the shroud, the circumferential locations of the minimum and maximum values are shifted to higher  $\theta$ -values due to the impact of the region of increased streamwise Mach number.

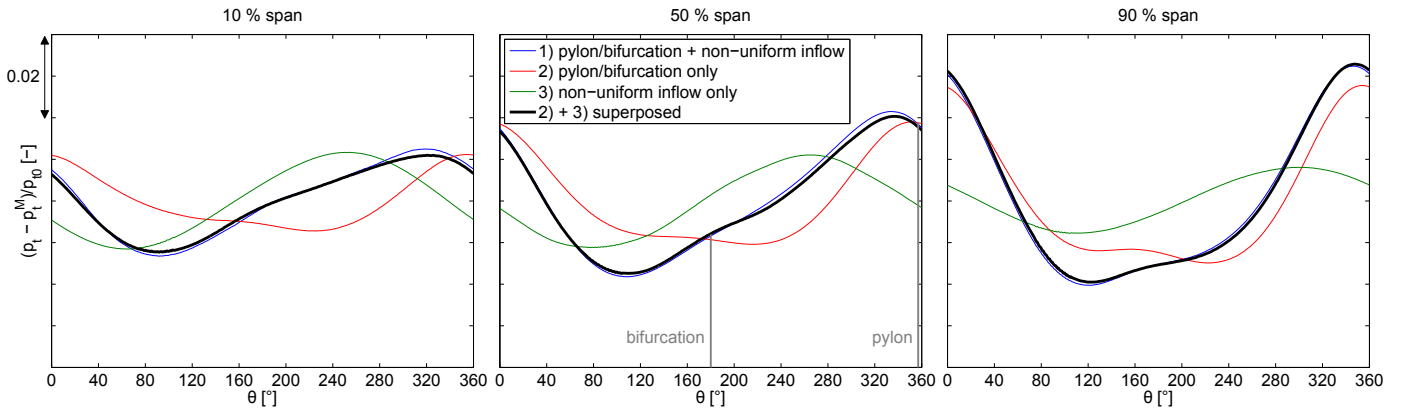


Figure 6-5: Superposition of the contributions from non-uniform inflow and pylon/bifurcation upstream influence to the circumferential stagnation pressure distortion in the long-inlet baseline propulsor at cruise.

Superposition of the stagnation pressure variations from cases 2 and 3 agrees with the full-domain result (case 1) to within 0.15 % of the mass-averaged stagnation pressure,  $\frac{p_t^M}{p_{t0}}$ , suggesting that the mechanisms contributing to the distortion transfer are de-coupled and reductions in the incidence and stagnation pressure distortions can be achieved by addressing the mechanisms independently.

The stagnation pressure variations due to the pylon upstream influence are up to twice as high as the variations induced by the non-uniform inflow near the shroud, indicating that pylon upstream influence is the dominant mechanism for the distortion transfer in the baseline propulsor at cruise. Rotor blade losses increase whenever the local operating point is shifted away from the design point, with rotor incidence  $i \neq i_{des}$ . Thus, non-axisymmetric FEGV designs with circumferentially-varying vane spacing to offset the pylon upstream influence offer a potential for improved propulsor performance [32, 78, 83]. This approach is discussed in more detail in Chapter 8.

The shape and thickness of the pylon cross-sections could potentially be modified to alleviate the rotor back pressure distortion generated by the pylon potential field [84].

Inlet length, inlet droop, and the inner inlet contours can be varied to mitigate the contribution from non-uniform inflow to the incidence distortion and distortion transfer and extending the spinner length leads to increased flow straightening and reduced circumferential incidence variation near the hub. For the long-inlet baseline at cruise, the pylon upstream influence dominates and would have to be addressed first to improve performance. However, the relative contributions of the pylon and bifurcation upstream influence and the non-uniform inflow to the incidence distortion and distortion transfer depend on the operating condition and inlet length. In a short-inlet configuration at off-design operating conditions with high angles-of-attack, the contribution from the non-uniform inflow outweighs the pylon upstream influence contribution. In contrast, at cruise, the pylon upstream influence significantly affects the incidence distortion and stagnation pressure distortion in the bypass duct, even for reduced inlet lengths. The impact of reducing the pylon upstream influence in a candidate short-inlet configuration is discussed in Chapter 9. The pylon geometry itself is not changed in this work.

# Chapter 7

## Metrics and Sensitivities

The operating conditions for the assessment of the nacelle and fan stage performance are discussed first in this Chapter. Next, the rationale for using engine propulsive efficiency  $\eta_{prop}$  to evaluate the goodness of the candidate short-inlet designs is explained. Finally, the results of a sensitivity analysis emphasize the importance of limiting rotor losses in short-inlet designs, as the impact of fan efficiency penalties on propulsive efficiency can outweigh any benefits from reduced nacelle drag.

### 7.1 Operating Conditions

A large number of operating conditions are typically used by engine and airframe manufacturers in the design process of inlets and nacelles and the engine performance must be demonstrated at a variety of flight conditions during the certification. Due to the computational cost of full-domain CFD simulations, it was not practical to consider the entire list of operating conditions in this work. Instead, a subset of conditions was defined in collaboration with the industry partner. The objective was to include those conditions expected to limit the design of short inlets and nacelles due to nacelle drag penalties or increased incidence distortion levels, jeopardizing fan and LPC stability or exacerbating fan aero-mechanical challenges. The operating conditions are listed in Table 7.1. At cruise, the engine is at 5° angle-of-attack due to the wing upwash. The off-design wing  $C_{L\max}$  condition features the largest angle-

of-attack, which the engine can be subjected to in flight. At cross-wind, inlet flow separation and rotor incidence distortion represent the primary concerns.

Table 7.1: Operating conditions.

Condition		Mach number $M_0$	Altitude $h_0$	Engine angle-of-attack $AoA$
1	Cruise ADP	0.8	35,000 ft	5°
2	Wing $C_{Lmax}$	0.25	14,000 ft	29°
3	Max. cross-wind (30 kts)	0.0442	SL + 15 C	(90°)
4	Take-off rotation	0.25	SL + 15 C	17°
5	Take-off level	0.25	SL + 15 C	0°

A set of inlet and nacelle design criteria was provided by the industry partner for each operating condition to guide the design and performance assessment of the candidate short-inlet propulsors. At cruise, wave drag contributes to engine total drag and must be minimized to avoid penalties in propulsor performance. At the off-design conditions, the criteria include fully attached inlet flow to maximize inlet stagnation pressure recovery and limit rotor incidence distortion [18]. Separation-free inlet flow is particularly challenging to achieve in short-inlet designs. Thus, alternative design guidelines are proposed in this work, as discussed in Chapter 9.

For the first three conditions listed in Table 7.1, the Mach number and streamline distributions are depicted in Fig. 7-1. The dividing streamlines between internal and external flows are shown to highlight the outward shift of the stagnation point on the inlet lip at low flight speeds. The dependence of the stagnation point location on operating condition and the formation of supersonic flow regions on the outside of the nacelle at cruise and along the lower inlet lip at wing  $C_{Lmax}$  lead to important design implications for short-inlet propulsors, which are discussed in the next chapter.

The Mach number distribution at the cross-wind condition is shown on the bottom in Fig. 7-1. Here, the nacelle surface is contoured by the isentropic Mach number,

$$M_{is} = \sqrt{\frac{2}{\gamma - 1} \left( \left( \frac{p_{t0}}{p} \right)^{\frac{\gamma-1}{\gamma}} - 1 \right)}, \quad (7.1)$$

to illustrate regions of increased flow acceleration. In Equation 7.1, the local

pressure and free-stream stagnation pressure are denoted by  $p$  and  $p_{t0}$ , respectively. The inlet flow is fully attached for the baseline design. However, short inlets with thin inlet lip shapes exhibit an increased tendency for flow separation and require flow control concepts to prevent separation, as discussed in Section 10.4.

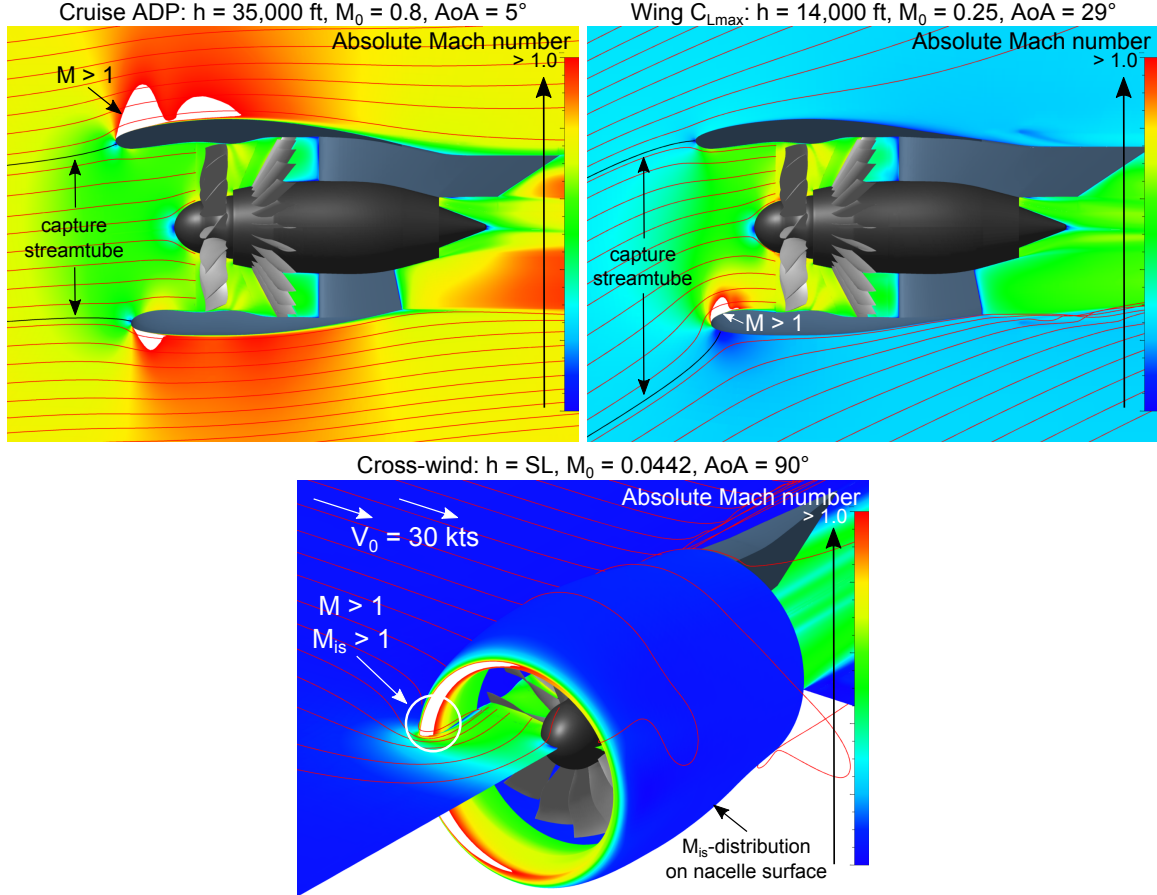


Figure 7-1: Mach number distribution and upstream dividing streamlines at cruise (top left), wing  $C_{L\text{max}}$  (top right), and cross-wind (bottom) operating conditions for baseline propulsor.

Numerical challenges render CFD simulations at the cross-wind condition particularly difficult [85, 86]. At cross-wind, the flow solver must be capable of dealing with both incompressible and transonic flow regions in the low Mach number free-stream and in the inlet flow, respectively. The flow field can include regions of separation and reattachment in the inlet and reversed flow on the leeward side of the nacelle. Finally, the size of the streamtube capture area requires an increase in the computational domain relative to other operating conditions (as discussed in Section 5.4.2).

The location of the ground plane has been demonstrated to affect the tendency of the inlet flow to separate [87] but is not modeled in the present analysis to limit computational cost and modeling complexity.

While the wing  $C_{L\max}$  condition is important in the certification process of the aircraft and engine, it usually is not encountered in a typical flight mission. In contrast, any mission includes the take-off rotation condition which was therefore included in the short-inlet design assessment to quantify fan efficiency penalties due to increased incidence distortion. The Mach number distribution at take-off rotation is shown for the baseline propulsor in the left-hand plot in Fig. 7-2. If fully attached flow is achieved at the wing  $C_{L\max}$  condition, flow separation does not usually represent a challenge at take-off rotation due to the lower angle-of-attack. An additional condition with level inflow was defined to address the propulsor performance just before take-off rotation due to the increased tendency for the flow to separate at the upper inlet lip in candidate designs with short, thin inlets and nacelles. The Mach number distribution for the take-off level condition is illustrated in the right-hand plot in Fig. 7-2.

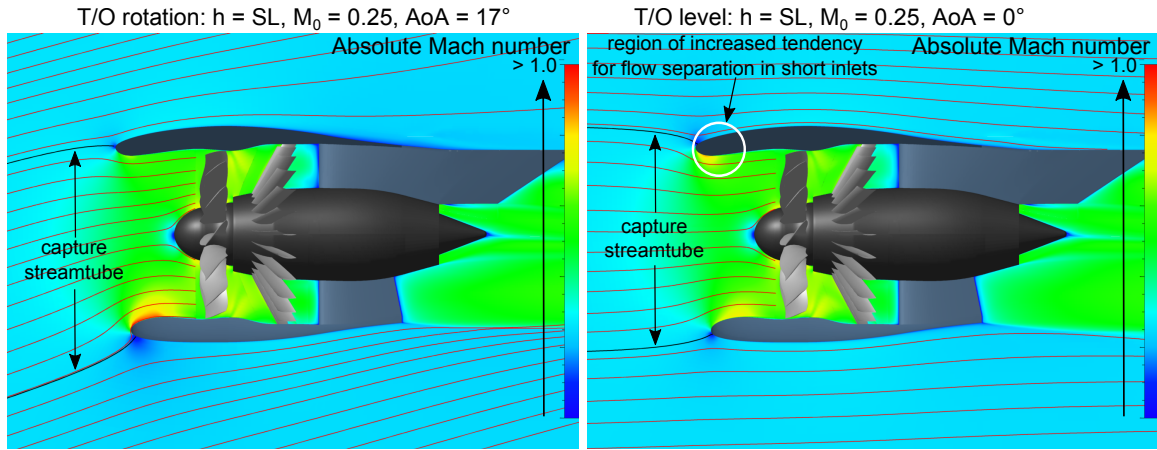


Figure 7-2: Mach number distribution and upstream dividing streamlines at take-off rotation (left) and take-off level operating conditions for baseline propulsor.

Other operating conditions in the nacelle design and engine and aircraft certification process include for example the engine-out flight condition (free-stream Mach number  $M_0 = 0.6$ , altitude  $h = 22,000 \text{ ft}$ , and angle-of-attack  $AoA = 4^\circ$ ). The engine-out condition needs to be addressed in the design process to ensure that the

flow along the external nacelle surface does not separate and the moment on the aircraft due to windmilling drag is limited [88]. In the present analysis, the engine-out operating condition is not considered. While the internal inlet contour is not expected to affect windmilling drag, the candidate short-inlet designs presented in this thesis should be assessed at the engine-out condition in future work to determine any necessary modifications to the external nacelle shapes.

## 7.2 Performance Metrics

The comparison of candidate short-inlet propulsors and the evaluation of whether a short-inlet design achieves the success goal of equal or improved propulsor performance relative to the long-inlet baseline require the definition of a system level metric. The engine propulsive efficiency  $\eta_{prop}$  captures both the changes in the nacelle aerodynamic performance due to variations in external shock strength or surface area and changes in the fan stage performance due to variations in incidence distortion and distortion transfer through the bypass duct. Engine propulsive efficiency measures the conversion of shaft power into propulsive power minus the lost power due to nacelle drag and is used to quantify and compare propulsor system level performance.

With the engine propulsive power given as the product of net thrust minus nacelle external drag,  $T_{net} - D_{nac}$ , and the flight velocity  $V_0$ , and the power input denoted by  $P_{total}$ , the engine propulsive efficiency is defined as

$$\begin{aligned}\eta_{prop} &\triangleq \frac{\text{propulsive power} - \text{lost power due to nacelle drag}}{\text{shaft power input}} \\ &= \frac{(T_{net} - D_{nac}) V_0}{P_{shaft}}.\end{aligned}\tag{7.2}$$

In Equation 7.2, the nacelle drag is defined as the drag from the external nacelle surfaces, consisting of skin friction and pressure drag. The propulsive efficiency for the bypass duct is defined as an additional metric by following an approach proposed by Lord [3]. The fan bypass propulsive efficiency  $\eta_{prop,bypass}$  captures the impact

of changes in the fan stage performance (due to changes in incidence distortion or distortion transfer) on the conversion of shaft power into propulsive power without considering the influence of the nacelle aerodynamics and can be calculated by adding the lost power due to nacelle drag to the engine propulsive power in Equation 7.2,

$$\eta_{prop,bypass} \triangleq \frac{\text{propulsive power of bypass stream}}{\text{shaft power input}} = \frac{T_{net}V}{P_{shaft}}. \quad (7.3)$$

The dependence of the fan bypass propulsive efficiency on fan pressure ratio is illustrated in Fig. 1-3. The fan bypass propulsive efficiency is associated with the control volume CV II, shown in blue in Fig. 7-3. In contrast, the engine propulsive efficiency is associated with both the control volume CV I, shown in green in Fig. 7-3, and the control volume CV II.

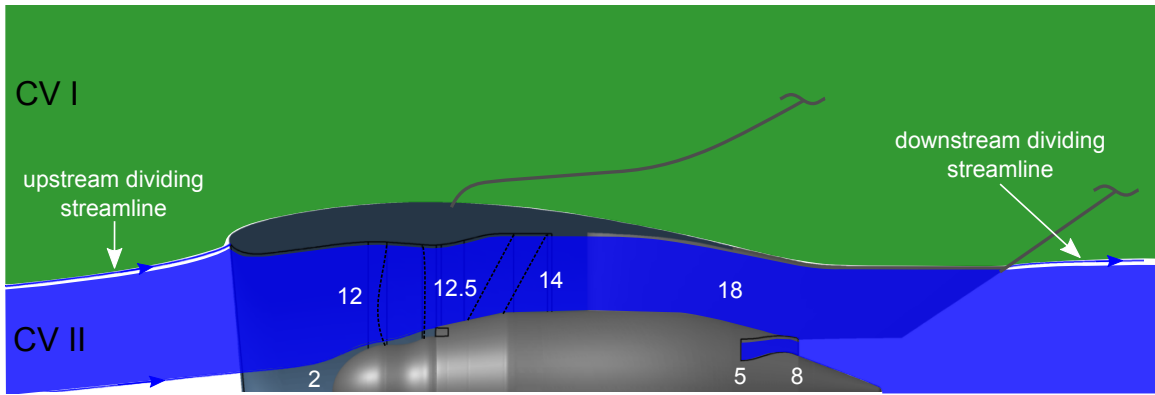


Figure 7-3: Control volume definition for the calculation of propulsive efficiency.

The total shaft power input consists of the power input to the fan bypass,  $P_{fan}$ , and the equivalent power in the core exhaust on a closed cycle basis,  $P_{core}$ ,

$$P_{shaft} = P_{fan} + P_{core}. \quad (7.4)$$

The power input to the fan bypass is determined from

$$P_{fan} = w_{12} (h_{t12.5} - h_{t12}), \quad (7.5)$$

where the stagnation enthalpy rise through the fan rotor is denoted by  $h_{t12.5} - h_{t12}$ , with stations 12 and 12.5 up- and downstream of the fan rotor in the bypass stream,

respectively, as marked in Fig. 7-3. The mass flow through the bypass duct is given by  $w_{12}$ . The equivalent power in the core exhaust is computed from

$$P_{core} = w_5 \frac{1}{2} V_{jet}^2 - w_2 \frac{1}{2} V_0^2, \quad (7.6)$$

where  $w_2$  and  $w_5$  are the core inlet and core exhaust mass flows, respectively, and the core jet velocity downstream of the propulsor is denoted by  $V_{jet}$ .

In addition to the engine propulsive efficiency, the following metrics are evaluated to diagnose the changes in performance between different inlet and nacelle designs:

1. Fan adiabatic efficiency  $\eta_{fan}$
2. Inlet pressure recovery  $\pi_{inlet}$
3. Nacelle viscous drag  $D_{nac,visc}$  (at cruise)
4. Nacelle pressure drag  $D_{nac,p}$  (at cruise)
5. Core inflow stagnation pressure distortion (at off-design conditions)
6. Rotor blade loading variation (at off-design conditions)

Determining the split between thrust and drag from full-domain CFD results requires the integration of static pressure along the upstream and downstream dividing stream-surfaces. The calculation of  $T_{net} - D_{nac}$ , the assessment of the thrust/drag split and the nacelle drag breakdown into viscous and pressure drag, and the determination of total power input from full-domain body force or URANS results are described next.

## 7.3 Calculation of Engine Propulsive Efficiency from CFD Simulations

### 7.3.1 Net Thrust Minus Nacelle External Drag

A control volume approach by Lord [89] is adopted to determine the net thrust minus nacelle external drag,  $T_{net} - D_{nac}$ . The control volume is shown in red in Fig. 7-4.

The pylon surface portion wetted by the fan bypass stream is included within the control volume, whereas the top surface of the pylon as modeled in the simulations is excluded. The momentum balance for the control volume CV 1 is given by

$$\begin{aligned}
 - \int_{CV} (p - p_0) \vec{n}_1 \cdot \vec{i} dA + & \int \vec{\tau} \cdot \vec{i} dA + F_{pylon} = \int V_x \rho \vec{V} \cdot \vec{n}_1 dA. \quad (7.7) \\
 & \text{external nacelle} & \text{fan, core nozzles} \\
 & + \text{inlet internal} & + \text{engine inlet} \\
 & + \text{core cowl and plug} \\
 & + \text{internal pylon}
 \end{aligned}$$

The outward-pointing unit normal vector on the surface of the control volume is denoted by  $\vec{n}_1$  in 7.7 and  $\vec{i}$  is the unit vector in streamwise direction. The force exerted by the propulsor on the pylon is equal to the engine net thrust minus the nacelle external drag,

$$F_{pylon} = T_{net} - D_{nac} = T_{gross} - D_{ram} - D_{nac}. \quad (7.8)$$

In Equation 7.8, the net thrust,  $T_{net}$ , can be split up into gross thrust,  $T_{gross}$ , and ram drag,  $D_{ram}$ . The quantities needed to determine the force exerted by the propulsor on the pylon are typically available from the CFD solution, either from a body force calculation or the time-averaged URANS result.

The pressure integral on the left-hand side in Equation 7.7 includes contributions from all of the solid surfaces within the control volume, as well as from the inlet and fan bypass and core nozzle planes. The shear stress integrals are computed for the solid surfaces, i.e. the external nacelle surface, part of the internal inlet surface, the core cowl and core plug surfaces, and part of the pylon surface. The momentum term on the right-hand side is determined at the inlet and fan bypass and core nozzle axial cross-sections. The formulation using the control volume CV 1 is straightforward to implement for three-dimensional CFD simulations.

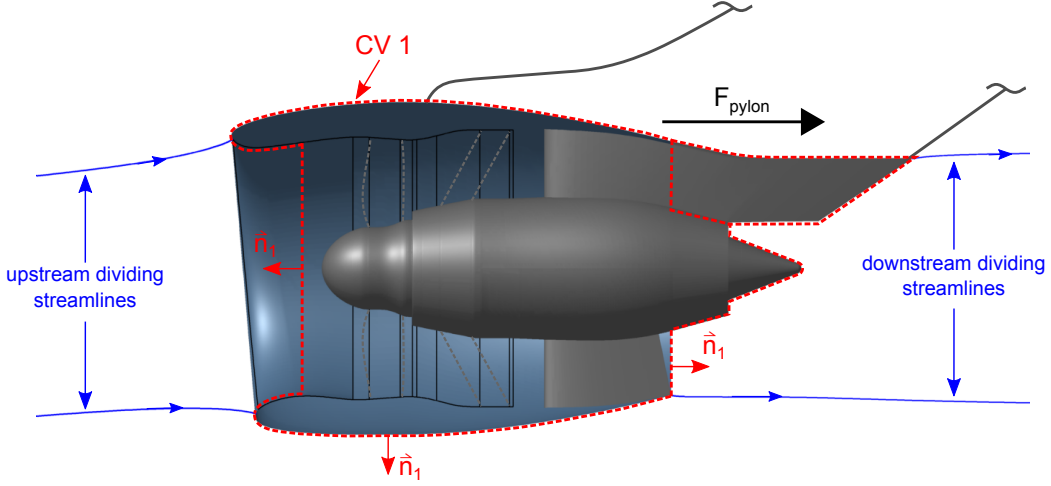


Figure 7-4: Control volume 1 for the calculation of net thrust minus nacelle external drag from three-dimensional CFD simulations.

### 7.3.2 Thrust/Drag Split and Nacelle Drag Breakdown

Determining the split between thrust and nacelle drag requires additional control volumes as illustrated in Fig. 7-5. The momentum balance for the control volume CV 2 gives the following result:

$$\begin{aligned}
 - \int_{\text{upstream dividing SL}} (p - p_0) \vec{n}_2 \cdot \vec{i} dA + \int_{\text{inlet internal}} \vec{\tau} \cdot \vec{i} dA + \int_{\text{engine inlet}} (p - p_0) \vec{n}_2 \cdot \vec{i} dA &= \int_{\text{engine inlet}} (V_x - V_0) \rho \vec{V} \cdot \vec{n}_2 dA \\
 + \text{inlet internal}
 \end{aligned} \tag{7.9}$$

In low-FPR propulsors, one of the main challenges in splitting up the force on the pylon into thrust and drag is due to the bypass nozzle pressure ratio possibly being below the pressure ratio at which the Mach number is sonic,  $\frac{p_{t18}}{p_0} < \frac{p_{t18}}{p^*} \approx 1.89$ . In this case, the nozzle is unchoked and, in contrast to a choked nozzle, the internal flow at the nozzle exit is affected by the presence of the external stream. The pressure at the nozzle exit is increased above the level that would result for static flow conditions at the same nozzle pressure ratio due to the curvature of the external flow streamlines. The external flow effect causes a suction force  $F_{p,boattail}$  on the nacelle trailing edge

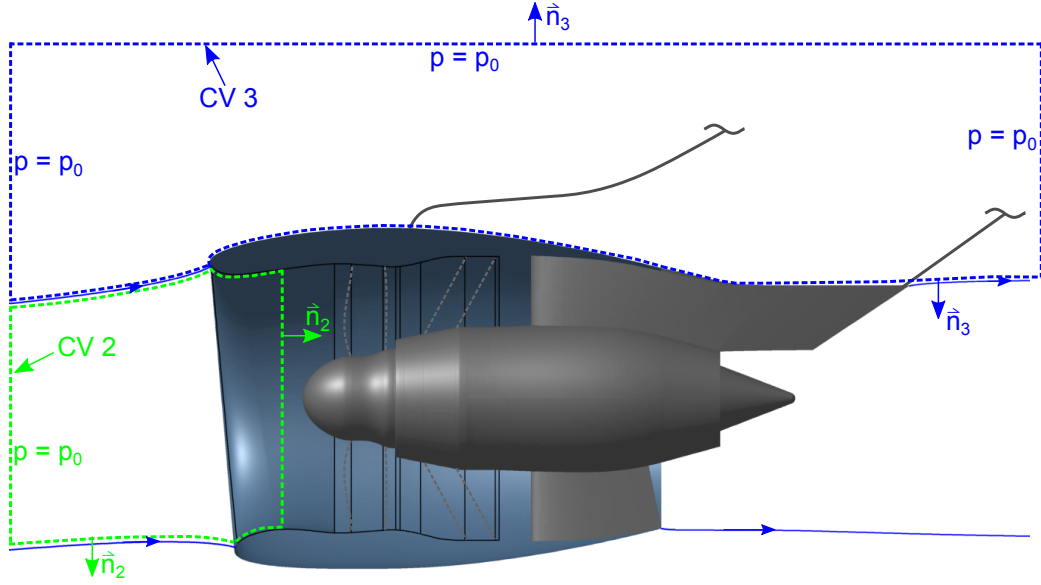


Figure 7-5: Control volumes 2 and 3 for the breakdown of thrust and nacelle viscous and pressure drag from three-dimensional CFD simulations.

(or boattail) which is compensated by the pressurization of the core cowl and core plug [90]. This effect is demonstrated in Fig. 7-6, which shows the static pressure coefficient distribution extracted from a body force simulation. To correct for the external flow effect in the thrust and drag book-keeping, the pressure integral along the dividing streamline must be accounted for in the calculation of gross thrust and nacelle drag. With the unit normal definition used for the control volume CV 3 in Fig. 7-5, the suction force on the boattail is given by

$$F_{p,boattail} = - \int_{\text{downstream dividing SL}} (p - p_0) \vec{n}_3 \cdot \vec{i} dA. \quad (7.10)$$

An alternative expression for the net thrust minus nacelle external drag is obtained by using Equation 7.9 to substitute for the inlet terms in Equation 7.7, and adding and subtracting the downstream dividing streamline pressure term from Equation 7.10:

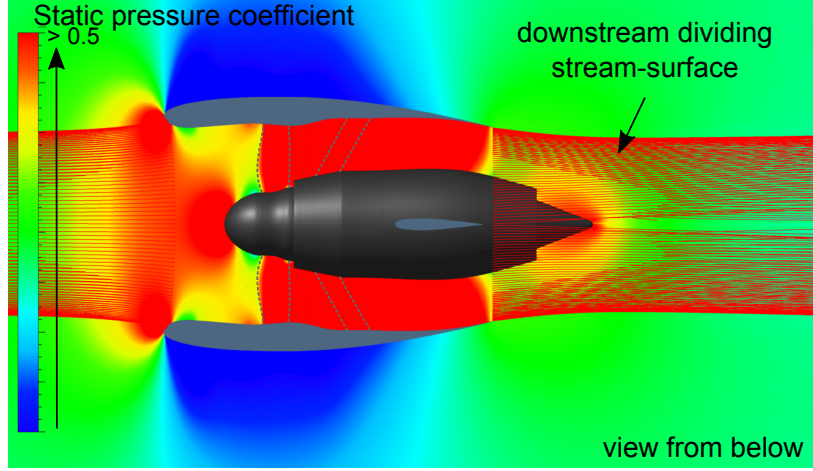


Figure 7-6: Pressurization of core cowl and plug due to external flow effect in an unchoked nozzle.

$$\begin{aligned}
 F_{pylon} = T_{net} - D_{nac} &= T_{gross} - D_{ram} - D_{nac} = \\
 &[ \int V_x \rho \vec{V} \cdot \vec{n}_1 dA + \int (p - p_0) \vec{n}_1 \cdot \vec{i} dA + \int \vec{\tau} \cdot \vec{i} dA + \int (p - p_0) \vec{n}_3 \cdot \vec{i} dA ] \\
 &\text{fan, core nozzles} \quad \text{fan, core nozzles} \quad + \text{core cowl} \quad \text{downstream} \\
 &+ \text{engine inlet} \quad + \text{core cowl} \quad + \text{internal pylon} \quad \text{dividing SL} \\
 &+ \text{internal pylon} \\
 \\
 &- [w_{inlet} V_0] - [ \int \vec{\tau} \cdot \vec{i} dA + \int (p - p_0) \vec{n}_1 \cdot \vec{i} dA ] \\
 &\text{nacelle} \quad \text{upstream dividing SL} \\
 &\text{external} \quad + \text{external nacelle} \\
 &+ \text{downstream dividing SL}
 \end{aligned} \tag{7.11}$$

In Equation 7.11, the three terms in the brackets are gross thrust, ram drag, and nacelle external drag, respectively. In addition, the two nacelle external drag terms correspond to nacelle viscous and nacelle pressure drag, respectively. The sum of the two integrals in the red bracket can be negative for conditions with high leading edge suction and should really be called the external force. The label nacelle external drag is used here since sum of the two terms in the red bracket is positive

for the propulsors assessed in this work at the cruise condition. The formulation in Equation 7.11 enables the determination of the thrust/drag split and the nacelle drag breakdown. However, in comparison to the formulation given in Equation 7.7, it is significantly more challenging to implement, primarily due to the requirement for calculating pressure integrals over the upstream and downstream stream-surfaces between internal and external flows.

The coordinates of the streamlines in the dividing stream-surfaces and the static pressure values along the streamlines are extracted from the full-domain body force simulations using the Numeca's post-processing capabilities. The pressure integrals over the stream-surfaces are determined after interpolating the streamline data onto a structured mesh. The upstream and downstream stream-surfaces between the internal and external streams are shown in Fig. 7-7 for the baseline propulsor at cruise. The pressure integrals are determined up to streamwise locations at which the local pressure is equal to the ambient pressure.

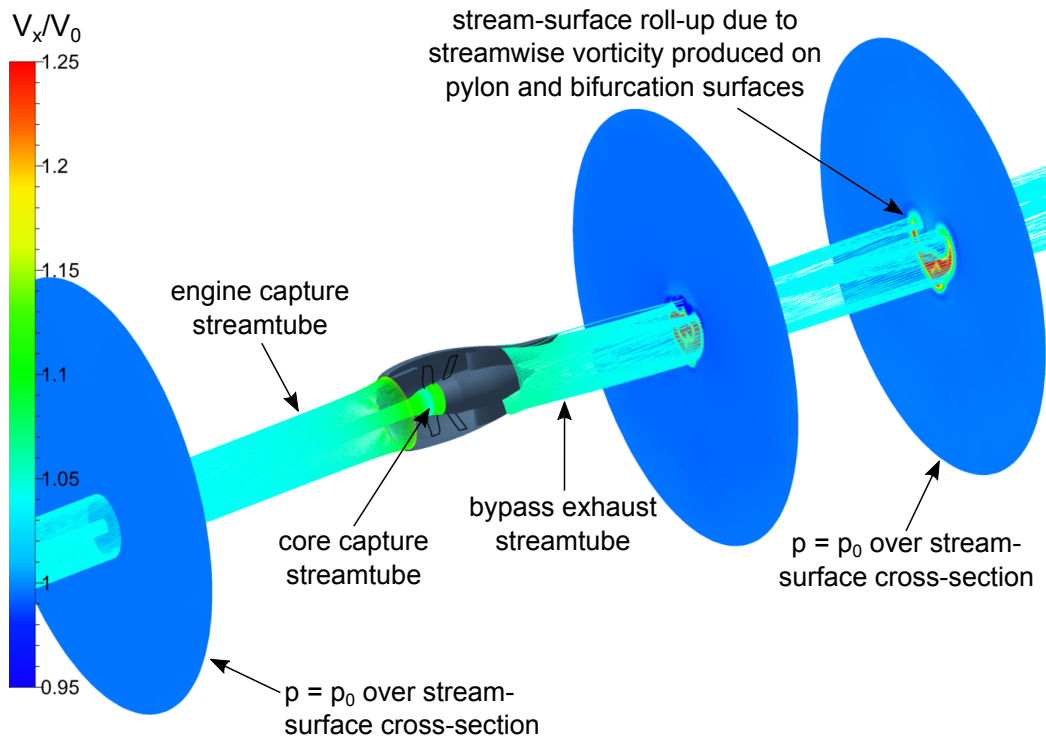


Figure 7-7: Engine capture streamtube (upstream dividing stream-surface) and bypass exhaust streamtube (downstream dividing stream-surface) extracted from body force results for the baseline propulsor at cruise.

There are several numerical challenges associated with quantifying the thrust/drag breakdown from Equation 7.11. The downstream stream-surface is three-dimensional due to the roll-up caused by streamwise vorticity, as indicated in Fig. 7-7, and the interpolative nature of integrating the pressure terms on the dividing stream-surfaces can lead to errors of up to 5 %. The inaccuracies introduced by the interpolation of the static pressure onto the streamlines and a structured mesh could be reduced in an adaptive grid solver which could align the grid lines with the dividing streamlines [90].

An additional difficulty is due to the blunt shapes of the nacelle and core nozzle trailing edges are blunt. At the nozzle trailing edges, the origin of the downstream dividing streamlines is not clearly defined. In the present analysis, the locus of the dividing stream-surface is determined by marching radially inward from the outer trailing edge radius until the bypass or core exhaust mass flow rate is achieved.

The calculation of the pressure integral along the upstream dividing stream-surface depends on the accurate determination of the stagnation line on the inlet lip. For the medium level grid listed in Table 5.2, it was found that moving only one grid point away from the stagnation line led to errors in the pressure integral of up to 10 %.

Equations 7.7 and 7.11 provide two different formulations for the net thrust minus nacelle external drag, labeled formulation 1 and formulation 2, respectively, in the following analysis. Formulation 1 is straightforward to implement, whereas the implementation of formulation 2 is complicated by numerical challenges. To verify the calculation of net thrust minus nacelle external drag from formulation 2, the two formulations are used to determine the propulsive efficiency, as defined in Equation 7.2, and the results are compared in Fig. 7-8 for the inlet designs generated in the preliminary inlet length study discussed in Section 5.2. The results agree to within 1 %. The discrepancies are attributed to interpolation errors in calculating the pressure integrals needed in formulation 2.

Formulation 1 is more robust and reliable than formulation 2 and was always used to determine  $T_{net} - D_{nac}$  in the calculation of the propulsive efficiency. The pressure integrals along the upstream and downstream dividing stream-surfaces were computed only to evaluate changes in the nacelle pressure drag.

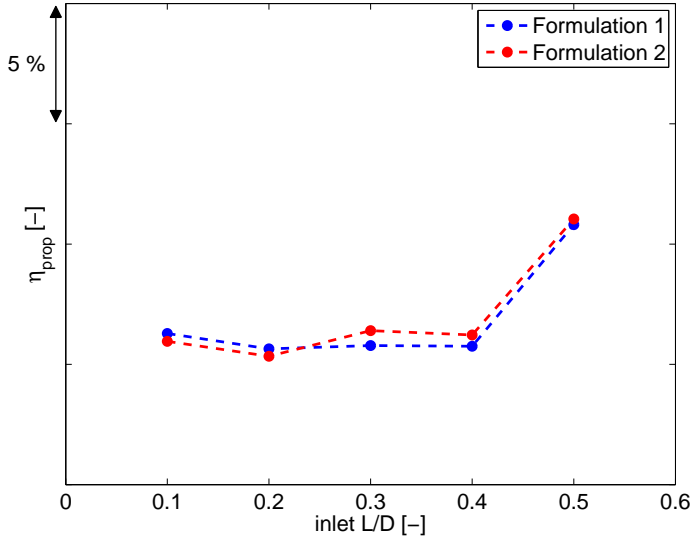


Figure 7-8: Comparison of propulsive efficiency computed based on two different formulations for net thrust minus nacelle external drag.

### 7.3.3 Shaft Power Input

In addition to the net thrust minus nacelle external drag, the shaft power input is required to compute propulsive efficiency. The shaft power input is computed from Equations 7.4, 7.5, and 7.6. The bypass duct mass flow,  $w_{12}$ , the core inlet mass flow,  $w_2$ , and the core exhaust mass flow,  $w_5$ , are readily available from the CFD results. The stagnation enthalpy rise across the rotor,  $h_{t12.5} - h_{t12}$ , is computed from body force results directly or by time-averaging the URANS simulation flow field. The core jet velocity,  $V_{jet}$ , can be determined from the the URANS results or analytically based on the isentropic expansion to ambient pressure,

$$\frac{V_{jet}}{V_0} = \sqrt{1 + \frac{2\Delta h_t}{V_0^2}}, \quad (7.12)$$

where  $\Delta h_t = h_{t8} - h_{t0}$  is the enthalpy rise in the core flow. The calculation of  $V_{jet}$  from the time-averaged URANS solution is made difficult by the three-dimensional nature of the flow field downstream of the engine due to the influence of the pylon and bifurcation. The conceptual approach employed is to follow the core exhaust streamtube up to the streamwise location at which the local static pressure is equal to the ambient pressure,  $p = p_0$ , as depicted in the left-hand plot in Fig. 7-9. The axial

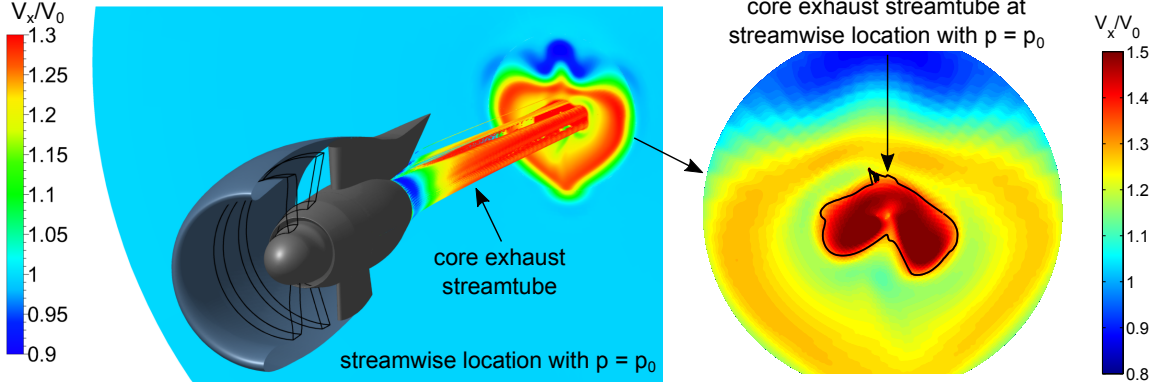


Figure 7-9: Core exhaust streamtube and axial velocity distribution at  $p = p_0$  (left) and core exhaust streamtube cross-section (right) extracted from body force simulation for baseline propulsor at cruise.

velocity on a plane at this location is extracted and the boundary of the core exhaust streamtube on this plane is determined, as illustrated in the right-hand plot in Fig. 7-9. The jet velocity is computed next by mass-averaging the axial velocity over the region bounded by the core exhaust streamtube. The accurate calculation of the core jet velocity is critical since the propulsive efficiency is sensitive to any changes in  $V_{jet}$ : a 10 % variation in  $V_{jet}$  results in a 2 % change in propulsive efficiency. Therefore, the mass flow through the streamtube,  $w_{streamtube}$ , is determined in addition to  $V_{jet}$  and compared against the core nozzle mass flow,  $w_5$ . The origin of the stream-surface at the blunt core nozzle trailing edge is adjusted until  $w_{streamtube} = w_5$ . The URANS-based results for the core jet velocity agreed to within 0.1 % with the analytical result for the baseline and short-inlet candidate propulsors.

## 7.4 Sensitivity Analysis - What Matters Most?

The potential for reduced weight and drag represents the main motivation for shortening the inlet and the nacelle in low-FPR propulsors. At the same time, short-inlet designs can result in increased levels of rotor incidence distortion and reductions in fan efficiency. To quantify the impact of nacelle drag reductions and fan efficiency changes on propulsor performance, the sensitivity of the engine propulsive efficiency to fan efficiency,  $\eta_{fan}$ , nacelle viscous drag,  $D_{nac,visc}$ , nacelle pressure drag,  $D_{nac,p}$ ,

and total nacelle drag,  $D_{nac}$ , is presented Fig. 7-10. While one parameter is varied, all other quantities are kept constant. The change in fan efficiency is assumed to be at constant fan pressure ratio, such that a reduction in fan efficiency corresponds to an increase in the stagnation enthalpy rise across the fan,  $h_{t12.5} - h_{t12}$ , i.e. an increase in the power requirement. A 1 % reduction in fan efficiency corresponds to a 0.85 % reduction in propulsive efficiency, whereas a 1 % reduction in total nacelle drag results in a 0.07 % increase in propulsive efficiency.

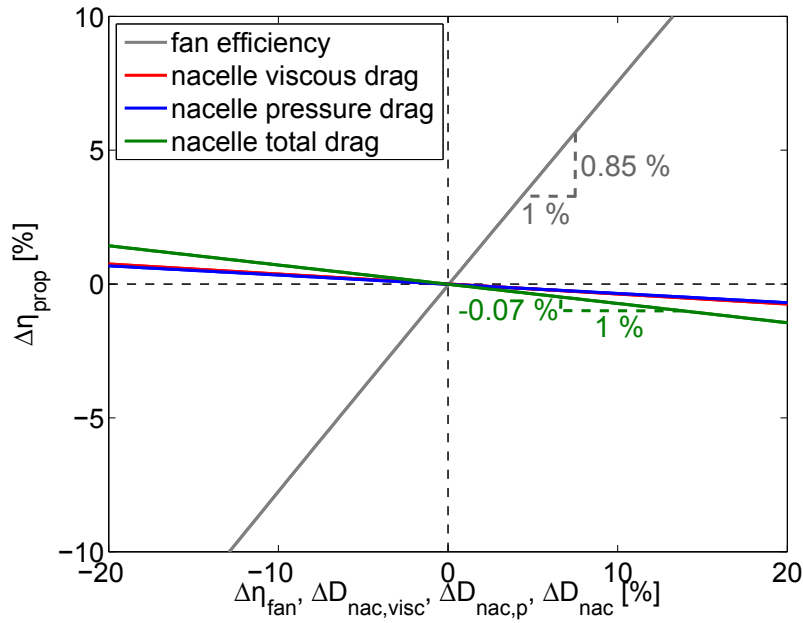


Figure 7-10: Sensitivity of engine propulsive efficiency with respect to changes in rotor efficiency and nacelle drag contributions at cruise.

Nacelle external drag reductions of 15 % and more are possible by shortening the inlet from  $L/D = 0.5$  to  $L/D = 0.19$ , enabling significant improvements in propulsor performance. However, the sensitivity analysis highlights the importance of limiting rotor incidence distortion and rotor losses in short-inlet designs since any benefits from nacelle drag reductions can be outweighed by the impact of fan efficiency penalties. The trade-off between reductions in nacelle external drag on the one hand and reductions in fan efficiency on the other hand is further discussed in the next chapter and in the presentation of two candidate short-inlet designs with  $L/D = 0.25$  and  $L/D = 0.19$ .

# Chapter 8

## Short Inlet and Nacelle Design Strategy

A strategy and guidelines for the design of short inlets and nacelles is presented in this chapter based on the requirements on the inlet and nacelle shapes, which are outlined in the first section. A performance assessment of inlet designs with inlet length over fan diameter  $L/D$  as low as 0.02 suggested that inlets with length lower than approximately  $L/D = 0.2$  do not achieve the performance levels offered by the baseline configuration at cruise and incur prohibitive fan efficiency penalties at off-design conditions. Consequently, the design strategy is focused on inlets with  $L/D$  of 0.2 and above.

### 8.1 Design Requirements and Challenges

The design requirements for inlets and nacelles are set by trades between the propulsor performance at cruise and multiple off-design conditions. Slender, streamlined inlet and nacelle shapes are required to mitigate wave drag at cruise. In contrast, thicker inlet lips with round leading edges are needed for separation-free inlet performance and low inlet flow distortion levels at low-speed, high angle-of-attack conditions.

The streamlines dividing internal and external flows are depicted in Fig. 8-1 for a design with  $L/D = 0.19$ . The streamtube capture area is smallest at cruise, the

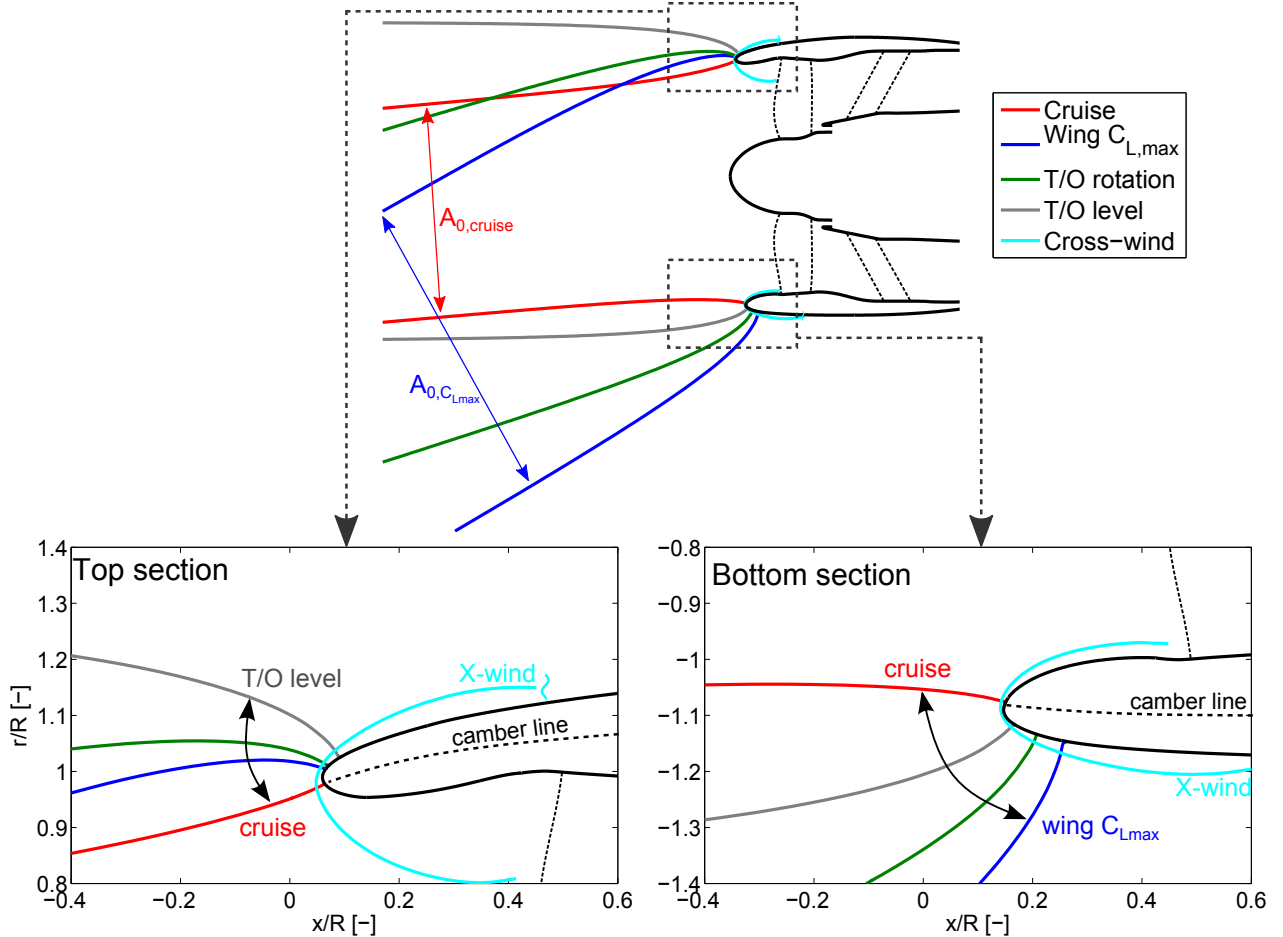


Figure 8-1: Dividing streamlines between internal and external flows for a candidate inlet design with  $L/D = 0.19$  at critical operating conditions.

mass flow ratio is smaller than one,  $MFR_{cruise} = \frac{A_0}{A_{HL}} < 1$ , and the stagnation point is located on the inside of the inlet lip. At low-speed conditions, such as wing  $C_{L,\max}$  or T/O rotation, the streamtube capture area grows, the mass flow ratio is larger than one,  $MFR_{low-speed} > 1$ , and the stagnation point shifts outward to the nacelle external surface.

Relative to the other operating conditions, the free-stream Mach number is lowest at the cross-wind condition,  $M_{0,X-wind} = 0.0442$ , and the streamtube capture area is largest. Two streamlines close to the inlet lip are shown at the top and bottom of the nacelle, respectively, for the cross-wind condition. In conventional inlet designs, the requirement for attached flow in the inlet at the cross-wind condition is a driver for increased inlet lip thickness around the entire circumference. Because the top section

must be thin to mitigate drag penalties at cruise, separation-free inlet flow could not be satisfied for the candidate design with  $L/D = 0.19$  at cross-wind. For inlets with  $L/D$  smaller than about 0.25, flow control such as blow-in doors in the inlet may be required to reduce separation and alleviate inlet flow distortion. The performance of the  $L/D = 0.19$  candidate nacelle design at the cross-wind operating condition with and without blow-in doors is quantified in Section 10.4.

At cruise, the strength of the shock on the front nacelle surface is governed by the inlet lip and nacelle external shapes downstream of the stagnation point. Limiting the shock strength and wave drag penalties requires aligning the outer nacelle geometry with the incoming dividing streamline and limiting the curvature along the outer portion of the inlet lip. If the two-dimensional nacelle profiles are viewed as airfoils, the camber angle should be chosen such that the front inlet and nacelle shape is oriented towards the incoming streamline and the local angle-of-attack on the airfoil is minimized, as indicated on the bottom in Fig. 8-1. The flow upwash due to the wing potential field results in a  $5^\circ$  angle-of-attack of the free-stream relative to the engine axis of rotation. As a consequence, the top section is at a larger local angle-of-attack than the bottom section and therefore requires a larger camber angle to limit the over-speed on the nacelle external surface.

While short-nacelle designs with positive camber angles promote low Mach numbers on the nacelle external surface, the outward shift in the stagnation point for low-speed operating conditions requires reduced camber angles or “un-cambered” airfoil profiles to limit the flow acceleration along the inlet internal surface and provide for separation-free inlet flow. The take-off level operating condition is representative of a low-speed condition with low engine angle-of-attack. At the top section, the stagnation point shift between off-design and cruise is largest for the take-off level condition. The stagnation point moves outward and downstream on the nacelle external surface. The flow accelerates around the inlet lip as shown on the right-hand plot in Fig. 7-2 for the baseline propulsor. In short inlets with thin profiles, the flow tends to separate in the inlet. The requirement for attached inlet flow and low rotor incidence distortion at the take-off level condition sets the lower limit on the inlet thickness.

At the bottom section, the shift in the stagnation point between off-design and cruise is largest for the wing  $C_{L\max}$  condition with  $AoA = 29^\circ$ . Compared to the top section, an increased lip thickness is required for separation-free inlet flow and limited flow acceleration around the inlet lip at off-design. Reducing the airfoil camber angle proved to be an effective design technique for determining the required inlet lip orientation for separation-free inlet flow at wing  $C_{L\max}$  while limiting external flow acceleration at cruise. The parametric description of the bottom inlet lip and the design strategy are described in Section 8.3.

Compared to the design of long inlets, an additional challenge unique to short inlets arises due to the continuous decrease of the flow area throughout the inlet, illustrated in the top plot in Fig. 8-2. In the long inlet, the reduction in flow area between the highlight and throat is followed by an increase up to the spinner leading edge location. As the spinner thickness grows, the flow area decreases up to the fan face. The average Mach number reaches a local maximum at the throat, as shown in the center plot in Fig. 8-2, and the reduction in the flow area between the highlight and inlet throat is accompanied by a flow acceleration approaching the fan face, where  $M_{fan\ face} = 0.63$ . In combination with the inflow at angle-of-attack, the local flow acceleration along the bottom inlet surface is at a maximum close to the throat, as indicated by the isentropic Mach number distribution in the bottom plot in Fig. 8-2. This local maximum is reached far upstream of the rotor, as shown in the Mach number contour plots on the left in Fig. 1-5 or on the top left in Fig. 7-1. While the averaged Mach number is highest at the fan face, the flow radial and circumferential non-uniformities caused by the angle-of-attack inflow are smallest at the fan face due to the flow straightening through the inlet.

Spinner geometries with extended axial length are needed in short inlets to alleviate flow non-uniformities near the hub and mitigate the stagnation pressure distortion in the core inlet. As a result, the flow area monotonically decreases throughout the inlet and the location of the maximum flow acceleration near the shroud is close to the location of the maximum averaged Mach number at the fan face, as depicted in the right-hand plot in Fig. 1-5. Due to the proximity of the region of high Mach

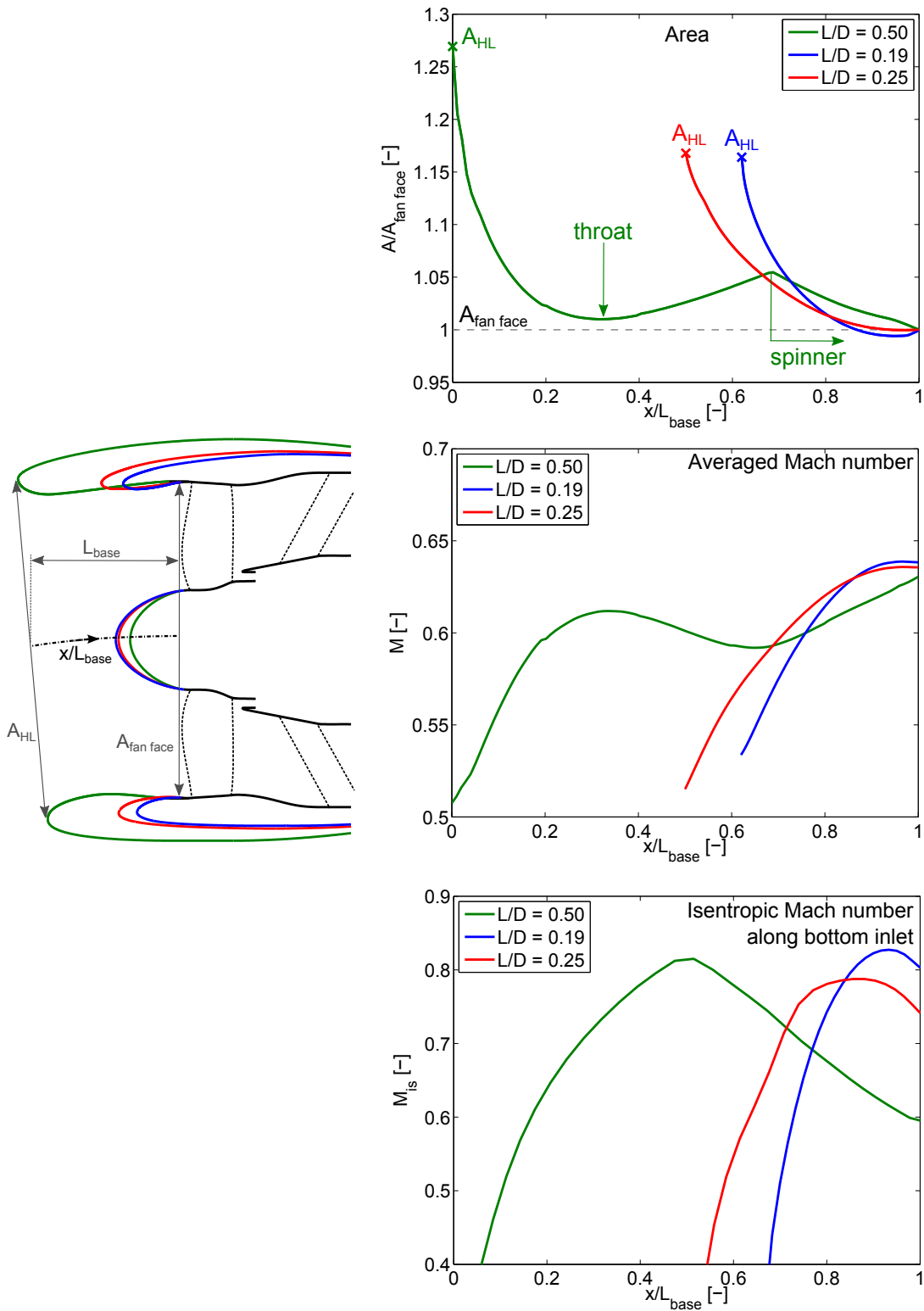


Figure 8-2: Distributions of inlet area (top) and averaged Mach number (center) through the inlet and isentropic Mach number along the bottom inlet surface (bottom) for  $L/D = 0.5$ ,  $L/D = 0.25$ , and  $L/D = 0.19$  propulsors at cruise.

number to the fan face, incidence distortion is enhanced, leading to increased rotor losses.

In Section 6.2, both the non-uniform inflow and the pylon upstream influence were demonstrated to contribute to the incidence distortion for the baseline propulsor at cruise. In short inlets at high angle-of-attack off-design conditions, the contribution from the non-uniform inflow dominates the incidence distortion and the distortion transfer. As an example, the rotor incidence is presented in Fig. 8-3 for the candidate design with  $L/D = 0.19$  at the wing  $C_{L\max}$  condition. The rotor incidence  $i$  is shown relative to the incidence at the peak efficiency point on the speedline at wing  $C_{L\max}$ <sup>1</sup>,  $i_{des}$ , to highlight the increased impact of the angle-of-attack inflow and the reduced contribution from the pylon and bifurcation upstream influence. The following aerodynamic mechanisms are responsible for the distortion in fan face incidence:

1. The pylon upstream influence results in a local increase of the rotor back pressure and the rotor incidence.
2. The flow acceleration around the lower inlet lip leads to a region of high axial Mach number and reduced rotor incidence.
3. The angle-of-attack flow at the fan face results in regions of negative circumferential Mach number,  $M_\theta < 0$ , analogous to counter-swirl and increased rotor incidence.
4. On the opposite side, the angle-of-attack flow at the fan face leads to regions of positive circumferential Mach number,  $M_\theta > 0$ , analogous to co-swirl and reduced incidence
5. The flow acceleration around the spinner leads to reduced rotor incidence at the top of the spinner surface.

The incidence variation near the shroud is affected by the shape of the inlet lip and inlet internal contour and the design requirements on the top and bottom

---

<sup>1</sup>To compute the incidence at the peak efficiency operating point, single-passage RANS simulations were carried out at uniform inflow without the pylon and bifurcation.

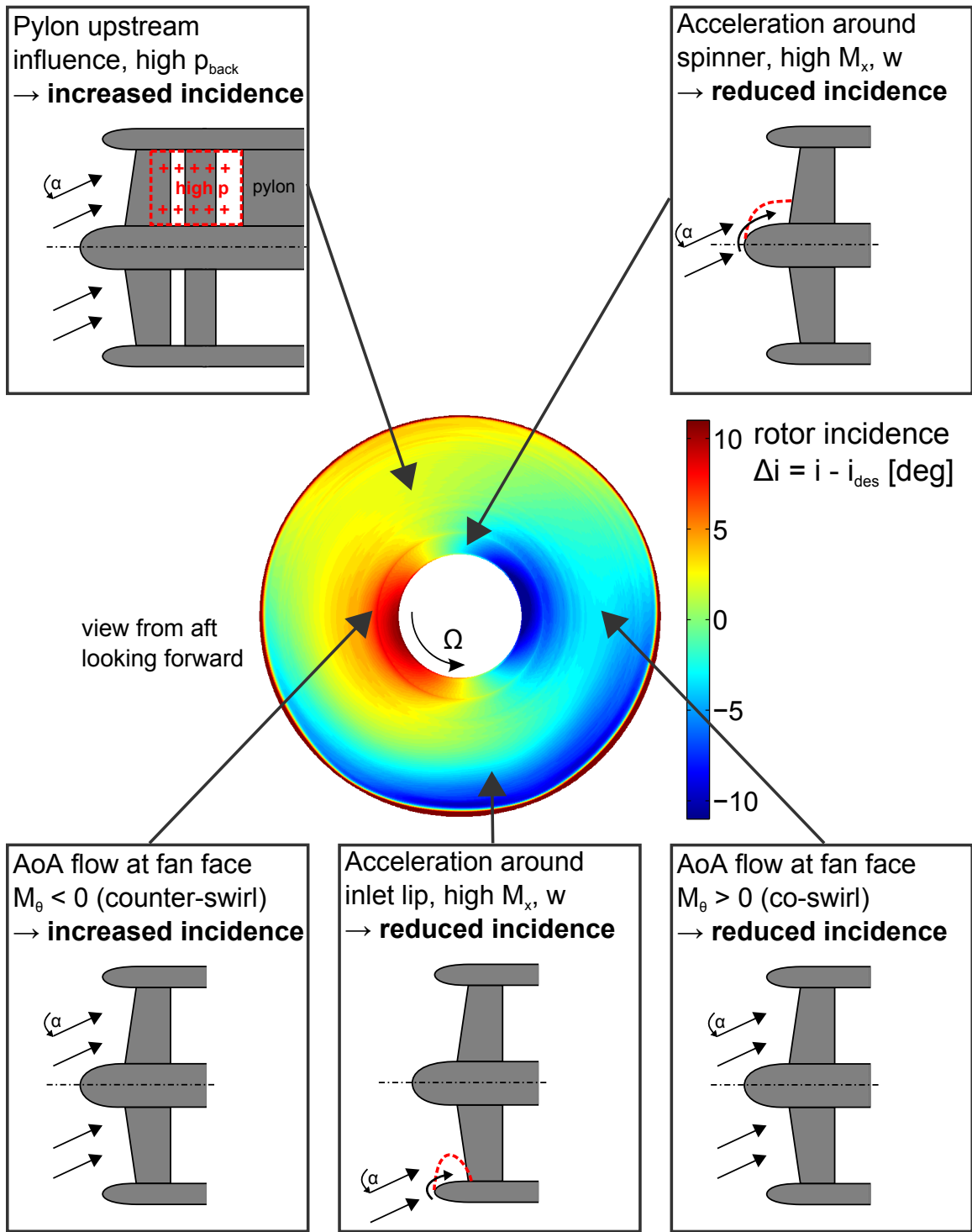


Figure 8-3: Rotor incidence distortion mechanisms (incidence distribution shown at wing  $C_{L\max}$  operating condition for candidate short-inlet design with inlet  $L/D = 0.19$ ).

inlet geometries are outlined above. The incidence variation due to the non-uniform inflow at mid-span can only be reduced by increasing the inlet length and thereby enhancing the flow straightening through the inlet. Finally, near the hub, the spinner shape plays an important role in the incidence distribution. Spinner geometries with increased axial length limit the incidence distortion near the hub but lead to increased acceleration around the inlet lip and increased incidence distortion over the outer span at low-speed conditions, since the stagnation point is shifted outward along the outer nacelle surface relative to short spinner shapes. The trade-offs in design and off-design performance for multiple spinner designs are assessed in Section 8.4.

## 8.2 Limiting the Short-Inlet Design Space

In this section, the performance of two short-inlet designs with  $L/D = 0.1$  and  $L/D = 0.02$  is summarized. The Mach number distributions at cruise and the axial Mach number distributions at the wing  $C_{L\max}$  operating condition are presented in the left- and right-hand plots in Fig. 8-4, respectively. The results for the inlet design with  $L/D = 0.1$  are shown in the top plots. At cruise, a strong shock forms on the nacelle external surface. At the shock, the maximum Mach number is increased by  $\Delta M_{max} = 0.18$  relative to the long-inlet baseline design, resulting in increased wave drag. At the wing  $C_{L\max}$  condition, the flow accelerates around the lower inlet lip, resulting in a region of high Mach number over the outer span and flow separation at the shroud. The circumferential variation of rotor incidence at mid-span is depicted in the left-hand plot in Fig. 8-5. The difference between the minimum and maximum values grows by  $6.9^\circ$  relative to the baseline propulsor. Due to the large variations in incidence, the rotor losses increase, and the fan efficiency is reduced by 8.4 %.

The orbits of the local rotor operating point in terms of the work coefficient  $\Psi_{h_t}$  are presented on the right in Fig. 8-5 for the baseline and the two short-inlet configurations. In addition, the results of steady, single-passage simulations with uniform inflow between choke and the numerical stability limit are shown. The mean work coefficient and incidence operating points are marked by the x-symbols.

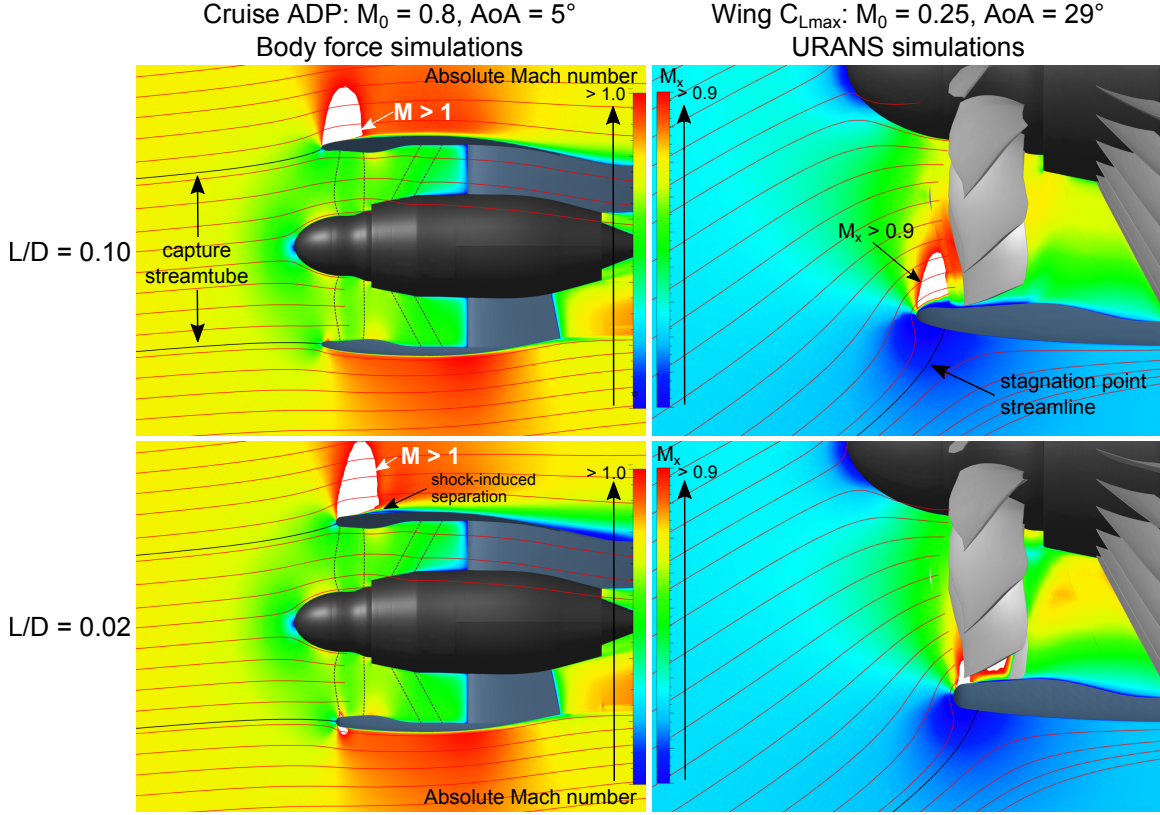


Figure 8-4: Mach number distribution at cruise (left) and axial Mach number distribution at wing  $C_{L\max}$  operating condition (right) for candidate short-inlet propulsors with  $L/D = 0.10$  and  $L/D = 0.02$ .

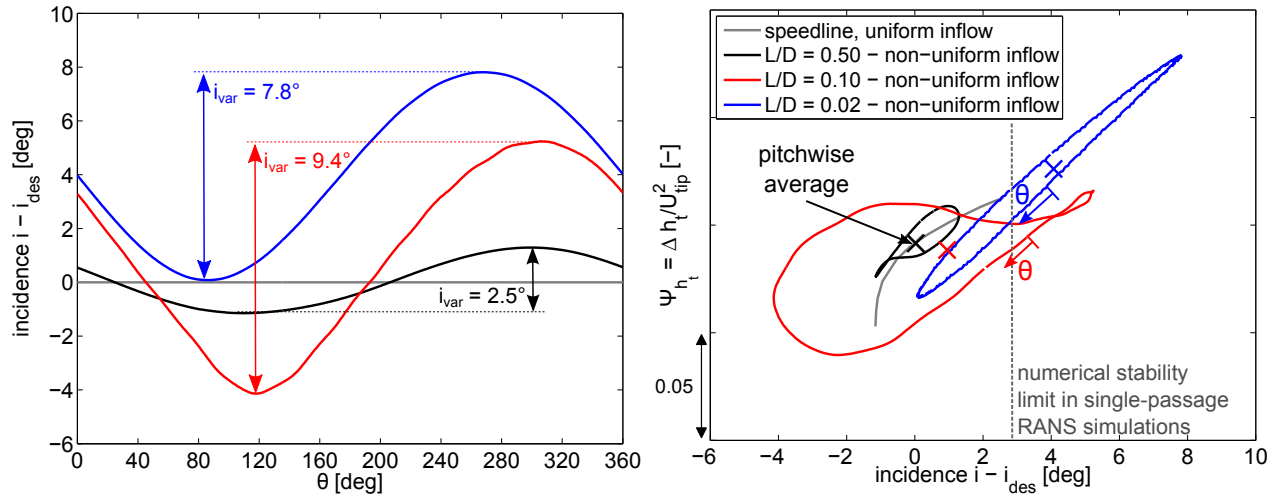


Figure 8-5: Time-averaged URANS results of the circumferential variation of rotor incidence at mid-span (left) and orbits of local rotor operating conditions along the circumference at mid-span for the baseline configuration with  $L/D = 0.5$  and the short-inlet configurations with  $L/D = 0.1$  and  $L/D = 0.02$  at wing  $C_{L\max}$  operating condition.

Table 8.1: Performance overview of short-inlet propulsors with  $L/D = 0.19$ ,  $L/D = 0.10$  and  $L/D = 0.02$  relative to  $L/D = 0.5$  baseline configuration.

Condition/Metric		$L/D = 0.19$ (optimized)	$L/D = 0.10$ (not optimized)	$L/D = 0.02$ (not optimized)
<b>Cruise ADP</b>				
- maximum external Mach number	$\Delta M_{max}$	+0.02	+0.18	+0.51
- fan efficiency	$\Delta \eta_{fan}$	-1.6 %	-2.5 %	-3.6 %
<b>Wing <math>C_{L_{max}}</math></b>				
- relative difference in corrected flow	$\Delta w_c$	+0.1 %	+3.1 %	+7.8 %
- incidence variation at mid-span	$\Delta i_{var,mid}$	+3.5°	+6.9°	+5.3°
- fan efficiency	$\Delta \eta_{fan}$	-3.9 %	-8.4 %	-14.5 %

In this analysis, the bypass nozzle area is kept constant between the simulations for the long-inlet and the short-inlet cases. Due to the increased inlet flow non-uniformities and the aerodynamic blockage created by the flow separation at the bottom inlet lip, the operating condition for the  $L/D = 0.1$  design is shifted to a 3.1 % lower corrected flow and the mean incidence at mid-span increases by 1.1°. For a consistent fan performance comparison at equal corrected flows, the variable-area nozzle would have to be opened up. Since an increase in the nozzle area requires remeshing and additional simulations, the performance comparison is carried out here at equal nozzle area. It is acknowledged that part of the fan efficiency penalty could be recovered by increasing the corrected flow.

Due to the large excursions of the local operating points relative to the speedline data (used to define the body force simulations) at wing  $C_{L_{max}}$ , it was not possible to obtain a converged solution with the body force method. While the presented flow field and performance results at cruise were computed using body force simulations, the performance assessment at the wing  $C_{L_{max}}$  condition required URANS simulations. The performance of the  $L/D = 0.1$  design relative to the long-inlet baseline is summarized in Table 8.1. Compared to the candidate short-inlet propulsor with  $L/D = 0.19$ , which is described in detail in Chapter 10, the performance of the  $L/D = 0.1$  configuration is reduced at both cruise and wing  $C_{L_{max}}$ . In addition to the substantial fan efficiency penalty, the large increase in the incidence variation is likely to cause blade structural and LPC stability issues.

Part of the increase in the incidence variation for the  $L/D = 0.1$  design at the wing  $C_{L\max}$  operating condition is due to flow acceleration around the bottom inlet lip and the region of high Mach number at the fan face, as illustrated on the top right in Fig. 8-4. This high Mach number region at the fan face can be eliminated by further reducing the inlet length. Thus, the feasibility of an additional design with  $L/D = 0.02$  was tested. The flow fields at cruise and wing  $C_{L\max}$  are shown on the bottom left and right in Fig. 8-4, respectively. Due to the increased bluntness of the inlet lip, the maximum Mach number on the nacelle external surface at cruise is increased to  $\Delta M_{max} = 0.51$  relative to the baseline propulsor and the flow at the nacelle surface separates due to the increased adverse pressure gradient across the shock. As hypothesized, the incidence variation at mid-span at the wing  $C_{L\max}$  condition is reduced compared to the  $L/D = 0.1$  design. However, the fan face flow is now at a large angle-of-attack over the entire span since the removal of the inlet eliminates any flow straightening upstream of the fan face. The increased incidence distortion results in an additional fan efficiency penalty and, relative to the baseline propulsor, the fan efficiency is reduced by  $\Delta \eta_{fan} = -14.5\%$ . The large increase in the external Mach number at cruise and the considerable reduction in fan performance at the off-design condition suggest that a configuration without an inlet is not viable.

It is important to note that both the  $L/D = 0.1$  and the  $L/D = 0.02$  designs were not optimized. By re-designing the nacelle external surface and the inlet lip shapes, some improvement in performance at design and off-design could be achieved. However, the design space is restricted by structural constraints on the maximum nacelle diameter and by geometric constraints due to the face case location and there are not many options to modify the inlet and nacelle shapes. In both designs, reducing the inlet thickness would mitigate the over-speed at cruise but thinner inlet shapes would only exacerbate the incidence distortion at the low-speed conditions. A configuration without an inlet would offer increased weight and nacelle viscous drag advantages due to the reduction in nacelle surface area but is unlikely to be compatible with a fan design such as the one used in the baseline propulsor. A variable-pitch capability would possibly be required to achieve acceptable off-design fan performance.

In summary, the increased wave drag penalties at cruise and the increased fan performance penalties observed at both design and off-design conditions for the two ultra-short inlet designs resulted in the decision to limit the lower end of the inlet range in the parametric exploration of the short-inlet design space to approximately  $L/D = 0.2$ . The observations suggest that propulsor performance benefits relative to the long-inlet baseline are most likely possible for inlet lengths above  $L/D = 0.2$ .

### 8.3 Design Approach and Guidelines

Since there are considerable differences in the requirements on the top and bottom sections of the inlet and nacelle, two sets of design guidelines are presented. The design framework described in Chapter 5 enables the independently modification of the top and bottom inlet and nacelle geometries. However, since the inlet and nacelle surface geometries between  $\theta = 0^\circ$  and  $180^\circ$  are a function of the shapes at the top and bottom, any change in one of the sections results in changes in the inlet and nacelle surfaces. At each design iteration, the body force simulations provide a fast method to assess the impact of local changes in the top and bottom inlet and nacelle contours on the three-dimensional inlet and external flow field.

To determine whether inlets with  $L/D$  between 0.2 and 0.3 can offer system level performance benefits compared to the  $L/D = 0.5$  baseline, two candidate designs were obtained. The nacelle maximum diameter was reduced relative to the baseline to limit flow acceleration over the aft part of the nacelle surface at cruise. The nacelle thickness was defined in collaboration with the industry partner.

The first short-inlet design was aimed at determining whether a propulsor with an inlet as short as  $L/D = 0.2$  is feasible and whether this propulsor would enable a performance advantage over the long-inlet baseline. The design optimization resulted in a small reduction of the lower inlet length such that the final design had an inlet length of  $L/D = 0.19$ . While this design comes close to meeting the design criteria provided by the industry partner, its performance is reduced compared to the long-inlet baseline due to increased rotor incidence distortion and fan efficiency

penalties. As a result, a second design with an increased inlet length of  $L/D = 0.25$  was generated. This design is demonstrated to offer system level performance benefits relative to the long-inlet baseline, as discussed in Chapter 9. While the two designs are used as examples, the design strategy described in this section is applicable to a wider range of inlet lengths.

### 8.3.1 Top Inlet and Nacelle Section

The shape of the top inlet and nacelle section is critical for limiting the external flow acceleration and wave drag at cruise. Supercritical airfoil shapes provide for low drag due to reduced flow acceleration on the upper surface and an approximately uniform supersonic plateau, followed by a weak shock downstream of mid-chord. The design philosophy behind supercritical airfoils is described for example by Harris [7] or Goldsmith and Seddon [22]. The design of nacelles which take advantage of the supercritical airfoil characteristics are discussed for example by Langley [91] or Barber et al. [92]. In the current work, supercritical airfoils serve as the starting point for the design of the top inlet and nacelle sections.

For an inlet with  $L/D = 0.19$ , the design approach is illustrated in Fig. 8-6. Based on the constraints on the maximum nacelle diameter, the thickness of the supercritical airfoil shape is selected. The present example shows the NASA SC(2)-0710 airfoil [7] with 10% thickness. The shroud geometry is defined as part of the fan stage design and the nacelle boattail radial location is set by the required nozzle area at the cruise. In the first step, the aft part of the airfoil is modified to satisfy the constraints on fan case and boattail geometry. The modified geometry is shown in red in Fig. 8-6.

The second step is the modification of the inlet internal shape and the front part of the nacelle external geometry. The camber line geometry of the preliminary design must be aligned with the incoming stagnation point streamline to reduce the over-speed in the external flow, as discussed in Section 8.1. Reducing the inlet lip thickness is effective in further alleviating the over-speed at cruise. However, a smaller inlet lip thickness results in an increase in the local over-speed along the inlet at low-speed operating conditions, which enhances the rotor incidence distortion. In the candi-

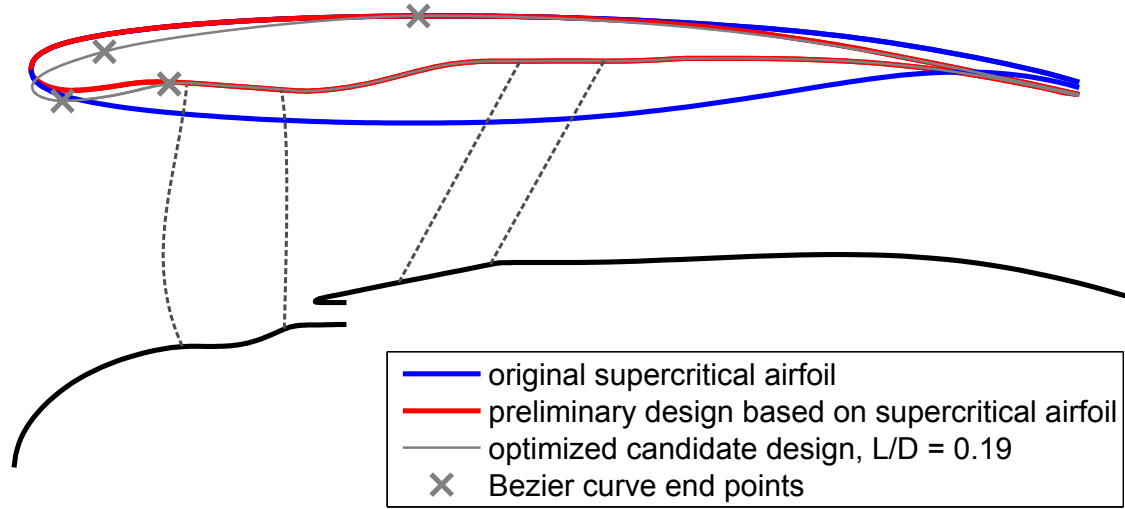


Figure 8-6: Example for top inlet and nacelle shape description based on the supercritical airfoil NASA SC(2)-0170 [7].

date short-inlet design presented in this thesis, the minimum inlet lip thickness was set by the requirement for fully attached inlet flow at the take-off level condition. Each design was evaluated using body force simulations at cruise, wing  $C_{L\max}$ , and take-off operating conditions and the inlet and nacelle surface pressure distributions were extracted along with the maximum external Mach number at cruise and the incidence distortion at the off-design conditions. Between 20 and 30 design iterations were required to obtain inlet and nacelle shapes with acceptable design and off-design performance ( $M_{max} \approx M_{max,base}$  at cruise, attached inlet flow and low incidence distortion at the off-design conditions) in the design of the candidate inlets with  $L/D = 0.25$  and  $L/D = 0.19$ . The optimized top inlet and nacelle shape for the  $L/D = 0.19$  design is presented in gray in Fig. 8-6.

### 8.3.2 Bottom Inlet and Nacelle Section

In contrast to the top part of the inlet, the bottom part requires a thicker inlet lip to mitigate flow separation and incidence distortion at off-design conditions. In short inlets, the shape of the inlet also plays an important role in reducing the region of high Mach number over the outer span at cruise and limit fan efficiency penalties.

An elliptical description of the bottom inlet leading edge geometry was implemented to determine the important parameters for limiting external flow acceleration at cruise and over-speed along the inlet internal surface at the wing  $C_{L\max}$  condition. The parametric description is depicted in Fig. 8-7 for an inlet with  $L/D = 0.25$ . The inlet and nacelle leading edge shape is split up into two sections on either side of the inlet highlight location. Each section is described by a super-ellipse, defined in Equation 5.1, with ellipse semi-diameters  $a$  and  $b$  and exponents  $m$  and  $n$ . The orientation of the profile camber line at the leading edge relative to the axial location is controlled by the angle  $\gamma$ . Based on this set of parameters, a parameter study was carried out using body force simulations. An example for the evaluation of the leading edge angle  $\gamma$  is presented in Table 8.2.

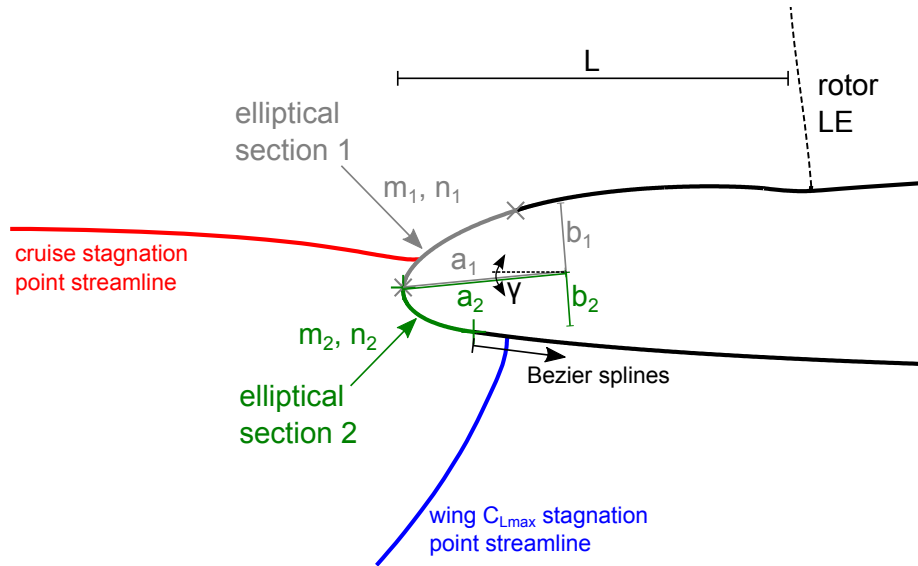


Figure 8-7: Parametric description of bottom inlet leading edge.

Table 8.2: Evaluation of inlet leading edge orientation angle  $\gamma$  as part of a parameter study for the bottom inlet shape.

Evaluation	Factors				Observation	
	$\gamma$	$a/L$	$a/b$	$m = n$	cruise, $M_{max}$	wing $C_{L\max}$ , $M_{x,max,FF}$
1	4°	0.45	2.85	2	1.075	0.945
2	6°	0.45	2.85	2	1.122	0.933
3	8°	0.45	2.85	2	1.179	0.908
4	10°	0.45	2.85	2	1.225	0.868

By increasing  $\gamma$ , the camber line is more aligned with the inflow at the low-speed, high angle-of-attack conditions and the highlight area is increased. As a result, the over-speed along the inlet internal surface is reduced and the maximum axial Mach number at the fan face,  $M_{x,max,FF}$ , decreases. The downside of increasing  $\gamma$  is the increase in the maximum Mach number on the nacelle external surface,  $M_{max}$ , at cruise. Based on the outcomes of the parameter study, a candidate short-inlet design with  $L/D = 0.25$  was generated, which provides for separation-free inlet flow at the wing  $C_{Lmax}$  condition and exhibits a small region of supersonic flow on the lower nacelle external surface. The key design concept was to define an inlet leading edge shape which limits the swing in the stagnation point between cruise and wing  $C_{Lmax}$ . This design is presented in the next chapter.

## 8.4 Spinner Design

The spinner shape can play an important role in the propulsor performance at both design and off-design operating conditions. In general, compared to a long-inlet design, shortening the inlet requires some increase in the axial spinner length to reduce the incidence distortion near the hub. In short inlets, spinner designs extending forward of the inlet highlight plane enable performance benefits at cruise, where the mass flow ratio is below one. The trades in design and off-design performance due to an increase in the spinner length are quantified next.

For three different spinner designs, the Mach number distributions at cruise and the wing  $C_{Lmax}$  condition, computed with body force simulations, are presented in Fig. 8-8. A short-inlet propulsor with  $L/D = 0.2$  is shown at the top with a conventional spinner, labeled the baseline spinner in the following analysis. Compared to the long-inlet baseline propulsor, the spinner length  $L_{sp}$  (defined as the axial length between the spinner leading edge and the fan face location) is increased by 27% to provide for an increased flow straightening near the hub. A configuration featuring the same inlet, but with an extended spinner, is presented in the center plots. Compared to the baseline spinner, the axial spinner length was increased by a factor of three.

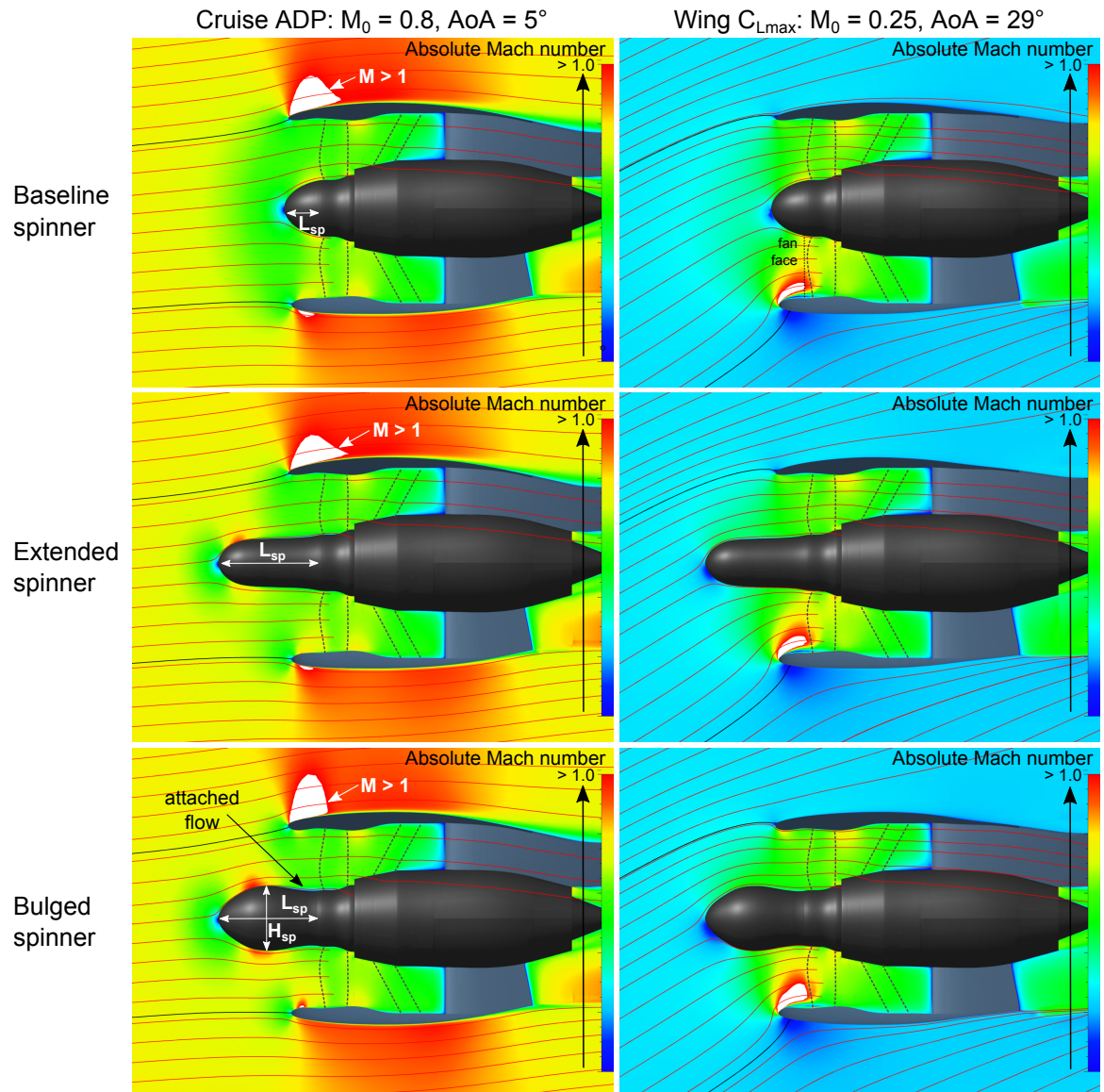


Figure 8-8: Axial Mach number and streamline distributions based on body force simulations for  $L/D = 0.2$  inlet with baseline spinner (top), extended spinner (center), and bulged spinner (bottom) designs at cruise (left) and wing  $C_{L\text{max}}$  (right).

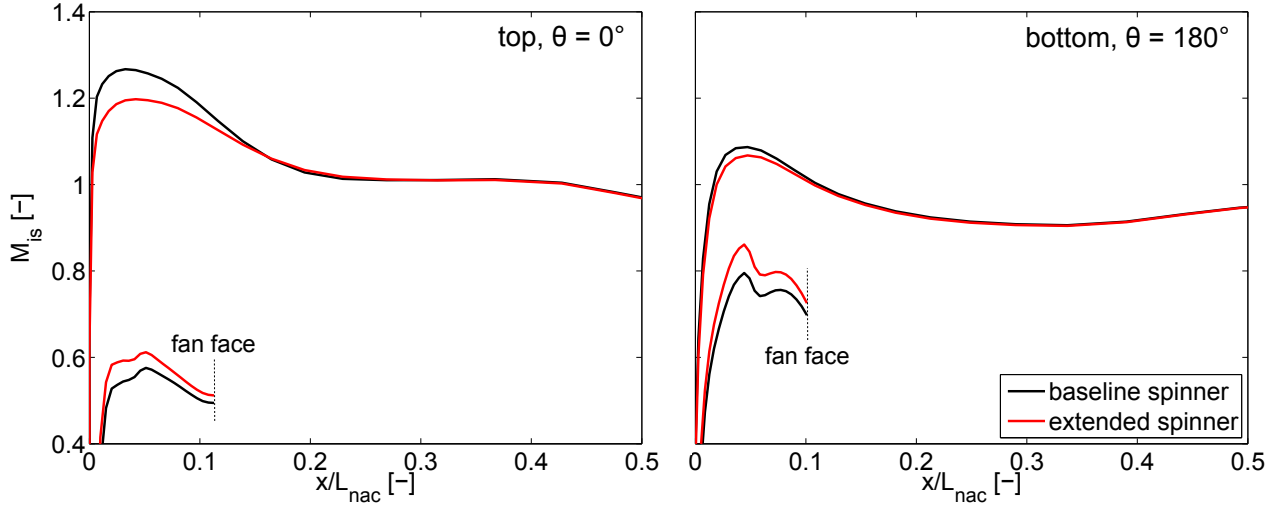


Figure 8-9: Isentropic Mach number along nacelle external and inlet surfaces at top (left) and bottom (right) for  $L/D = 0.2$  nacelle design with baseline and extended spinner shapes at cruise.

The impact of lengthening the spinner on the nacelle aerodynamic performance at cruise is illustrated in Fig. 8-9. Here, the isentropic Mach number is plotted along the inlet internal and nacelle external surfaces at the top and bottom of the nacelle, respectively. Extending the spinner results in an outward shift of the stagnation point, which is accompanied by a reduction in the acceleration on the nacelle external surface (and an increase in the acceleration along the inlet internal surface). In the present example, the maximum Mach number at the shock is reduced by  $\Delta M_{max} = 0.1$  at the top. While the reduction in the external Mach number yields wave drag benefits, the enhanced flow acceleration along the inlet leads to a local increase in the Mach number near the shroud, which adversely affects the fan performance.

At the wing  $C_{Lmax}$  operating condition, where the mass flow ratio is larger than one and the stagnation point is located on the outer nacelle surface, extending the spinner length can also lead to fan efficiency penalties. At the bottom of the nacelle, the stagnation point is moved downstream on the outer nacelle surface. As a result, the region of high Mach number grows and the maximum axial Mach number at the fan face is increased by  $\Delta M_{x,max} = 0.05$ , as demonstrated in the left-hand plot in Fig. 8-10, where the axial Mach number is plotted along the span at the fan face location

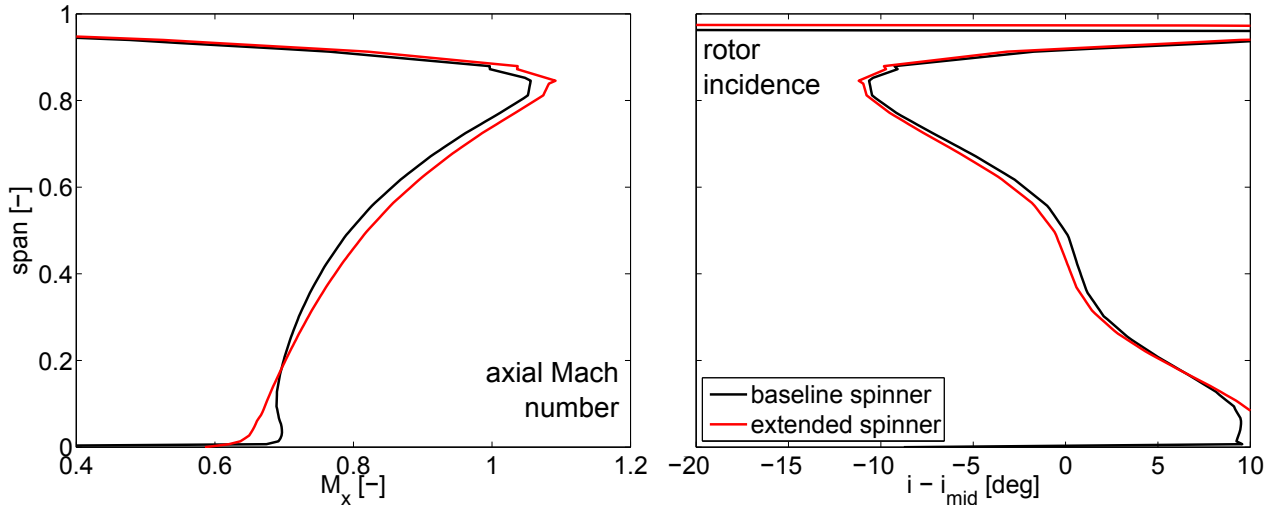


Figure 8-10: Spanwise profiles of axial Mach number (left) and rotor incidence relative to mid-span incidence (right) for  $L/D = 0.2$  nacelle with baseline and extended spinner shapes at wing  $C_{L\max}$ .

marked on the top right in Fig. 8-8. The increase in the axial Mach number results in an additional reduction of the minimum rotor incidence of  $\Delta i_{min} = 1^\circ$ , as shown in the right-hand plot in Fig. 8-10, and the increased incidence distortion leads to a reduction in fan efficiency. Similar trends were observed at other low-speed operating conditions such as take-off rotation.

The third spinner design shown in the bottom plots in Fig. 8-8 was motivated by an experimental study presented by Larkin and Schweiger [26]. By increasing the spinner thickness upstream of the inlet highlight plane, the stagnation point on the inlet is shifted even further outward, enabling additional reductions in the external flow acceleration. Axisymmetric simulations in MTFLOW were carried out to determine a maximum spinner thickness  $H_{sp}$  and a spinner shape with fully attached flow between the maximum thickness location and the fan face. While advantages in the nacelle performance are possible, the reduction in the flow area through the inlet results in increased Mach numbers at the fan face and fan performance penalties at the critical operating conditions relative to the baseline spinner configuration.

In summary, increasing the spinner axial length reduces the maximum Mach numbers in the external flow and reduces incidence distortion near the hub but increases

incidence distortion over the outer span. In addition, extended spinner shapes increase the propulsor weight and reduce the inlet pressure recovery due to increased viscous losses. In short-inlet designs with  $L/D > 0.2$ , it was found that the maximum Mach numbers at cruise could be limited to the values achieved by the long-inlet baseline propulsor by shaping the outer nacelle surface. The more important challenge was to mitigate rotor incidence distortion and fan efficiency penalties, both at design and off-design conditions. Thus, the two short-inlet propulsors presented in Chapters 9 and 10 feature a conventional spinner design.

## 8.5 Re-Cambered Rotor Blade Design

Due to the increased fan-inlet coupling in short inlets, the rotor interacts with a region of high Mach number flow over the outer span at the bottom inlet. Both at design and off-design, the rotor incidence is reduced near the tip over the lower half of the circumference, as shown in the center and on the right in Fig. 8-11 for the candidate short-inlet designs with  $L/D = 0.25$  and  $L/D = 0.19$ , respectively. In the regions of low incidence, the rotor locally operates close to choke and the losses in the rotor are increased compared to the long-inlet baseline propulsor. The fan performance penalties caused by the increased interaction between rotor and non-uniform inlet flow are further discussed and quantified in Chapters 9 and 10. The focus of this section is on the rotor blade design.

The baseline fan stage was designed for a conventional inlet, which mitigates the inflow non-uniformity and provides for low levels of incidence distortion at the fan face, even at operating conditions with high angles-of-attack. To alleviate the increase in the rotor losses due to the interaction between the rotor and the high Mach number region in short inlets, a shift in the peak efficiency operating point of the rotor to lower incidences is required, which can be achieved for example by modifying the blade camber distribution.

To demonstrate the rotor loss increase over the outer span in short inlets, results for the baseline rotor design are presented first. The rotor loss coefficient  $\omega$  is depicted

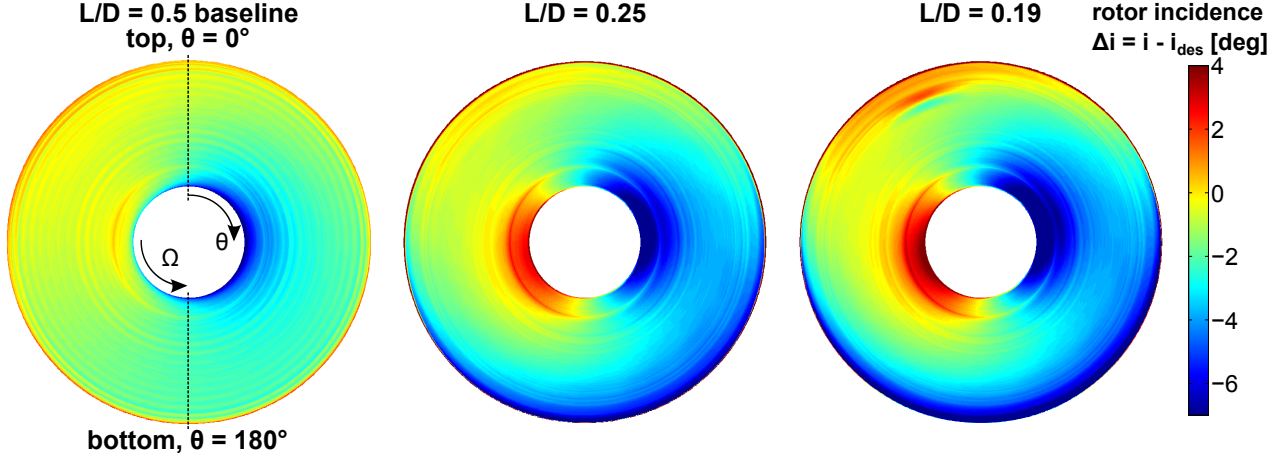


Figure 8-11: Increase in the rotor incidence distortion for the candidate short-inlet designs with  $L/D = 0.25$  (center) and  $L/D = 0.19$  (right) at cruise compared to the long-inlet baseline propulsor (left). The results are for the baseline rotor design and were computed using URANS simulations.

at cruise and wing  $C_{L\max}$  in the left- and right-hand plots in Fig. 8-12, respectively. The black and gray lines represent the dependence of the loss coefficient on incidence at 50 %, 75 %, and 95 % span for uniform inflow. Steady, single-passage RANS simulations were used to determine the pitchwise-averaged flow field over a range of operating points from choke to stall. The reduction of the pitchwise-averaged relative stagnation pressure,  $p_{t,rel}$ , through the rotor was determined for multiple spanwise locations, enabling the calculation of the loss coefficient from  $\omega = \frac{p_{t,rel,12} - p_{t,rel,13}}{p_{t,rel,12} - p_{t,12}}$ , where stations 12 and 13 denote the fan face and rotor trailing edge locations, respectively. The incidence results are shown in Fig. 8-12 relative to the design point value determined from the steady, single-passage RANS simulations.

Full-domain URANS simulations are used to determine the impact of non-uniform inflow on the loss generation through the rotor blade row. The evaluation of the rotor losses in the region of reduced incidence over the outer span at the bottom of the fan face (at  $\theta = 180^\circ$ ) was of particular interest. However, the determination of the local rotor performance from an unsteady simulation is a challenging post-processing task. A time-averaged solution is required in the absolute frame of reference and the rotating blades must be eliminated from the final time-averaged solution, as discussed for example by Fidalgo et al. [35], who used a procedure based on gate functions

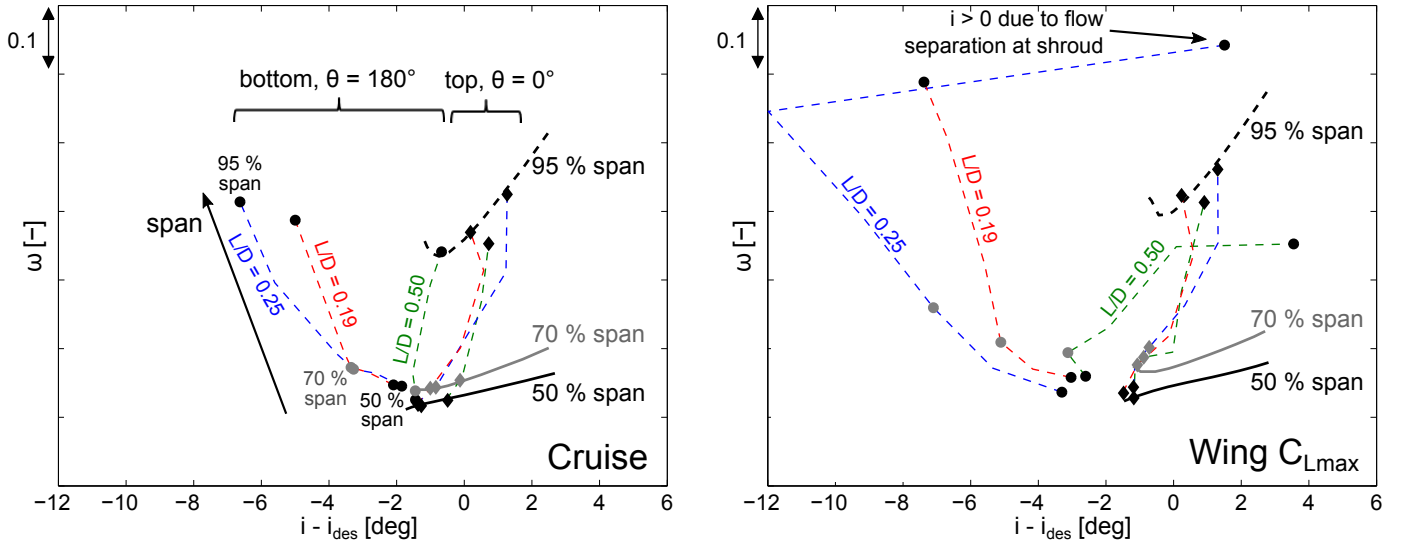


Figure 8-12: Rotor stagnation pressure loss at cruise (left) and wing  $C_{L\max}$  (right) operating conditions.

developed by Adamczyk [55] to compute time-averaged particle paths through the rotor. A simplified approach is used in the current analysis to limit the computational cost associated with the post-processing of the time-dependent flow fields.

The focus of the current analysis is on the local performance of the rotor at the top ( $\theta = 0^\circ$ ) and bottom ( $\theta = 180^\circ$ ) of the fan face, where the time-averaged absolute flow angle is close to zero along the span, as shown in Fig. 8-13. A time-averaged flow solution in the bladed domains was not computed. Instead, along the span at  $\theta = 0^\circ$  and  $\theta = 180^\circ$ , the circumferential shift of a particle is approximated as the absolute flow angle at the rotor trailing edge.

In Fig. 8-12, the local loss coefficient is computed from the time-averaged flow solution at  $\theta = 180^\circ$  for several spanwise locations between mid-span and the blade tip. The results are shown by the dashed green ( $L/D = 0.5$ ), red ( $L/D = 0.25$ ), and blue ( $L/D = 0.19$ ) lines. Towards the blade tip, the incidence is reduced and the rotor losses increase. For reference, the local rotor losses are computed at the top of the fan face ( $\theta = 0^\circ$ ) for the same spanwise locations. In Fig. 8-12, the left legs of the dashed lines correspond to the circumferential location with  $\theta = 180^\circ$ , while the right legs correspond to the circumferential location with  $\theta = 0^\circ$ . At the top of the fan face, the

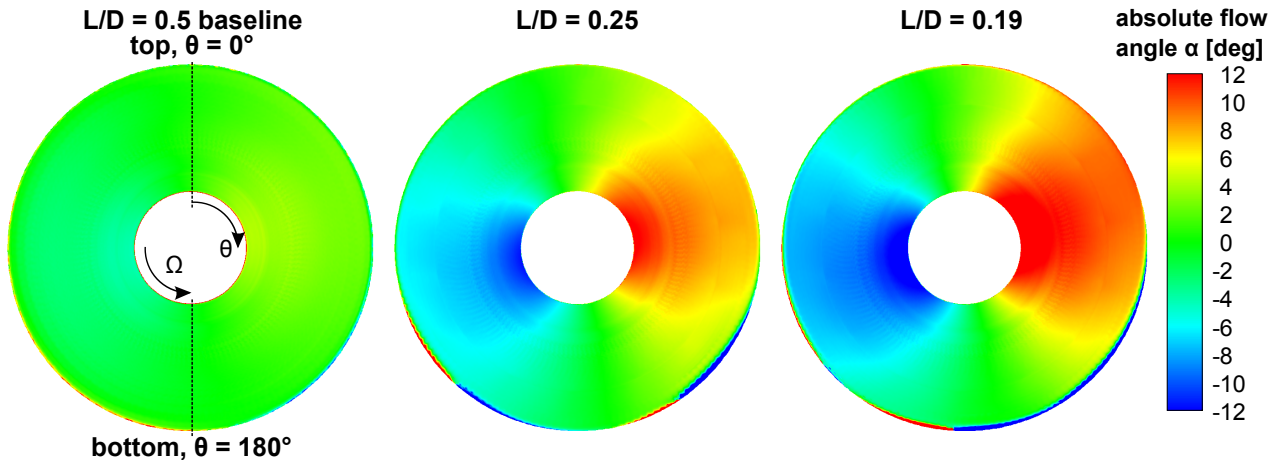


Figure 8-13: Absolute flow angle distributions at the fan face for the candidate short-inlet designs with  $L/D = 0.25$  (center) and  $L/D = 0.19$  (right) compared to the long-inlet baseline propulsor (left) at the wing  $C_{L\max}$  operating condition.

incidence increases towards the tip due to the pylon upstream influence (as described in Section 6.2). At 95 % span and  $\theta = 180^\circ$ , the local loss coefficient increases by 15 % for the  $L/D = 0.25$  design relative to the long-inlet baseline propulsor. For the  $L/D = 0.19$  design, the loss coefficient increases by 24 %.

At the wing  $C_{L\max}$  operating condition, the trends are similar, but the increase in the Mach number over the outer span at the fan face for the short-inlet designs relative to the baseline is larger than at cruise. Consequently, the rotor incidence is further reduced and the rotor losses increase even more than at cruise. The loss coefficient at 95 % span increases by 68 % for the  $L/D = 0.25$  design and by 82 % for the  $L/D = 0.19$  design. The positive incidence values at 95 % span in the  $L/D = 0.19$  design are due to a region of reversed flow at the shroud, as shown in Fig. 10-5.

At both the cruise and the wing  $C_{L\max}$  operating conditions, a reduction in the rotor losses at  $\theta = 180^\circ$  was expected by shifting the loss buckets to lower incidences. However, if the loss bucket is shifted to lower incidences, the reduction in the loss coefficient at  $\theta = 180^\circ$  is accompanied by an increase at  $\theta = 0^\circ$ . This trade-off is discussed below after the description of the modifications to the rotor blade design required to shift the loss buckets.

Shifting the peak efficiency operating point to lower incidences requires the reduction of the local camber line angle  $\kappa$  at the leading edge, i.e. opening up the blade.

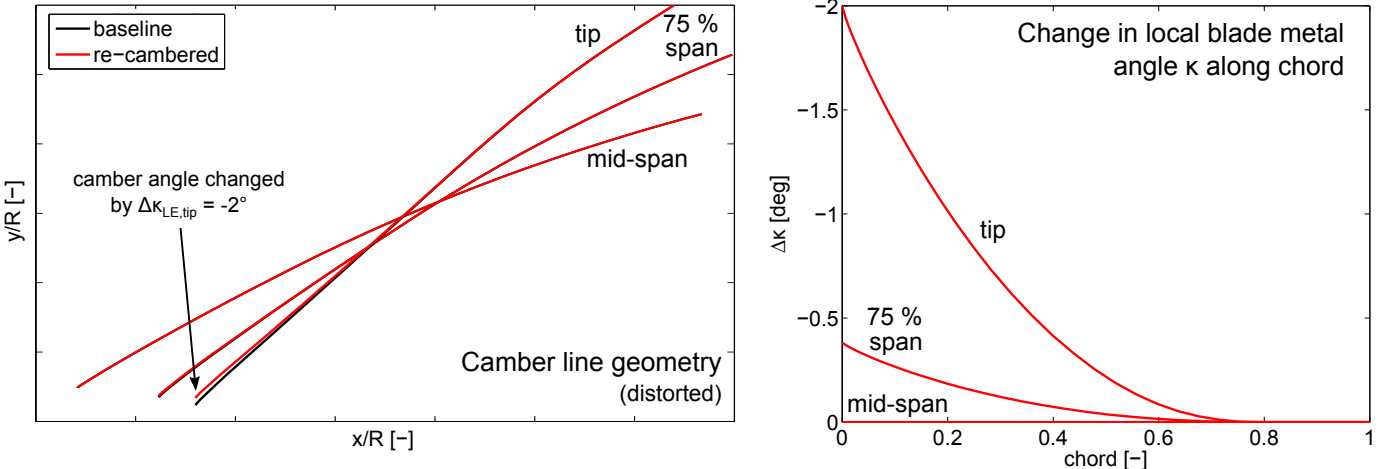


Figure 8-14: Camber line distribution for baseline and re-cambered blade (left) and change in local blade metal angle  $\kappa$  along the chord (right) for  $\Delta\kappa_{LE,tip} = -2^\circ$ .

The largest reduction in  $\kappa$  is required in the region of minimum incidence near the tip. To re-camber the blade, the blade inlet angle at the blade tip,  $\kappa_{LE,tip}$ , was changed by  $\Delta\kappa_{LE,tip}$ . The blade design was modified over the outer 50 % span only. The blade outlet angle,  $\kappa_{TE}$ , was kept constant to maintain the rotor work output.

The re-design approach is illustrated in Fig. 8-14. The camber line geometry is shown at mid-span, 75 % span, and at the tip in the left-hand plot, and the change in the local blade metal angle along the chord is depicted in the right-hand plot. A parabolic distribution was assumed at a given spanwise location between the leading edge and 80 % chord. Downstream of the 80 % chord location, the camber line distribution was not changed. Similarly, a parabolic distribution in  $\Delta\kappa$  was assumed along the leading edge between the rotor tip and mid-span. The axial chord length and the rotor thickness distribution were not altered in the current approach.

The rotor performance of the re-cambered blade designs was tested using steady, single-passage RANS simulations with uniform inflow. The fan efficiency is presented for two rotor re-designs in Fig. 8-15. Opening up the blade increases the choke mass flow by approximately 0.3 % per  $2^\circ$  reduction in the blade inlet angle at the tip and, as expected, the peak efficiency operating point is shifted to higher corrected flows.

The performance of the re-cambered rotor designs and the dependence of the change in fan efficiency on  $\Delta\kappa_{LE,tip}$  under non-uniform inflow conditions was assessed

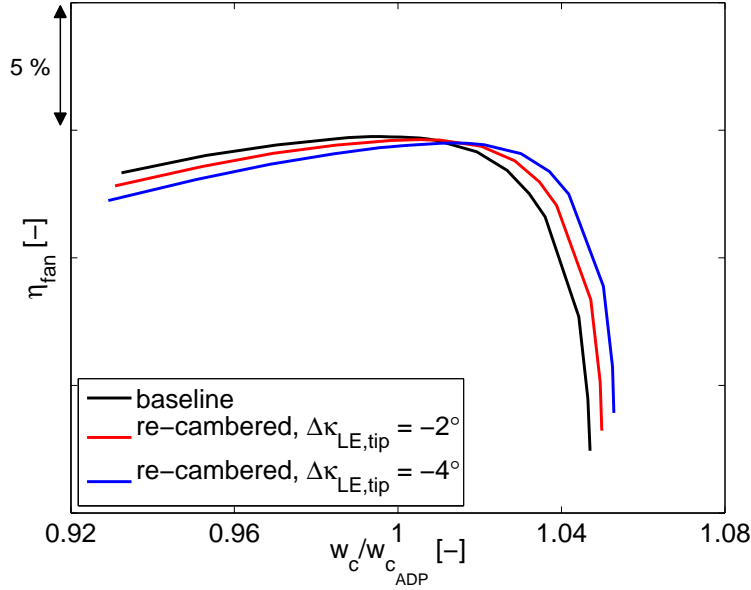


Figure 8-15: Fan efficiency results from steady, single-passage RANS simulations with uniform inflow at cruise with shift of peak efficiency operating point to higher corrected flows for re-cambered rotor designs relative to baseline rotor.

using full-annulus URANS simulations. The change in the fan efficiency relative to the baseline rotor is shown in Fig. 8-16 for rotor re-designs with  $\Delta\kappa_{LE,tip} = -1^\circ$ ,  $-2^\circ$ , and  $-4^\circ$  in the candidate short-inlet propulsor with  $L/D = 0.25$  at the cruise and wing  $C_{L\max}$  operating conditions. As hypothesized, the rotor performance improves for small values of  $\Delta\kappa_{LE,tip}$ . If the blade inlet angle at the tip is changed by more than approximately  $\Delta\kappa_{LE,tip} = -2^\circ$ , the reduction of the rotor losses over the outer span in the bottom half of the rotor revolution is outweighed by the increase in the rotor losses over the top half of the rotor revolution. As a result, the benefits of the rotor re-design decrease. The URANS simulations suggest a benefit of approximately  $\Delta\eta_{fan} = 0.15\%$  at cruise. At the wing  $C_{L\max}$  operating condition, the suggested benefits are higher due to larger increase in the rotor losses at the bottom of the inlet, as shown on the right in Fig. 8-12.

In summary, shortening the inlet and nacelle can lead to changes in the design requirements for the rotor. A rotor designed for a long inlet does not necessarily provide the optimum performance in a short-inlet propulsor and performance improvements can be enabled by re-designing the rotor.

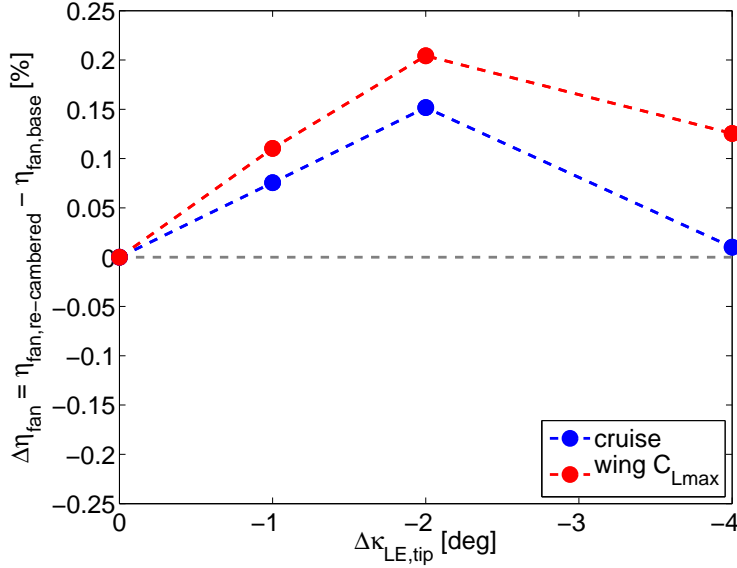


Figure 8-16: Change in fan efficiency for re-cambered rotor design relative to baseline rotor in the  $L/D = 0.25$  candidate short-inlet design from steady, full-domain RANS simulations at the cruise and wing  $C_{Lmax}$  operating conditions.

## 8.6 Mitigating the Pylon Upstream Influence

The pylon potential field disturbance significantly affects the aerodynamic performance of the fan stage performance and can result in forced excitation of the fan rotor and increased noise generation [77]. In aircraft engines, part of the challenge posed by the pylon upstream influence is due to the requirement for small axial spacings between rotor, stator, and pylon/bifurcation to limit engine length and weight. The dissection of the incidence distortion mechanisms in Section 6.2 suggests that reductions in the incidence distortion could be achieved by mitigating the pylon upstream influence.

The instantaneous distribution of the static pressure near the blade tip based on a full-annulus URANS simulation is presented in Fig. 8-17 for the candidate short-inlet propulsor with  $L/D = 0.19$  at the cruise operating condition. Upstream of the pylon near  $\theta = 0^\circ$ , the increased static pressure results in an increase in rotor loading. Due to its reduced thickness, the bifurcation upstream influence is lower. In addition, the axial Mach number at the fan face is locally increased near  $\theta = 180^\circ$ , and the rotor operates close to choke, leading unloaded blades.

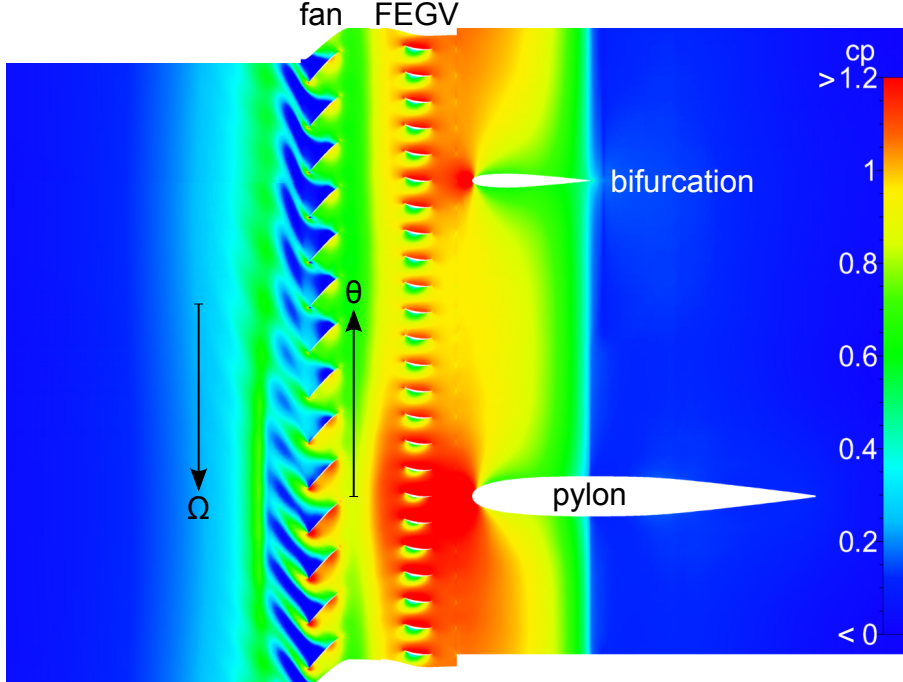


Figure 8-17: Instantaneous static pressure coefficient distribution at 95 % span for the  $L/D = 0.19$  candidate short-inlet design at cruise extracted from a URANS simulation.

Aside from affecting the rotor performance, the pylon upstream influence also changes the incidence on the stator. Since the stator design in the baseline fan stage features flat loss buckets, the stator losses are not significantly increased by the interaction with the pylon. Nevertheless, small performance benefits are likely possible by varying the stagger distribution to provide for design incidence around the entire circumference.

Depending on the design of the fan stage, the loss generation in the rotor and stator blade rows due to the presence of a pylon can be substantial, as demonstrated for example by Unno et al. [32] or Ooba et al. [83]. An example for the optimization of the stator stagger circumferential distribution in the presence of two bifurcations is presented by Milli and Bron [78]. Wadia et al. [93] investigated the potential of non-uniform stagger distributions to reduce the influence of the strut and splitter potential field in a military engine but concluded that a swept and leaned outlet guide vane design with a uniform stagger angle distribution offered the best balance in design and off-design engine performance.

While the interaction with the pylon and bifurcation does not significantly increase the losses in the fan exit guide vanes of the advanced fan stage used in this work, the rotor performance is affected and can be improved by circumferentially non-uniform stator designs. Rubbert et al. [94] presented a design concept for offsetting the pylon upstream influence through tailoring the exit guide vanes at each circumferential location. The primary condition for completely shielding the rotor from the non-uniform pressure field upstream of the pylon is that a uniform mass flux distribution is maintained through the stator. The stator blade trailing edge angle was identified as the main parameter governing the mass flux distribution and a uniform distribution could be achieved for a circumferentially varying trailing edge angle. Several theoretical models and methods with different degrees of sophistication were introduced for the design of the individual stator blades. The approach leads to different shapes for each stator blade, which increases manufacturing costs compared to a stator design with identical blades but a non-uniform stagger angle distribution.

The body force method provides a framework for the design of non-axisymmetric stator blades, since the local blade metal angle is a direct input parameter in the definition of the body force distributions. The impact of circumferentially varying the stagger and/or camber distribution can be assessed by specifying a  $\theta$ -dependent function for the blade metal angle  $\kappa$ . Using this approach to design a non-axisymmetric stator geometry was beyond the scope of this work. Instead, a best-case scenario is considered by assuming a stator design which completely offsets the pylon and bifurcation upstream influence. Without actually defining such a design, the impact of eliminating the back pressure distortion on the rotor performance can be quantified by removing the pylon and bifurcation from the computational model. The same approach was used in quantifying the distortion transfer mechanisms discussed in Section 6.2. The rotor and system level performance benefits of eliminating the pylon upstream influence are presented in the next Chapter for the candidate short-inlet design with  $L/D = 0.25$ .

# Chapter 9

## Candidate Short-Inlet Design -

**L/D = 0.25**

Using the design strategy and the inlet and nacelle design framework outlined in the previous chapters, a candidate short-inlet design with  $L/D = 0.25$  was defined. The candidate design meets the goal of achieving equal or better engine propulsive efficiency compared to the baseline long-inlet propulsor at cruise while the fan efficiency penalty is limited to a maximum of 2 % at the off-design conditions. Body force simulations were used in the design optimization of the inlet and nacelle surface geometries and URANS simulations were carried out to verify the performance of the candidate design. This chapter presents the outcomes of the URANS assessment at design and off-design operating conditions. The focus is on the change in propulsor and component performance relative to the baseline configuration and the characterization of the aerodynamic mechanisms responsible for the performance changes.

### 9.1 Overview of Design Characteristics and Performance

The top and bottom inlet and nacelle profiles of the candidate short-inlet design with  $L/D = 0.25$  and the baseline case with  $L/D = 0.5$  are depicted in Fig. 9-1 and an

overview of the design parameters is presented in Table 9.1. The maximum nacelle diameter is reduced in the short inlet relative to the baseline design to mitigate the flow acceleration along the aft part of the nacelle surface. The highlight area is reduced to limit the over-speed along the nacelle external surface at cruise. The consequence of reducing the highlight area is an increase in the mass flow ratio at all operating conditions. Due to the increase in *MFR*, the flow acceleration along the bottom inlet lip is enhanced at the high angle-of-attack conditions and the rotor incidence distortion is considerably increased, which is quantified in the following sections. The spinner length is increased by 27 % to alleviate the inlet flow distortion near the hub.

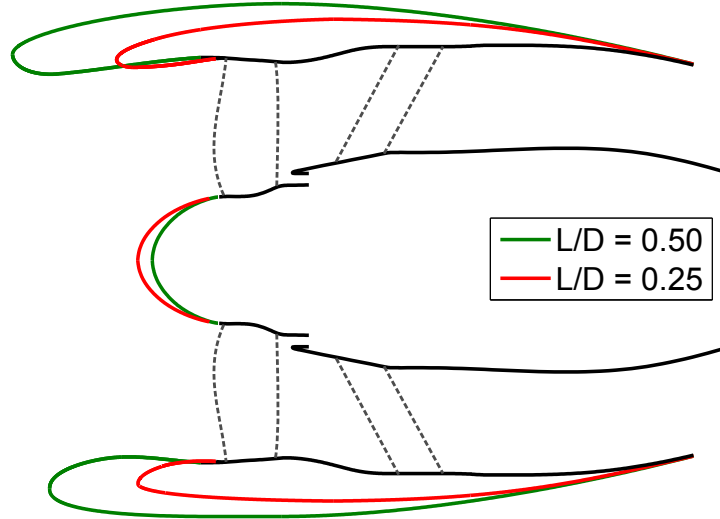


Figure 9-1: Top and bottom inlet and nacelle sections for the baseline configuration with  $L/D = 0.5$  and the  $L/D = 0.25$  candidate short-inlet design.

The design and off-design performance of the candidate short-inlet propulsor is summarized in Table 9.2. The cross-wind condition was not included in the assessment of the  $L/D = 0.25$  design but is addressed in the next Chapter for the second candidate short-inlet design with  $L/D = 0.19$ . The impact of eliminating the pylon upstream influence on the propulsor performance was assessed at cruise only due to the large computation times associated with full-annulus URANS simulations (approximately one week per operating condition).

Table 9.1: Inlet and nacelle design parameters for the baseline and be  $L/D = 0.25$  candidate short-inlet designs.

	$L/D = 0.5$ baseline	$L/D = 0.25$
Inlet droop	$5^\circ$	$3^\circ$
Max. diameter to fan diameter $D_{max}/D$	1.27	1.19
Contraction ratio $A_{HL}/A_{throat}$	1.26	1.17
Mean highlight to max. diameter ratio $D_{HL}/D_{max}$	0.85	0.88
Spinner length $x/D$	0.15	0.19
Inlet mass flow ratio $MFR = A_0/A_{HL}$		
- cruise	0.74	0.79
- wing $C_{Lmax}$	1.62	1.76
- T/O rotation	1.59	1.73

At cruise, the candidate inlet and nacelle design comes close to meeting the baseline propulsor performance, even if the back pressure distortion is not reduced by a tailored non-axisymmetric FEGV design and the rotor geometry is not modified. Compared to the baseline case, the engine propulsive efficiency is reduced by 0.14 % for the candidate short-inlet configuration and the net thrust minus nacelle drag is 0.5 % lower. The nacelle drag is reduced by 16.0 % due to the reduction in the wetted nacelle area. However, the benefits from the nacelle drag reduction are more than offset by a fan efficiency penalty of  $-1.11\%$  due to the increase in the rotor incidence distortion. The reduction in nacelle weight reduces the thrust requirement for the aircraft and the propulsor size could possibly be reduced, resulting in additional weight benefits and further reducing the required power input to the fan. Therefore, the candidate short-inlet propulsor is suggested to possibly offer performance benefits on the aircraft system level over a configuration powered by the long-inlet baseline propulsor.

At the off-design conditions, the fan performance is reduced compared to the baseline case, since the short inlet does not mitigate the inflow non-uniformities to the extent provided by the long inlet. At the wing  $C_{Lmax}$  condition, the inflow non-uniformity is largest and consequently, the fan efficiency is reduced the most. The circumferential variation of the stagnation pressure is defined here as the differ-

Table 9.2: Performance overview of the  $L/D = 0.25$  candidate short-inlet propulsor relative to the  $L/D = 0.5$  baseline.

Condition/Metric		baseline rotor with pylon	baseline rotor without pylon	re-cambered rotor without pylon
<b>Cruise ADP</b>				
- propulsive efficiency	$\Delta\eta_{prop}$	<b>-0.14 %</b>	<b>+0.12 %</b>	<b>+0.25 %</b>
- nacelle drag	$D_{nac}$	-16.0 %	-16.2 %	-16.2 %
- fan efficiency	$\Delta\eta_{fan}$	-1.11 %	-0.86 %	-0.71 %
<b>Wing C<sub>Lmax</sub></b>				
- fan efficiency	$\Delta\eta_{fan}$	-2.02 %	not computed	-1.53 %
- core inlet $p_t$ -variation at mid-span	$\Delta p_{t,var,mid}$	+7.5 %		+7.8 %
- blade tip variation of lift coefficient	$\Delta c_{l,var,tip}$	+12.8 %		+10.8 %
<b>T/O rotation</b>				
- fan efficiency	$\Delta\eta_{fan}$	-1.71 %	not computed	-1.28 %
<b>T/O level</b>				
- fan efficiency	$\Delta\eta_{fan}$	-1.11 %	not computed	-0.67 %

ence between the maximum and minimum stagnation pressure values relative to the circumferentially-averaged result,

$$p_{t,var} = \left( \frac{p_t - p_t^M}{p_t^M} \right)_{max} - \left( \frac{p_t - p_t^M}{p_t^M} \right)_{min}, \quad (9.1)$$

where  $p_t^M$  denotes the circumferentially-averaged, mass-weighted stagnation pressure at a given spanwise location

Similarly, at a given spanwise location, the variation of the lift coefficient is defined as the difference between the maximum and minimum loading relative to the time-averaged result,

$$c_{l,var} = \left( \frac{c_l - \bar{c}_l}{\bar{c}_l} \right)_{max} - \left( \frac{c_l - \bar{c}_l}{\bar{c}_l} \right)_{min}, \quad (9.2)$$

where  $\bar{c}_l$  is lift coefficient, time-averaged over a full rotor revolution. The circumferential distributions of the core inlet stagnation pressure and the lift coefficient are presented in Section 9.4.

For a non-axisymmetric FEGV design which completely shields the rotor from the pylon and bifurcation upstream influence, the fan efficiency of the candidate propulsor can be increased by 0.25 % and the propulsive efficiency increases by 0.26 %, which

results in a 0.12 % propulsive efficiency advantage over the long-inlet baseline without taking into account any aircraft system level benefits. It must be noted that this comparison is inconsistent since a tailored FEGV design would also improve the baseline propulsor performance. However, the removal of the pylon and bifurcation highlights the benefits enabled by an advanced FEGV design compared to axisymmetric geometries. Finally, an additional fan efficiency benefit of 0.15 % is achieved by re-cambering the rotor, as outlined in Section 8.5. The fan performance improvement translates to a propulsive efficiency increase of 0.13 % relative to the baseline rotor performance in the candidate short-inlet. In addition, the combination of re-cambering the blades and shielding the rotor from the pylon and bifurcation upstream influence alleviates the fan performance penalties at the off-design operating conditions.

## 9.2 Performance at Cruise

The absolute Mach number distributions for the baseline and the candidate short-inlet propulsor with the re-cambered rotor are depicted on the top left and top right in Fig. 9-2, respectively. Limiting the flow acceleration along the nacelle external surface was one of the main objectives in the short-inlet design strategy outlined in the previous chapter and the size of the region of supersonic flow along the front part of the upper surface was kept similar while the the maximum Mach number at the shock only increased by  $\Delta M_{max} = 0.02$ .

At the lower nacelle surface, the short-inlet design features a significantly reduced supersonic flow region. However, there is a local region of high flow acceleration just downstream of the inlet highlight location as indicated in the isentropic Mach number distribution along the lower nacelle external surface on the right in Fig. 9-3. This peak is a consequence of the round inlet lip shape required for attached inlet flow at the wing  $C_{Lmax}$  condition. A reduction in the local over-speed could be achieved by aligning the outer nacelle shape with the incoming stagnation point streamline. However, the cost of this design change would be an increased flow acceleration along the inlet internal surface at off-design conditions, followed by the separation of the

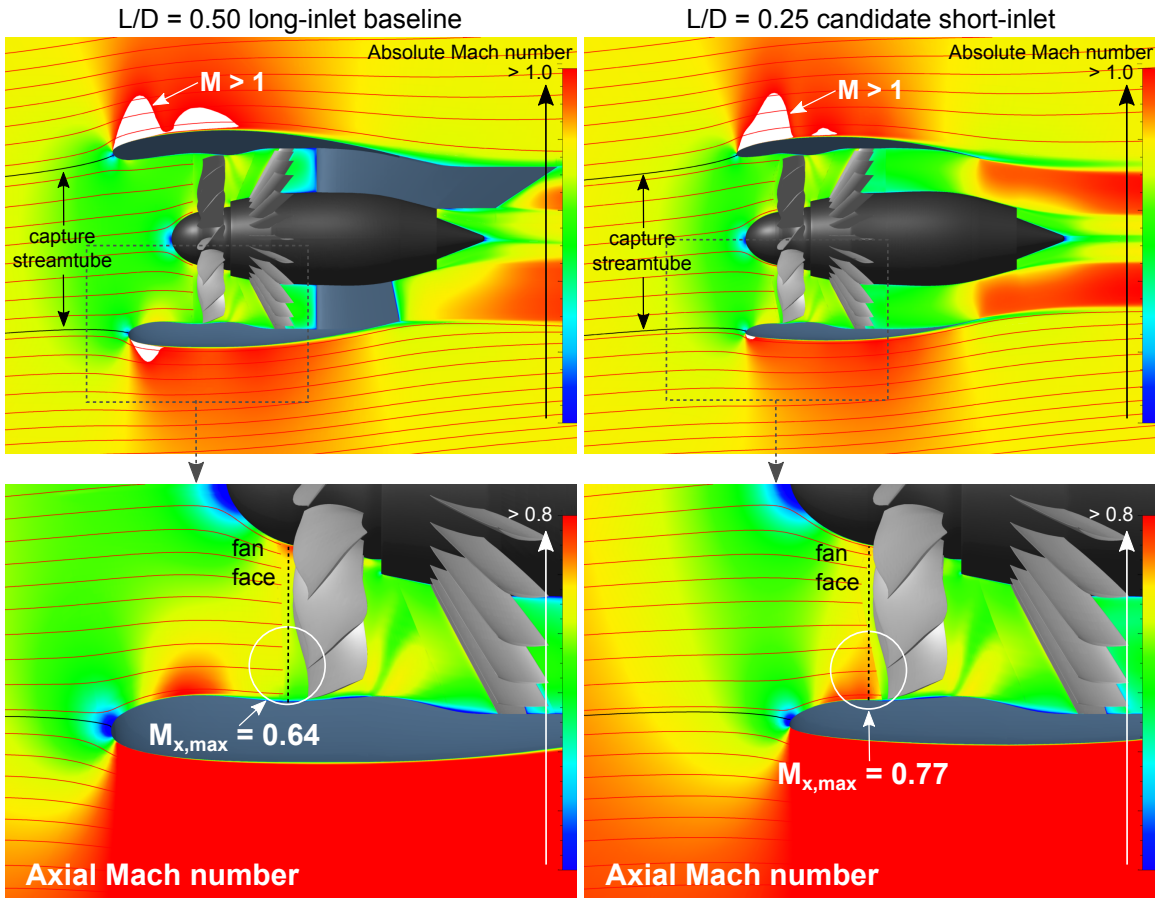


Figure 9-2: Mach number distribution (top) and axial Mach number distribution (bottom) for the baseline propulsor (left) and the candidate short-inlet design with  $L/D = 0.25$  (right) at cruise.

inlet flow and an increased incidence distortion at the fan face. As indicated in Fig. 9-3, the flow acceleration along the short-nacelle external surface is not considerably increased along the circumference. As a result, the pressure drag increases by only 1.4 % relative to the baseline nacelle. The nacelle viscous drag decreases by 23.0 % due to the reduction in surface area and the total drag is reduced by 16.2 %. The changes in the total drag and the drag components are summarized in Table 9.3.

Due to the reduction in surface area, the relative contribution of the viscous drag component to the nacelle total drag decreases in the short-inlet propulsor, as indicated in Table 9.4, and the relative importance of the pressure drag rises. In the light of the increased pressure drag contribution, mitigating the over-speed on the external nacelle surface is particularly important in short-nacelle configurations.

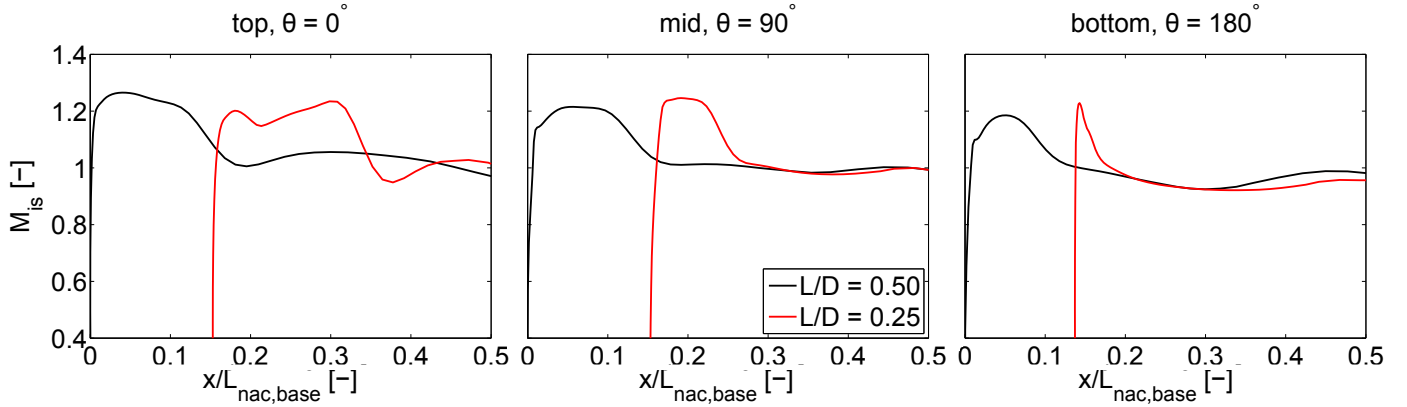


Figure 9-3: Isentropic Mach number along nacelle external surface at three circumferential locations for the baseline propulsor ( $L/D = 0.5$ ) and the candidate short-inlet configuration ( $L/D = 0.25$ ) at cruise.

Table 9.3: Relative change in nacelle drag for the  $L/D = 0.25$  design compared to the  $L/D = 0.5$  baseline.

Component		$L/D = 0.25$
nacelle total drag	$D_{nac}$	-16.2 %
nacelle viscous drag	$D_{nac,visc}$	-23.0 %
nacelle pressure drag	$D_{nac,p}$	+1.4 %

Table 9.4: Drag breakdown for the  $L/D = 0.25$  design compared to the  $L/D = 0.5$  baseline.

Component		$L/D = 0.50$	$L/D = 0.25$
viscous drag contribution	$D_{nac,visc}/D_{nac}$	0.72	0.66
pressure drag contribution	$D_{nac,p}/D_{nac}$	0.28	0.34

The ideal propulsive efficiency of an isolated ducted propulsor can be expressed in terms of the fan pressure ratio and the flight Mach number only [3]. For low-FPR propulsors at  $M_0 = 0.8$ , the ideal propulsive efficiency of the fan bypass stream is between 85 % and 90 %, as illustrated in Fig. 1-3. The actual propulsive efficiency is approximately 10 % lower due to the internal losses in the fan stream. The engine propulsive efficiency metric used in this work additionally accounts for the lost power due to the external nacelle drag. The breakdown of the losses relative to an isolated ducted propulsor with ideal propulsive efficiency into internal (rotor losses, stator

losses, bypass duct losses) and external (nacelle drag) losses is presented in Table 9.5. The results are given for the short-inlet configuration with the pylon and bifurcation to enable a consistent comparison of the change in the relative importance of the internal losses. The contribution from the external losses decreases by approximately 8% due to the reduction in the total nacelle drag and the increase in the rotor losses. In the candidate short-inlet propulsor, the fan efficiency decreases by 1.11 %, as shown in Table 9.2 and the reasons for this efficiency penalty are discussed next.

Table 9.5: Loss breakdown relative to an isolated ducted propulsor with ideal propulsive efficiency into internal and external losses for the  $L/D = 0.25$  design with pylon and bifurcation compared to the  $L/D = 0.5$  baseline.

Component	$L/D = 0.50$	$L/D = 0.25$
internal losses	54.4 %	62.3 %
external losses	45.6 %	37.7 %

The axial Mach number distributions in the inlet flow are presented for the baseline and short-inlet propulsors in the bottom left and right in Fig. 9-2, respectively. At the bottom of the short inlet, there is a region of increased axial Mach number over the outer span at the fan face. The maximum axial Mach number in this region is increased by  $\Delta M_{x,max} = 0.13$ . The spanwise distribution of the axial Mach number at the fan face location indicated in Fig. 9-2 is depicted in the left-hand plot in Fig. 9-4. The increase in the axial Mach number further reduces the rotor incidence by up to  $\Delta i = -5^\circ$  over the outer span, as shown in the right-hand plot in Fig. 9-4, resulting in the local rotor operating point to shift towards choke. The interaction of the rotor with the high Mach number region is one of the main reasons for the 1.11 % reduction in fan efficiency. In addition, the inlet provides reduced flow straightening and the flow is at a positive angle-of-attack throughout the inlet, leading to an increased incidence distortion between the hub and mid-span, as illustrated in Fig. 8-11.

As discussed in Section 7.4, limiting fan efficiency penalties is critical for achieving high propulsive efficiency. Some of the fan performance penalty can be recovered by shielding the rotor from the pylon upstream influence ( $\Delta \eta_{fan} = +0.25\%$ ) or by modifying the blade camber distribution and increasing the incidence on the blade over the outer span ( $\Delta \eta_{fan} = +0.15\%$ ).

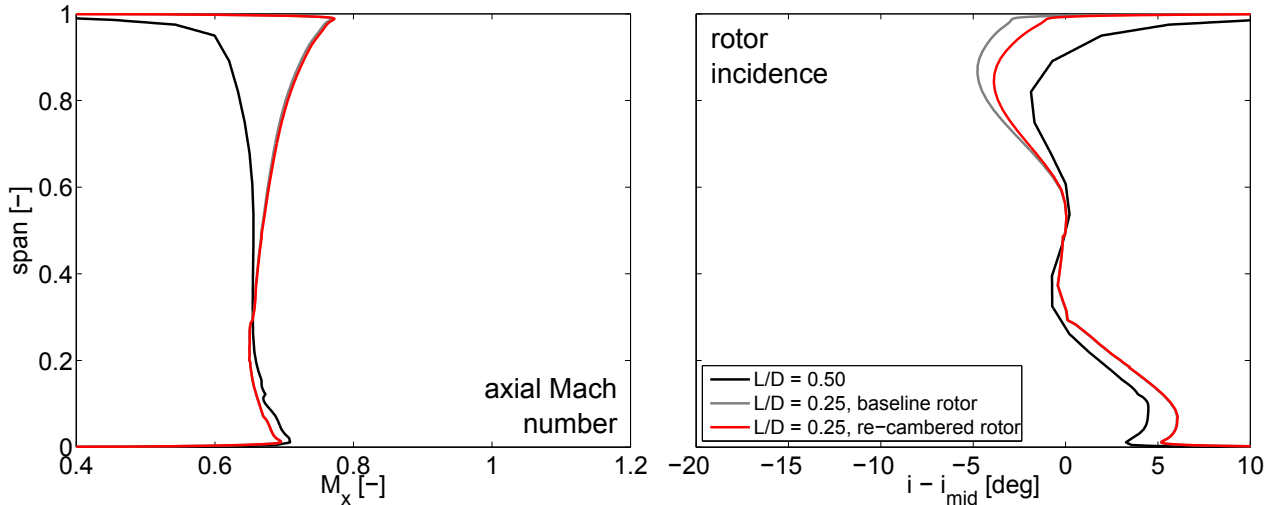


Figure 9-4: Time-averaged spanwise profiles of axial Mach number (left) and rotor incidence relative to mid-span incidence (right) at the fan face for the baseline propulsor ( $L/D = 0.5$ ) and the candidate short-inlet configuration ( $L/D = 0.25$ ) at cruise.

Increasing the inlet length is the most effective strategy to limit the fan efficiency penalties since the axial distance between the fan face and the location of the maximum streamwise Mach number is enhanced in a longer inlet and the flow non-uniformity due to the angle-of-attack inflow is reduced. Without changes in the rotor or FEGV design, increasing the inlet length from  $L/D = 0.19$  to  $L/D = 0.25$  resulted in a cruise fan efficiency benefit of more than 0.5 %. The performance assessment of the two short-inlet propulsors suggest the inlet length for improved propulsor performance relative to the baseline case is an  $L/D$  above 0.25 since the fan efficiency benefits from an additional increase in the inlet length would likely outweigh the penalties due to the increased nacelle viscous drag.

### 9.3 Performance at Off-Design Conditions

At the wing  $C_{L_{max}}$  condition, the fan efficiency is reduced by 2.02 % relative to the long-inlet baseline. The fan efficiency penalty can be reduced to 1.53 % by offsetting the pylon upstream influence and re-cambering the rotor over the outer span. At wing  $C_{L_{max}}$ , the mass flow ratio is  $MFR = 1.76$  and the stagnation point at the bottom

inlet is located on the nacelle external surface. The stagnation point streamlines and the Mach number distributions are presented in the left- and right-hand plots in Fig. 9-5 for the baseline and short-inlet propulsors, respectively.

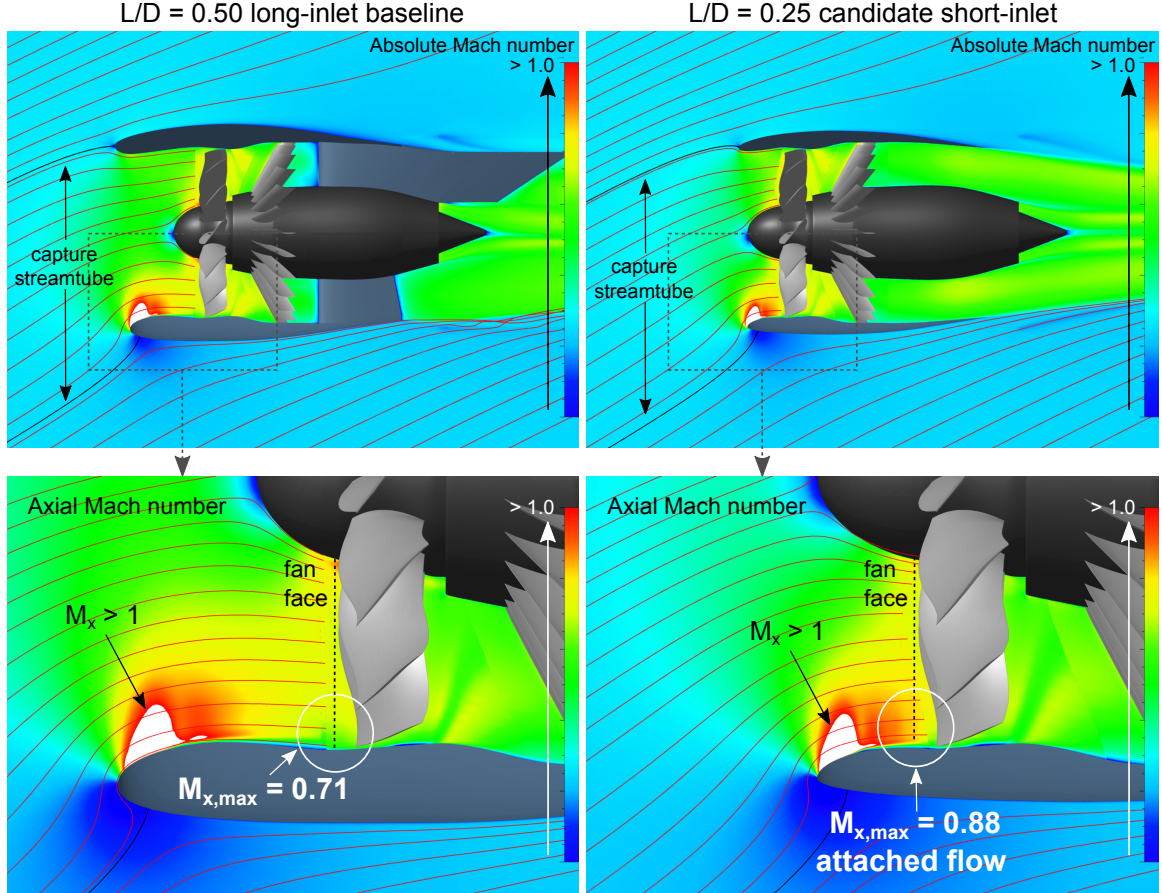


Figure 9-5: Mach number distribution (top) and axial Mach number distribution (bottom) for the baseline propulsor (left) and the candidate short-inlet design with  $L/D = 0.25$  (right) at the wing  $C_{L\max}$  condition.

The inlet flow accelerates around the inlet lip, resulting in a supersonic flow region followed by a shock. Due to the thinner leading edge shape, the over-speed along the inlet internal surface is increased at wing  $C_{L\max}$  and the minimum static pressure coefficient on the inlet surface is reduced by 11 %, as shown in Fig. 9-6. By controlling the curvature along the inlet internal shape, the short-inlet design provides for a region of approximately constant surface pressure downstream of the location of  $c_{p,min}$ , similar to the long-inlet case. Due to the plateau in the surface pressure distribution, the shock strength is limited and a shock-induced separation is avoided.

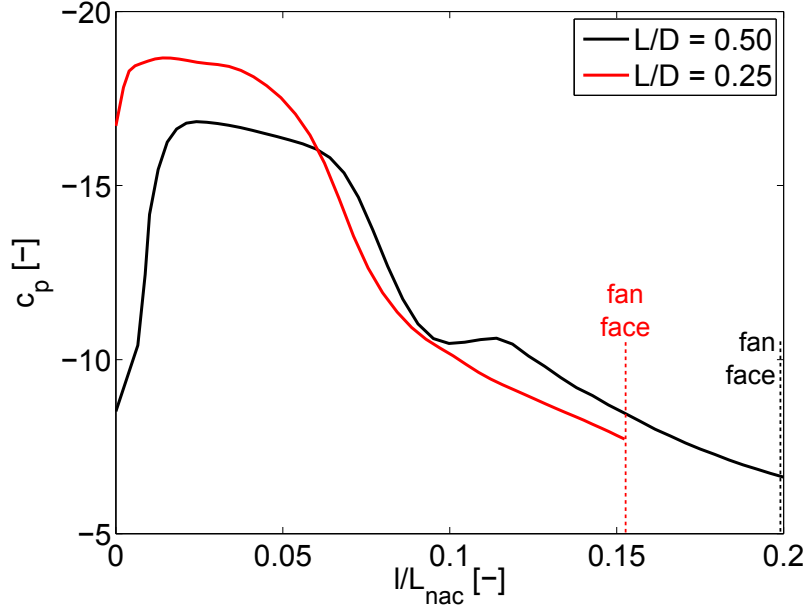


Figure 9-6: Static pressure coefficient along lower inlet lip for the baseline propulsor ( $L/D = 0.5$ ) and the candidate short-inlet configuration ( $L/D = 0.25$ ) at the wing  $C_{L\max}$  operating condition.

In the short inlet, the local region of accelerated flow is not mitigated as much as in the long inlet and the flow distortion at the fan face is substantially enhanced. The spanwise distributions of the axial Mach number and the rotor incidence at the bottom inlet fan face location marked in Fig. 9-5 are depicted in Fig. 9-7. Relative to the baseline propulsor, the maximum Mach number at the fan face increases by  $\Delta M_{x,max} = 0.17$  and the minimum incidence is reduced by up to  $\Delta i = -10^\circ$  near the shroud. By re-cambering rotor blades, the minimum incidence is increased by up to  $\Delta i_{min} = +2^\circ$ , leading to an increase in the fan efficiency.

The increase in the incidence distortion over the entire fan face in the short-inlet propulsor is illustrated in the left-hand plot in Fig. 9-8. The contour shows the difference in the incidence distribution between the short-inlet and the baseline cases,  $\Delta i = i_{L/D=0.25} - i_{L/D=0.50}$ . In addition to the reduced incidence over the outer span between  $\theta = 90^\circ$  and  $270^\circ$ , the reduced flow straightening in the shorter inlet leads to an increase in the incidence distortion between hub and mid-span.

The change in the local fan efficiency,  $\Delta \eta_{fan} = \eta_{L/D=0.25} - \eta_{L/D=0.50}$ , is presented in the right-hand plot in Fig. 9-8. The local fan efficiency is determined here using a

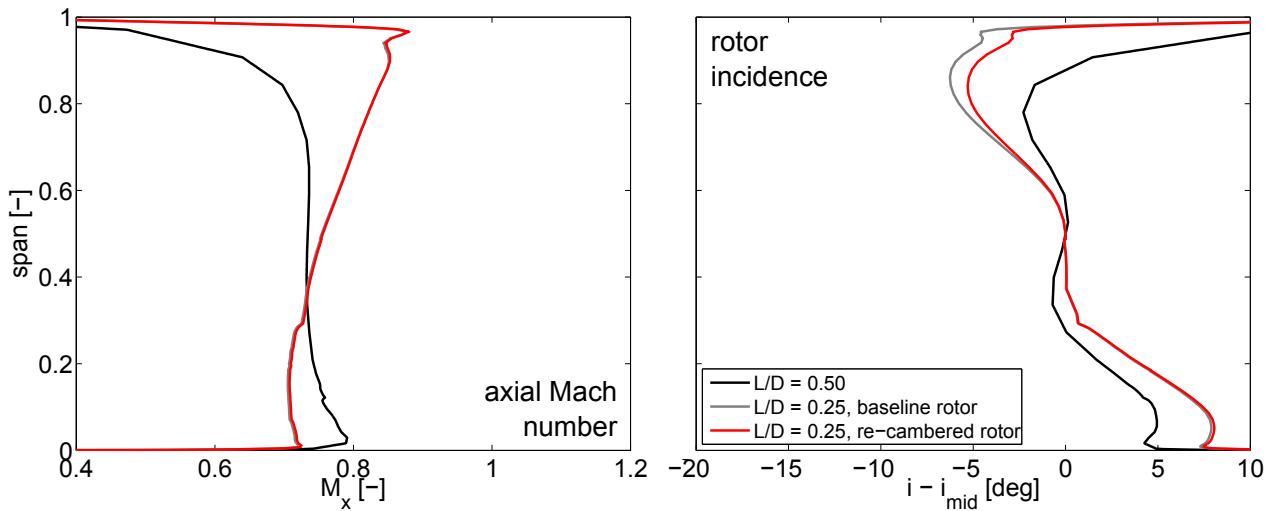


Figure 9-7: Time-averaged spanwise profiles of axial Mach number (left) and rotor incidence relative to mid-span incidence (right) at the fan face for the baseline propulsor ( $L/D = 0.5$ ) and the candidate short-inlet configuration ( $L/D = 0.25$ ) at the wing  $C_{L\max}$  operating condition.

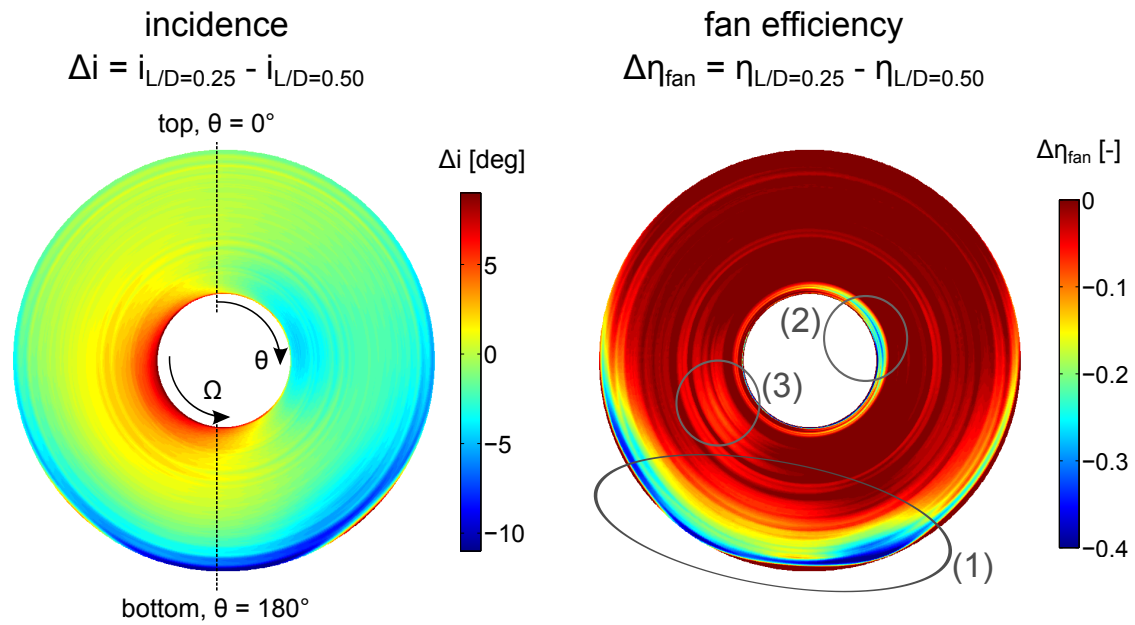


Figure 9-8: Difference in rotor incidence (left) and fan efficiency (right) for the candidate short-inlet design with  $L/D = 0.25$  relative to the long-inlet baseline propulsor (left) at the wing  $C_{L\max}$  condition.

simplified approach for tracking particles through the time-averaged rotor flow field, which was outlined in Section 8.5. Even though this approach can lead to errors of up to  $15^\circ$  in the circumferential location of the local efficiency values, it is still useful to highlight the primary areas of increased rotor losses. In the short-inlet propulsor, the bulk of the losses is due to the incidence reduction over the outer span between  $\theta = 90^\circ$  and  $270^\circ$ , labeled as region (1) in Fig. 9-8. In region (2) near the hub, the rotor losses increase due to the angle-of-attack flow at the fan face and the increased flow acceleration around the spinner. Finally, the reduced flow straightening provided by the inlet increases the incidence distortion the rotor losses near mid-span in region (3). The combined effect of these loss generation mechanisms is a fan efficiency penalty of 2.02 %, as listed in Table 9.2.

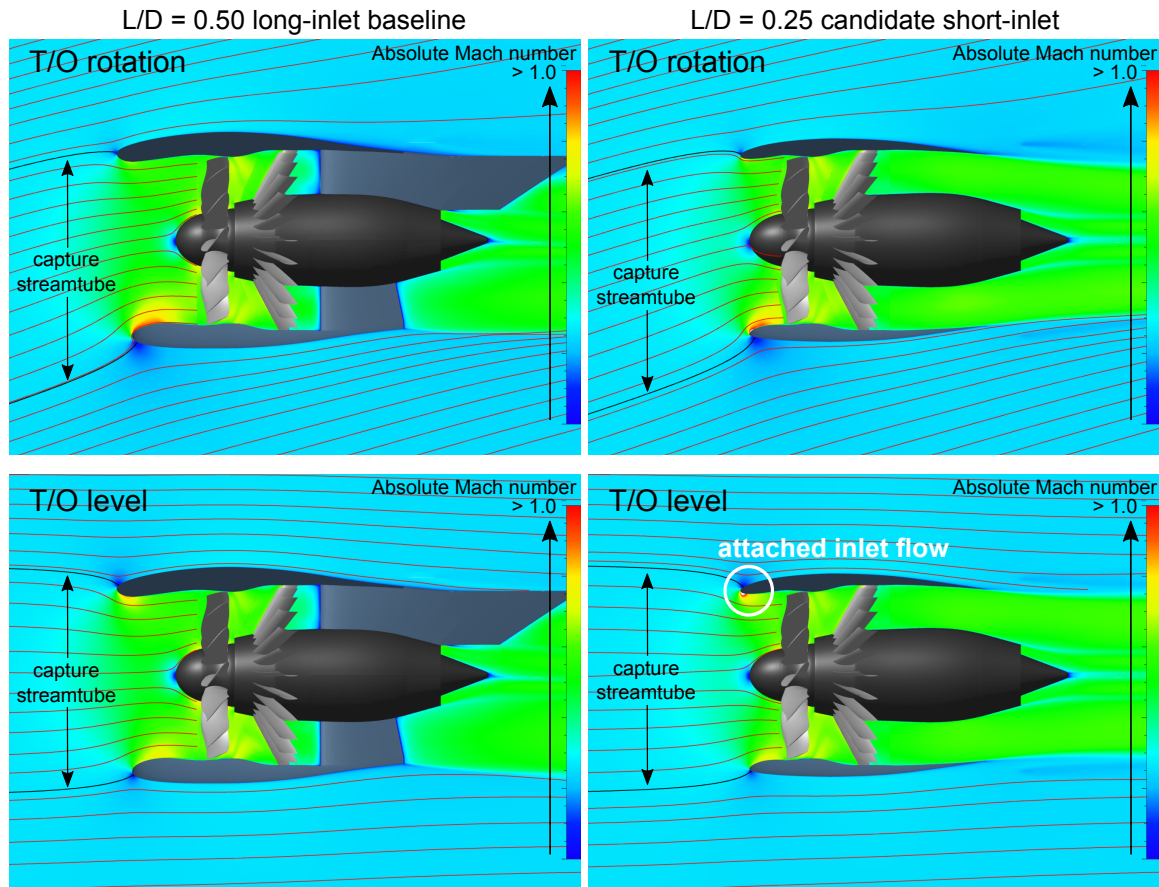


Figure 9-9: Mach number distributions for the baseline propulsor (left) and the candidate short-inlet design with  $L/D = 0.25$  (right) at the T/O rotation and T/O level operating conditions.

The fan performance penalty at the take-off rotation operating condition is due to the same aerodynamic mechanisms which are responsible for the reduction in fan efficiency at wing  $C_{L\max}$ . The Mach number distributions at take-off rotation are depicted in the top left and top right in Fig. 9-9 for the baseline and short-inlet propulsors, respectively. Compared to the wing  $C_{L\max}$  condition, the flow is at a lower angle-of-attack, resulting in a reduction in the interaction of the rotor with the region of increased Mach number at the bottom inlet. Consequently, the fan efficiency is reduced by only 1.71 %, and re-cambering the rotor and eliminating the pylon potential field impact improves the efficiency by 0.43 %. At low-speed level inflow, the flow acceleration is locally increased at the top inlet lip, as shown in the bottom plots in Fig. 9-9. In the short-inlet, the incidence is reduced over the upper half of the rotor revolution, resulting in a fan efficiency penalty of 1.11 %.

In addition to the aerodynamic performance penalty, the short-inlet design provides reduced acoustic attenuation and noise shielding opportunities compared to the long inlet. The aero-acoustic performance is not addressed in this work. However, the work by Prasad and Feng [95] suggests that the dissipation of the upstream-propagating rotor-locked shocks responsible for the inlet tone noise is increased by the mean flow acceleration throughout the short inlet and the over-speed near the inlet lip. The increased acoustic attenuation potential due to the local regions of increased streamwise Mach number flow could limit the noise penalty of the short-inlet propulsor compared to the long-inlet case and is recommended to be explored in future work.

In summary, the off-design performance of the candidate short-inlet propulsor with  $L/D = 0.25$  is reduced compared to the long-inlet propulsor due to the increased incidence distortion over the entire fan face. Design changes with the objective of improving the off-design performance are likely to result in a reduction in the nacelle aerodynamic performance at cruise. Benefits are expected by reducing the interaction of the rotor with the local regions of high Mach number flow, which could be achieved by increasing the inlet length or by implementing advanced concepts such as pitching the fan case, which is discussed in Chapter 10.

## 9.4 Evaluation of Design Criteria at Wing $C_{L\max}$

The wing  $C_{L\max}$  condition has received particular attention throughout this thesis due to the challenges for inlet and rotor performance presented by the high levels of inlet flow non-uniformity. Conventional inlet design criteria include the requirement for separation-free flow and constrain the minimum surface pressure coefficient to critical levels to limit the over-speed along the bottom inlet. Due to the increased fan-inlet coupling in short inlets, more general criteria are needed in terms of the response of the rotor and downstream blade rows to the non-uniform inlet flow. Two potentially limiting factors were identified in collaboration with the industry partner:

1. Reduced stall margin of the low pressure compressor (LPC) due to the increased circumferential stagnation pressure variations in the core inlet flow.
2. Increased fan blade stress due to the unsteady loading variation experienced by the rotor in the non-uniform inlet flow.

Fan stall was suggested to be less critical than the LPC stall and fan aero-mechanical challenges. Without including the impact of the inlet flow distortion on the rotor performance, a short-inlet design optimization may yield inlet designs with inlet flow distortion and core inflow stagnation pressure distortion levels which are not acceptable for a given fan blade structure and LPC definition. Essentially, the following questions must be asked in the design of short inlets:

1. How much incidence distortion can be handled by the fan rotor and the LPC?
2. How short can the inlet be before the LPC stalls or the rotor blades require structural modifications?

The following sections present an evaluation of the differences in the circumferential stagnation pressure variation in the core inlet and the time-dependent fan rotor blade loading between the short-inlet propulsors and the baseline configuration. The discussion includes the results for the second candidate short-inlet design with  $L/D = 0.19$ , which is presented in more detail in the next chapter.

### 9.4.1 Core Inflow Stagnation Pressure Distortion

The relative difference of the local stagnation pressure,  $p_t$ , to the circumferentially-averaged value,  $p_t^M$ , at mid-span of the core inlet is depicted in Fig. 9-10. The incidence is reduced between  $\theta = 0^\circ$  and  $\theta = 180^\circ$  due to the high positive angle-of-attack at the fan face, as illustrated on the left in Fig. 9-8 for the  $L/D = 0.25$  design. Consequently, the stagnation pressure is reduced. The opposite effect results in an increase of the stagnation pressure between  $\theta = 180^\circ$  and  $360^\circ$ .

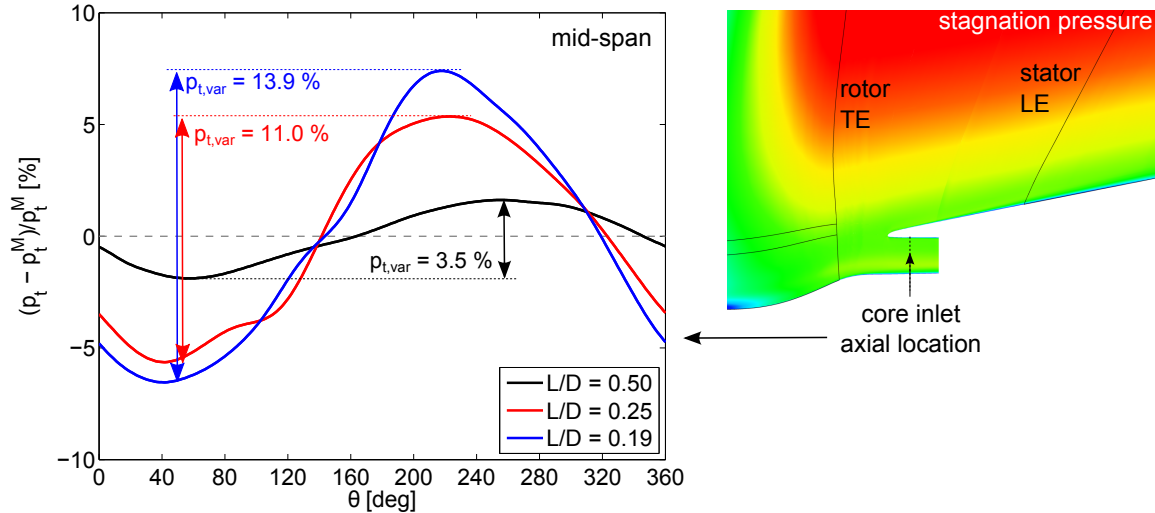


Figure 9-10: Circumferential stagnation pressure variation at mid-span of core inlet duct for the baseline propulsor ( $L/D = 0.5$ ) and the candidate short-inlet configurations ( $L/D = 0.25$  and  $L/D = 0.19$ ) at the wing  $C_{L\max}$  operating condition.

The stagnation pressure varies by up to 3.5 % around the mean in the baseline propulsor. In the  $L/D = 0.25$  short-inlet configuration, the peak-to-peak amplitude increases to 11.0 % due to the increased flow distortion near the hub. For an  $L/D$  of 0.19, the variation increases to a maximum of 13.9 %, which was suggested by the industry partner to be close to the limit of the acceptable inflow distortion for the LPC. An additional increase in the pressure variation would possibly require variable-pitch inlet guide vanes upstream of the first LPC rotor. Based on this assessment, a minimum  $L/D$  of approximately 0.2 is recommended for adequate LPC stall margin.

The presented stagnation pressure variations are based on the time-averaged flow field obtained in URANS simulations but can also be extracted from a body force

solution. Combined with a suitable method for estimating the LPC stability based on the circumferential stagnation pressure distortion levels, the developed body-force-based design framework would enable the evaluation of the change in LPC stall margin due to changes in the inlet length and shape at each design iteration. To reduce the risk of generating an inlet design with unacceptable incidence distortion near the hub, a maximum allowable stagnation pressure variation could be included as an additional constraint in a manual or automated inlet design optimization.

#### 9.4.2 Time-Dependent Blade Loading

The variation of the fan blade loading along the circumference directly affects the blade stresses and structural design requirements. The blade loading is evaluated here in terms of the lift coefficient at a given spanwise location. The time-dependent lift coefficient  $c_l(t)$  is determined by integrating over the difference in the static pressure distributions between the suction and pressure surfaces, where the surface pressures are extracted for a single blade over a full rotor revolution in a URANS simulation. The variation of the lift coefficient,  $c_l(t)$ , around the time-averaged value,  $\bar{c}_l$ , is presented for a rotor revolution with period  $T$  at mid-span and 90 % span in the top and bottom plots in Fig. 9-11, respectively.

The direction of the rotor rotation is defined in Fig. 9-8. Over the first half of the revolution, the blade encounters increased incidence and the loading is increased relative to the time-average. Over the second half, the rotor incidence decreases, resulting in a reduction in the lift coefficient. The local increase in the blade loading at  $t/T = 0.5$  and  $t/T = 1$  is due to the bifurcation and pylon upstream influence, respectively. The long inlet reduces the distortion from the angle-of-attack inflow and, compared to the pylon and bifurcation upstream influence, the impact of the non-uniform inflow is significantly increased in the short-inlet propulsors.

Relative to the long inlet, the maximum variation in the lift coefficient at mid-span increases by 20 % in the  $L/D = 0.25$  inlet and by 28 % in the  $L/D = 0.19$  inlet. At 90 % span, the increase in the maximum variation is reduced to 13 % in the  $L/D = 0.25$  inlet and 14 % in the  $L/D = 0.19$  inlet since the mean lift coefficient,  $\bar{c}_l$ ,

is increased towards to tip. The impact of the circumferential variation in loading on the blade stresses was not addressed in this work.

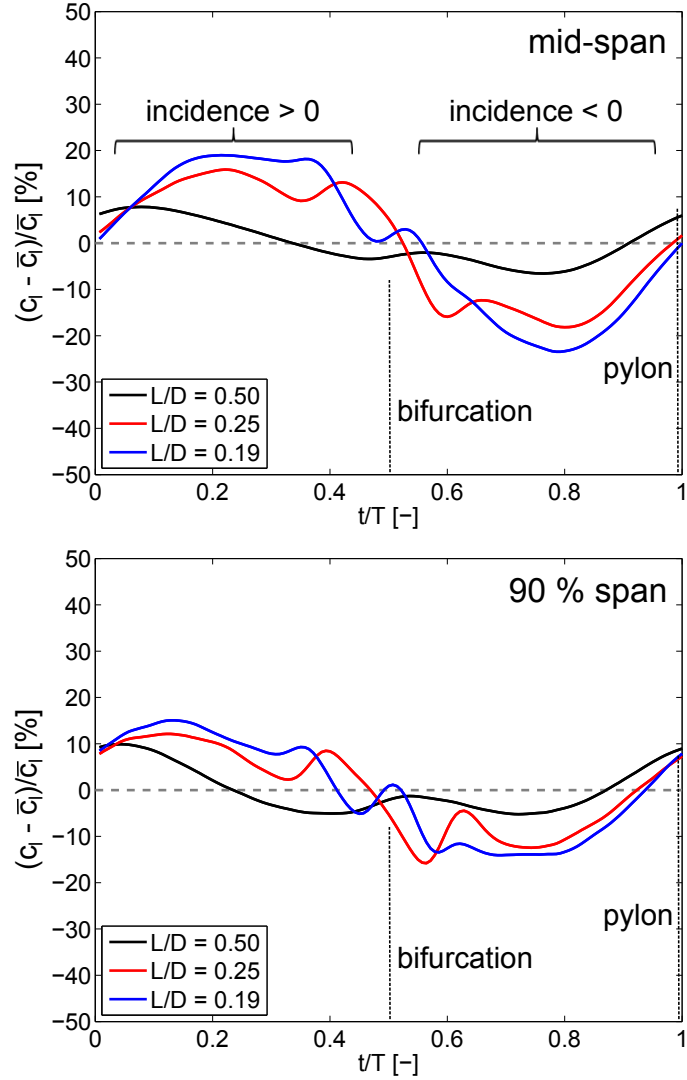


Figure 9-11: Time-dependent variation of blade lift coefficient at mid-span (top) and 90 % span for the baseline ( $L/D = 0.5$ ) and the candidate short-inlet configurations ( $L/D = 0.25$  and  $L/D = 0.19$ ) at the wing  $C_{L\max}$  operating condition.

The blade loading could be determined directly from body force simulations by tracking the normal body force  $f_n$  around the circumference. The body force simulations also provide the circumferential incidence variation, which gives insight into the range of local operating conditions encountered by the rotor. A maximum allowable normal force or incidence variation could be specified as a constraint in the short-inlet design optimization to ensure that critical blade stresses are not exceeded.

# Chapter 10

## Candidate Short-Inlet Design -

**L/D = 0.19**

The performance assessment of two short-inlet designs with  $L/D = 0.02$  and  $L/D = 0.1$  presented in Section 8.2 suggested that shortening the inlet beyond an  $L/D$  of 0.2 increases the incidence distortion and leads to a dramatic drop-off in the rotor performance over the entire range of operating conditions. A candidate short-inlet design with  $L/D = 0.19$  was generated using body force simulations to quantify the propulsor performance at the recommended lower  $L/D$  limit. The results of URANS simulations, used to check the performance of the design, are presented in the first part of this chapter. Advanced concepts needed to take full advantage of the nacelle drag and weight benefits offered in a short-inlet design with  $L/D = 0.19$  are the focus of the second part of this chapter.

### 10.1 Overview of Design Characteristics and Performance

The inlet and nacelle contours of the  $L/D = 0.19$  candidate design are presented in Fig. 10-1 and the design characteristics are listed in Table 10.1. Compared to the  $L/D = 0.25$  design, the maximum nacelle diameter is further reduced to limit

the flow acceleration over the aft part of the nacelle. A small decrease in the inlet highlight area is necessary to limit the over-speed along the nacelle external surface at cruise. The spinner is extended forward by 5 % to mitigate the impact of the inlet flow distortion near the hub. Due to the additional increase in the spinner length and the reduction in the inlet length, the spinner leading edge is located upstream of the inlet highlight axial location, which is one of the major differences in the design characteristics compared to conventional long-inlet configurations.

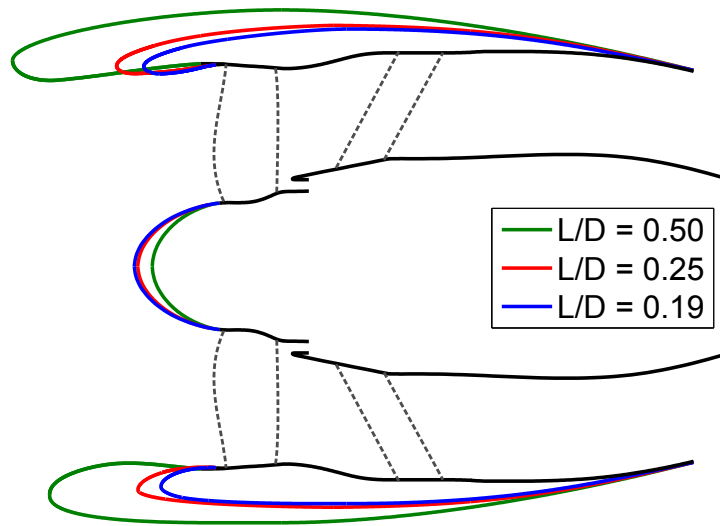


Figure 10-1: Top and bottom inlet and nacelle sections for the baseline  $L/D = 0.5$  and the  $L/D = 0.25$  and  $L/D = 0.19$  candidate short-inlet designs.

Based on the performance trends presented in the previous chapter, a combination of altering the rotor blade design and tailoring the stator vanes to offset the pylon upstream influence is expected to reduce the fan efficiency penalty by approximately 0.5 %. However, the sensitivity analysis presented in Section 7.4 suggests that the fan efficiency would have to be increased by almost 1 % to recover the 0.8 % propulsive efficiency penalty relative to the baseline. The results confirm the hypothesis that an  $L/D$  of approximately 0.2 represents a lower limit in the short-inlet design space.

Table 10.1: Inlet and nacelle design parameters for the baseline and the  $L/D = 0.25$  and  $L/D = 0.19$  candidate short-inlet designs.

	$L/D = 0.5$ baseline	$L/D = 0.25$	$L/D = 0.19$
Inlet droop	5°	3°	2.4°
Max. diameter to fan diameter $D_{max}/D$	1.27	1.19	1.17
Contraction ratio $A_{HL}/A_{throat}$	1.26	1.17	1.16
Mean highlight to max. diameter ratio $D_{HL}/D_{max}$	0.85	0.88	0.89
Spinner length $x/D$	0.15	0.19	0.20
Inlet mass flow ratio $MFR = A_0/A_{HL}$			
- cruise	0.74	0.79	0.80
- wing $C_{Lmax}$	1.62	1.76	1.77
- T/O rotation	1.59	1.73	1.74

Table 10.2: Performance overview of the  $L/D = 0.19$  and  $L/D = 0.25$  candidate short-inlet propulsors relative to the  $L/D = 0.5$  baseline.

Condition/Metric		$L/D = 0.25$ re-cambered rotor without pylon	$L/D = 0.19$ baseline rotor with pylon
<b>Cruise ADP</b>			
- propulsive efficiency	$\Delta\eta_{prop}$	+0.25 %	-0.80 %
- nacelle drag	$D_{nac}$	-16.2 %	-17.8 %
- fan efficiency	$\Delta\eta_{fan}$	-0.71 %	-1.63 %
<b>Wing <math>C_{Lmax}</math></b>			
- fan efficiency	$\Delta\eta_{fan}$	-1.53 %	-3.94 %
- core inlet $p_t$ -variation at mid-span	$\Delta p_{t,var,mid}$	+7.8 %	+10.4 %
- blade tip variation of lift coefficient	$\Delta c_{l,var,tip}$	+12.8 %	+14.0 %
<b>Cross-wind</b>			
- fan efficiency	$\Delta\eta_{fan}$	not computed	-1.53 % (*)
- inlet pressure recovery	$\Delta\pi_{inlet}$		+0.002 (*)
<b>T/O rotation</b>			
- fan efficiency	$\Delta\eta_{fan}$	-1.28 %	-2.48 %
<b>T/O level</b>			
- fan efficiency	$\Delta\eta_{fan}$	-0.67 %	-1.85 %

(\*) with blow-in doors in inlet

## 10.2 Performance at Cruise

The Mach number distribution for the  $L/D = 0.19$  candidate nacelle design is shown in the top right plot in Fig. 10-2 and the isentropic Mach number along the nacelle external surface is presented at three circumferential locations in Fig. 10-3. By reducing the inlet highlight area and aligning the orientation of the inlet lip with the stagnation point streamline, the flow acceleration along the upper nacelle surface ( $\theta = 0^\circ$ ) was limited to the level achieved by the long-inlet baseline design. There is a slight increase in the maximum Mach number along the lower nacelle surface ( $\theta = 180^\circ$ ), which led to a small increase of the nacelle pressure drag component (+1.6 %), as summarized in Table 10.3.

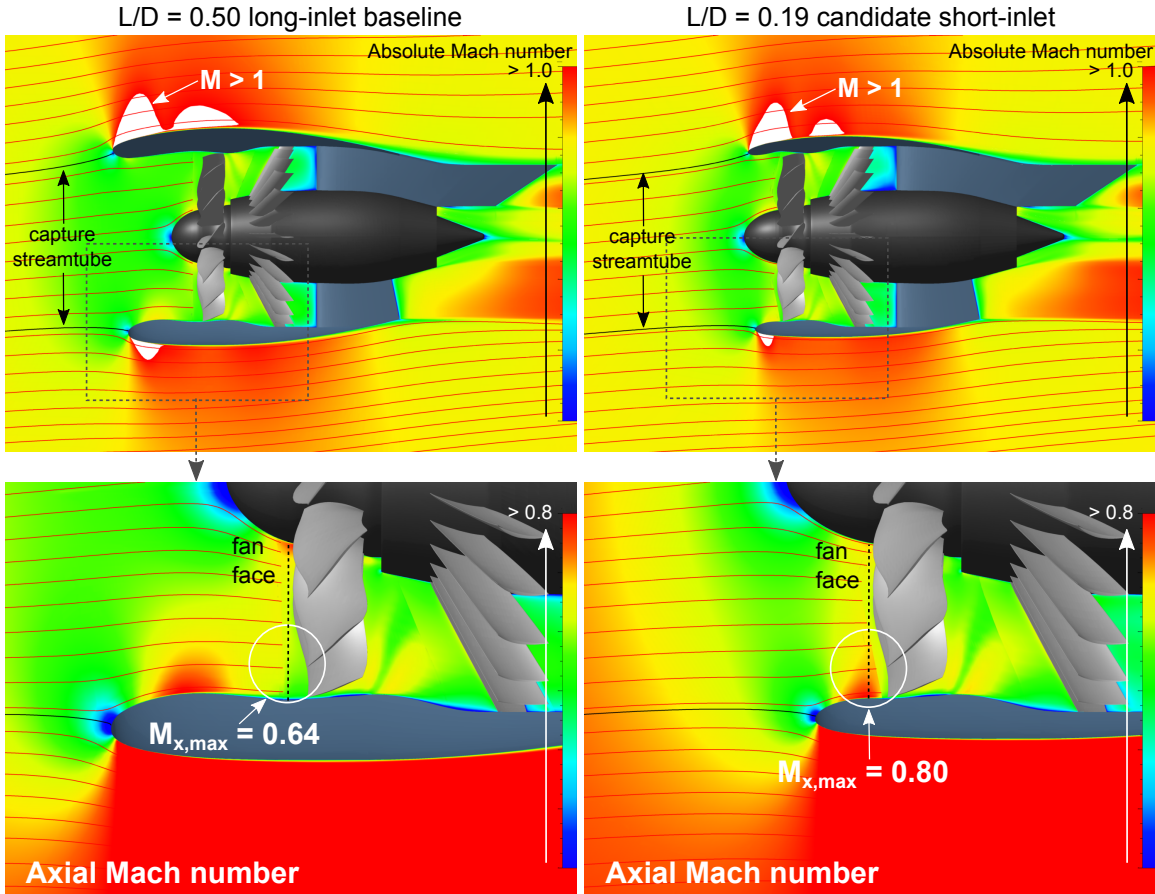


Figure 10-2: Mach number distribution (top) and axial Mach number distribution (bottom) for the baseline propulsor (left) and the candidate short-inlet design with  $L/D = 0.19$  (right) at cruise.

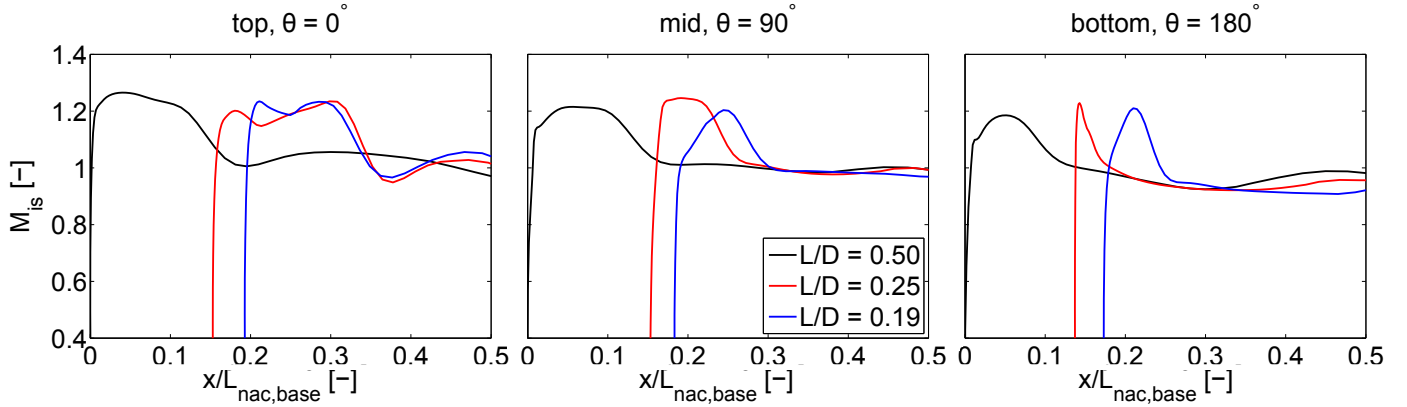


Figure 10-3: Isentropic Mach number along nacelle external surface at three circumferential locations for the baseline propulsor ( $L/D = 0.5$ ) and the candidate short-inlet configurations ( $L/D = 0.25$  and  $L/D = 0.19$ ) at cruise.

Table 10.3: Relative change in nacelle drag for the  $L/D = 0.25$  and  $L/D = 0.19$  designs compared to the  $L/D = 0.5$  baseline.

Component		$L/D = 0.25$	$L/D = 0.19$
nacelle total drag	$D_{nac}$	-16.2 %	-17.8 %
nacelle viscous drag	$D_{nac,visc}$	-23.0 %	-25.4 %
nacelle pressure drag	$D_{nac,p}$	+1.4 %	+1.6 %

The viscous drag contribution to the nacelle total drag, presented in Table 10.4, is further reduced for the  $L/D = 0.19$  design relative to the  $L/D = 0.25$  candidate short-inlet propulsor due to the reduction in the wetted nacelle area. Following the analysis outlined in Section 9.2, the breakdown of the losses from the ideal performance of an isolated ducted propulsor into internal and external losses is summarized in Table 10.5. The relative importance of the internal losses further increases in the  $L/D = 0.19$  propulsor due to the degradation in rotor performance and the additional reduction in the external nacelle drag.

As in the  $L/D = 0.25$  design, the fan performance penalty relative to the baseline case is due to the combined impact of the reduced flow straightening in the short inlet and the local increase in the Mach number at the fan face in the bottom inlet flow, as illustrated in the bottom plots in Fig. 10-2. The spanwise profiles of axial Mach number and rotor incidence at the bottom inlet location are presented in the left- and right-hand plots in Fig. 10-4, respectively. Due to the reduction in  $L/D$

Table 10.4: Drag breakdown for the  $L/D = 0.25$  and  $L/D = 0.19$  designs compared to the  $L/D = 0.5$  baseline.

Component		$L/D = 0.50$	$L/D = 0.25$	$L/D = 0.19$
viscous drag contribution	$D_{nac,visc}/D_{nac}$	0.72	0.66	0.65
pressure drag contribution	$D_{nac,p}/D_{nac}$	0.28	0.34	0.35

Table 10.5: Loss breakdown relative to an isolated ducted propulsor with ideal propulsive efficiency into internal and external losses for the  $L/D = 0.25$  and  $L/D = 0.19$  designs compared to the  $L/D = 0.5$  baseline.

Component	$L/D = 0.50$	$L/D = 0.25$	$L/D = 0.19$
internal losses	54.4 %	62.3 %	65.5 %
external losses	45.6 %	37.7 %	34.5 %

from 0.25 to 0.19, the maximum axial Mach number at the fan face is increased by  $\Delta M_{x,max} = +0.03$  and the local incidence decreases by up to  $-2.5^\circ$ . Aside from the increase in the incidence variation near the shroud, the inlet flow non-uniformities are also increased between the hub and mid-span due to the reduced flow straightening, resulting in an additional reduction in the rotor performance and a fan efficiency penalty of  $\Delta\eta_{fan} = -1.63\%$  relative to the  $L/D = 0.5$  baseline configuration.

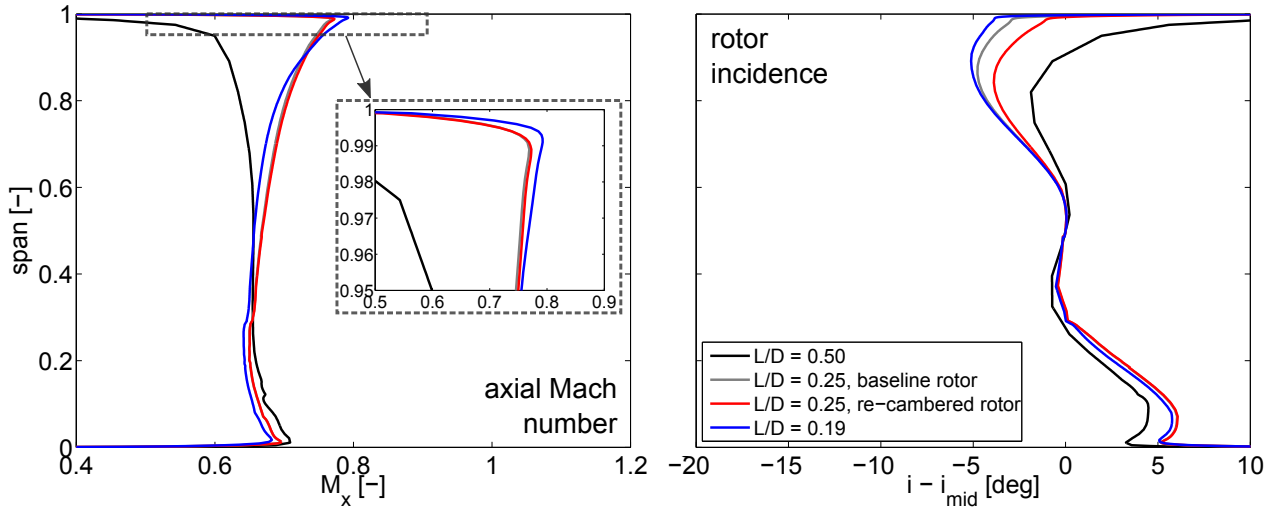


Figure 10-4: Time-averaged spanwise profiles of axial Mach number (left) and rotor incidence relative to mid-span incidence (right) at the fan face for the baseline propulsor ( $L/D = 0.5$ ) and the candidate short-inlet configurations ( $L/D = 0.25$  and  $L/D = 0.19$ ) at cruise.

## 10.3 Performance at Off-Design Conditions

Similar to the candidate short-inlet design with  $L/D = 0.25$ , the design intent for the  $L/D = 0.19$  inlet was to provide for fully attached inlet flow at the wing  $C_{L\max}$  operating condition. However, in contrast to the  $L/D = 0.25$  design, separation-free flow could only be obtained with inlet shapes which resulted in considerably elevated maximum Mach numbers in the external flow and an increased wave drag penalty and a small region of separated flow was accepted in the  $L/D = 0.19$  design. The absolute and axial Mach number distributions for the baseline and  $L/D = 0.19$  candidate short-inlet propulsor are shown in the top and bottom plots in Fig. 10-5, respectively.

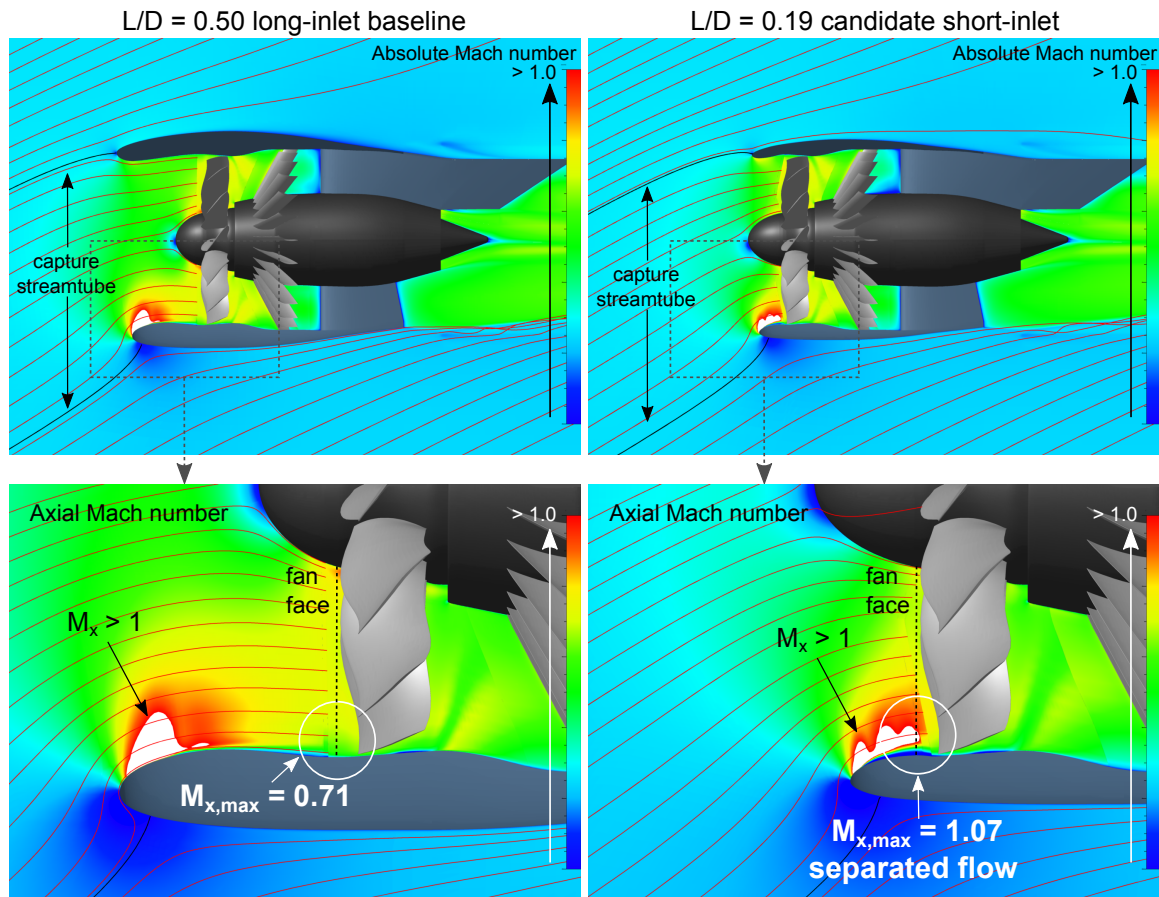


Figure 10-5: Mach number distribution (top) and axial Mach number distribution (bottom) for the baseline propulsor (left) and the candidate short-inlet design with  $L/D = 0.19$  (right) at the wing  $C_{L\max}$  condition.

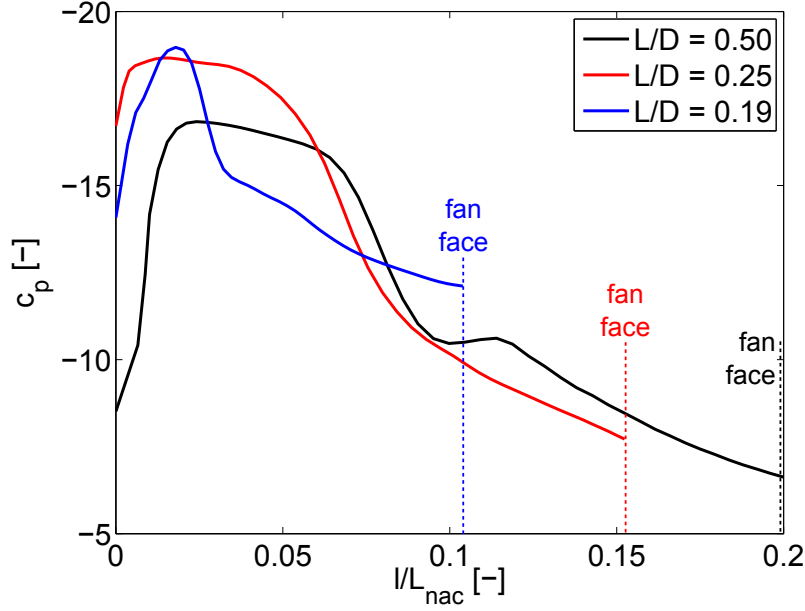


Figure 10-6: Static pressure coefficient along lower inlet lip for the baseline propulsor ( $L/D = 0.5$ ) and the candidate short-inlet configurations ( $L/D = 0.25$  and  $L/D = 0.19$ ) at the wing  $C_{L\max}$  operating condition.

Due to the reduction in the inlet length, an extended region of reduced curvature along the bottom inlet internal surface could not be implemented and the surface pressure distribution, shown in Fig. 10-6, features a distinct minimum pressure peak resulting in a shock which induces boundary layer separation. Downstream of the shock, the flow re-accelerates between approximately 60 % and 95 % span and the axial Mach number is supersonic at the fan face, as illustrated in the spanwise profile on the left in Fig. 10-7. Compared to the  $L/D = 0.25$  design, the maximum axial Mach number increased by  $\Delta M_{x,max} = +0.29$ , resulting in a local reduction in rotor incidence of up to  $\Delta i = -7.5^\circ$ , as shown on the right in Fig. 10-7, and causing the local rotor operating condition to further shift towards choke.

The difference in the local rotor incidence between the short- and long-inlet cases is illustrated on the left in Fig. 10-8. Compared to the results for the  $L/D = 0.25$  design shown in Fig. 9-8, the circumferential incidence variation is further enhanced over the entire fan face. The evaluation of the local efficiency difference indicates that most of the rotor losses are due to the supersonic inflow near the shroud over the lower half of the rotor revolution (region 1) and the reduced mitigation of the inflow

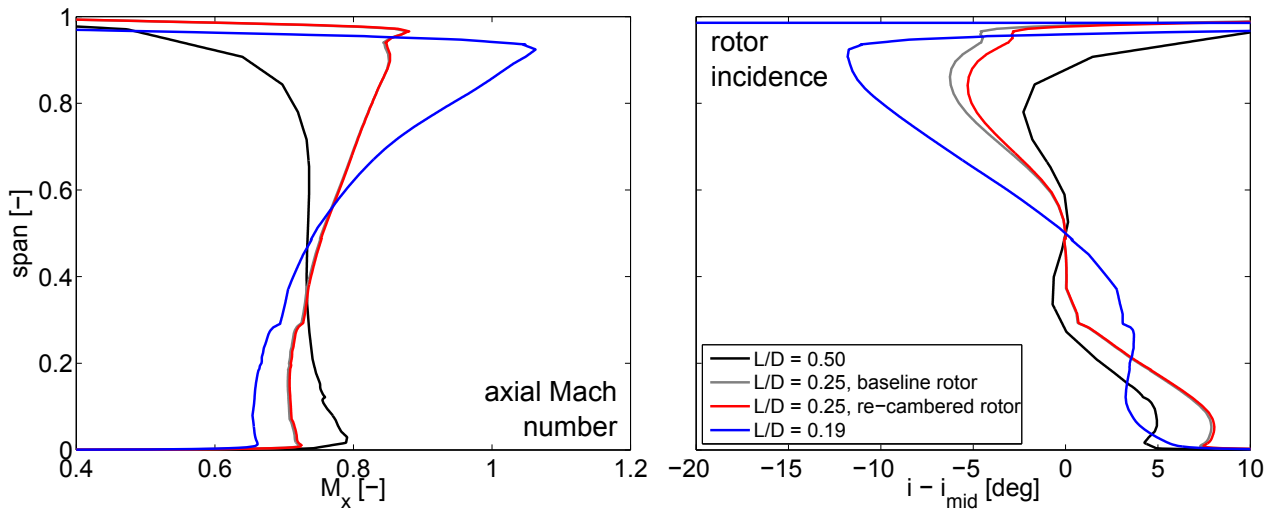


Figure 10-7: Time-averaged spanwise profiles of axial Mach number (left) and rotor incidence relative to mid-span incidence (right) at the fan face for the baseline propulsor ( $L/D = 0.5$ ) and the candidate short-inlet configurations ( $L/D = 0.25$  and  $L/D = 0.19$ ) at the wing  $C_{L\max}$  operating condition.

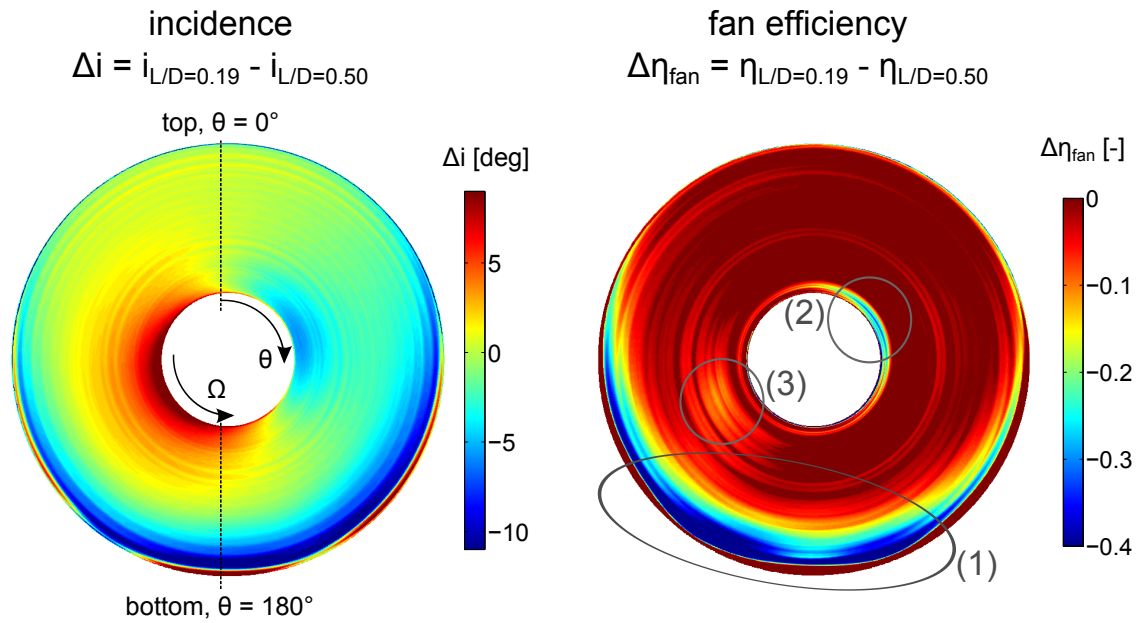


Figure 10-8: Difference in rotor incidence (left) and fan efficiency (right) for the candidate short-inlet design with  $L/D = 0.19$  relative to the long-inlet baseline propulsor (left) at the wing  $C_{L\max}$  condition.

non-uniformities near the hub (region 2) and near mid-span (region 3). As a result, the (integrated) fan efficiency decreases by  $\Delta\eta_{fan} = -3.94\%$  relative to the baseline propulsor and the circumferential stagnation pressure distortion in the core inflow is close to the maximum allowable variation for sufficient LPC stall margin.

The Mach number distributions at the take-off conditions are presented on the left and right in Fig. 10-9, respectively, for the baseline and the  $L/D = 0.19$  short-inlet propulsors. The inlet flow is fully attached at both angle-of-attack and level inflow with  $M_0 = 0.25$ . It should be noted that the increased mass flow ratio at low Mach numbers ( $M_0 < 0.25$ ) and angles-of-attack before take-off rotation is expected to result in flow separation at the top of the inlet. This flow separation can be mitigated with a flow injection system outlined in the next section.

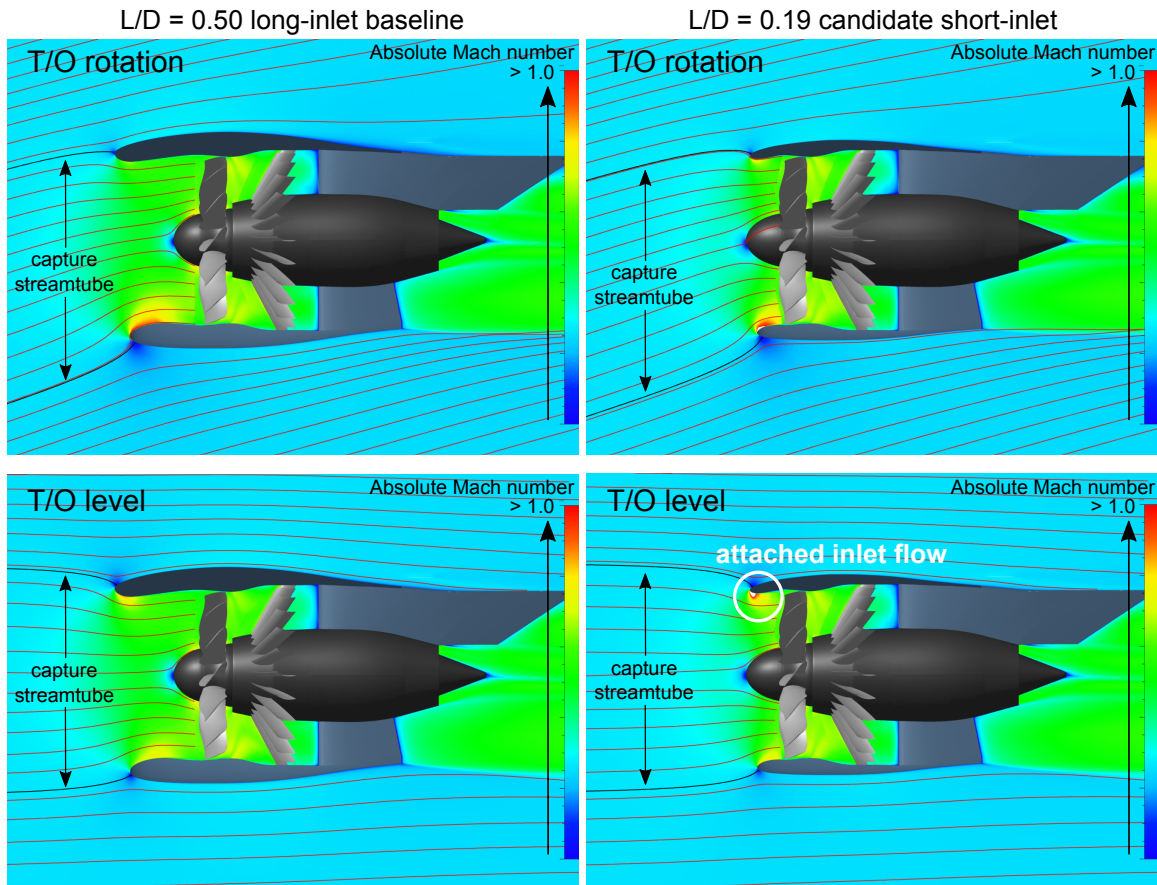


Figure 10-9: Mach number distribution for the baseline propulsor (left) and the candidate short-inlet design with  $L/D = 0.19$  (right) at the T/O rotation and T/O level operating conditions.

## 10.4 Advanced Concepts

The design and off-design performance assessment of the two short-inlet candidate designs presented in this thesis suggests that pushing the limits of the short-inlet design space and capitalizing on the drag and weight benefits offered by short nacelles with inlets of length  $L/D$  at or below 0.2 requires the implementation of advanced concepts. Two concepts to mitigate the impact of the inflow distortion on the rotor performance in short inlets at cruise and low-speed off-design operating conditions are discussed next. In the first part, the focus is on alleviating the rotor incidence distortion at cruise. In the second part, the short-inlet propulsor performance at cross-wind with and without blow-in doors in the inlet is presented.

### 10.4.1 Pitched Fan Case

The cruise condition assumes a  $5^\circ$  angle-of-attack on the propulsor due to the influence of the flow upwash generated by the wing. In short inlets, the flow at the fan face is at a positive angle-of-attack. The degradation in the rotor performance due to the increase in incidence distortion is the primary driver for the propulsive efficiency penalty incurred by the  $L/D = 0.19$  short-inlet configuration. The incidence distortion could be reduced for example by pitching the fan case and aligning the fan rotor axis of rotation with the angle-of-attack inflow. A sketch of this concept is provided in Fig. 10-10. In the pitched fan case concept, the bypass and core nozzles would be required to provide exhaust flow in the flight direction. Alternatively, the transition from the angled fan rotor shaft to an un-pitched core shaft may be realized through the implementation of an advanced gearbox design.

To quantify the potential for rotor performance improvements in the pitched fan case configuration, a URANS simulation for the  $L/D = 0.19$  candidate short-inlet design was carried out at level inflow. The time-averaged rotor incidence distribution is shown in the center and on the right in Fig. 10-11 for the  $L/D = 0.19$  inlet design in a conventional and a pitched fan case configuration, respectively. For reference, the results for the baseline propulsor at  $AoA = 5^\circ$  are presented in the left-hand

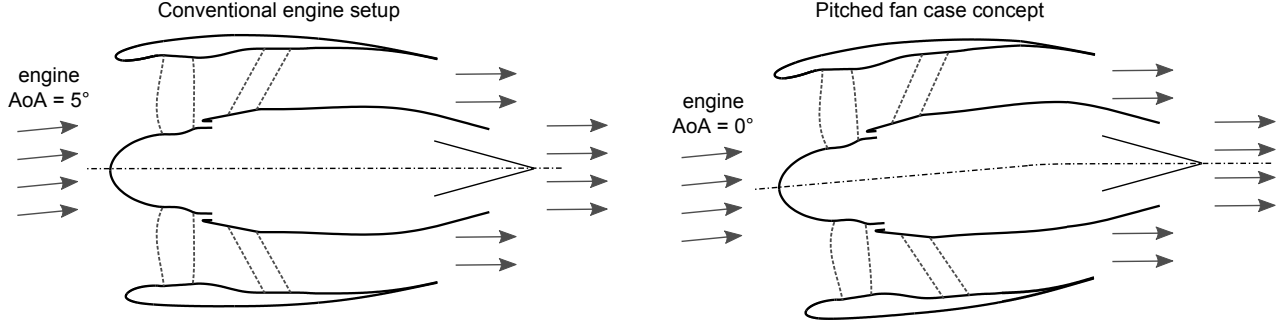


Figure 10-10: Pitched fan case concept.

plot. As expected, the circumferential incidence distortion is significantly reduced by aligning the fan axis of rotation with the incoming flow. The circumferential incidence variation near the hub, at mid-span, and near the blade tip are depicted on the left, in the center, and on the right in Fig. 10-12. The incidence distortion is mitigated at each spanwise location, with the largest reductions observed near the endwalls.

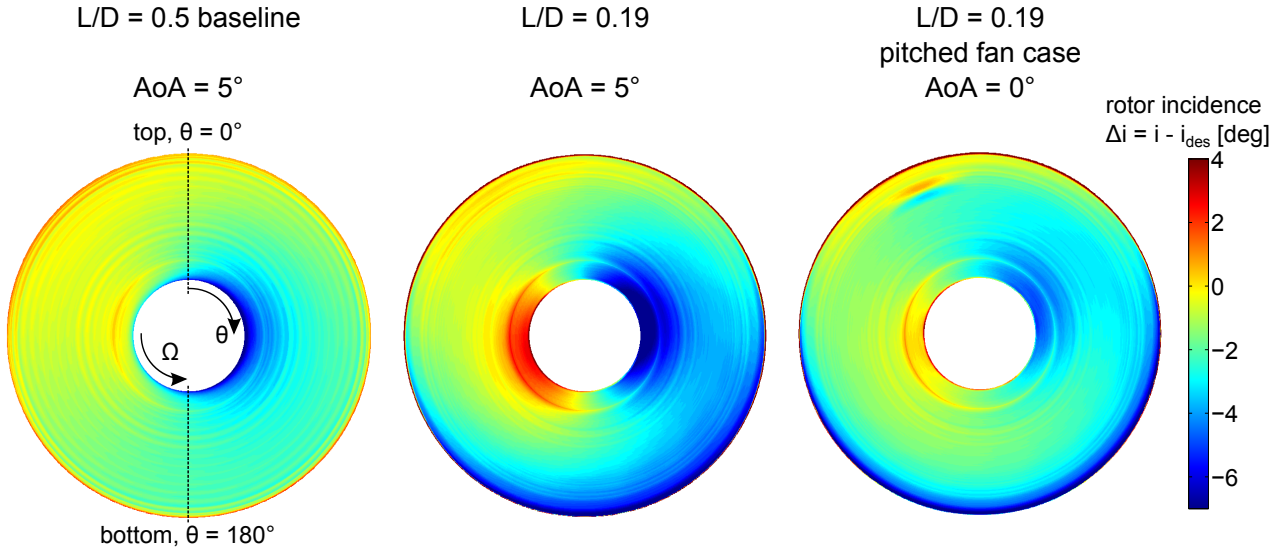


Figure 10-11: Rotor incidence distortion for the baseline long-inlet configuration (left) and the short-inlet designs without (center) and with a pitched fan case (right) at the cruise condition.

The reduction in incidence distortion over the entire fan face results in a fan efficiency benefit of  $\Delta\eta_{fan} = 0.8\%$ , which translates to a propulsive efficiency increase of  $\Delta\eta_{prop} \approx 0.7\%$  (assuming constant nacelle drag) and would raise the  $L/D = 0.19$  propulsor performance close to the level achieved by the baseline configuration.

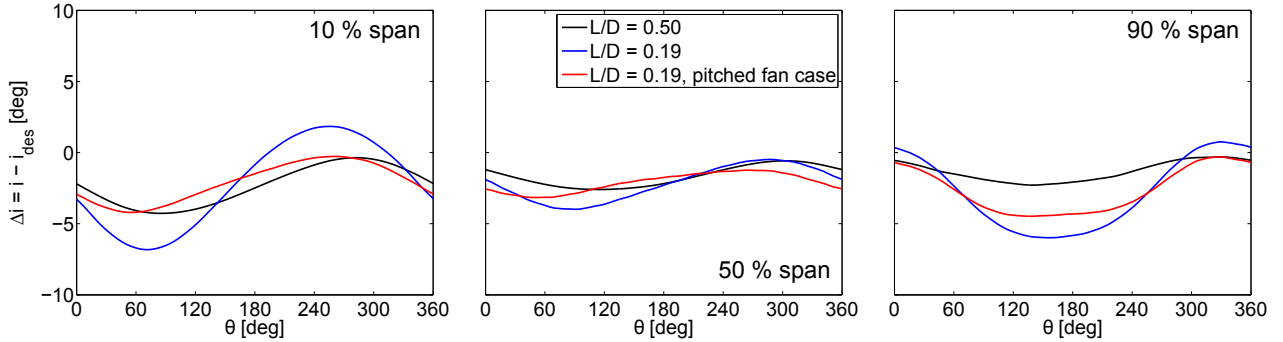


Figure 10-12: Variation of rotor incidence at 10 % span (left), 50 % span (center), and 90 % span (right) for the baseline inlet and the  $L/D = 0.19$  design with and without pitched fan case configuration at cruise.

The remaining rotor incidence variation observed in the pitched fan case configuration in Figs. 10-11 and 10-12 is due to the pylon and bifurcation upstream influence near  $\theta = 0, 360^\circ$  and  $\theta = 180^\circ$ , respectively, and due the circumferential and radial flow re-distribution through the inlet generated by the non-axisymmetric surfaces. Additional reductions in the incidence distortions are feasible by defining an inlet geometry designed for level inflow and shielding the rotor from the pylon and bifurcation potential fields. The nacelle shape would also have to be re-designed as the thicker bottom lip causes a large increase in the maximum Mach numbers in the external flow if the nacelle design is kept the same.

In addition to the fan performance improvement at cruise, the pitched fan case configuration also offers benefits at off-design conditions with high angles-of-attack. At wing  $C_{L\max}$ , the engine angle-of-attack is reduced from  $29^\circ$  to  $24^\circ$ , resulting a fan efficiency increase of  $\Delta\eta_{fan} = 0.5\%$  compared to the conventional configuration.

#### 10.4.2 Blow-In Doors at Cross-Wind

The Mach number distributions on the horizontal plane at the cross-wind operating condition are presented for the baseline and the  $L/D = 0.19$  short-inlet propulsor on the left and right in Fig. 10-13, respectively. The distributions are extracted from URANS simulations. While the computational domain was extended compared to the other operating conditions to account for the increase in the streamtube capture

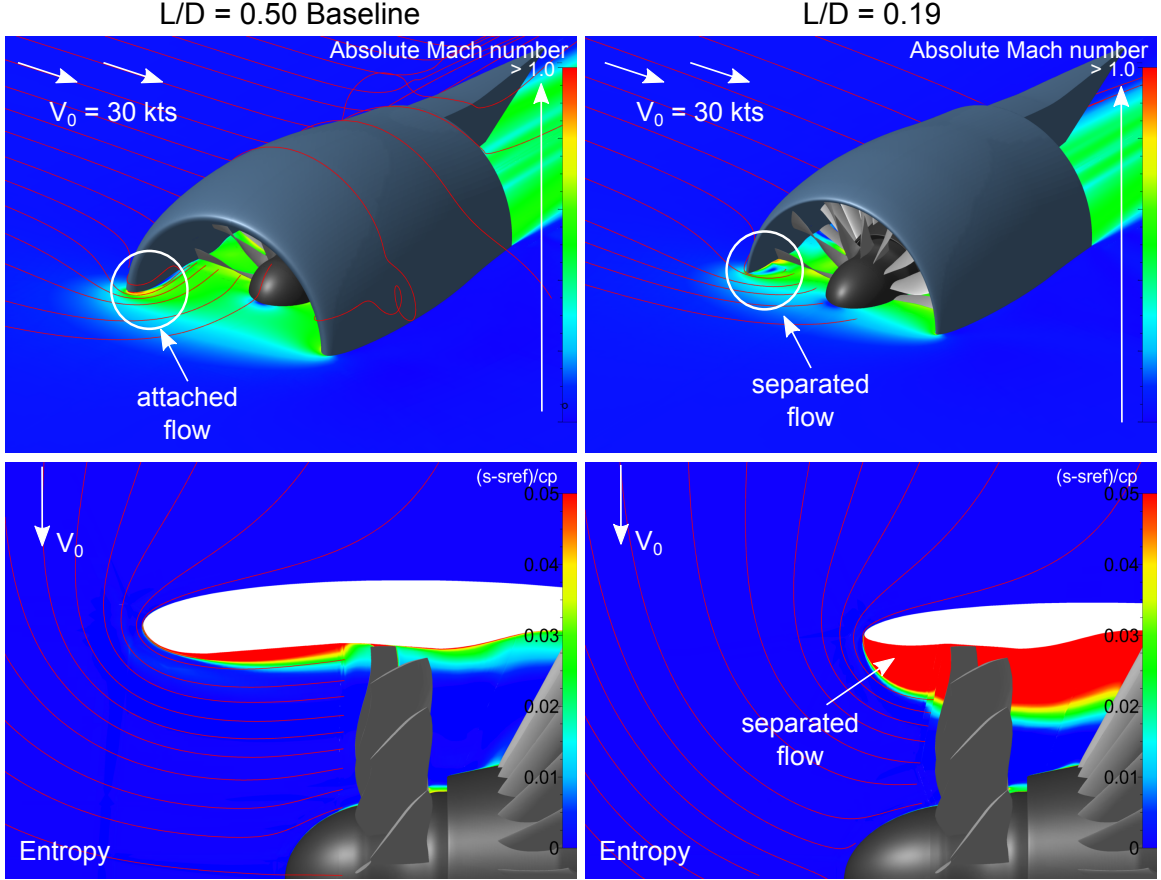


Figure 10-13: Time-averaged distributions of Mach number (left) and entropy (right) for the baseline inlet (left) and the candidate short-inlet design with  $L/D = 0.19$  (right) at the cross-wind operating condition.

area, the ground plane was not modeled. As a result, the inlet vortex, which can impact the rotor performance at the cross-wind condition [96, 97], is not captured. The focus of the current analysis is on the increased tendency for the flow to separate in short inlets. In the long-inlet design, the over-speed at the inlet lip is controlled by constraining the maximum curvature near the highlight location and the inlet flow is separation-free at the cross-wind condition. In the short inlet, the flow cannot accommodate the increased curvature at the thin inlet lip and consequently separates, resulting in a large region of recirculation and increased losses, as illustrated in the entropy distributions on the horizontal plane in the bottom plots in Fig. 10-13.

Compared to the baseline case, the inlet stagnation pressure recovery,  $\pi_{inlet} = \frac{p_{t2}}{p_{t0}}$ , is reduced by 1% in the short inlet,  $\Delta\pi_{inlet} = \pi_{inlet,L/D=0.19} - \pi_{inlet,L/D=0.50} = -0.01$ .

In addition, the separated flow region creates aerodynamic blockage and reduces the corrected flow by 25 % if the bypass nozzle area is held constant. Due to the degradation in the inlet performance, the fan efficiency decreases by  $\Delta\eta_{fan} = -8.5 \%$ .

To overcome the inlet flow separation and alleviate the incidence distortion, a blow-in door system in the inlet is considered. The suggested concept has been employed in previous ultra-short inlet installations, for example in the integration of the JT3D/TF33 engine on the C-141 military airlifter [98]. This installation featured a slotted inlet with 12 sets of outer doors mounted on the nacelle cowl. The doors open against a spring force if the pressure drop between the low-pressure region on the inlet internal side and the pressure in the external flow on the outside of the inlet exceeds a critical value. By injecting additional mass flow into the inlet flow, flow separation is avoided and the inlet flow non-uniformities are alleviated. Blow-in doors were also used in early installations of the JT9D engine on the Boeing 747-100.

While blow-in door systems have been demonstrated to improve the performance of inlet and fan at low-speed conditions, the increase in take-off noise and additional weight and system complexity would likely prevent a mass-injection system from being implemented in future installations. Despite these disadvantages, blow-in doors are considered here to quantify the potential for fan performance benefits due reductions in the inlet flow non-uniformity in a short-inlet propulsor at the crosswind operating condition.

A computational model of the mass injection system was set up to quantify the potential for improved inlet performance through the implementation of blow-in doors in the candidate short-inlet propulsor. The computational model is illustrated in Fig. 10-14. On the nacelle external surface, a region with an outlet boundary condition is specified to draw mass flow into the inlet. The static pressure at the boundary is set to the fan face value. The mechanism to turn the flow through the blow-in door is not modeled. Instead, an inlet boundary condition is specified on the inlet internal surface with the stagnation temperature set equal to the free-stream value and the stagnation pressure assumed to be reduced relative to the free-stream value by the viscous losses inside of the blow-in door system. In addition, an outflow angle  $\beta$  between the surface

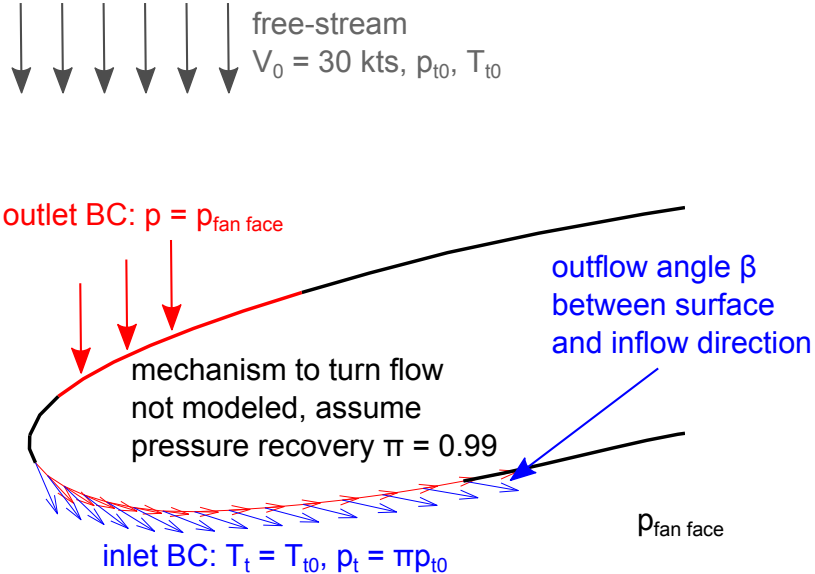


Figure 10-14: Computational model of blow-in doors in inlet of  $L/D = 0.19$  candidate design.

tangential direction and the inflow direction is defined to simulate the turning of the flow between the inlet and the exit of the blow-in doors. The axial extents of the regions with mass extraction and injection are chosen based on the mass flow needed to achieve the engine corrected flow provided by the baseline configuration and the requirement for equal mass flows at the inlet and the exit of the blow-in doors.

The Mach number distributions on the horizontal plane for the  $L/D = 0.19$  short-inlet propulsor with and without mass injection are given in the top left and right in Fig. 10-15, respectively, and the stagnation pressure distributions at the fan face are presented in the bottom plots. The blow-in doors are demonstrated to achieve fully attached inlet flow and alleviate the stagnation pressure distortion. The loss in inlet pressure recovery relative to the long-inlet baseline is completely recovered with the blow-in doors. As shown in Fig. 10-16, the corrected flow is increased by 30 % relative to the the configuration without mass injection and the reduction in the inlet flow distortion translates to a 7 % improvement in fan efficiency. The speedline computed at the take-off condition is included in Fig. 10-16 to approximate the trend in efficiency over a range of corrected flows. The bypass nozzle area was not changed in the comparison of the propulsor performance at cross-wind.

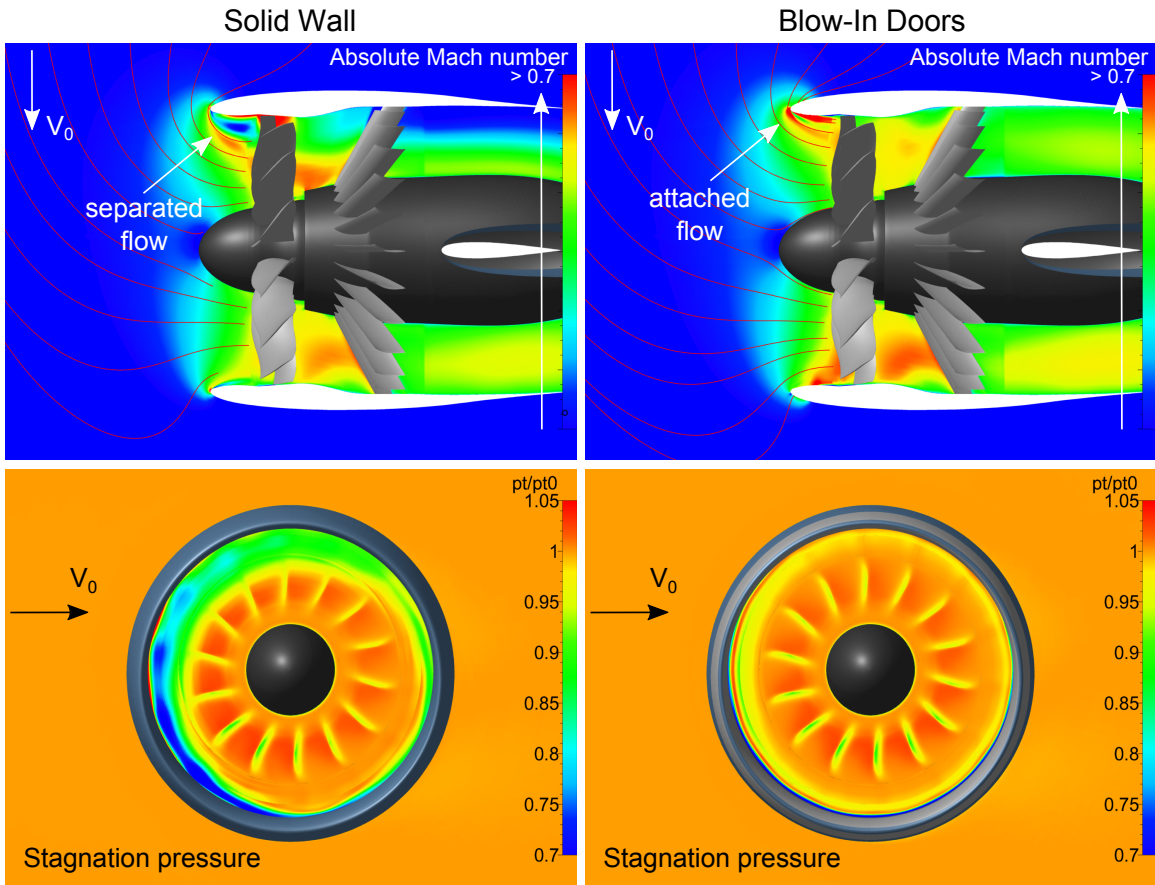


Figure 10-15: Time snapshot of distributions of Mach number (top) and stagnation pressure at the fan face (bottom) for the candidate short-inlet design with solid inlet (left) and blow-in doors in the inlet (right) at the cross-wind operating conditions.

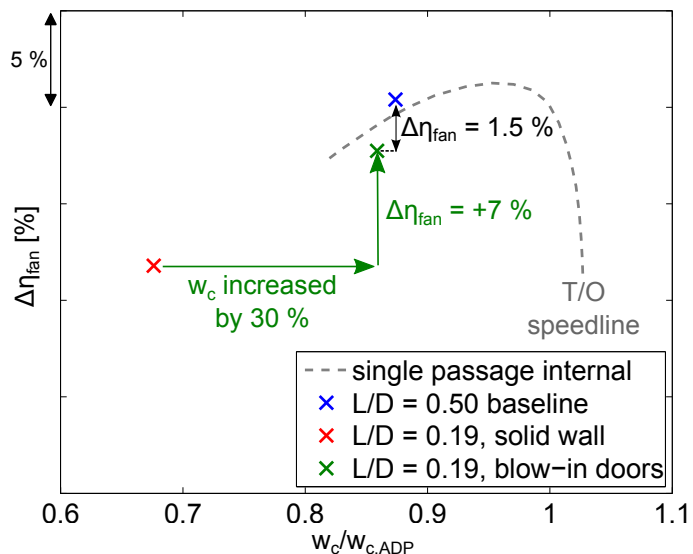


Figure 10-16: Increase in corrected flow and fan efficiency due to blow-in doors in the candidate short inlet with  $L/D = 0.19$  at the cross-wind operating condition.

In summary, inlet mass injection is demonstrated as an effective strategy to enhance the performance of short inlets and achieve fan performance similar to long-inlet configurations. However, in the light of the increase in propulsor weight and system complexity due to the integration of a system of blow-in doors, future work is recommended to address the question of whether an increased inlet length to an  $L/D$  of between 0.25 and 0.4 would be sufficient in reducing the inlet flow distortion to an acceptable level in terms of fan performance.

# Chapter 11

## Conclusions and Future Work

The objective of this thesis was to explore the uncharted territory of short inlets and nacelles for low-FPR propulsors, determine the aerodynamic mechanisms limiting the design of short inlets, and define a short inlet-fan system with equal or improved propulsive efficiency relative to a long-inlet baseline configuration with an inlet length over fan diameter ratio of  $L/D = 0.5$ .

A short-inlet configuration with  $L/D = 0.25$  was presented which maintains the cruise propulsive efficiency of the baseline case while limiting fan efficiency penalties to below  $\Delta\eta_{fan} = -1.5\%$  and providing for sufficient LPC stability margin at the off-design operating conditions. The enabling idea in the design of the candidate short inlet and nacelle was the development of a body-force-based fan model to account for the enhanced coupling between the fan stage and the non-uniform inlet flow. A summary and conclusions of this work are presented next, followed by recommendations for future work based on the findings in this thesis.

### 11.1 Summary

The requirement for capturing the increased fan-inlet and fan-exhaust interaction in the design process of short inlets and nacelles for low-FPR propulsors motivated the use of body force representations of the rotor and stator blade rows. The development of the body-force-based approach was the focus of Chapter 3.

The validation of the body-force-based approach was presented in Chapter 4. The determination of the body force field is based on the blade surface pressures extracted from steady, single-passage RANS simulations over the entire blade surface and a single body force distribution was demonstrated to capture the off-design increase in the blade losses along a speedline. The method's capabilities were evaluated using results from full-domain URANS simulations. The inflow distortion in short inlets is associated with shaft-order disturbance wavelengths and characterized by reduced frequencies of 0.4 and below. At these conditions, the method captures the coupling of the rotor and the inlet flow and the distortion transfer with sufficient accuracy, enabling the assessment of the impact of inlet, nacelle, and spinner design changes on the propulsor performance. For flow conditions, in which unsteadiness plays a more important role, unsteady body force simulations and the implementation of a time-lag model to account for the delayed response of the body force to changes in the inflow may be required.

In contrast to two-dimensional actuator disk models, the flow property changes are spread over the axial extent of the blade domain in the developed body-force-based approach and the axial flow re-distribution within the blade row is captured. Due to the dependence of the body force on the blade camber geometry, the three-dimensional body force method allows to assess the impact of changes in the blade stagger and camber definition on the inlet and rotor performance.

The body force method is coupled with a Bezier-spline-based description of the three-dimensional inlet and nacelle surfaces. The integrated design framework was outlined in Chapter 5. The body-force-based design method was demonstrated to reduce the computational cost by up to two orders compared to full-annulus URANS simulations by enabling simplified mesh topologies and eliminating the need for mixing planes or rotating domains with sliding interfaces. In combination with a modular and automated grid setup, a fast and flexible design framework was provided for the parametric exploration of the short-inlet design territory.

In Chapter 6, a baseline configuration at the low end of the current inlet design practice ( $L/D = 0.5$ ) was introduced. The computational model of the baseline

propulsor includes the bypass and core exhaust flows, the core inflow, and the pylon and bifurcation in order to capture the fan-exhaust interactions, in particular the influence of the pylon potential field on the rotor performance. The stagnation pressure distortion was shown to be the superposed result of the de-coupled contributions from the pylon upstream influence and the impact of the non-uniform inlet flow. The interaction of the rotor with the pylon potential field was suggested to be the dominant mechanism for the incidence distortion in the baseline propulsor at cruise.

Engine propulsive efficiency was introduced in Chapter 7 as the critical metric in the evaluation of candidate short-inlet designs. The engine propulsive efficiency captures the impact of inlet and nacelle design changes on the fan stage and on the nacelle aerodynamic performance. The outcomes of a sensitivity analysis for the engine propulsive efficiency highlighted the importance of limiting fan performance penalties in short-inlets, as the benefits from reduced nacelle drag can be offset by the increase in rotor losses if the incidence distortion is elevated.

The results of a parametric inlet length study designs suggested that the propulsor performance suffers from a drop-off in fan efficiency and a significant increase in the core inflow stagnation pressure distortion at off-design conditions if the inlet length is shortened to an  $L/D$  of 0.1. In the light of these findings, the focus of the design strategy presented in Chapter 8 was on short-inlet and -nacelle shapes with an  $L/D$  above approximately 0.2.

Two optimized candidate short-inlet designs were defined using body force simulations. The first design features an  $L/D = 0.25$  and was the focus of Chapter 9. The short-inlet propulsor was demonstrated to come close to reaching the baseline propulsor performance without changes to the rotor and stator blade designs. By accounting for aircraft system level benefits due to the reduction in nacelle drag and weight, this propulsor was hypothesized to offer fuel burn benefits over an installation based on the baseline configuration. Two concepts were suggested to further enhance the propulsor performance: (1) modifying the rotor camber distribution to mitigate the impact of the incidence distortion due to the high Mach number region and (2) eliminating the rotor back pressure distortion due to the pylon and bifurca-

tion potential fields through assuming an appropriately tailored FEGV design. By implementing both of these concepts, the candidate short-inlet propulsor achieved a 0.25 % higher propulsive efficiency relative to the baseline configuration.

The second optimized design with  $L/D = 0.19$  was presented in Chapter 10. The nacelle drag was reduced by 17.8 % compared to the baseline propulsor due to the reduction in nacelle area. However, the increased coupling between the rotor and the non-uniform inlet flow resulted in a fan efficiency penalty of 1.6 %, translating to a 0.8 % lower propulsive efficiency at cruise. At the low-speed, high angle-of-attack conditions such as wing  $C_{L\max}$ , the reduction in inlet length from an  $L/D$  of 0.25 to 0.19 yields an additional increase in the incidence distortion over the entire fan face and causes the rotor to locally operate near choke. As a result, the fan efficiency penalty rises to 3.9 % and the circumferential stagnation pressure distortion in the core inflow is large enough to exhaust most of the LPC stability margin. A configuration with a pitched fan case and a system of blow-in doors in the inlet were presented to alleviate the inlet flow distortion at design and off-design conditions.

## 11.2 Synthesis of Short-Inlet Design Strategy

The developed strategy for the design of short inlets is driven by the competing requirements for low nacelle drag at cruise and low rotor incidence distortion at off-design conditions. Limiting the flow acceleration and avoiding shocks on the aft part of the nacelle external surface at cruise requires a reduction of the maximum nacelle diameter in short inlets and nacelles compared to conventional designs.

The top inlet and nacelle profiles must be slender and at the leading edge, the profile camber line must be aligned with the stagnation point streamline to limit the over-speed around the outer nacelle surface at cruise. The minimum inlet lip thickness is constrained by the requirement for separation-free inlet flow at off-design conditions such as take-off level or cross-wind.

The orientation of the bottom inlet lip was found to be a key parameter in alleviating the over-speed along the inlet internal surface at low-speed, high angle-of-

attack conditions. “Un-cambered” profiles with thick inlet lip shapes are required for separation-free inlet flow and limited incidence distortion at off-design conditions.

Extending the spinner shifts the stagnation point outward to the nacelle external surface and represents an effective strategy for alleviating the over-speed on the outer nacelle surface at cruise. Extended spinner shapes can enable thicker inlet leading edge profiles for benefits at low-speed conditions. The downside of increasing the spinner length is the enhanced over-speed along the inlet internal surface at off-design conditions due to the outward shift in the stagnation point and a balanced design must be achieved between improved cruise and reduced off-design propulsor performance.

A coupled inlet-fan design approach is needed to maximize the performance of a short-inlet propulsor. Inlet length and shape modifications lead to changes in the fan blade design requirements, such as the capability to deal with a region of increasing fan face Mach number as the inlet is shortened. By accounting for the changes in the requirements in the blade design, for example by altering the camber distribution, the rotor performance can be improved, leading to propulsor system level benefits.

The developed design strategy employs a combination of supercritical airfoils and a parametric description of the lower inlet lip to balance the contradictory requirements set by the design and off-design conditions. The increased interaction of the rotor with the region of high Mach number over the outer span at the bottom inlet was identified as the main aerodynamic mechanism limiting the design of short inlets. Consequently, the presented design approach placed particular emphasis on alleviating the over-speed along the lower inlet lip at the cruise and off-design conditions.

For conventional nacelle and inlet designs with an  $L/D$  between 0.5 and 0.85, nacelle laminar flow control has been demonstrated to provide reductions of 1 – 2 % in overall aircraft drag, which translate directly into an improved specific fuel consumption [18]. In low-FPR propulsors with large fan diameters, nacelle laminar flow control would allow longer inlets with the same nacelle drag offered by short inlets without flow control. Laminar flow control would shift the maximum in engine propulsive efficiency to a larger inlet  $L/D$  and longer inlets mitigate the rotor incidence distortion and alleviate fan efficiency penalties relative to a conventional inlet length.

The wing upwash at cruise is the main driver for inlet droop and the main source for the increase in incidence distortion in short inlets compared to long inlets. Alternative engine integration concepts such as for example fuselage-mounted or over-the-wing installations could reduce the engine angle-of-attack and alleviate the incidence distortion and rotor losses in short inlets.

## 11.3 Key Outcomes and Conclusions

The conclusions deduced from the results in this work are divided into two categories: those which apply to the development of general design guidelines for short inlets using the new body-force-based inlet and nacelle design framework and those which are specific to the assessment of the two candidate short-inlet designs.

The general conclusions regarding the body force method and the short-inlet design strategy are:

1. A body-force-based model of the fan captures the increased fan-inlet coupling and the distortion transfer in short-inlet propulsors. Combined with a spline-based tool for the definition of three-dimensional inlet and nacelle surface geometries, the body-force-based approach enables the parametric exploration of the short-inlet design space.
2. The interaction of the fan rotor with a region of high Mach number over the outer span at the fan face is identified as the key aerodynamic mechanism limiting the design of short inlets. The local increase in the Mach number is driven by the flow acceleration along the inlet internal surface coupled with a reduction in effective flow area at cruise and due to a supersonic over-speed around the bottom inlet lip at low-speed conditions with high angles-of-attack.
3. A short-inlet design strategy based on supercritical airfoils and a parametric description of the inlet shape including the orientation of the inlet lip relative to the stagnation point streamline is demonstrated as an effective approach to limit wave drag at cruise and achieve fully attached flow at off-design conditions.

- As the inlet is shortened, there is a hypothesized optimum in the propulsive efficiency due to two competing effects: (1) fan efficiency penalties due to increased inlet flow non-uniformity and (2) reduced nacelle drag and increased inlet pressure recovery due to reduced surface area. The results for inlet pressure recovery  $\pi_{inlet}$ , nacelle drag  $D_{nac}$ , fan efficiency  $\eta_{fan}$ , and propulsive efficiency  $\eta_{prop}$  are summarized in Fig. 11-1 for the baseline and the two optimized candidate short-inlet propulsors. All of the results are relative to the baseline propulsor and the data points are connected by trend lines. The dependence of the inlet pressure recovery and the nacelle drag on  $L/D$  is close to linear. However, the fan efficiency, which drives the changes in propulsive efficiency, is non-linear in  $L/D$ . Guided by the sensitivity analysis, the trend in the propulsive efficiency is constructed from the curves for  $\pi_{inlet}$ ,  $D_{nac}$ , and  $\eta_{fan}$ , and the maximum in propulsive efficiency is suggested to fall between an  $L/D$  of 0.25 and 0.4.

The specific conclusions are:

- A feasible short-inlet design with  $L/D = 0.25$  is demonstrated to achieve an engine propulsor efficiency close to the  $L/D = 0.5$  baseline propulsor performance ( $\Delta\eta_{prop} = -0.14\%$ ) at cruise. In this case, the nacelle drag benefit of 16% is outweighed by the rotor performance penalty of 1.1% due to the increase in rotor incidence distortion. At the off-design conditions, fully attached inlet flow is maintained and the reduction in fan efficiency is limited to 2%.
- Modifying the rotor blade camber distribution over the outer span to reduce radial incidence distortion enables a fan efficiency improvement of 0.15% at cruise, which translates to an increase of 0.1% in propulsive efficiency.
- Shielding the rotor from the pylon and bifurcation upstream influence increases the fan efficiency by 0.25% and leads to an engine propulsive efficiency benefit of 0.26%. Alleviating the interaction of the rotor with the pylon and bifurcation potential fields can be achieved for example through a tailored, non-axisymmetric FEGV design.

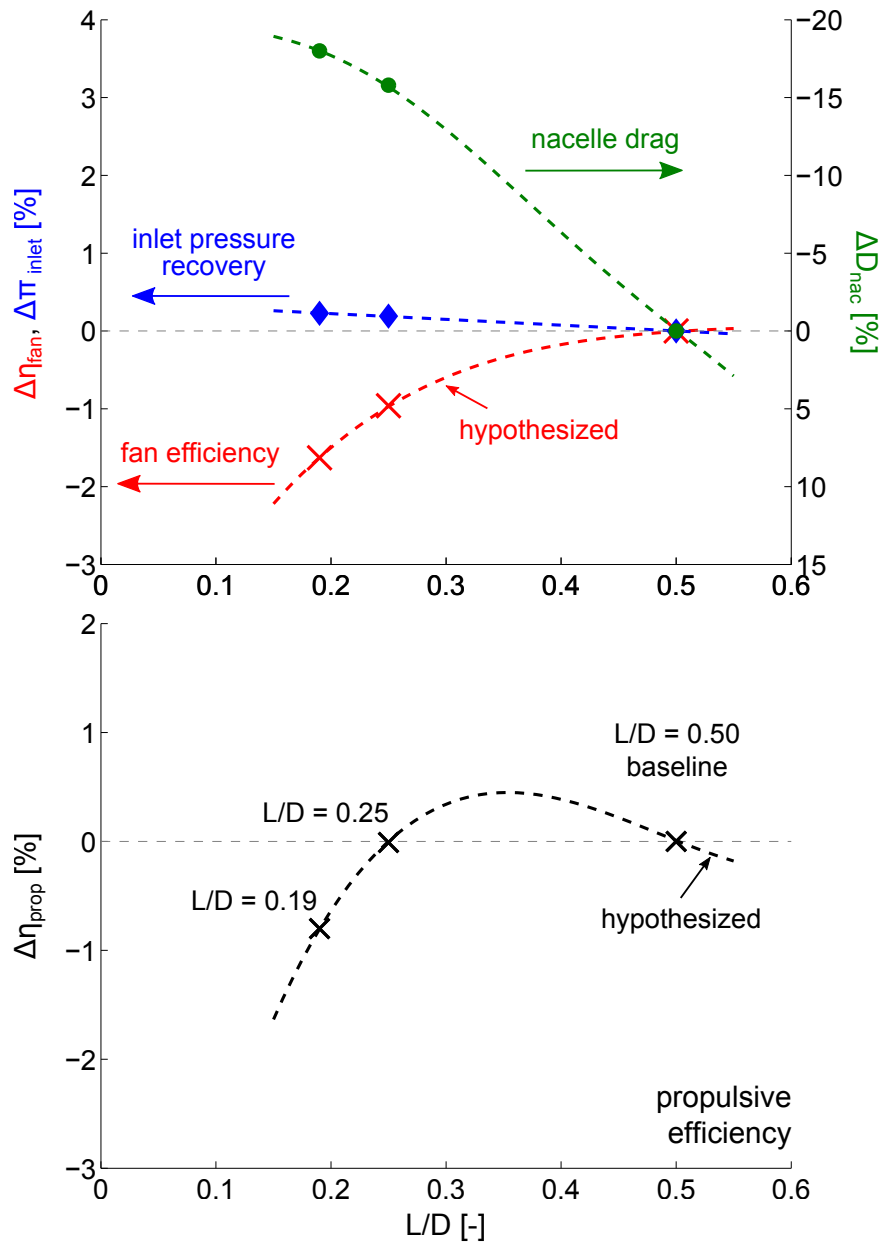


Figure 11-1: Hypothesized optimum in propulsive efficiency with inlet  $L/D$  (bottom) as a result of the competing effects between fan efficiency, nacelle external drag and inlet pressure recovery (top).

4. A candidate short-inlet design with  $L/D = 0.19$  offers a 17.8% reduction in nacelle drag over the long-inlet baseline case. The considerable increase in the interaction of the rotor with the non-uniform inlet flow results in a fan efficiency penalty of 1.6% at cruise, leading to a propulsive efficiency reduction of 0.8%. At the off-design operating conditions, the fan efficiency is reduced by up to 3.9% relative to the long-inlet baseline propulsor.
5. To take advantage of the additional drag and weight reductions in inlets with  $L/D < 0.25$ , advanced concepts are suggested in order to achieve a design and off-design performance similar to the long-inlet baseline propulsor. Aligning to fan rotor axis with the inflow at cruise by pitching the fan case reduces the rotor incidence distortion and increases the fan efficiency by 0.8%. The integration of blow-in doors in the inlet eliminates flow separation at low-speed conditions such as cross-wind. Due to the increased weight and complexity of active flow control such as blow-in doors, aero-mechanical challenges due to the increased blade loading variations, and the reduced potential for acoustic treatment along the inlet surfaces, low-FPR propulsors featuring inlets with  $L/D$  below 0.25 are unlikely.

## 11.4 Recommendations for Future Work

The performance assessment presented in this thesis is focused on the comparison of short-inlet configurations relative to a long-inlet baseline case without accounting for the impact of short-nacelle installations on the aircraft system level. The evaluation of the short-inlet and -nacelle designs could be extended to account for the change in aircraft performance due to the reduction in the thrust requirement enabled by weight and drag benefits. The reduction in thrust requirement allows the propulsor to be scaled to a smaller size, offering additional weight and drag benefits. For a given aircraft mission, the potential reduction in the fuel burn consumption achieved by a short-inlet propulsor with improved engine propulsive efficiency could be quantified using aircraft design and optimization methods such as for example TASOPT

(Transport Aircraft System OPTimization, [99]) or FLOPS (FFlight OPTimization Software, [100]), which account for changes in nacelle weight and interference drag through appropriate empirical correlations. The nacelle drag can be extracted directly from full-annulus body force or URANS simulations with the methodology presented in this thesis. The reduction in nacelle weight possibly also offers structural benefits in the pylon design.

Installation challenges due to the larger diameters of low-FPR, high-BPR propulsors include for example a reduced nacelle-ground clearance, which may require a reduction in the vertical distance between the upper nacelle surface and the wing leading edge. In addition, the installation of shorter nacelles could result in a reduction of the horizontal distance between the inlet highlight location and the wing leading edge. The impact of the reduced distance between the high Mach number region on the front part of the outer nacelle surface and the pylon and wing structures on interference drag should be addressed.

In addition to the wing  $C_{L\max}$ , cross-wind, and take-off operating conditions addressed in this thesis, there are other conditions which play an important role in the design of the inlet and the nacelle. A specific example is the engine-out “windmill” condition, where the rotor is in free-wheeling mode and the mass flow ratio is significantly lower than when the engine is operational. Due to the reduction in the mass flow ratio, there is considerable flow spillage over the nacelle leading edge with potentially supersonic over-speed and a substantial increase in wave drag. The moment on the aircraft due to the windmilling drag caused by the loss of an engine at takeoff governs the size of the aircraft vertical stabilizer required to maintain yaw control [88]. The windmilling drag generated by the two candidate short-inlet propulsors defined in this work should be quantified since the presented designs feature slender upper inlet lips which might cause prohibitive wave drag penalties at the engine-out condition.

Based on the outcomes of this thesis, it is hypothesized that an inlet design with an  $L/D$  between 0.25 and 0.4 could achieve additional propulsor performance benefits at cruise relative to the  $L/D = 0.25$  candidate short-inlet design due to the expected

reduction in incidence distortion and fan efficiency penalty. A small increase in the inlet length would also enable rounder inlet leading edge shapes, alleviating the supersonic over-speed along the inlet internal speed at off-design operating conditions such as wing  $C_{L\max}$  or cross-wind and mitigating the expected wave drag penalty at the engine-out condition. An additional inlet design with an  $L/D$  in the range of 0.3 to 0.35 could be defined to test the hypothesis of achieving an improved propulsive efficiency compared to the long-inlet baseline.

Due to the low computational cost enabled by the body force simulations, the design framework developed in this thesis could be extended to allow for an automated optimization of the inlet and nacelle shapes. Appropriate limits on the circumferential incidence distortion or the magnitude and circumferential variation of the normal body force should be defined to account for fan blade stress constraints. Similarly, the stagnation pressure distortion in the core inflow could be constrained to a critical value to ensure a sufficient LPC stability margin. By including these constraints in an optimization, the impact of the non-uniform inflow and the fan blade aero-mechanical design and the LPC stability could be quantified during the design process based on the body force results.

The reduction in fan noise attenuation potential and shielding opportunities provided by short inlets should be addressed. The body-force-based approach has been successfully used to estimate upstream-propagated tonal fan noise [57, 58] through non-uniform flow. Modeling rotor-stator interaction would require obtaining accurate blade wakes using the body force approach and accounting for the impact of blade row blockage on noise propagation.



# Bibliography

- [1] NASA. State-of-the-art subsonic engine sfc, 1998.
- [2] Hughes, C. The Promise and Challenges of Ultra High Bypass Ratio Engine Technology and Integration. In *49th AIAA Aerospace Sciences Meeting and Exhibit*, Orlando, FL, January 4-7 2011.
- [3] Lord, W. Fan Stream Performance in High-BPR Turbofan Engines. MIT GTL Seminar Series, September 2008.
- [4] Hughes, C. Aircraft Engine Technology for Green Aviation to Reduce Fuel Burn. In *3rd AIAA Atmospheric Space Environments Conference*, Honolulu, HI, June 27-30 2011. AIAA 2011-3531.
- [5] Kerner, J. An Assessment of Body Force Representations for Compressor Stall Simulation. Master's thesis, MIT, Department of Aeronautics and Astronautics, February 2010.
- [6] Gong, Y., Tan, C., Gordon, K., and Greitzer, E. A Computational Model for Short-Wavelength Stall Inception and Development in Multistage Compressors. *Journal of Turbomachinery*, 121:726–734, October 1999.
- [7] Harris, C. NASA Supercritical Airfoils. Technical Report TP-2969, NASA, March 1990.
- [8] Brand, M. An Improved Blade Passage Model for Estimating Off-Design Axial Compressor Performance. MS thesis, MIT, Department of Aeronautics and Astronautics, September 2013.

- [9] Green, J. Mitigating the Environmental Impact of Aviation: Opportunities and Priorities. Technical report, Report of the Greener by Design Science and Technology Sup-Group, published by the Royal Aeronautical Society, July 2005.
- [10] Owens, R., Hasel, K., and Mapes, D. Ultra High Bypass Turbofan Technologies for the Twenty-First Century. In *26th AIAA/SAE/ASME/ASEE Joint Propulsion Conference*, Orlando, Florida, July 16-18 1990. AIAA paper 1990-2397.
- [11] Powell, C., and Preisser, J. NASA Subsonic Jet Transport Noise Reduction Research. In *22nd Congress of International Council of the Aeronautical Sciences*, Harrogate, United Kingdom, August 28-September 1 2000. paper ICAS 2000-3.9.1 (IL).
- [12] Suder, K., Delaat, J., Hughes, C., Arend, D., and Celestina, M. NASA Environmentally Responsible Aviation Project's Propulsion Technology Phase I Overview and Highlights of Accomplishments. In *51st AIAA Aerospace Sciences Meeting*, Dallas, TX, January 7-10 2013. AIAA 2013-0414.
- [13] Cumpsty, N. Preparing for the Future: Reducing Gas Turbine Environmental Impact - IGTI Scholar Lecture. *Journal of Turbomachinery*, 132, October 2010.
- [14] Neise, W., and Enghard, L. Technology Approach to Aero Engine Noise Reduction. *Aerospace Science and Technology*, 7:352–363, 2003.
- [15] Hall, C., and Crichton, D. Engine Design Studies for a Silent Aircraft. *Journal of Turbomachinery*, 129:479–487, 2007.
- [16] de la Rosa Blanco, E., Hall, C., and Crichton, D. Challenges in the Silent Aircraft Engine Design. In *45th AIAA Aerospace Sciences Meeting and Exhibit*, Reno, Nevada, January 8-11 2007. AIAA paper 2007-454.
- [17] MacIsaac, B., and Langton, R. *Gas Turbine Propulsion Systems*. AIAA Education Series. John Wiley and Sons, Limited, West Sussex, United Kingdom, 1st edition, 2011.

- [18] Lord, W., MacMartin, D., and Tillman, T. Flow Control Opportunities in Gas Turbine Engines. In *Fluids 2000*, Denver, Colorado, June 19-22 2000. AIAA paper 2000-2234.
- [19] Michel, U. The Geared Turbofan Technology - Opportunities, Challenges, and Readiness Status. In *1st CEAS European Air and Space Conference*, Berlin, Germany, September 10-13 2007.
- [20] Dunican, M. Installation of Innovative Turbofan Engines on Current Transport Airplanes. In *AIAA/AHS/ASEE Aircraft Design, Systems, and Operations Meeting*, St. Louis, Missouri, September 14-16 1987. AIAA paper 1987-2921.
- [21] Zimbrick, R., and Colehour, I. An Investigation of Very High Bypass Ratio Engines for Subsonic Transports. In *24th AIAA/ASME/SAE/ASEE Joint Propulsion Conference Proceedings*, Boston, Massachusetts, July 11-13 1988. AIAA paper 1988-2953.
- [22] Seddon, J., and Goldsmith, E. *Intake Aerodynamics*, volume II of *AIAA Education Series*. American Institute of Aeronautics and Astronautics, Inc., Washington, DC, 1999.
- [23] Hsiao, E., Naimi, M., Lewis, J., Dalbey, K., Gong, Y., and Tan, C. Actuator Duct Model of Turbomachinery Components for Powered-Nacelle Navier-Stokes Calculations. *Journal of Propulsion and Power*, 17(4):919–927, July-August 2001.
- [24] Boldman, D., Iek, C., Hwang, D., Jeracki, R., Larkin, M., and Sorin, G. Evaluation of Panel Code Predictions With Experimental Results of Inlet Performance for a 17-Inch Ducted Prop/Fan Simulator Operating at Mach 0.2. In *27th AIAA/SAE/ASME/ASEE Joint Propulsion Conference*, Sacramento, California, June 24-27 1991. AIAA paper 1991-3354.
- [25] Boldman, D., Iek, C., Hwang, D., Larkin, M., and Schweiger, P. Effect of a Rotating Propeller on the Separation Angle of Attack and Distortion in Ducted

Propeller Inlets. In *31th AIAA Aerospace Sciences Meeting and Exhibit*, Reno, Nevada, January 11-14 1993. AIAA paper 1993-0017.

- [26] Larkin, M., and Schweiger, P. Ultra High Bypass Nacelle Aerodynamics: Inlet Flow-Through Nacelle High Angle of Attack Distortion Test. Technical Report CR-1992-189149, NASA, July 1992.
- [27] Mendenhall, M., and Spangler, S. Theoretical Study of Ducted Fan Performance. Technical Report CR-1970-1495, NASA, January 1970.
- [28] Hirose, N., and Asai, K. Euler Flow Analysis of Turbine Powered Simulation and Fanjet Engine. *Journal of Jet Propulsion*, 7(6):1015–1022, 1991.
- [29] Uenishi, K., Pearson, M., Lehnig, T., and Leon, R. CFD-Based 3D Turbofan Nacelle Design System. In *8th AIAA Applied Aerodynamics Conference*, Portland, Oregon, August 20-22 1990. AIAA paper 1990-3081.
- [30] Chen, H., Yu, N., Rubbert, P., and Jameson, A. Flow Simulations for General Nacelle Configurations Using Euler Equations. In *21th AIAA Aerospace Sciences Meeting*, Reno, Nevada, January 10-13 1983. AIAA paper 1983-0539.
- [31] Bush, R. Engine Face and Screen Loss Models for CFD Applications. AIAA paper 1997-2076, June 1997.
- [32] Unno, M., Kodama, H., Nozaki, O., and Nishizawa, T. Unsteady Three Dimensional Navier-Stokes Simulations of Fan-OGV-Strut-Pylon Interaction. In *International Society for Airbreathing Engines*, Bangalore, India, September 3-7 2001. ISABE-2001-1197.
- [33] Marble, F. *Three-Dimensional Flow in Turbomachines*, volume X of *High Speed Aerodynamics and Jet Propulsion*, Hawthorne, W. R., ed. Princeton University Press, Princeton, NJ, pp. 83-166 edition, 1964.
- [34] Longley, J., and Greitzer, E. Inlet Distortion Effects in Aircraft Propulsion Systems. In *AGARD Lecture Series 183 on "Steady and Transient Performance*

*Prediction of Gas Turbine Engines*", pages 6–1 – 6–18. AGARD-LS-183, May 1992.

- [35] Jerez Fidalgo, V., Hall, C., and Colin, Y. A Study of Fan-Distortion Interaction Within the NASA Rotor 67 Transonic Stage. *Journal of Turbomachinery*, 134, September 2012.
- [36] Iek, C., Boldman, D., and Ibrahim, M. Analysis of an Advanced Ducted Propeller Subsonic Inlet. In *30th Aerospace Sciences Meeting and Exhibit*, Reno, Nevada, January 6-9 1992. AIAA paper 1992-0274.
- [37] Iek, C., Boldman, D., and Ibrahim, M. Three-Dimensional Viscous Flow Analysis of an Advanced Ducted Propeller Subsonic Inlet. *Journal of Propulsion and Power*, 11(2):236–243, 1995.
- [38] Gong, Y. *A Computational Model for Rotating Stall and Inlet Distortions in Multistage Compressors*. Ph.D. thesis, MIT, Department of Aeronautics and Astronautics, March 1999.
- [39] Daggett, D. Ultra-Efficient Engine Technology Systems Integration and Environmental Assessment. Technical Report CR-2002-211754, NASA, July 2002.
- [40] Daggett, D., Brown, S., and Kawai, R. Ultra-Efficient Engine Diameter Study. Technical Report CR-2003-212309, NASA, May 2003.
- [41] McCall, J., Tracksdorf, P., and Heinig, K. Advanced Ducted Engine Nacelle Aerodynamics and Integration Testing. *Journal of Engineering for Gas Turbines and Power*, 114:809–815, October 1992.
- [42] Ingraldi, A., Kariya, T., Re, R., and Pendergraft, O. Interference Effects of Very High Bypass Ratio Nacelle Installations on a Low-Wing Transport. *Journal of Engineering for Gas Turbines and Power*, 114:802–808, October 1992.
- [43] Wie., Y., Collier, F., Wagner, R., Viken, J., and Pfenninger, W. Design of a Hybrid Laminar Flow Control Engine Nacelle. In *30th Aerospace Sciences Meeting and Exhibit*, Reno, Nevada, January 6-9 1992. AIAA paper 1992-0400.

- [44] Albert, M., and Bestle, D. Aerodynamic Design Optimization of Nacelle and In-take. In *Proceedings of ASME Turbo Expo 2013: Turbine Technical Conference and Exposition*, San Antonio, TX, June 3-7 2013. GT2013-94857.
- [45] Hawthorne, W., and Novak, R. The Aerodynamics of Turbomachinery. *Annual Reviews of Fluid Mechanics*, 1:341–366, January 1969.
- [46] Smith, L. The Radial Equilibrium Equation of Turbomachinery. *Journal of Engineering for Power*, 88:1–12, January 1966.
- [47] Hynes, T., and Greitzer, E. A Method for Assessing Effects of Inlet Flow Distortion on Compressor Instability. *Journal of Turbomachinery*, 109:371–379, July 1987.
- [48] Escuret, J., and Garnier, V. Numerical Simulations of Surge and Rotating-Stall in Multi-Stage Axial-Flow Compressors. In *30th AIAA/SAE/ASME/ASEE Joint Propulsion Conference*, Indianapolis, Indiana, June 27-29 1994. AIAA paper 1994-3202.
- [49] Longley, J. Calculating the Flowfield Behaviour of High-Speed Multi-Stage Compressors. ASME paper 97-GT-468, 1997.
- [50] Takata, H., and Nagano, S. Nonlinear Analysis of Rotating Stall. *Journal of Engineering for Power*, pages 279–293, October 1972.
- [51] Demargne, A., and Longley, J. Comparisons Between Measured and Calculated Stall Development in Four High-Speed Multi-Stage Compressors. ASME paper 97-GT-467, 1997.
- [52] Hale, A., and O'Brien, W. A Three-Dimensional Turbine Engine Analysis Compressor Code (TEACC) For Steady State Inlet Distortion. *Journal of Turbomachinery*, 120:422–430, July 1998.
- [53] Hale, A., Davis, M., and Sirbaugh, J. A Numerical Simulation Capability for Analysis of Aircraft Inlet-Engine Compatibility. *Journal of Engineering for Gas Turbines and Power*, 128:473–481, July 2006.

- [54] Xu, L., Hynes, T., and Denton, J. Towards Long Length Scale Unsteady Modeling in Turbomachines. In *Proceedings of the Institution of Mechanical Engineers, Part A: Journal of Power and Energy*, volume 217:75, 2003.
- [55] Adamczyk, J. Model Equations for Simulating Flows in Multistage Turbomachinery. In *30th International Gas Turbine Conference and Exhibit*, Houston, TX, March 18-21 1985. ASME Paper 85-GT-226.
- [56] Xu, L. Assessing Viscous Body Forces for Unsteady Calculations. *Journal of Turbomachinery*, 125:425–432, July 2003.
- [57] Defoe, J., Narkaj, A., and Spakovszky, Z. A Novel MPT Noise Methodology for Highly-Integrated Propulsion Systems with Inlet Flow Distortion . In *15th AIAA/CEAS Aeroacoustics Conference*, Miami, Florida, May 11-13 2009. AIAA paper 2009-3366.
- [58] Defoe, J., Narkaj, A., and Spakovszky, Z. A Body Force-Based Method for Prediction of Multiple-Pure-Tone Noise: Validation. In *16th AIAA/CEAS Aeroacoustics Conference*, Stockholm, Sweden, June 7-9 2010. AIAA paper 2010-3747.
- [59] Chima, R. A Three-Dimensional Unsteady CFD Model of Compressor Stability. Technical Report TM-2006-214117, NASA, February 2006.
- [60] Stewart, M. Axisymmetric Aerodynamic Numerical Analysis of a Turbofan Engine. ASME Paper 95-GT-338, 1995.
- [61] Chima, R. Calculation of Multistage Turbomachinery Using Steady Characteristic Boundary Conditions. In *36th AIAA Aerospace Sciences Meeting and Exhibit*, Reno, Nevada, January 12-15 1998. AIAA paper 1998-0968.
- [62] Moore, R. and Reid, L. Performance of Single-Stage Axial Flow Transonic Compressor with Rotor and Stator Aspect Ratios of 1.19 and 1.26, Respectively, and with Design Pressure Ratio of 1.82. Technical Report TP-1338, NASA, 1978.

- [63] Benneke, B. A Methodology for Centrifugal Compressor Stability Prediction. MS thesis, MIT, Department of Aeronautics and Astronautics, September 2009.
- [64] Greitzer, E., Tan, C., and Graf, M. *Internal Flow - Concepts and Applications*. Cambridge Engine Technology Series, 1st edition, 2004.
- [65] Moore, F. A Theory of Rotating Stall of Multistage Compressors, Parts I-III. *Journal of Engineering for Gas Turbines and Power*, 106:313–336, April 1984.
- [66] Lindau, J., and Owen, A. Nonlinear Quasi-Three-Dimensional Modeling of Rotating Stall and Surge. AIAA paper 1997-2772, 1997.
- [67] Lorentz, G. *Bernstein Polynomials*. American Mathematical Society, AMS Chelsea Publishing, 2nd edition, 1997.
- [68] Korakianitis, T., Rezaienia, M., Hamakhan, I., Avital, E., and Williams, J. Aerodynamic Improvements of Wind-Turbine Airfoil Geometries with the Prescribed Surface Curvature Distribution Blade Design (Circle) Method. In *Proceedings of ASME Turbo Expo 2011*, Vancouver, British Columbia, Canada, June 6-10 2011. GT2011-46728.
- [69] Melin, T., Amadori, K., and Krus, P. Parametric Wing Profile Description for Conceptual Design. In *3rd CEAS European Air and Space Conference*, Venice, Italy, October 24-28 2011.
- [70] Numeca International. *IGG User Manual Version 9.0*. Brussels, Belgium, April 2013.
- [71] Drela, M. *MTFLOW 2.03 - Multi-passage ThroughFLOW Design/Analysis Program*. Massachusetts Institute of Technology, 2010.
- [72] Numeca International. *FINE/Turbo User Manual Version 9.0*. Brussels, Belgium, April 2013.
- [73] Tecplot, Inc. *Tecplot 360 2013 User's Manual Release 1*. Bellevue, WA, 2013.

- [74] Spalart, P. and Allmaras, S. A One-Equation Turbulence Model for Aerodynamic Flows. In *30th Aerospace Sciences Meeting and Exhibit*, Reno, NV, January 6-9 1992. AIAA 1992-0439.
- [75] Barry, B., Parke, S., Brown, N., Riedel, H., and Sitzmann, M. The Flight Testing of Natural and Hybrid Laminar Flow Nacelles. In *Proceedings of ASME Turbo Expo 1994: Power for Land, Sea and Air*, The Hague, Netherlands, June 13-16 1994. ASME paper 94-GT-408.
- [76] Numeca International. *Autogrid 5 User Manual Version 9.0*. Brussels, Belgium, April 2013.
- [77] Green, J. Forced Response of a Large Civil Fan Assembly. In *Proceedings of ASME Turbo Expo 2008: Power for Land, Sea and Air*, Berlin, Germany, June 9-13 2008. GT2008-50319.
- [78] Milli, A., and Bron, O. Fully Parametric High-Fidelity CFD Model for the Design Optimisation of the Cyclic Stagger Pattern of a Set of Fan Outlet Guide Vanes. In *Proceedings of ASME Turbo Expo 2009: Power for Land, Sea and Air*, Orlando, FL, June 8-12 2009. GT2009-59416.
- [79] Naik, D., Ingraldi, A., and Pendergraft, O. Experimental Study of Pylon Geometries for Transport Aircraft. In *30th AIAA Aerospace Sciences Meeting and Exhibit*, Reno, NV, January 6-9 1992.
- [80] Crichton, D., Xu, L., and Hall, C. Preliminary Fan Design for a Silent Aircraft. *Journal of Turbomachinery*, 129:184–191, 2007.
- [81] Crichton, D., de la Rosa Blanco, E., Law, T., and Hileman, J. Design and Operation for Ultra Low Noise Take-Off. In *45th AIAA Aerospace Sciences Meeting and Exhibit*, Reno, NV, January 8-11 2007. AIAA 2007-456.
- [82] Michel, U. The Benefits of Variable Area Fan Nozzles in Turbofan Engines. In *49th AIAA Aerospace Sciences Meeting including the New Horizons Forum and Aerospace Exposition*, Orlando, FL, January 4-7 2011. AIAA 2011-226.

- [83] Ooba, Y., Murooka, T., Yamane, T., Nozaki, O., and Ishiyama, T. Unsteady Three-Dimensional Simulation Research of Fan-OGV-Strut-Pylon Interaction in Japanese ECO Engine Project. In *49th AIAA Aerospace Sciences Meeting and Exhibit*, Orlando, FL, January 4-7 2011. AIAA 2011-979.
- [84] Tschirner, T., Pfitzner, M., and Merz, R. Aerodynamic Optimisation of an Aeroengine Bypass Duct OGV-Pylon Configuration. In *Proceedings of ASME Turbo Expo 2002*, Amsterdam, The Netherlands, June 3-6 2002. GT2003-30493.
- [85] Colin, Y., Aupoix, B., Boussuge, J., and Chanez, P. Numerical Simulation and Analysis of Crosswind Inlet Flows at Low Mach Numbers. In *Proceedings of the 8th International Symposium on Experimental and Computational Aerothermodynamics of Internal Flows*, Lyon, France, July 2007.
- [86] Colin, Y., Aupoix, B., Boussuge, J., and Chanez, P. Prediction of Crosswind Inlet Flows: Some Numerical and Modelling Challenges. In *Proceedings of the 8th International Symposium on Experimental and Computational Aerothermodynamics of Internal Flows*, Lyon, France, July 2007.
- [87] Hall, C., and Hynes, T. Measurements of Intake Separation Hysteresis in a Model Fan and Nacelle Rig. *Journal of Propulsion and Power*, 22(4):872–879, July-August 2006.
- [88] Prasad, D., and Lord, W. Internal Losses and Flow Behavior of a Turbofan Stage at Windmill. *Journal of Turbomachinery*, 132, July 2010.
- [89] Lord, W. Thrust/Drag Control Volume Notes. Technical report, Pratt & Whitney, December 1991.
- [90] Malecki, R., and Lord, W. Aerodynamic Performance of Exhaust Nozzles Derived from CFD Simulation. In *31st AIAA/ASME/SAE/ASEE Joint Propulsion Conference and Exhibit*, San Diego, CA, July 10-12 1995. AIAA paper 1995-2623.

- [91] Langley, M. The Design of Axisymmetric Cowls for Podded Nacelles for High By-Pass Turbofan Engines. *Aeronautical Research Council*, 1979.
- [92] Barber, T., Ives, D., Nelson, D., and Miller, R. Computational Design and Validation Tests of Advanced-Concept Subsonic Inlets. *Journal of Propulsion*, 1(2):97–102, March-April 1985.
- [93] Wadia, A., Szucs, P., and Gundy-Burlet, K. Design and Testing of Swept and Leaned Outlet Guide Vanes to Reduce Stator-Strut-Splitter Aerodynamic Flow Interactions. *Journal of Turbomachinery*, 121:416–427, 1998.
- [94] Rubbert, P., Boctor, M., Cowan, S., and LaPrete, R. Concept and Design of Stators Tailored to Shield a Fan from Pressure Disturbances Arising in the Downstream Fan Duct. In *10th AIAA Aerospace Sciences Meeting*, San Diego, CA, January 17-19 1972. AIAA 1972-84.
- [95] Prasad, D., and Feng, J. Propagation and Decay of Shock Waves in Turbofan Engine Inlets. *Journal of Turbomachinery*, 127(1):118–127, 2005.
- [96] De Siervi, F., Viguier, H., Greitzer, E., and Tan, C. Mechanisms of Inlet-Vortex Formation. *Journal of Fluid Mechanics*, 124:173–207, 1982.
- [97] Brix, S., Neuwerth, G., and Jacob, D. The Inlet-Vortex System of Jet Engines Operating Near the Ground. In *18th AIAA Applied Aerodynamics Conference*, Denver, CO, January 14-17 2000. AIAA 2000-3998.
- [98] Hünecke, K. *Flugtriebwerke - Ihre Technik und Funktion*. Motorbuch Verlag, Stuttgart, Germany, 5 edition, 1980.
- [99] Greitzer, E., Bonnefoy, P., de la Rosa Blanco, E., Dorbian, C., Drela, M., Hall, D., Hansman, R., Hileman, J., Liebeck, R., Lovegren, J., Mody, P., Pertuze, J., Sato, S., Spakovszky, Z., Tan, C., Hollman, J., Duda, J., Fitzgerald, N., Houghton, J., Kerrebrock, J., Kiwada, G., Kordonowy, D., Parrish, J., Tylko, J., Wen, E., and Lord, W. N+3 Aircraft Concept Designs and Trade Studies,

Final Report - Volume 2. Technical Report CR-2010-216794/VOL2, NASA, December 2010.

- [100] L. McCullers. Aircraft Configuration Optimization Including Optimized Flight Profiles. In *Recent Experiences in Multidisciplinary Analysis and Optimization, Part 1*. NASA, Langley Research Center, 1984.
- [101] Kottapalli, A. Development of a Body Force Model for Centrifugal Compressors. MS thesis, MIT, Department of Aeronautics and Astronautics, September 2013.
- [102] Cumpsty, N. *Compressor Aerodynamics*. Krieger Publishing Company, Malabar, Fl, reprint edition, 2004.
- [103] MathWorks. *Matlab R2013a Documentation*. Natick, MA, March 2013.
- [104] Numeca International. *CFView User Manual Version 9.0*. Brussels, Belgium, April 2013.
- [105] Kiwada, G. Development of a Body Force Description for Compressor Stability Assessment. MS thesis, MIT, Department of Aeronautics and Astronautics, February 2008.

# Appendix A

## Original Blade Passage Model by Gong

### A.1 Interpretation of Normal Force Formulation

This chapter represents a detailed interpretation of Gong's original blade passage approach [38] by the thesis author based on extensive discussions at the Gas Turbine Laboratory.

#### A.1.1 Derivation of Normal Force Component Due to Blade Loading $\vec{f}_{n_{\nabla_p}}$

The derivation of  $\vec{f}_{n_{\nabla_p}}$  is discussed here using Fig. A-1, adopted from [101], which shows a blade passage with staggered spacing  $h$ , local blade metal angle  $\kappa$ , and deviation  $\delta$ . The blade metal angle  $\kappa = \kappa(x, r)$  is defined as the local angle between the camber line and the axial direction. The deviation angle is defined as the angle between the local relative flow direction and the local camber line,

$$\delta = \beta - \kappa, \quad (\text{A.1})$$

where the relative flow angle is given by  $\beta = \frac{W_\theta}{W_x}$ . Radial components of velocity and blade force are assumed negligible,  $\frac{W_r}{W} \ll 1$  and  $\frac{f_{n,r}}{f_n} \ll 1$ .

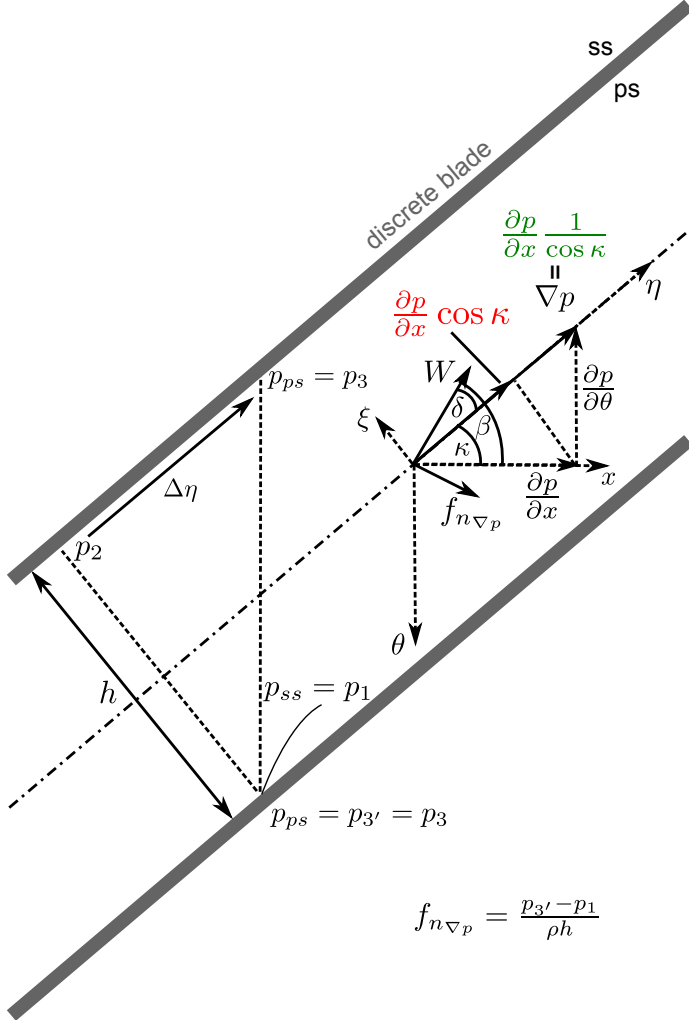


Figure A-1: Normal force component due to blade loading.

For small deviation angles, the normal force due to the pressure difference across a blade is approximated by

$$f_{n\nabla p} = \frac{p_{ps} - p_{ss}}{\rho h} = \frac{p_{3'} - p_1}{\rho h} = \frac{p_3 - p_1}{\rho h}, \quad (\text{A.2})$$

where  $p_{3'} = p_3$  for identical blades and uniform inflow. Assuming a straight staggered channel with a pressure gradient in the direction of the channel,  $\nabla p = \frac{\partial p}{\partial \eta}$ , the pressure at location 3 can be expressed as

$$p_3 = p_2 + \Delta\eta \frac{\partial p}{\partial \eta} = p_2 + h \tan \kappa \frac{\partial p}{\partial \eta}. \quad (\text{A.3})$$

Since the pressure gradient is assumed to be in the direction of the blade passage, the cross-passage component is zero,  $\frac{\partial p}{\partial \xi} = 0$ , and therefore the pressures at stations 1 and 2 are equal,  $p_1 = p_2$ . Combining Equations A.2 and A.3 yields

$$f_{n_{\nabla p}} = \frac{1}{\rho} \frac{\partial p}{\partial \eta} \tan \kappa. \quad (\text{A.4})$$

Gong expressed the in-passage component of the pressure gradient as a function of the axial pressure gradient only since  $\frac{\partial p}{\partial \theta} = 0$  when modeling axisymmetric flow and assumed  $\frac{\partial p}{\partial \theta} = 0$ , such that

$$\frac{\partial p}{\partial \eta} = \frac{\partial p}{\partial x} \cos \kappa, \quad (\text{A.5})$$

yielding a final expression for the normal force component due to the pressure gradient in a staggered channel of

$$f_{n_{\nabla p}} = \frac{1}{\rho} \frac{\partial p}{\partial x} \sin \kappa. \quad (\text{A.6})$$

However, it is important to note here that the formulation of the in-passage component of the pressure gradient in Equation A.5 is inconsistent, since for  $\frac{\partial p}{\partial \theta} = 0$ , the pressures at locations 1 and 3 are equal,  $p_1 = p_3$ , such that there is no pressure difference across the blade, and  $f_{n_{\nabla p}} = 0$  from Equation A.2. Since the derivation is based on a blade passage with discrete blades, the circumferential component of the pressure gradient is actually non-zero (and there is a non-zero pressure difference across the blade), and the correct expression of the in-passage component of the pressure gradient as a function of geometry and its axial component is

$$\frac{\partial p}{\partial \eta} = \frac{\partial p}{\partial x} \frac{1}{\cos \kappa}, \quad (\text{A.7})$$

resulting in a normal force component due to the pressure gradient in a staggered channel of

$$f_{n_{\nabla p}} = \frac{1}{\rho} \frac{\partial p}{\partial x} \frac{\sin \kappa}{\cos^2 \kappa}. \quad (\text{A.8})$$

A second inconsistency in the derivation of  $f_{n_{\nabla p}}$  is the assumption of  $\frac{\partial p}{\partial \xi} = 0$ . In a straight channel, this assumption is valid assuming that the influence of incidence is captured by the second force term in Equation 3.7,  $f_{n_\delta}$ . However, for blades with non-zero camber angle,  $\kappa_{TE} - \kappa_{LE} > 0$ , where  $\kappa_{LE}$  and  $\kappa_{TE}$  denote the local blade metal angles at leading edge (LE) and trailing edge (TE), respectively, the relative streamlines turn through the blade row even if the incoming flow is aligned with the leading edge blade metal angle and incidence is zero. The streamline curvature is not captured if  $\frac{\partial p}{\partial \xi} = 0$  is assumed through the blade row. The implications of the inconsistencies in the calculation of  $f_{n_{\nabla p}}$  and the consequences of neglecting the  $\frac{\partial p}{\partial \xi}$ -terms will be discussed in Section A.2.

### A.1.2 Derivation of Normal Force Component Due to Response to Change in Local Deviation $\vec{f}_{n_\delta}$

Gong proposed a two-dimensional blade passage model as depicted in Fig. A-2 with blade spacing  $h$ , local blade metal angle  $\kappa$ , and deviation  $\delta$ . The flow in the blade passage is locally modeled as flow in a straight duct, with axes  $\eta$  and  $\xi$  in blade passage direction and normal to the passage, respectively. Consequently, the local velocity vector  $\vec{W}$  consists of components  $W_\eta$  in passage direction and  $W_\xi$  normal to passage direction. Radial components of velocity and blade force are again assumed negligible,  $\frac{W_r}{W} \ll 1$  and  $\frac{f_{n,r}}{f_n} \ll 1$ .

Applying conservation of momentum in  $\xi$ -direction for steady, inviscid, compressible flow gives

$$W_\eta \frac{\partial W_\xi}{\partial \eta} + W_\xi \frac{\partial W_\xi}{\partial \xi} = -\frac{1}{\rho} \frac{\partial p}{\partial \xi} + f_{n_{\delta,\xi}}. \quad (\text{A.9})$$

In Equation A.9, the cross-passage component of the normal force due to the response to changes in deviation is denoted by  $f_{n_{\delta,\xi}}$ . With  $W_\xi = W \sin \delta$ , the second term on the left-hand side can be re-written as

$$W_\xi \frac{\partial W_\xi}{\partial \xi} = \frac{\partial (\frac{1}{2} W_\xi^2)}{\partial \xi} = \frac{1}{2} \frac{\partial (W^2 \sin^2 \delta)}{\partial \xi} \approx 0. \quad (\text{A.10})$$

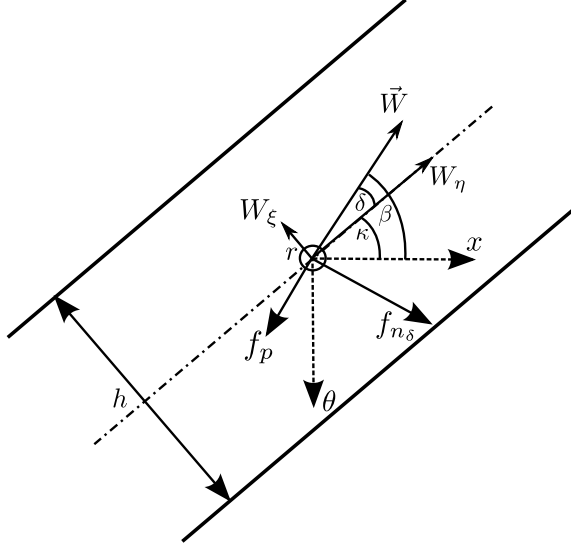


Figure A-2: Gong's blade passage with forces normal and parallel to local flow direction,  $f_{n_\delta}$  and  $f_p$ .

For small angles of deviation,  $\sin^2 \delta \ll 1$ , so this term is negligible compared to the other terms in Equation A.9. As before, the pressure gradient  $\nabla p = \frac{\partial p}{\partial \eta}$  is assumed to be in the direction of the passage, and  $\frac{\partial p}{\partial \xi} = 0$ . The component of the normal body force normal to the blade passage thus becomes

$$f_{n_{\delta,\xi}} = W_\eta \frac{\partial W_\xi}{\partial \eta}. \quad (\text{A.11})$$

Instead of the blade chord  $c$ , which cannot be defined locally, the staggered spacing of the blades to be represented by the body force field,  $h$ , is introduced as the characteristic length scale to approximate the in-passage component of the normal velocity gradient,  $\frac{\partial W_\xi}{\partial \eta} \approx \frac{W_\xi}{h}$ , and the blade-passage-normal component of the normal force is now given by

$$f_{n_{\delta,\xi}} \sim \frac{W_\eta W_\xi}{h}. \quad (\text{A.12})$$

The force is assumed to scale with a body force coefficient  $K_{n,\xi}$ , such that

$$f_{n_{\delta,\xi}} = K_{n,\xi}(x, r, \delta, M_{rel}) \frac{W_\eta W_\xi}{h}. \quad (\text{A.13})$$

For small deviations and  $\cos \delta = \frac{f_{n\delta,\xi}}{f_{n\delta}} \approx 1$ , the normal force is approximated by

$$f_{n\delta} = K_n(x, r, \delta, M_{rel}) \frac{W_\eta W_\xi}{h}. \quad (\text{A.14})$$

The components of the normal force  $f_{n\delta}$  are given by

$$\vec{f}_{n\delta} = \begin{bmatrix} f_{n\delta,r} \\ f_{n\delta,\eta} \\ f_{n\delta,\xi} \end{bmatrix} = \frac{K_n(x, r, \delta, M_{rel})}{h} \frac{W_\eta W_\xi}{W} \begin{bmatrix} 0 \\ W_\xi \\ -W_\eta \end{bmatrix}. \quad (\text{A.15})$$

The staggered spacing between the blades is defined as

$$h = \frac{2\pi r \sqrt{\sigma} \cos \kappa}{B}, \quad (\text{A.16})$$

where  $\sigma$  and  $B$  are the solidity and the number of fan blades, respectively. The square-root dependence on solidity assumes Carter's rule [102]. In Equation A.15, the velocity components  $W_\eta$  and  $W_\xi$  can be expressed in terms of the blade metal angle  $\kappa$  and the axial and circumferential velocities,  $W_x$  and  $W_\theta$ ,

$$\begin{bmatrix} W_\eta \\ W_\xi \end{bmatrix} = \begin{bmatrix} \cos \kappa & -\sin \kappa \\ -\sin \kappa & -\cos \kappa \end{bmatrix} \begin{bmatrix} W_x \\ W_\theta \end{bmatrix}. \quad (\text{A.17})$$

With Equations A.15 and A.17, the normal force due to local changes in deviation can be written as

$$f_{n\delta} = \frac{K_n(x, r, \delta, M_{rel})}{h} W_\eta W_\xi \quad (\text{A.18})$$

$$= -\frac{K_n(x, r, \delta, M_{rel})}{h} (W_x \cos \kappa - W_\theta \sin \kappa) (W_x \sin \kappa + W_\theta \cos \kappa) \quad (\text{A.19})$$

$$= \frac{K_n(x, r, \delta, M_{rel})}{h} W^2 \cos(\beta - \kappa) \sin(\beta - \kappa) \quad (\text{A.20})$$

$$= \frac{K_n(x, r, \delta, M_{rel})}{h} W^2 \frac{1}{2} \sin(2\delta), \quad (\text{A.21})$$

with components

$$\vec{f}_{n_\delta} = \begin{bmatrix} f_{n_{\delta,x}} \\ f_{n_{\delta,r}} \\ f_{n_{\delta,\theta}} \end{bmatrix} = \frac{f_{n_\delta}}{W} \begin{bmatrix} -W_\theta \\ 0 \\ W_x \end{bmatrix}. \quad (\text{A.22})$$

In Equation A.19, the velocity components can be expressed as  $W_x = W \cos \beta$  and  $W_\theta = -W \sin \beta$ , and with Equation A.1, the direct dependence of the normal force on deviation in Equation A.21 is derived.

If the force on the left-hand side and the velocity components on the right-hand side of Equation A.18 are known from experimental data, empirical correlations, or CFD results, the body force coefficient  $K_n$  can be determined from Equation A.23.

$$K_n(x, r, \delta, M_{rel}) = \frac{f_{n_\delta} h}{W_\eta W_\xi} = \frac{f_{n_\delta} h}{W^2 \frac{1}{2} \sin(2\delta)} \quad (\text{A.23})$$

The extraction of the blade force  $f_{n_\delta}$  and flow field data from CFD data and the computation of the body force coefficient  $K_n$  are discussed in detail in Section 3.4.

It is important to note that the assumption of  $\frac{\partial p}{\partial \xi} = 0$  in Equation A.9 implies that streamline curvature is not adequately accounted for in the normal force model. The implications of this assumption are discussed in Section A.2.

## A.2 Discussion of Gong's Body Force Model

From Equations 3.7, A.8, and A.21, the normal force is given by

$$f_n = f_{n_{\nabla p}} + f_{n_\delta} = \frac{1}{\rho} \frac{\partial p}{\partial x} \frac{\sin \kappa}{\cos^2 \kappa} + \frac{K_n(x, r, \delta, M_{rel})}{h} W^2 \frac{1}{2} \sin(2\delta). \quad (\text{A.24})$$

To illustrate the implications of neglecting the cross-passage component of the pressure gradient ( $\frac{\partial p}{\partial \xi} = 0$ ) in the derivation of normal body force Equation A.24, the flow through a notional curved channel with zero blade metal angle at some axial location  $x = x_2$ , as depicted in Fig. A-3, is adopted from [101]. At this location, it is also assumed that the relative flow angle  $\beta$  is equal to the local blade metal angle  $\kappa$ .

At station 1, the blade metal angle is positive, and there is a force in the positive  $f_n$ -direction turning the flow but at station 2, with  $\kappa = 0$ , both components in Equation A.24 are zero, and the blade passage model dictates a zero normal body force,  $f_n = 0$ . In a blade passage with discrete blades, the relative streamline has a radius of curvature at  $x = x_2$ , and a non-zero normal force balances the centripetal acceleration of the fluid particles along the curved streamline. The normal force is generated by the pressure gradient normal to the relative streamline, set up by the pressure difference between the pressure and suction sides in a blade passage. In the body force representation, the normal pressure gradient must be captured by the normal force model. The blade passage model presented by Gong does not capture the normal force at  $x = x_2$ . However, the relative flow is still turned since there will be a deviation between the relative flow and the blade metal direction in the adjacent downstream cell, leading to a non-zero normal force.

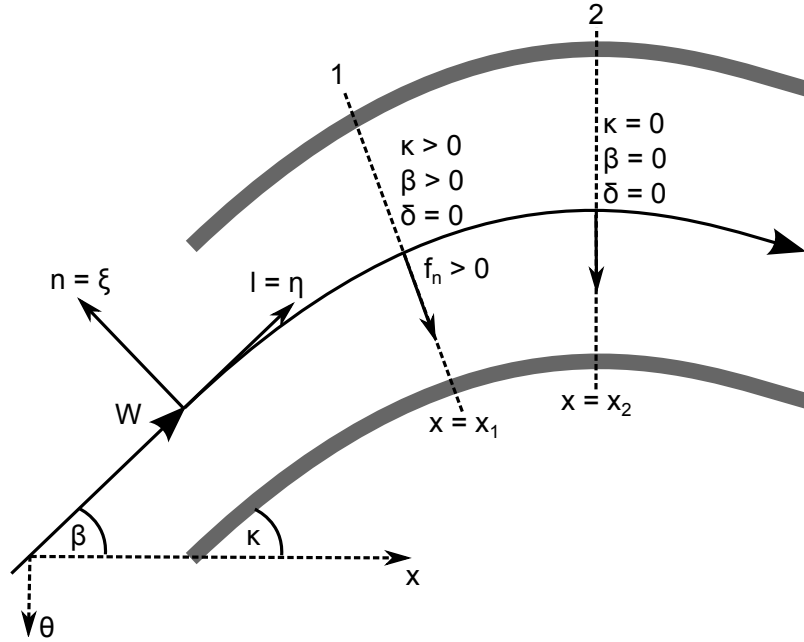


Figure A-3: Example blade passage with blade metal angle  $\kappa = 0$  to illustrate inconsistency in Equation A.24.

The dependency of the normal force due to the local change in deviation,  $f_{n\delta}$ , on  $\sin \delta$  is further examined next. The formulation of  $f_{n\delta}$  implies that there is a non-zero force turning the streamline towards the local blade metal direction whenever

streamline and camber line are not aligned locally. The behavior of the normal force is sketched in Fig. A-4 for a nominal compressor or fan blade camber line at three different operating conditions: (1) near stall, (2) at design, and (3) near choke.

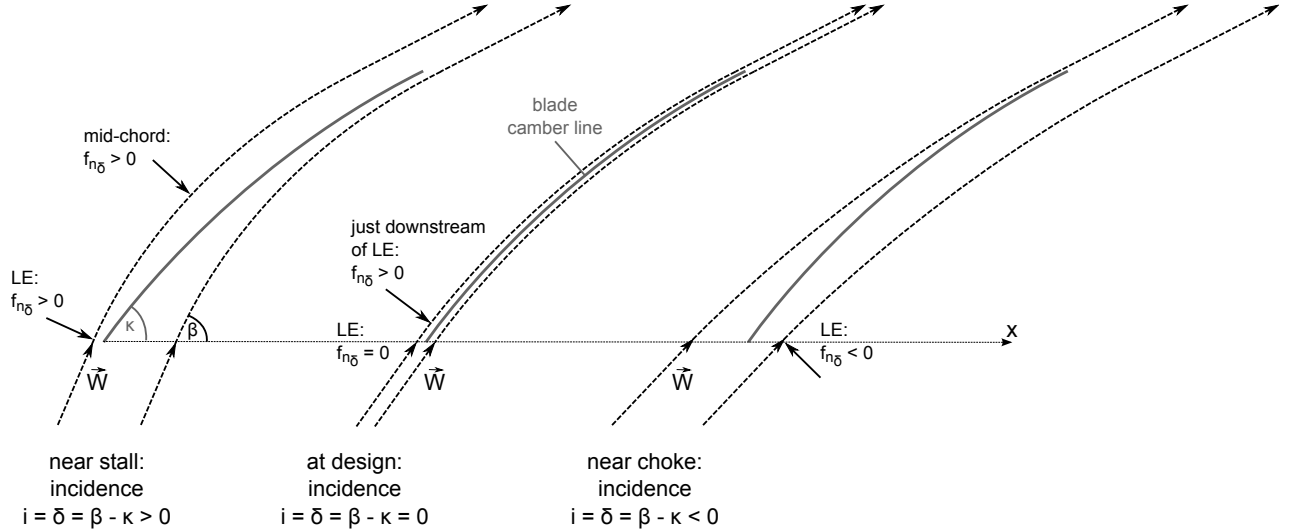


Figure A-4: Normal force at positive incidence (near stall), zero incidence (design), and negative incidence (near choke).

- **Near stall:** The incidence or deviation at the blade row inlet (LE) is positive,  $\delta > 0$ , and the flow angle is larger than the blade metal angle resulting in a normal force in the positive  $f_n$ -direction. Along the body force domain from blade row inlet (LE) to blade row exit (TE), the force continues to act in the positive  $f_n$ -direction (as indicated in Figs. A-2 or A-4), turning the relative streamline towards the blade metal direction.
- **At design:** The deviation at the blade row inlet is zero,  $\delta = 0$ , and the normal force is zero. At the next grid point in streamwise direction, the streamline is still at the same angle since it has not been turned but the local blade metal angle changes to a new value at this grid point. In a fan or compressor, the blade metal angle typically decreases along the chord. Consequently, the deviation will be positive at the second grid point inside of the blade row domain, leading to a normal force in the positive  $f_n$ -direction which turns the flow back towards the blade metal direction.

- Near choke: The incidence or deviation at the blade row inlet is negative,  $\delta > 0$ . A non-zero normal force in negative  $f_n$ -direction locally turns the flow towards the blade metal direction.

An important practical implication of the normal body force formulation in Equation A.24 is an inherent stability in the model. If there is a large discrepancy between the local relative flow direction and the blade metal direction, the model will always respond with a normal force turning the flow back towards the blade metal direction. This positive feedback characteristic enables body force calculations to be initialized from constant initial conditions with large differences between the initial and the converged flow fields.

The behavior of the normal force response to local changes in deviation near stall, at design, and near choke on the take-off speedline is qualitatively shown in Fig. A-5 for the advanced fan used in the current work. Circumferentially-averaged flow field data from single-passage RANS simulations is used here to reconstruct  $f_{n\delta}$ . Near stall, the force near the leading edge is largest due to the large positive incidence or deviation. Near choke, the force is negative.

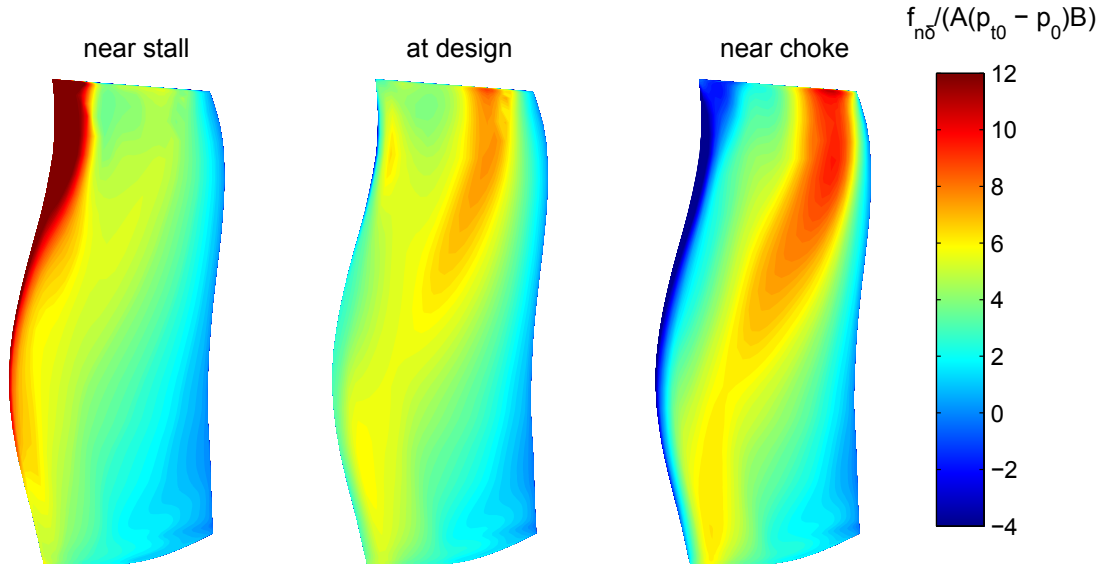


Figure A-5: Normal force due to change in local deviation  $\frac{f_{n\delta}}{A(p_{t0} - p_0)B}$  for T/O corrected speed. Positive leading edge incidence near stall results in a positive  $f_{n\delta}$ , while negative incidence near choke leads to negative force values (geometry distorted).

## Appendix B

# Force Extraction from Steady RANS Simulations

As shown in Equation 3.13, the circumferentially-averaged net force normal to the pitchwise-averaged relative flow,  $\bar{f}_n$ , is required in the determination of the body force coefficient  $K_n$ . The force extraction procedure employed in the present work is depicted in Fig. B-1. The force extraction procedure involves three different grids with the following characteristics and requirements:

1. Blade geometry input grid (e.g. CAD): rotor or stator geometries are typically available as airfoil profiles at multiple spanwise locations from computer-aided design (CAD) tools or preliminary calculations, for example from streamline curvature methods.
2. RANS (or Euler) grid: the original blade geometry is used to define the solid surfaces in the grid generation for the steady, single-passage RANS simulations. An example for a three-dimensional single-passage RANS grid is shown on the left in Fig. 3-7. The RANS grid is required to have sufficient resolution to capture the endwall and blade surface boundary layers as well as three-dimensional flow features such as rotor wakes or tip leakage and tip vortices. Details on the RANS grid generation and the grid convergence study for the rotor and stator meshes are presented in Section 5.4.4.

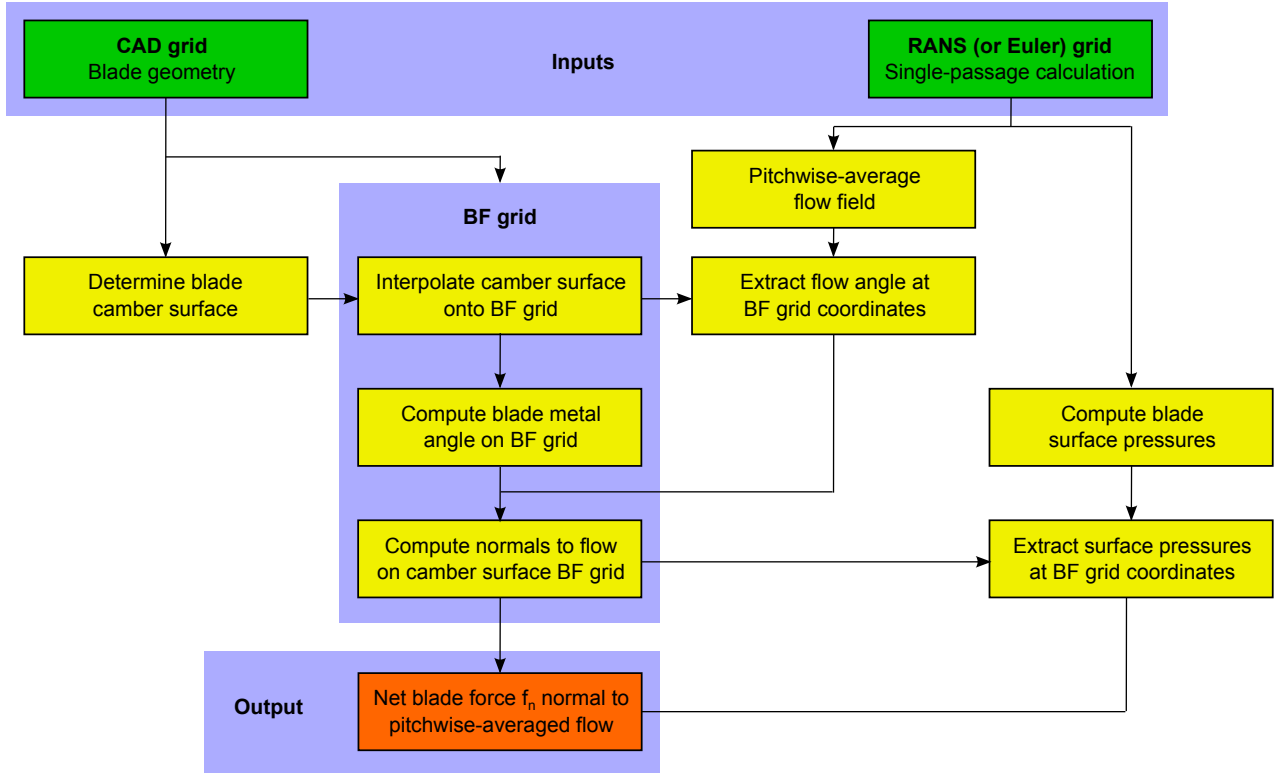


Figure B-1: Overview of the calculation of the net blade force normal to the pitchwise-averaged relative flow from single-passage RANS simulations.

3. Body force grid: the grid used in the body force simulations is set up with the body force domains corresponding to the blade surfaces projected onto the meridional plane. An example for the meridional mesh topology used in the body force simulations is presented in Fig. C-1. For a given speedline, the determination of the viscous body force coefficients  $K_{p1}$  and  $K_{p2}$  in Equation 3.11 requires the iterative comparison of body force results to data from steady, single-passage RANS calculations. Since the speedline is computed with uniform inflow conditions, a full-annulus grid is not required. In the present work, a three-dimensional grid with 10° circumferential extent was generated to carry out initial “single-passage” body force simulations. An example for a single-passage body force grid is shown on the right in Fig. 3-7.

The net blade force  $\bar{f}_n$  and the pitchwise-averaged flow quantities required to determine the body force coefficient  $K_n$  can be computed on either of the three grids.

The main advantages of selecting the body force grid coordinates as the basis for the force extraction process is that interpolation errors are minimized and quantities can be “hard-coded” during body force simulations, i.e. a value of a particular quantity such as the normal force can be assigned to each grid point inside of the body force domains.

Hard-coding flow field quantities or force components extracted from the RANS simulations can be useful in diagnostic tests during the implementation of the body force method. More importantly, hard-coding the blade metal and blade lean distributions  $\kappa(x, r)$  and  $\lambda(x, r)$  (required to compute the normal force  $f_n$  given in Equation A.24) eliminates the need for an analytical representation such as a polynomial approximation in axial and radial coordinates, which would be required if the RANS grid was selected as the basis for the force extraction process. Since polynomial fits always introduce some errors, the accuracy of the body force method can be increased by hard-coding the blade metal angle. In addition, computation times are reduced since there is no need to evaluate polynomials at each grid point.

An inherent disadvantage of choosing the body force grid over any other grid and hard-coding geometric quantities such as the blade metal angle is that the pre-processing steps including the force extraction must be carried out each time the body force grid is modified. In contrast, if polynomials are used to approximate the blade metal angle, the resulting body force description is grid-independent. An integrated pre-processing framework combining Numeca post-processing capabilities and Matlab scripts was developed in this work to automate the force extraction process, yielding turn-around times of approximately 10 minutes for an entire speedline. Reducing the pre-processor computation times enabled trading grid independency for increased accuracy in the body force calculations.

With the geometry definition, the body force grid, and the three-dimensional flow field from a steady, single-passage RANS simulation in place, the following steps are carried out to obtain the net blade force normal to the pitchwise-averaged flow,  $\bar{f}_n$ :

1. The camber surface coordinates are determined from the blade surface geometry if not readily available.

2. The camber surface geometry is interpolated onto the body force grid using the Delaunay triangulation approach implemented in Matlab's scattered data interpolation functions [103]. With the camber surface coordinates, the local blade metal angle  $\kappa(x, r)$  is determined at each grid point inside of the body force domain  $(x, r)_{BF}$ . An example for the interpolation of the camber surface geometry onto the body force grid is shown in Fig. B-2. The blade metal angle distribution is normalized here by the blade metal angle  $\kappa_{ref}$  at mid-span and mid-chord.

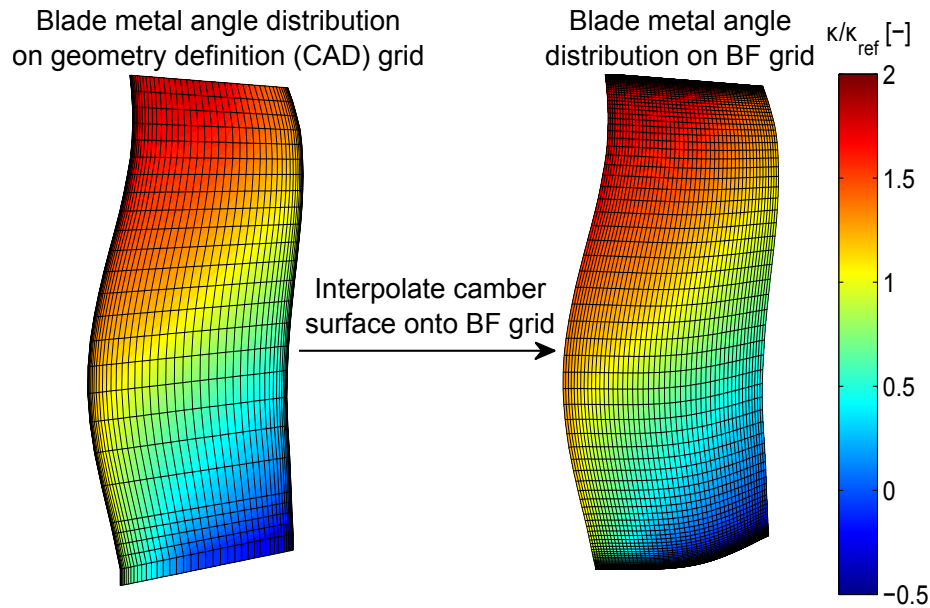


Figure B-2: Interpolation of camber surface geometry and blade metal angle onto body force grid (geometry distorted).

3. The three-dimensional flow field from steady, single-passage RANS simulation is pitchwise-averaged and the pitchwise-averaged relative flow angle  $\bar{\beta}$  is extracted at the body force grid coordinates  $(x, r)_{BF}$ . In this work, the pitchwise-averaged flow field is computed from the three-dimensional RANS result using Numeca's post-processor CFView [104].
4. For each spanwise grid line, the unit vectors  $\hat{n}_{ps}$  and  $\hat{n}_{ss}$  normal to the local relative flow direction on the pressure and suction sides are computed along the camber line set up by the body force grid coordinates, as depicted in Fig. B-3

for the front part of an airfoil section near the hub. The vectors are not normal to the camber line but normal to the relative streamline, with the difference in angle corresponding to the local deviation. The camber line is used only as a reference location.

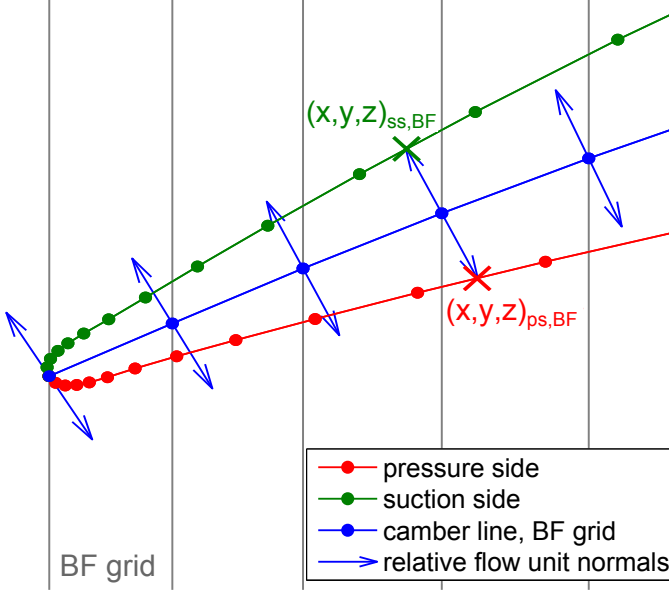


Figure B-3: Blade leading edge geometry near rotor hub with unit vectors normal to relative flow along camber line (geometry distorted).

5. The determination of the net blade force normal to the relative flow requires the extraction of the blade surface pressures at coordinates  $(x, y, z)_{ps}$  and  $(x, y, z)_{ss}$  on the pressure and suction sides, respectively, as shown in Fig. B-3. For a given point on the body force grid, the coordinates  $(x, y, z)_{ps}$  and  $(x, y, z)_{ss}$  are defined by the intersections of the line set up by the unit normals and the pressure and suction surfaces. The blade surface pressures  $p_{ps}$  and  $p_{ss}$  on the pressure and suction sides are extracted for each body force grid point using Numeca CFView.
6. Given the blade surface pressures and unit normals for each body force grid point, the net blade force normal to the local relative flow per unit area,  $\bar{f}_{n,A}^{bl}$ , is calculated from

$$\vec{f}_{n,A}^{bl}(x,r) = \hat{n}_{ps} p_{ps} + \hat{n}_{ss} p_{ss}. \quad (B.1)$$

To determine the body force coefficient  $K_n$  in Equation 3.13, the normal force per unit mass, averaged over one blade passage, is required, as given by

$$\bar{f}_n^{bl}(x,r) = \frac{f_{n,A}(x,r)}{\bar{\rho} \frac{2\pi r}{B} K \cos \bar{\beta}}. \quad (B.2)$$

In Equation B.2, the local pitchwise-averaged density is denoted by  $\bar{\rho}$  and the blade pitch is given by  $\frac{2\pi r}{B}$ . The magnitude of the net blade force normal to the local relative flow per unit area is given by  $f_{n,A}$ . The force must be averaged over the cross-passage length in the direction normal to the local pitchwise-averaged relative flow, thus the blade pitch is multiplied by  $\cos \bar{\beta}$ . The cross-passage length is multiplied by a free-area ratio  $K$  to exclude the blade volume, as the normal force per unit volume only acts on the volume of the fluid in the blade passage. The free-area ratio is given by

$$K = \frac{\frac{2\pi r}{B} - t}{\frac{2\pi r}{B}}, \quad (B.3)$$

where the local blade thickness is denoted by  $t$ . The calculation of the net blade force normal to the local relative flow is illustrated in Fig. B-4 and an example for the net normal force distribution is presented in Fig. B-5 for the first 50% chord near the blade hub.

7. With the normal force per unit mass defined in Equation B.2, the pitchwise-averaged relative velocity  $\bar{W}$  and local deviation  $\bar{\delta}$ , and the normal force component due to the pressure gradient in a staggered channel  $\bar{f}_{n_{\nabla p}}$ , as defined in Equation A.8, the body force coefficient  $K_n$  can be determined for a given operating point on a speedline from Equation 3.13. To capture changes in the blade force response to changes in the inflow conditions, steps 1-6 are carried out for multiple operating points along a given speedline, and  $K_n$  is calculated

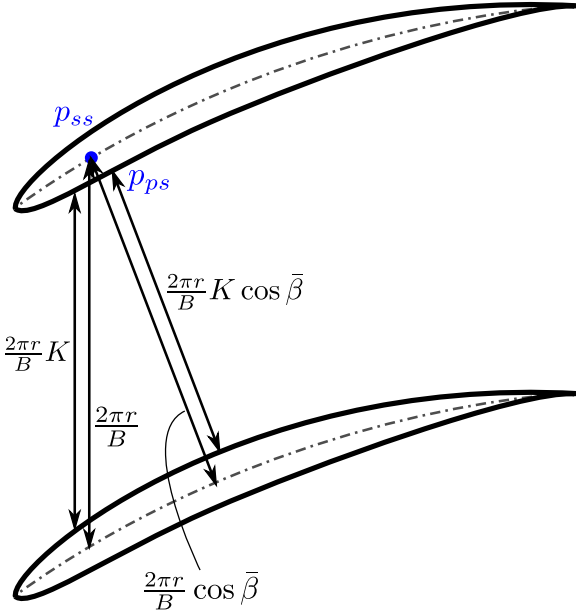


Figure B-4: Cross-passage length normal to the local pitchwise-averaged relative flow direction used in the calculation of the net blade force.

using a least-square polynomial approach, resulting in a single set of body force distributions  $K_n(x, r)$ , as depicted in Fig. 3-6.

An additional challenge arises in the calculation of  $K_n$  whenever the pitchwise-averaged flow is locally parallel to the blade, i.e. the flow angle  $\bar{\beta}$  is equal to the blade metal angle  $\kappa$ , and the deviation  $\bar{\delta}$  is zero. At this condition, the model for the normal force response to the local deviation dictates  $\bar{f}_{n\delta} = 0$ , from Equation A.21. In the RANS simulations with blades,  $\bar{f}_{n\delta} = 0$  is not guaranteed, leading to spurious singularities due to the dependence of  $K_n$  on  $\frac{1}{\sin(2\bar{\delta})}$ , as given by Equation 3.13. The least-square polynomial approach to approximate  $K_n$  as a function of axial and radial coordinates introduces large errors when applied to distributions with singularities. An offset constant  $C$  is added to the in-passage component of the local velocity  $W_\xi$ , defined by Equation A.19. The modified in-passage velocity component becomes

$$W_\xi = W_x \sin \kappa + W_\theta \cos \kappa + CW_{ref}. \quad (\text{B.4})$$

If the free-stream velocity is chosen as reference velocity  $W_{ref}$ , values between  $C = 0.5 - 0.75$  were found to be sufficiently large to eliminate singularities in  $K_n$ . The

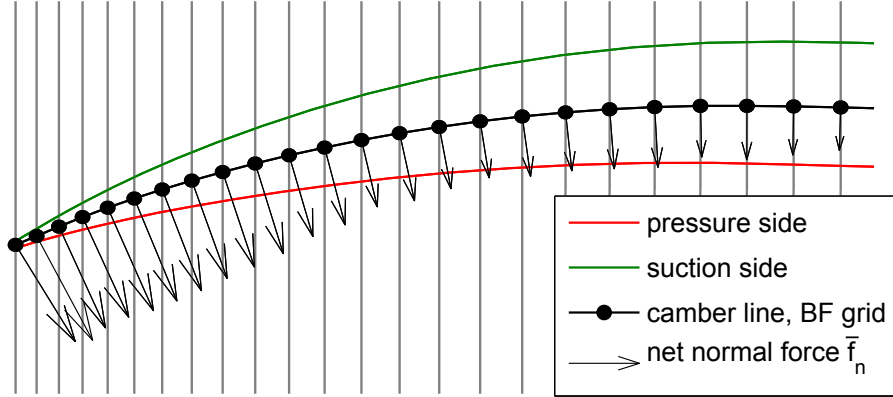


Figure B-5: Net force normal to relative flow along camber line on body force grid near rotor hub (geometry distorted).

offset  $CW_{ref}$  must be included both in the determination of  $K_n$  and in the formulation of the source terms used in the implementation of the body force method. Spurious singularities in  $K_n$  are a consequence of the RANS-based force extraction process and the modifications to  $W_\xi$  are not necessarily required if the body force coefficient  $K_n$  is determined from empirical correlations at a limited number of spanwise locations only - for example at hub, mid-span, and tip, as in the work by Gong [38].

# Appendix C

## Implementation of Body Force Method in Existing Flow Solvers

The implementation of the body force method in a commercially available CFD software such as the structured flow solver Numeca FINE/Turbo (F/T) requires access to flow field quantities at each iteration. In Numeca F/T, a standalone subroutine written in FORTRAN is needed to define source terms depending on local flow field quantities. To incorporate the body force method in Numeca F/T, a solver library is compiled based on the body force subroutine. The implementation procedure is similar in Ansys FLUENT or CFX.

In Numeca F/T, a solver loop through each grid block is performed at each iteration. The swept volume of the blade row to be modeled by the body force representation is set up as a distinct grid block, and a flag in the solver loop controls whether or not source terms are added in a particular grid block. An example body force grid is presented in Fig. C-1 for the advanced fan stage used in this work. The axial extent of the rotor or stator block is defined by projecting the blade surface onto the meridional plane.

Most commercial flow solvers work in Cartesian coordinates and require source terms to be added in units of force per volume and work per volume. With the expressions for the normal and parallel body forces per unit mass from Equations 3.10 and 3.11, respectively, the source terms added to the momentum equations are

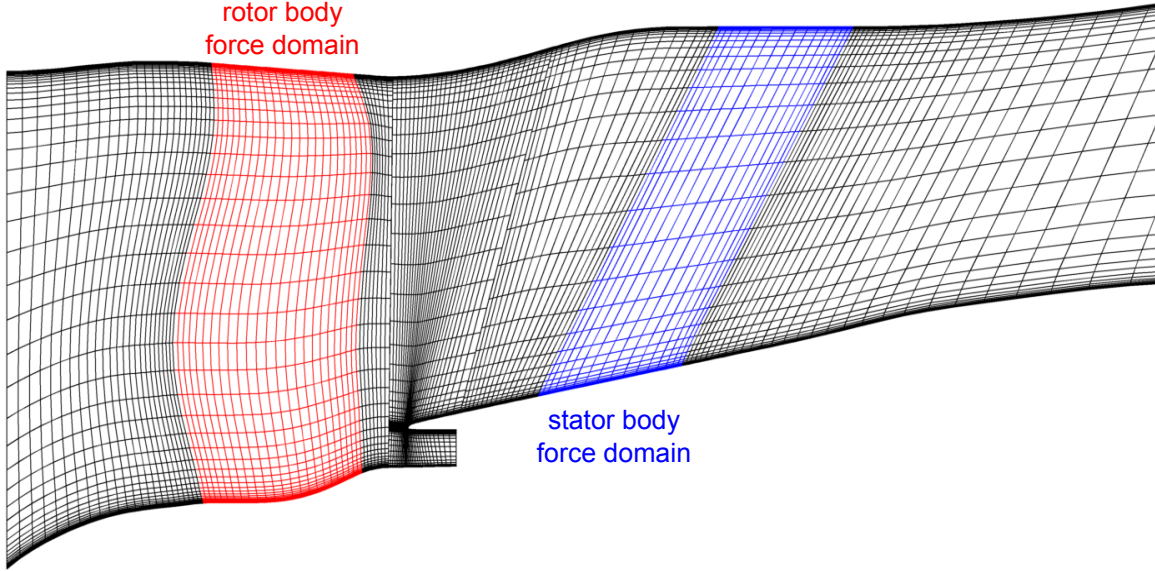


Figure C-1: Meridional grid used for body force simulations (distorted).

determined as forces per unit volume,

$$\begin{bmatrix} F_x \\ F_y \\ F_z \end{bmatrix} = \rho \begin{bmatrix} 1 & 0 & 0 \\ 0 & \cos\theta & -\sin\theta \\ 0 & \sin\theta & \cos\theta \end{bmatrix} \begin{bmatrix} f_{n,x} + f_{p,x} \\ f_{n,r} + f_{p,r} \\ f_{n,\theta} + f_{p,\theta} \end{bmatrix}. \quad (\text{C.1})$$

The source term added to the energy equation is determined using Equation 3.2,

$$\dot{W}_{source} = F_\theta \Omega r = \rho (f_{n,\theta} + f_{p,\theta}) \Omega r. \quad (\text{C.2})$$

It is important to note that depending on the solver architecture, the source terms have to be added to the residuals of the governing equations (Ansys FLUENT and CFX) or subtracted from the residuals (Numeca F/T).

# Appendix D

## Improved Body Force Method

A clean-sheet approach was used by Brand [8] to develop an improved body force method with a re-derived blade passage model for the normal and parallel force formulations. The objective was to capture (1) streamline curvature, (2) the influence of changes in the local flow on the normal force  $f_n$ , (3) the impact of incidence on the parallel force  $f_p$ , and (4) blade metal and aerodynamic blockage. The improved body force model was not used in the design of the short inlets presented in this thesis but is given here as a reference to be used in future work.

### D.1 Improved Normal Body Force Model

The body force field represents the pitchwise-averaged influence of the blade row on the flow. More specifically, the body force component normal to the flow generates the pitchwise-averaged flow turning provided by the blades.

The relative streamlines through a blade passage are sketched on the left in Fig. D-1. The pressure field and streamlines are non-axisymmetric due to the presence of the blades and at every location in the flow, the relative streamline curvature is balanced by the component of the pressure gradient normal to the streamline [64],

$$\frac{1}{\rho} \frac{\partial p}{\partial n} - W^2 \frac{\partial \beta}{\partial l} = 0. \quad (\text{D.1})$$

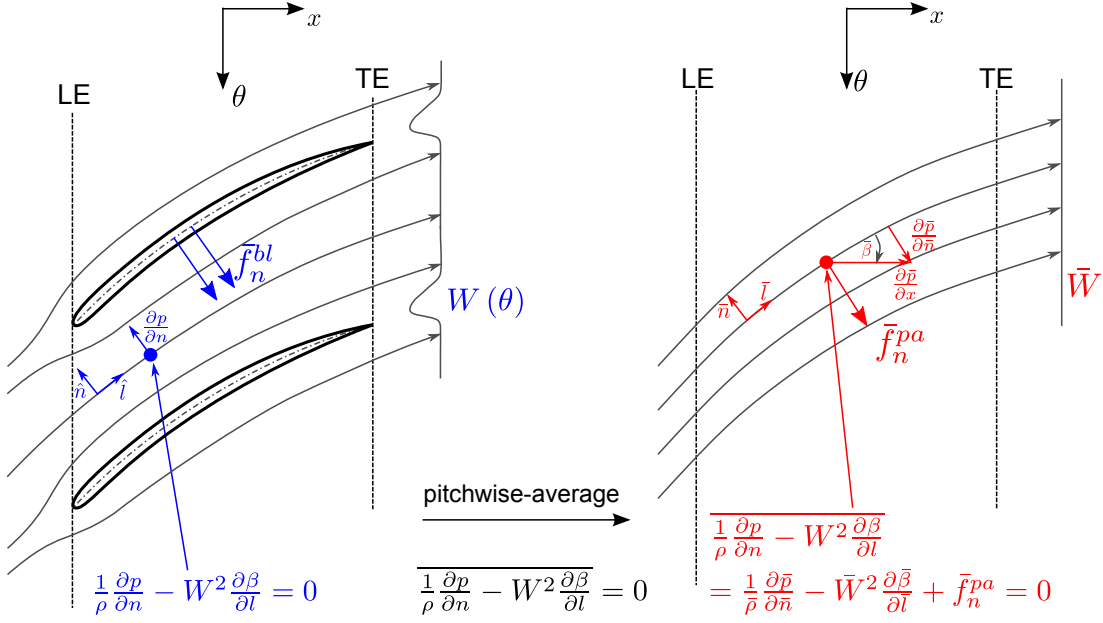


Figure D-1: Relative streamlines through passage with discrete blades (left) and pitchwise-averaged relative streamlines (right).

A pitchwise-average of the non-axisymmetric flow field can be defined as follows. The so-called blade force average, described in [105], is designed to preserve the blade force in the averaged, axisymmetric flow field. The blade force average defines the body force. A pitchwise-averaged representation of the flow through a blade row is depicted on the right in Fig. D-1.

Pitchwise-averaging Equation D.1 yields

$$\overline{\frac{1}{\rho} \frac{\partial p}{\partial n} - W^2 \frac{\partial \beta}{\partial l}} = \overline{\frac{1}{\rho} \frac{\partial p}{\partial n}} - \overline{W^2 \frac{\partial \beta}{\partial l}} = 0. \quad (\text{D.2})$$

Equation D.2 can be further expanded to obtain a formulation in terms of the averaged flow quantities,  $\bar{\rho}$ ,  $\bar{p}$ ,  $\bar{W}$ , and  $\bar{\beta}$ . In general, any flow quantity  $Q(\theta)$  can be expressed as the sum of the average value  $\bar{Q}$  and the deviation  $Q'(\theta)$ ,

$$Q(\theta) = \bar{Q} + Q'(\theta). \quad (\text{D.3})$$

Considering for example the streamline curvature term, it can be shown that the average of the streamline curvature term is not the same as the streamline curvature term determined from the averaged flow quantities,

$$\overline{W^2 \frac{\partial \beta}{\partial l}} \neq \bar{W}^2 \frac{\partial \bar{\beta}}{\partial l}, \quad (\text{D.4})$$

since  $\overline{W^2} = \bar{W}^2 + \overline{2WW'} + \overline{W'^2}$ . As a result, higher-order terms (*H.O.T.*) appear when Equation D.2 is formulated in terms of the averaged quantities,

$$\overline{\frac{1}{\rho} \frac{\partial p}{\partial n}} - \overline{W^2 \frac{\partial \beta}{\partial l}} = \frac{1}{\bar{\rho}} \frac{\partial \bar{p}}{\partial \bar{n}} - \bar{W}^2 \frac{\partial \bar{\beta}}{\partial \bar{l}} + \text{H.O.T.} = 0. \quad (\text{D.5})$$

The higher-order terms represent the influence of the blades in the averaged, axisymmetric flow field and correspond to the normal blade force,  $\text{H.O.T.} = -\bar{f}_n^{pa}$ , where the negative sign is introduced for consistency with the coordinate system used in Fig. D-1 and in [8],

$$\overline{\frac{1}{\rho} \frac{\partial p}{\partial n}} - \overline{W^2 \frac{\partial \beta}{\partial l}} = \frac{1}{\bar{\rho}} \frac{\partial \bar{p}}{\partial \bar{n}} - \bar{W}^2 \frac{\partial \bar{\beta}}{\partial \bar{l}} - \bar{f}_n^{pa} = 0. \quad (\text{D.6})$$

In the pitchwise-averaged flow field, the relative streamline curvature is no longer balanced by the component of the pressure gradient normal to the streamline. To establish the pitchwise-averaged stagnation pressure rise and flow turning without the presence of discrete blades requires the normal force  $\bar{f}_n^{pa}$  in the blade domain,

$$\bar{f}_n^{pa} = -\bar{W}^2 \frac{\partial \bar{\beta}}{\partial \bar{l}} + \frac{1}{\bar{\rho}} \frac{\partial \bar{p}}{\partial \bar{n}}. \quad (\text{D.7})$$

In the blade passage, the normal pressure gradient is in the positive  $\hat{n}$ -direction, as indicated in Fig. D-1. In the pitchwise-averaged flow field, the circumferential component of the pressure gradient is zero,  $\frac{\partial \bar{p}}{\partial \theta} = 0$ . The normal pressure gradient is due to the axial component of the pressure gradient only,  $\frac{\partial \bar{p}}{\partial \bar{n}} = \frac{\partial \bar{p}}{\partial x} \sin \bar{\beta}$ , and points in the negative  $\bar{n}$ -direction. Equation D.7 defines the normal force in the improved body force method and can also be derived from the full momentum equation along a relative streamline in the axisymmetric flow [8],

$$\frac{\partial \vec{W}}{\partial t} + (\vec{W} \cdot \nabla \vec{W}) = -\frac{1}{\bar{\rho}} \nabla \bar{p} + \vec{f} + (\text{viscous terms}) + (\text{fictitious forces}). \quad (\text{D.8})$$

For steady, inviscid flow without fictitious forces, and assuming negligible contributions from radial forces, velocities, and gradients, Equation D.8 can be reduced to the formulation in Equation D.7.

The pitchwise-averaged influence of the blade can alternatively be determined by computing the net blade force normal to the relative flow from the non-axisymmetric flow field and evenly distributing (or “smearing out”) the force over the mass in the blade passage. The net blade force can be calculated either from a control volume analysis of an angular segment between two blades [63, 105] or from the pressure difference across the blade. The latter approach was described in Appendix B. The resulting normal blade force per unit mass, smeared out over a passage, is then given by

$$\bar{f}_n^{bl}(x, r) = \frac{\hat{n}_{ps} p_{ps} + \hat{n}_{ss} p_{ss}}{\bar{\rho} \frac{2\pi r}{B} K \cos \bar{\beta}}, \quad (\text{D.9})$$

where the width of the blade passage normal to the relative flow is defined by  $\frac{2\pi r}{B} K \cos \bar{\beta}$ , with  $K$  denoting the free-area ratio to account for the blade metal blockage.

To illustrate the equivalence between the blade-force-averaged flow field with normal force  $\bar{f}_n = \bar{f}_n^{pa} = \bar{f}_n^{bl}$  and the pitchwise-averaged flow field through the rotor domain, the streamline curvature and pressure gradient force components are shown as dashed and solid black lines in Fig. D-2, respectively. The example given is the advanced fan stage used in this thesis at the cruise design point. The components are determined based on the pitchwise-averaged flow field extracted from a steady, single-passage RANS simulation and plotted along the axial direction at mid-span.

The normal body force,  $\bar{f}_n^{pa}$ , calculated from the pitchwise-averaged flow field, is shown in red in Fig. D-2 and the normal blade force,  $\bar{f}_n^{bl}$ , determined from the blade surface pressures, is plotted in blue. The distributions of  $\bar{f}_n^{bl}$  and  $\bar{f}_n^{pa}$  agree to within 10 %. The differences can be attributed to neglecting the radial velocity, force, and gradient terms in the derivation of  $\bar{f}_n^{pa}$ .

One interpretation of Equation D.7 can be given by expressing the local relative flow angle  $\bar{\beta}$  as the sum of the local blade metal angle and a local deviation angle,

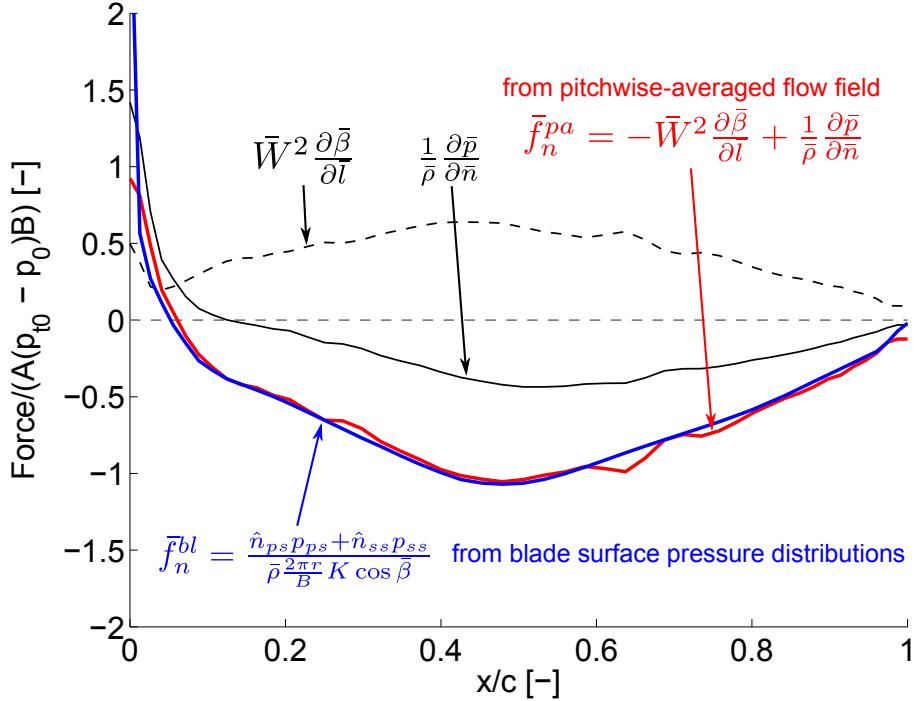


Figure D-2: Chordwise distributions of the smeared out blade force determined from the surface pressures and the normal force computed from the pitchwise-averaged streamline curvature and normal pressure gradient components for the fan rotor at mid-span.

$\bar{\beta} = \kappa + \delta$ . The normal force can then be formulated in terms of known flow field quantities ( $\bar{W}$ ,  $\bar{\rho}$ , and  $\frac{\partial \bar{p}}{\partial n}$ ), geometry ( $\frac{\partial \kappa}{\partial l}$ ), and the streamwise gradient of deviation, which is unknown and needs to be determined from simulations or correlations,

$$\bar{f}_n = -\bar{W}^2 \left( \frac{\partial \kappa}{\partial l} + \frac{\partial \bar{\delta}}{\partial l} \right) + \frac{1}{\bar{\rho}} \frac{\partial \bar{p}}{\partial n}. \quad (\text{D.10})$$

The streamwise gradient of deviation,  $\frac{\partial \bar{\delta}}{\partial l}$ , changes the amount of relative streamline curvature prescribed by the blade camber surface due to boundary layer displacement effects and can be thought of as a perturbation to the axisymmetric flow field. Defining a new non-dimensional parameter  $\Delta \equiv c \frac{\partial \bar{\delta}}{\partial l}$  as the link to the blade passage calculations, with the blade chord  $c$  introduced as reference length, the normal force can be re-written as

$$\bar{f}_n = -\bar{W}^2 \left( \frac{\partial \kappa}{\partial l} + \frac{1}{c} \Delta \right) + \frac{1}{\bar{\rho}} \frac{\partial \bar{p}}{\partial n}. \quad (\text{D.11})$$

The non-dimensional streamwise gradient of deviation can now be analytically computed from

$$\Delta = \left[ c \left( \frac{\frac{1}{\bar{\rho}} \frac{\partial \bar{p}}{\partial \bar{m}} - \bar{f}_n}{\bar{W}^2} - \frac{\partial \kappa}{\partial \bar{l}} \right) \right]. \quad (\text{D.12})$$

Similar to the approach employed in the determination of the body force coefficient  $K_n$ , pitchwise-averaged flow field quantities and the net normal force  $\bar{f}_n$  are extracted from steady, single-passage RANS simulations to compute  $\Delta$ . The force extraction process follows the steps outlined in Section B.

In order to capture the influence of changes in the local flow on the streamwise gradient of deviation, an analytical representation of  $\Delta$  in terms of geometric quantities ( $x$  and  $r$ ) and local relative velocity  $W$  was implemented in [8].

## D.2 Improved Parallel Body Force Model

Following Marble's work [33], the improved parallel force model is related to the meridional entropy gradient,  $\frac{\partial \bar{s}}{\partial \bar{m}}$ , by

$$\bar{f}_p = -\frac{\bar{W}_m}{\bar{W}} \bar{T} \frac{\partial \bar{s}}{\partial \bar{m}}, \quad (\text{D.13})$$

where  $\bar{W}_m$  denotes the meridional relative velocity. With  $\cos \bar{\beta} = \frac{\bar{W}_m}{\bar{W}}$ , Equation D.13 can be re-written as

$$\bar{f}_p = -\bar{T} \frac{\partial \bar{s}}{\partial \bar{m}} \cos \bar{\beta}. \quad (\text{D.14})$$

The parallel force  $\bar{f}_p$  is required to produce a given local meridional entropy gradient  $\frac{\partial \bar{s}}{\partial \bar{m}}$  at static temperature  $\bar{T}$  and relative flow angle  $\bar{\beta}$ .

Comparisons with the steady, single-passage RANS results demonstrated that the entropy rise along a given chordwise grid line through a blade row can be approximated as a linear distribution in the meridional coordinate  $m$ , such that the parallel force formulation becomes

$$\bar{f}_p(x, r) = -\bar{T}(x, r) \frac{\Delta \bar{s}}{\Delta \bar{m}}(r) \cos(\bar{\beta}(x, r)), \quad (\text{D.15})$$

where the entropy rise is given by  $\Delta \bar{s} = \bar{s}_{TE} - \bar{s}_{LE}$  and the meridional distance for a chordwise grid line is  $\Delta \bar{m} = \sqrt{(x_{TE} - x_{LE})^2 + (r_{TE} - r_{LE})^2}$ . For each spanwise location, the entropy rise can now be formulated in terms of leading edge incidence to capture the influence of changes in the operating point on the loss generation. The details of the parallel force implementation are presented in [8].

### D.3 Validation of Improved Body Force Model

Spanwise profiles for the percent difference in the stagnation pressure rise coefficient,  $\Psi_{pt} = \frac{p_{t,ds} - p_{t,us}}{p_{t,us} - p_{us}}$  between the body force and steady, single-passage RANS results are shown in the left-hand plot in Fig. D-3. The body force results agree to within 5 % with the steady RANS data between 10 % and 90 % span. The interaction between the hub boundary layer and the blade and tip leakage is not captured in the body force simulations, resulting in increased differences at the endwalls.

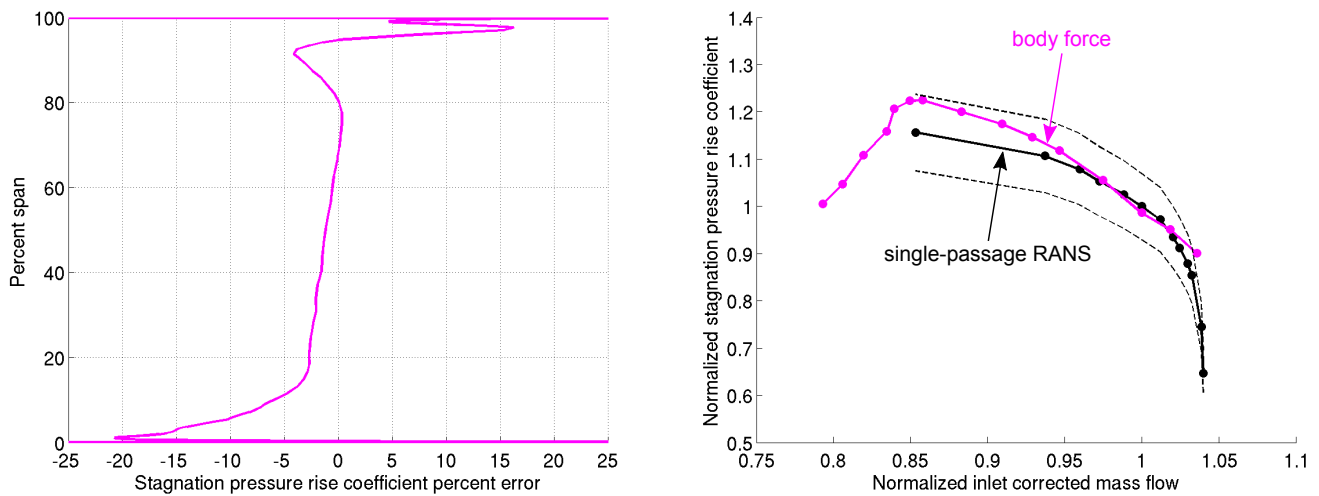


Figure D-3: Spanwise profile of relative difference in stagnation pressure rise coefficient between improved body force method and steady, single-passage RANS results at the cruise design point (left) and mass-averaged stagnation pressure rise coefficient across the fan operating range (right). The dashed lines correspond to  $\pm 7\%$  relative error. The plots are adopted from Brand [8].

The cruise speedline result for the stagnation pressure rise coefficient is compared to RANS data on the right in Fig. D-3. The dashed lines correspond to  $\pm 7\%$  relative error. The influence of incidence on blade loading is captured in the re-derived blade passage model. To demonstrate the body force method's usefulness in the stability assessment, the mass flow was reduced beyond the numerical stability boundary determined in the steady RANS simulations. The results demonstrate the method's capability of capturing the increased blade losses and a growing region of reversed flow at the blade tip, which is discussed in more detail in [8].

# Appendix E

## Pylon and Bifurcation Geometry

### Definition and Grid Generation

The bypass duct of the long-inlet baseline and the candidate short-inlet propulsors includes the FEGV, the upper pylon fairing, and the lower bifurcation. The fan-FEGV and FEGV-pylon axial spacings and the pylon and bifurcation geometries were defined using design guidelines provided by the industry partner. The pylon and bifurcation cross-sections are based on symmetrical NACA 0012 airfoils. The axial spacing between the FEGV and the pylon is determined based on the angle  $\epsilon_1$  between the pylon line of symmetry and the tangent to the pylon profile. A sketch of the pylon cross-sections is provided at the top in Fig. E-1. Multiple pylon cross-sections with constant thickness-to-chord ratio are defined between the hub and shroud. The axial location of the pylon LE is constant along the span, while the pylon TE is swept at an angle  $\epsilon_2$ . The pylon fairing closes out to zero thickness at the round TE, located at a considerable axial distance downstream of the core nozzle exit, as indicated in the bottom plot in Fig. E-1.

The pylon cross-sections are imported into Numeca's automated grid generation module Autogrid 5 [76]. After defining the mesh topology and specifying the grid resolution, the three-dimensional mesh is obtained using Autogrid's automated grid generation and optimization routines. The pylon mesh at mid-span is depicted in Fig. E-2 for the coarse grid level defined in Chapter 5. The extent of the pylon

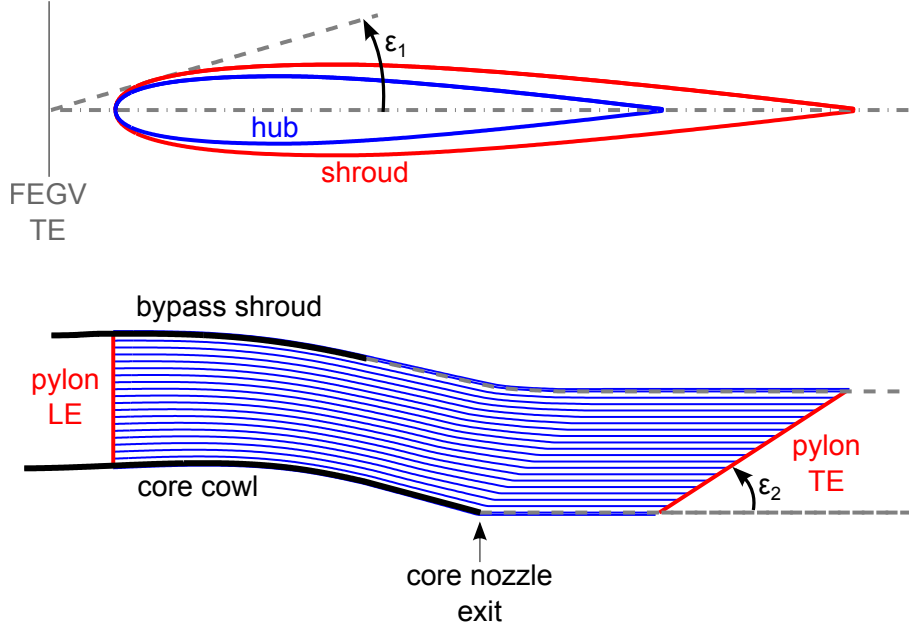


Figure E-1: Pylon fairing cross-sections at the hub and shroud (top, distorted) and leading and trailing edge locations in the meridional plane (bottom).

domains is presented in Fig. E-3. Additional grid blocks modeling the core outflow and nozzle plug and the external flow downstream of the nacelle TE are implemented in the pylon mesh using the “Meridional Technology Effect” feature in Autogrid. This strategy enables the automated definition of matching connections between the core and bypass exhaust flows and between the bypass exhaust and external flows. Non-matching connections in these regions would reduce the resolution of the shear layers downstream of the core nozzle and nacelle trailing edges and should be avoided.

For simulations at off-design conditions, the aft part of the bypass shroud geometry is modified to account for the dependency of the variable-area nozzle setting on operating condition. However, the changes in the bypass shroud geometry are small enough to maintain the same grid topology and a constant cell count for varying VAN settings. One of the key advantages enabled by the developed Autogrid-based meshing strategy is the automated generation of the pylon grid domains for varying bypass nozzle areas.

Similar to the pylon, the geometry of the lower bifurcation is based on symmetrical NACA profiles. The axial location of the bifurcation LE is assumed equal to the pylon

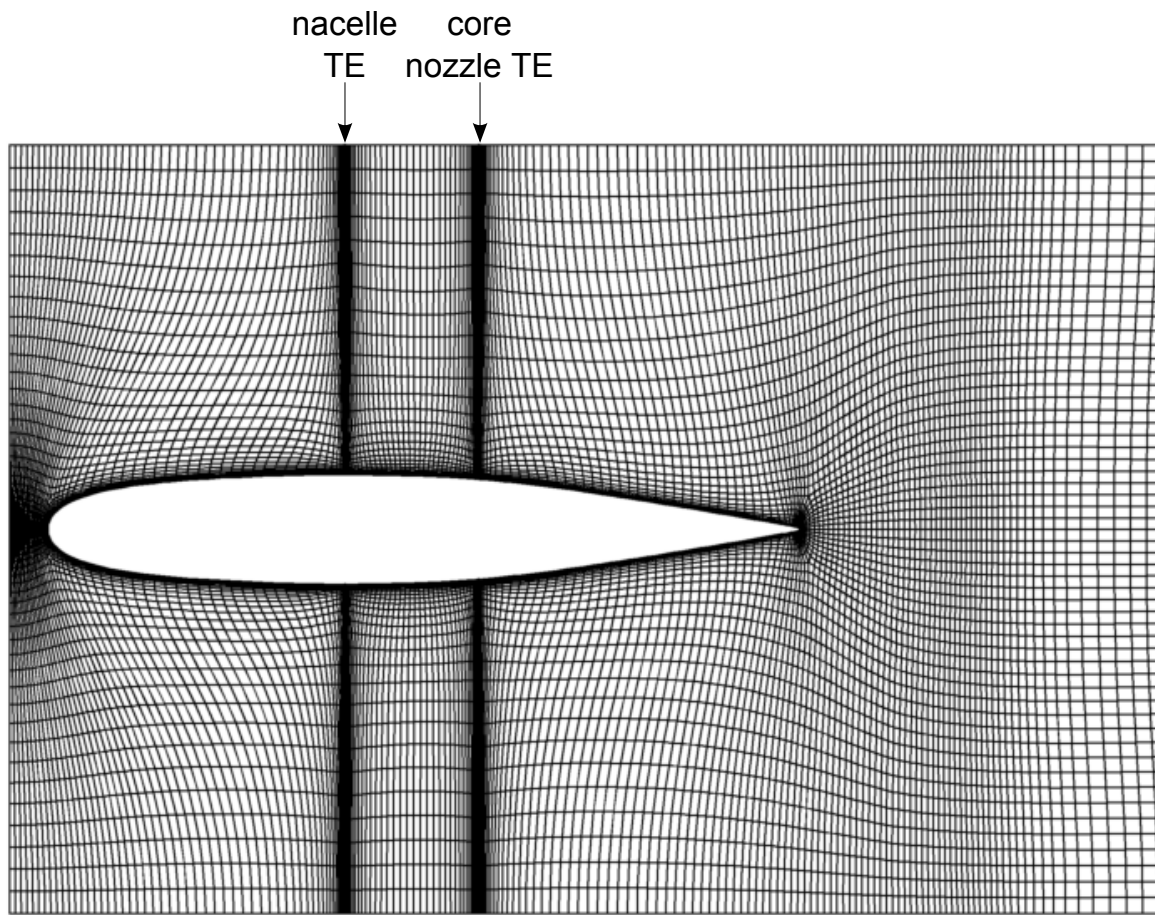


Figure E-2: Pylon mesh at mid-span (coarse grid level).

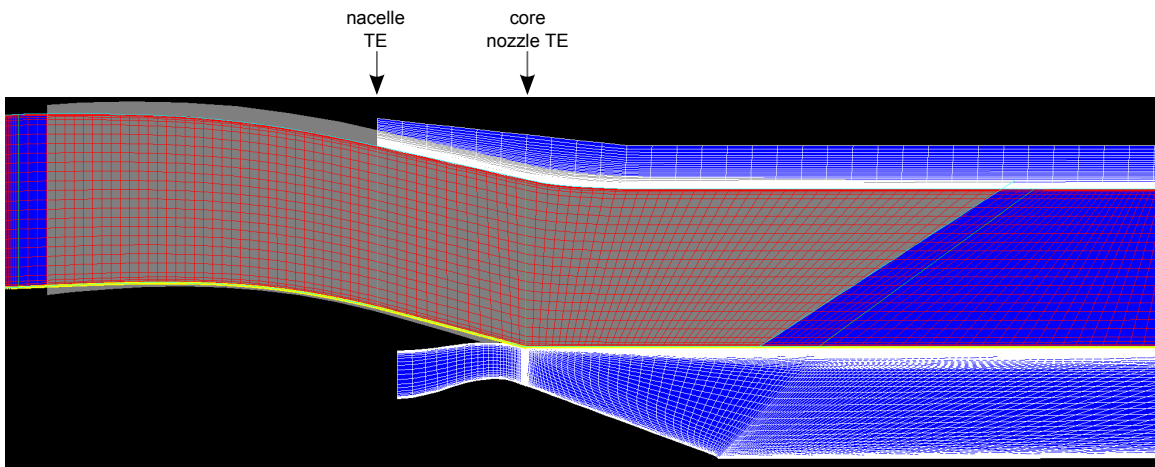


Figure E-3: Extent of pylon grid domain in meridional plane.

LE location. The bifurcation TE is normal to the cowl hub surfaces and closes out with the nacelle TE at the shroud, as depicted for example in Fig. 6-1. The grid generation of the bifurcation domains is simplified compared to the pylon domains since the bifurcation does not extend into the external flow downstream of the nacelle TE. The three-dimensional pylon and bifurcation grids are connected to the far-field mesh using non-matching boundary conditions as indicated in Fig. 5-7.